# Investigations on the Dynamics and Design of Uniflagellated Nanoswimmers using Resistive Force Theory

**THESIS**

Submitted in the partial fulfillment of the requirements for the degree of

**DOCTOR OF PHILOSOPHY**

by

**JITENDRA SINGH RATHORE**

Under the supervision of

**Prof. NITI NIPUN SHARMA**


**BIRLA INSTITUTE OF TECHNOLOGY & SCIENCE**

**PILANI – 333031 (RAJASTHAN) INDIA**

**2014**

# Investigations on the Dynamics and Design of Uniflagellated Nanoswimmers using Resistive Force Theory

**THESIS**

Submitted in the partial fulfillment of the requirements for the degree of

**DOCTOR OF PHILOSOPHY**

by

**JITENDRA SINGH RATHORE**

(2007PHXF402P)

Under the supervision of

**Prof. NITI NIPUN SHARMA**


BITS Pilani
Pilani | Dubai | Goa | Hyderabad

**BIRLA INSTITUTE OF TECHNOLOGY & SCIENCE**

**PILANI – 333031 (RAJASTHAN) INDIA**

**2014**


**BIRLA INSTITUTE OF TECHNOLOGY & SCIENCE**
**PILANI - 333031 (RAJASTHAN) INDIA**

# CERTIFICATE

This is to certify that the thesis entitled "**Investigations on the Dynamics and Design of Uniflagellated Nanoswimmers using Resistive Force Theory**" submitted by Jitendra Singh Rathore, ID.No. 2007PHXF402P for award of Ph.D. Degree of the institute, embodies original work done by him under my supervision.

Signature: _____

**Prof. NITI NIPUN SHARMA**

Professor, Mechanical Engineering Department
BITS-Pilani, Pilani Campus

Date: _____

*Dedicated*

*to*

*my late grandfather*

*Shri Raghuveer Singh Ji Shekhawat*

# ACKNOWLEDGEMENTS

First and foremost I am grateful to my respected supervisor Prof. Niti Nipun Sharma for his constant guidance and immeasurable insightfulness. It has been an honor to be his first Ph.D. student. He has always supported me with his patience, rigor and persistence. He helped me focus my question, and always gave the right critique.

I am immensely thankful to Prof. B N Jain, Vice-Chancellor, BITS-Pilani and Prof. G Raghurama, Director, BITS-Pilani for providing me the opportunity to teach in the Department of Mechanical Engineering of BITS-Pilani and allowing me to pursue my doctoral thesis by providing necessary facilities and financial support. I express my gratitude to Prof. S K Verma, Dean, Academic Research Division, BITS-Pilani for his constant official support and encouragement. I feel obliged to Prof. R K Mittal, Director (Special Projects) BITS-Pilani, Prof. Rambabu Kodali (former Head of the Department, Mechanical Engineering, BITS-Pilani) and Prof. Ajit Pratap Singh (Dean, Instruction and Admission, BITS-Pilani) for their support.

My sincere thanks to Prof. K S Sangwan, Head of the Department, Mechanical Engineering and entire faculty and staff of Department of Mechanical Engineering, BITS - Pilani for their kind moral support and assistance.

I thank Prof. M S Dasgupta, Prof. Sai Jagan Mohan, Doctoral Research Committee (DRC) and Doctoral Advisory Committee (DAC) members, Department of Mechanical Engineering, BITS-Pilani who spared their precious time to provide valuable suggestions that immensely helped in improving the quality of my Ph.D. thesis.

I also express my gratitude to all my colleagues in BITS-Pilani, in particular, Dr. Anshuman, Dr. B K Rout, Dr. Srikanta Routroy, Dr. Manoj Soni, Dr. Hitesh D Mathur, Dr. Arun Jalan, Dr. Murli Palla, Mr. K Vinayak, Mr. Sachin U Belgamwar, and Mr. Arshad Javed, who kept me motivated while I was engulfed into the thesis work. Special thanks to Dr. Sharad Shrivastava and Mr. Girish Kant for being with me in all the situations. I also take this opportunity to pay thanks to Mr. Maheshwar Dwivedy, Mr. S Subramanian, Mr. Rwitajit Majumdar, Mr. Deepak Krishnamurthy,

Mr. Rahul Singh, Ms. Neha Singh, and Ms. Shivani who have been a constant companion and source of inspiration during my time as a scholar.

I would also like to thanks Mr. Santosh Kumar Saini, Academic Registration & Counselling Division (ARCD), BITS-Pilani for his help in compilation of thesis. I also express my thanks to all other faculty and staff of ARC Division, BITS-Pilani, for their kind support and cooperation towards the completion of my thesis.

Finally, special thanks must go to my lovable family. My sincere thanks to my parents, my loving sisters and in laws for making all my dreams come true. Their love, support, motivation and all physical help have been immeasurable. My special loving thanks to my wife Aruna and my son Kumar Sambhav for all the sacrifices they have gone through these years for the successful completion of my thesis.

Dated: _____ **Jitendra Singh Rathore**

# ABSTRACT

Nanorobots are propitious to swim or fly compared with crawling and walking because of issues with desirable characteristics of high velocity, efficiency, specificity, controllability, and a simple propagation mechanism that can be realized with miniaturized parts. Inspired by the fact that microorganisms existing in nature function expeditiously under these circumstances, researchers have shown a great interest to conceptualize, model, analyze, and make micro-/nanosized swimmers (nanorobots) that can move in body fluids for applications such as targeted drug delivery, nanomedication, and in-viscera nanosurgery.

The study aims at dynamics and design of uniflagellated nanoswimmer with a focus on planar as well as helical wave propagation through a tapered flagellum. This study also proposes a methodology for assessing the candidature of any material for the fabrication of artificial flagella and possible manufacturing techniques.

To achieve the objective of proposed research, the thesis is divided in to six chapters. Since in this research study two separate cases of flagellar propulsion i.e. through uniform and tapered flagella, are used for their possible applications as nanorobots' propulsion mechanisms, the methodology, results and discussions are given separately under each heading and presented as different chapters (Chapters 3-4).

Chapter 1 introduces the problem i.e. investigation on dynamics of nanoswimmer. The significance of low Reynolds number and the limitations of propulsion modes at nanoscales are also presented. The aim of the present work is also given at the end of this chapter.

In Chapter 2, the reviews are organized chronologically in the field of flagellar propulsion and swimming strategies used in low Reynolds number hydrodynamics i.e. Planar wave propulsion and Helical wave propulsion. Scope of the present work is discussed at the end of this chapter.

Chapter 3 describes the solution methodology adopted for uniform flagella cases. Two strategies of flagellar propulsion; planar and helical wave propulsion, have been studied from a passive filament point of view. Design of propulsion with planar as well as helical flagella is proposed and a generalized analytical model is developed, simulated and

discussed. An elastohydrodynamic model of the filament has been created and the same is used to obtain the steady state shape of an elastic filament driven in a Stokes flow regime. Resistive Force Theory (RFT) which is very effective in predicting propulsion parameters for a given shape is used to study the propulsive dynamics of such a filament. The performance parameters of the developed model viz. velocity and efficiency have been computed based on resistive force theory and compared with those of the model available in literature. Optimization of physical parameters is carried out for each of the boundary conditions considered.

Chapter 4 presents investigation considering the effect of variation of diameter on planar and helical wave propagation. The modeling and simulation of planar wave as well as helical wave propagation through a tapered flagellum of a nanoswimmer for a given taper ratio is discussed. The performance parameters viz. velocity and efficiency are compared with the uniform diameter case. Taper diameter modeling of flagellum gives a superior performance by indicating higher velocity and efficiency.

The material selection for the flagella needs to be assessed on the criteria like biocompatibility, physical properties and technological feasibility. Chapter 5 provides a methodology for assessing the candidature of a material for the fabrication of artificial flagella that shall have implant capabilities and shortlist the potential material. The short listing is quintessential for attempts to engineer an artificial nanoswimmer.

Chapter 6 contains the summary of the conclusions and future scope of the present study.

***Keywords*****:** *Flagellar hydrodynamics, Micro/nano fluidics, Modeling in nanodomains, Nanorobotics, Nanoswimmer, Low Reynolds number flows, Motion of nanostructures, Nanoengineering*

# TABLE OF CONTENTS

# LIST OF TABLES

## LIST OF FIGURES

# LIST OF SYMBOLS

| | |
|---|---|
| $\rho$ | Fluid density |
| $\mu$ | Dynamic viscosity of fluid |
| $\vec{V}$ | Velocity vector |
| $p$ | Pressure |
| $t$ | Time |
| $\vec{F}$ | External force |
| Re | Reynolds number |
| $L$ | Length |
| $C_l$ | Tangential drag coefficients |
| $C_n$ | Normal drag coefficients |
| $\lambda$ | Flagella Wavelength |
| $T$ | External torque |
| $v$ | Translation velocity |
| $\omega$ | Flagellum angular speed |
| $\tilde{\nu}$ | Hyper-diffusion constant |
| $\dot{y}$ | First derivative of $y$ with respect to time |
| $y''''$ | Fourth derivative of $y$ with respect to space |
| $EI$ | Flexural/Bending rigidity |
| $Sp$ | Sperm number |
| $l$ | Scale length |
| $M$ | Torque generated |
| $F$ | Propulsive force |
| $U$ | Forward velocity |

| | |
|---|---|
| $r_h$ | Radius of head |
| $d$ | Half the thickness of the tail filament |
| $V_w$ | Wave speed |
| $h$ | Wave amplitude |
| $V_x$ | Velocity of flagellum in *x*-direction |
| $F_x$ | Thrust force |
| $l_o$ | Characteristic length |
| $\eta$ | Propulsion efficiency |
| $ds$ | Flagellum element |
| $\theta$ | Base angle of flagella |
| $dF_E$ | Elastic forces |
| $dF_V$ | Viscous forces |
| $E$ | Elasticity of the material of flagella |
| $I$ | Area moment of inertia |
| $y$ | Transverse displacement at any given position over length |
| $G$ | Maxima of time dependent slope |
| $y''$ | Second derivative of *y* with respect to space |
| $y'''$ | Third derivative of *y* with respect to space |
| $V_y$ | Transverse velocity |
| $dF_n$ | Normal force |
| $dF_l$ | Longitudinal force |
| $F_{head}$ | Drag due to the head |
| $\vec{r}$ | Position vector of any point on the flagellum |
| $\vec{v}_\perp$ | Transverse velocity of flagellum |

| | |
|---|---|
| $\tau_v$ | Viscous torque about centroidal axis |
| $V_z$ | Forward velocity for helical wave propelled nanoswimmer |
| $\Omega$ | Angular velocity of head |
| $F_z$ | Thrust force generated in case of helical wave propelled nanoswimmer |
| $M_z$ and $L_z$ | Components of torque generated due to circumferential force acting on the flagellum element |
| $\alpha(z)$ | Instantaneous amplitude |
| $\beta(z)$ | Pitch angle |
| $d\vec{s}_p$ | Projection of vector $d\vec{s}$ on a plane containing normal vector |
| $V_z$ | Swimming velocity in $z$ directions |
| $V_\theta$ | Swimming velocity in $\theta$ directions |
| $\varepsilon$ | Modification factor |
| $M_{head}$ | Torque experienced by spherical head |
| $C_n(x)$ | Local normal drag coefficients |
| $C_l(x)$ | Local longitudinal drag coefficients |
| $b_i$ | Radius of flagellum cross-section at $x = 0$ |
| $b_f$ | Radius of flagellum cross-section at $x = L$ |
| $k$ | Slope of linear taper |
| $I_o$ | Area moment of inertia at proximal end |

Chapter 1

# Introduction

## 1.1 SWIMMING: MACRO TO NANO

Moving things in nature present a wide variety of modes to achieve motion. More explicitly, some of them walk, others crawl, some hop, many fly and the remaining swim. Swimming becomes very important mode of motion as moving things become smaller in size. In fact, small sized objects are more propitious to swim or fly instead of crawl or walk [1-3]. Macro-sized swimmers propel themselves by hydrodynamic forces/thrust generated because of reversing the oar motion; oar may be hand in human swimming, fin flapping in fishes, actual oar of a boat/propeller in large/small sized ship sailing in water.

Hydrodynamics of macroswimmers are governed by the Navier-Stokes equation, which for an incompressible Newtonian fluid is given as [4]:

$$\rho\left(\frac{\partial \vec{V}}{\partial t}+\left(\vec{V}.\nabla\right)\vec{V}\right)=-\nabla p+\mu\nabla^2\vec{V}+\vec{F} \tag{1.1}$$

where $\rho$ is the fluid density, $\mu$ is the dynamic viscosity, $\vec{V}$ is the velocity vector and $p$ is the pressure, $\vec{F}$ is the other external forces acting over per unit volume, and $t$ is time. The left hand side in brackets represents the acceleration of the fluid; the first term represents the local acceleration, which vanishes if the flow is steady and the second term represents the convective acceleration, which involve the velocity change from point to point. The right hand side comprises three terms, which represents the forces due to pressure gradient, viscous stress tensor and other external forces exerted on a given volume, in the order respectively. Equation (1.1) holds for high Reynolds number (dimensionless number which is ratio of inertia forces to viscous forces) regime i.e. the inertial terms are much larger than the viscous terms and a macroswimmer rely on inertia for swim.

At small length scales (up to hundreds of micron), viscous forces dominate over the inertial forces leading to low values in Reynolds number ($\mathrm{Re} << 1$). In this regime, Navier-Stokes equation (1.1) reduces to Stokes equation because inertia terms are negligible and is given as

$$-\nabla p + \mu \nabla^2 \vec{V} = 0 \qquad (1.2)$$

Scientists and researchers [5-14] in last few decades have been interested in micro/nano swimmers. The small sized swimmers or for that matter miniaturization of any device in general has itself many advantages like resource conservation, low cost, low power consumption and easy disposability. Specially for nanoswimmers, small size of the order of a few hundreds of nanometers is additionally advantageous, because of being comparable to biologicals and therefore a possible use in bio-medical application.

Nature is very inventive in designing nanoswimmers as small sized organisms such as bacteria and many eukaryotic cells and their propulsion mechanism in a fluid environment. The environment is highly viscous to the miniaturized swimmers and exerts large resistive force to the miniaturized swimmers. The high viscosity of surrounding medium and low inertia of nano sized organism makes the governing hydrodynamics different from macro sized organisms and their motion difficult to happen at low Reynolds number. For example, nano sized organism swimming at low Reynolds number achieve motion by deforming the body rather than by using rigid cyclic oar motion as in macro size doers. Further, the motion is instantaneous and inertial forces are negligible for a nanoswimmer which is very different from a macroswimmer (overshooting from target point because of inertia is quite common for a macroswimmer). There are no external forces or torques except those exerted by surrounding fluid in context to nanoswimmer. The body undergoes asymmetric cyclic deformations and non-reciprocal motion in comparison to symmetric, reciprocal motion for a macroswimmer [2].

Nanoswimmers experience therefore, drastically different hydrodynamics compared to macro size swimming objects. For most sub-micron scale objects which are moving in water or any other fluid, the flow is characterized as Stokes flow and for this type of flow, the inertia terms in the Navier-Stokes equation are neglected. The time-dependent term are absent and implies that the generated propulsion force only depends on the relative position of propeller and not on the rate of motion. The concept of performing half of the stroke at a faster rate and the other half at a slower rate i.e. Scallop theorem (Figure 1.1), does not work towards propulsion in low Reynolds number domain.

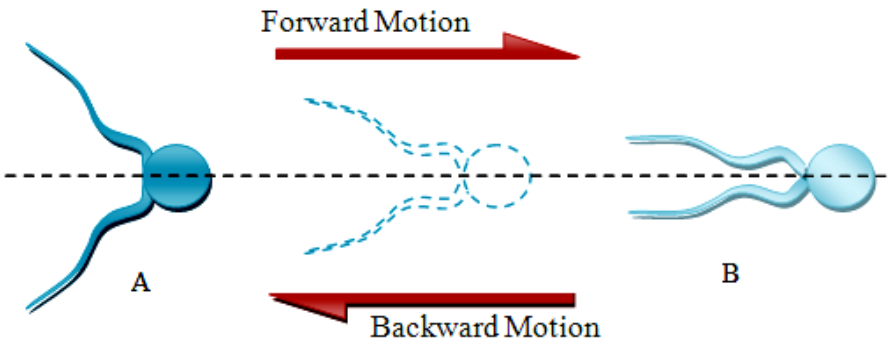


**Figure 1.1: Schematic depicting Purcell's scallop theorem**

For example in the motion of scallop (Figure 1.1), forward motion is by quickly closing scallop hinges (from position A to position B as shown in Figure 1.1) and then slowly opening (from position B to position A) leads to net translation at macro level (i.e. at $\mathrm{Re} \geq 1$). This happen because a quick closing causes a larger forward inertia force in comparison to lower backward inertia force during slow opening. The cycle of closing and opening therefore subjects the swimmer to net force forward and a net motion forward. But if the scallop were scaled down to be a few nanometers, this periodic forward and backward motion would cause negligibly different inertial force, more appropriately almost equal inertial force in forward and backward stroke and therefore results in no net displacement in nano regime (i.e. $\mathrm{Re} \ll 1$). Thus, reciprocal and time reversible motion fails in low Reynolds regime [2, 5, 7] and generated net propulsion depends on relative position of propeller and not on the rate of motion. The net propulsion has been efficiently achieved (as said in previous paragraph) by microorganisms by deforming their propellers and causing non reciprocal time irreversible motion.

The possibility of realization of an artificial autonomous swimming nanorobot (nanoswimmer) is possible by designing a deformable propeller in a mechanism to cause non reciprocal time irreversible motion. Such a nanoswimmer is going to be very useful having many applications in medical and health care for drug delivery and disease treatments [1, 8]. The subject of miniaturization has been initiated by R. Feynman [9] in his famous lecture "There’s Plenty of Room at the Bottom" first delivered at an American Physical Society meeting at Caltech in December 1959. After Feynman's talk, scientists and engineers have put forth tremendous effort and have come up with many micro/nano sized devices. The research towards realization of an autonomous nanoswimmer is also pursued for quite some time now and advancement in the direction

is available in literature [6, 13-15]. The feasibility of nanoswimmers is inspired by existence of organisms and biologicals at same size scales performing motion intelligently. Due to their small size, nanoswimmers move at very low Reynolds number (Re) because at small sizes the viscous forces are very high owing to significant surface effects and inertia is very less. Both the effects originate from the size miniaturization. Relevance of low Reynolds number is detailed in next section.

## 1.2 SIGNIFICANCE OF LOW REYNOLDS NUMBER

The Reynolds number (Re) is defined as the ratio of inertial force to the viscous forces per unit volume. It is written as [4]

$$\mathrm{Re} = \frac{\text{forces in fluid due to inertia}}{\text{forces due to friction (viscous)}} = \frac{\rho V L}{\mu}$$

where, $L$ is the length of the object, $V$ is the velocity, $\mu$ is the fluid viscosity, and $\rho$ is the density of fluid. So, flows at high Reynolds numbers are dominated by high inertia and/or low friction while at small Reynolds number, flow is one for which viscous forces are high and/or inertia is low.

The low inertia and high viscous forces are coupled with low efficiency and low convective motion in nano size regimes. For example, motion by beating of cilia and flagella at 30 μm/sec with 1% efficiency costs $2\times10^{-8}$ erg/s in bacterial movements [2]. The efficiency is too low when compared to ~30% in case of internal combustion engines. Though the efficiency is poor but is only a small fraction of the metabolism and the energy budget of the bacteria. The biological have sufficient amount of energy supply and are least concerned about energy efficiency. The issue of energy efficiency, though, will be of concern in nanorobots where power supply to the miniaturized robot and miniaturization of power supply both are going to be a challenge and nagging problem to engineers.

More explicitly, for example, in water ($\mu \approx 10^{-3}$ Pa.s, $\rho \approx 1000\,\mathrm{kg/m^3}$), a nanoswimmer such as *E. coli* bacteria ($L \approx 10\mu m$) with a typical velocity $V \approx 30\,\mu m/s$ has a Reynolds number $\mathrm{Re} \approx 10^{-5} - 10^{-4}$ whereas a human swimmer ($L \approx 2m$) paddling slowly in a swimming pool has a Reynolds number $\mathrm{Re} \approx 10^{4} - 10^{5}$. A human swimmer swims at a very high Reynolds number, and inertial terms are large. The human swimmer is able to glide (swims) long distance, however, a nanoswimmer like *E. coli* experiences high viscosity and almost negligible inertia thrust, and thus very small gliding (swimming) is possible. In a

world of low Reynolds number, the response of the fluid to the motion of boundaries is instantaneous [12-14]. So, when *E. coli* stops its motion, it is stopped immediately without any gliding or displacement.

Moreover, to achieve motion of an artificial nanoswimmer, two conditions need to be fulfilled. First, energy should be transformed into a mechanical deformation of the device. Second, the sequence of deformations must be cyclic and not time-reversible. The second requirement arises from the fact that fluid dynamics at nanometer scale is dominated by viscous rather than inertial terms. Keeping in view the issues and challenges discussed in above paragraph, design of propulsion mechanism for an artificial nanoswimmer is an interesting and challenging problem in front of scientists and engineers and is yet to be resolved. Purcell [2] has hypothesized three possible swimming mechanisms in low Reynolds number environments, namely; 'the flexible oar', 'corkscrew swimmer', and 'three link swimmer'. An example of the first case is eukaryotic cells use flagella (refer Figure 1.2a) that resemble elastic rods and exhibit a beating motion: internally generated stresses give rise to a series of bends that propagate towards the tip. In second case, helical shaped bacterial flagella (refer Figure 1.2b), driven at the bases by a reversible rotary engine, which rotates the attached flagellum to give a motion similar to that of a corkscrew. Purcell's three link swimmer (refer Figure 1.2c) had three rigid links that could move independently to generate a nonreciprocal motion. The three mechanisms are shown in Figure 1.2.

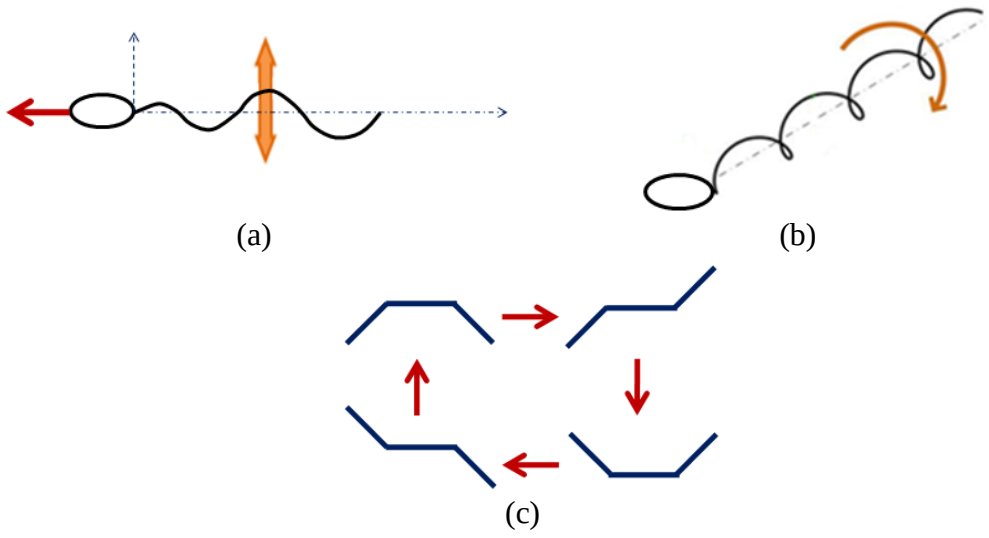


**Figure 1.2: Locomotion strategies [2] employed by nano-bio-organisms (a) beating flagellum, (b) rotating flagellum and (c) three-link swimmer**

Scientists have worked on the mechanism conjectured by Purcell and others [5, 7, 9, 13-15]. The state of art on design of propulsion mechanism for a nanoswimmer is still not materialized and the propulsion debate is still open. Keeping in view the great utility of nanoswimmer in drug delivery [1, 8], in viscera surgery [8], surveillance [13], it is interesting to work on realization of nanoswimmer and certainly therefore design for its propulsion mechanism.

## 1.3 MOTIVATION

Nanorobotics is emerging technology attempting to create miniaturized machines or swimmers of the size of a few hundred nanometers and below, consisting of components of nanoscale or molecular size and with certain functionalities of their macrocounterparts [13]. Nanorobots are more propitious to swim or fly [1]. In the past two decades, there has been an all around development in nanotechnology including nanofabrication, facilitating realization of nanorobots. Scientists and engineers have shown a great interest to conceptualize model, analyze and make nanosized machines, mechanisms and structures in past two decades [2-14]. The prime reason for advancing attempts in the field of nanorobotics are the unique applications of the nanorobots in medical, health care and environmental monitoring, which are attributable to the size of nanorobots comparable with biological entities. Moreover, feasibility of nanorobots is inspired by the existence of organisms and biologicals at the same size scales performing in robust manner and intelligently. There is growing literature on the subject and few attempts have been made towards the realization of autonomous nanoswimmers swimming in biological fluids. The state of art on nanorobots at present though still is in its nascent stage of evolution and synthesis of a fuel efficient nanoswimmer which performs controlled propulsion from internal excitations, and is still a distant dream.

Among many facet in the realization of nanoswimmer the motion by swimming is first challenge among others wherein we require an integral and efficient blending attempt of miniaturization of four major areas, namely, energy storage, transduction of energy to motion, transmission mechanism for motion in swimming and control of motion. This is shown schematically in Figure 1.3.

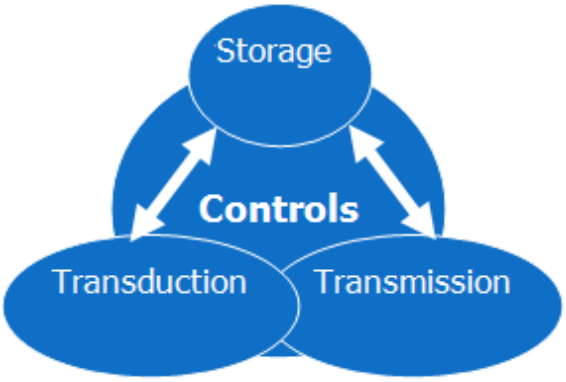


**Figure 1.3: Schematic of interrelated issues in motion of nanoswimmer**

For realizing motion of nanoswimmers, a well designed propulsion system is required which must overcome various resistive forces significant in nano-domains. Various scaling effects have been discussed in literature pertinent to motion of small-sized entities including synthesized particles and mechanisms and natural organisms [13]. For instance, energy has both storage and a transactional character. For nanoswimmers, onboard volume is a precious and limited commodity. Viscous forces dominate inertial and gravitational forces, so mass is almost irrelevant. Hence energy stored per unit volume ($J/m^3$) is an appropriate index for nanoscale energy storage devices. The issue of energy storage is further complicated because of related transduction and transmission issues. In context to motion of nanosized entities, some of the relevant issues and related problems are of significant importance for motion of nanoswimmers and are shown in Figure 1.4.

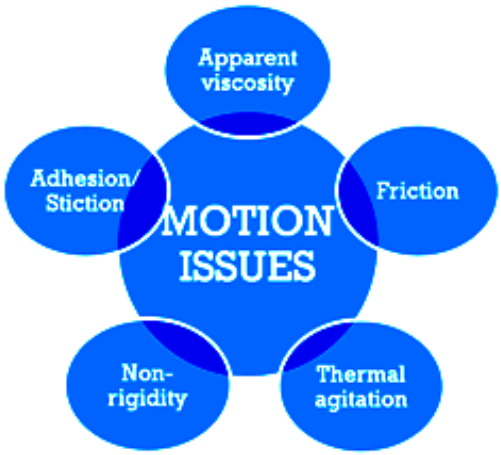


**Figure 1.4: Schematic of motion issues in nanodomains**

Further the understanding of physics of locomotion in nanosized domains is a problem of motion because at such size domains the object (in present case nanoswimmer) will encounter low Reynolds number i.e. high viscous and low inertia forces. Nanoswimmers are important because of their potential use for the purpose of drug delivery, monitoring and diagnostics for *in-vivo* biomedical application. They mimic microorganisms and mostly modeled as propelled by beating or rotating flagella. Survival and existence of microorganisms like *E. coli* at an operating efficiency of 1% is amazing but that is allowed in nature because the power consumption by *E. coli* in propelling themselves is of the order of Pico watts. Considering abundant amount of energy available in surrounding, *E. coli,* there is certainly no concern for low efficiency. The propulsion of *E. coli* is like a very inefficient car design but with unlimited supply of fuel. For an artificial nanoswimmer, the limitations like low efficiency is not tolerable and an improved design is a challenge posed to researchers. The design parameters like mechanism, shape and size of oar, material of oar needs to be investigated and optimized for realization of an efficient nanoswimmer. For example, in almost all models available in literature on design of propulsion mechanism of a nanoswimmer mostly flagella is used as oars and diameter of the flagellum is considered constant. In nature, though, the flagella of the nanoswimmer is not of constant diameter. The actual profile of flagella is tapered and the head of the nanoswimmer is a sphere in shape. The material consideration is also quite complex as far as usage/application of nanoswimmers matters. For example, for *in vivo* applications of a nanoswimmer, biocompatibility is of prime importance; fabrication technology with a kind of material may be a limitation in choice of the material. The debate therefore is to consider different designs of flagellum, model drag accordingly and investigate different designs to achieve certain acceptable efficiency, higher velocity, and higher thrust force in the motion of the nanoswimmer.

Along with modeling and design of shape and size of nanoswimmers, the material selection for the flagella is important but had been least addressed by researchers and needs to be assessed on the criteria like biocompatibility, physical properties and technological feasibility. The research is quintessential for attempts to engineer an artificial nanoswimmer. Keeping in mind *in vivo* medical applications of the artificial nanoswimmer, the present research has investigated the design issues namely, shape and material of the flagella of the nanoswimmer. Towards this objective, we present the available literature in context and formulate the problem statement investigated in next chapter.

## References


1. Requicha AAG (2003) Nanorobots, NEMS and Nanoassembly, Proc. IEEE, 91 (11), pp. 1922-1933.
2. Purcell EM (1977) Life at low Reynolds Number, Amer J Phys, 45, pp. 3-11.
3. Lighthill J (1989) Mathematical Biofluiddynamics, SIAM, Philadelphia, 3rd edition.
4. Happel J, and Brenner H (1965) Low Reynolds Number Hydrodynamics, Prentice Hall, Englewood Cliffs, NJ.
5. Childress S (1981) Mechanics of Swimming and Flying, Cambridge University Press, Cambridge, UK.
6. Rathore JS, and Sharma NN (2010) Engineering Nanorobot: Chronology of Modeling Flagellar Propulsion. J Nanotechnol Eng Med, Transactions of the ASME 1(3) 031001, pp. 1-6.
7. Brennen C, and Winet H (1977) Fluid Mechanics of Propulsion by Cilia and Flagella, Ann Rev Fluid Mech, 9, pp. 339-398.
8. Freitas RA Jr. (1999) Nanomedicine, Volume I: Basic Capabilities, Landes Bioscience, Georgetown, TX; http://www.nanomedicine.com/NMI.htm
9. R Feynman (1959) Annual Meeting of the American Physical Society. California Institute of Technology, December 29th, 1959.
10. Behkam B, and Sitti M (2005) Modeling and Testing of a Biomimetic Flagellar Propulsion Method for Microscale Biomedical Swimming Robots, Proc of International Conference on Advanced Intelligent Mechatronics, IEEE/ ASME, Monterey, California, July 24-28, 2005, pp. 37-42.
11. Wiggins CH, and Goldstein RE (1998) Flexive and Propulsive Dynamics of Elastica at Low Reynolds Number, Phy Rev Lett, 80, pp. 3879-3882.
12. Siva Kumar M, and Philominathan P (2009) The Physics of Flagellar Motion of E.coli during Chemotaxis, Biophys Rev, 2, pp. 13-20.
13. Sharma NN, and Mittal RK (2008) Nanorobot Movement: Challenges and Biologically Inspired Solutions, International Journal of Smart Sensing & Intelligent Systems, 1 (1), pp. 87-109.

14. Lauga E, and Powers TR (2009) The Hydrodynamics of Swimming Microorganisms, Reports on Progress in Physics, 72(9), pp. 1-58.
15. Wolgemuth CW, Powers TR, and Goldstein RE (2000) Twirling and Whirling: Viscous Dynamics of Rotating Elastic Filaments, Phy Rev Lett, 84, pp.1623-1626.

# Chapter 2

# Literature Review

## 2.1 INTRODUCTION

In the previous chapter, we discussed the relevance and motivation to investigate nanoswimmers. Here, nanoswimmer refers to an artificial swimmer having mechanism to propel with overall dimensions (ranging in size from 0.1-100 micrometers) below the millimeter range and made of nanometer scale components. The nanoswimmer consists of a tail i.e. a flagellum few micro-meters long, made of a bio-compatible material, which may be of uniform diameter throughout the length or of tapered diameter, attached to a spherical or an elongated head. The one with uniform diameter flagellum will be called in this thesis as "uniform diameter nanoswimmer" (UDN) and one with tapered flagellum will be called as "tapered nanoswimmer" (TN). Scientists and researchers [1-12] interest in nanoswimmer is increasing over the past few decades and significant published literature is available on nanoswimmer in context to their applications in drug delivery, nanorobotics, surveillance, fault diagnosis in pipes and many other. Most of the available literature on nanoswimmers is on the modeling and propulsion mechanisms.

The study of swimmer at low Reynolds number has a long history of scientific investigation starting from Ludwig [13] to a most recent study in Zhang et al. [14], has been discussed. This chapter reviews the modeling of physics as investigated since 1930 of flagellar propulsion for both planer and helical waves in engineering nanorobots. To examine the hydrodynamics of swimming microorganisms, researchers have proposed different theories to model the flagellar propulsion through planar wave and helical wave. Among existing theories in flagellar propulsion such as resistive force theory (RFT) [15], slender body theory (SBT) [16], the bead model (BM) [17] and boundary element method (BEM) [18], RFT has been widely used by researchers due to its simplicity and relative ease of application for obtaining approximate results for uniflagellated nanoswimmers, though it does not account for the interactions between the flagellum and the cell body or flow boundaries in a systematic manner. The progress in designing the propulsion system of a nanoswimmer are reviewed, and various interdisciplinary aspects of realizing

an autonomous nanoswimmer and issues in moving nanoswimmers have been presented chronologically. Further in this chapter, the gaps in the research and the problem statement of the thesis is given.

The Chapter is compiled in three more sections; the first gives a chronological compilation of significant work on modeling physics of flagellar propulsion. This is followed by the section in which gaps in the published research work has been compiled. Section 3 gives the conclusions and the problem statement of the thesis.

## 2.2 PHYSICS OF FLAGELLAR PROPULSION

Nanoswimmers experience drastically different hydrodynamics compared to macro scale swimming robots. The time-dependent terms in Navier-Stokes equation are absent and the propulsion force depends on the relative position of the propeller and not on the rate of motion (refer section 1.1 of Chapter 1). It has been shown that planar bending waves and corkscrew can create motion in nanosize domains. A recent experimental realization of the first man-made micro-swimmer [19], nanoswimmer speeding at 10 mm/sec [20], a controlled propulsion of artificial magnetic nanoswimmer [21], and fabrication of artificial bacterial flagella [22-23] are examples of engineered swimming motion in nanosized domain. The swimming nano-bio-organisms use active and rotating or beating cilia or rotating flagella [24-32] as major methods of movement (refer to Figure 2.1).

**Figure 2.1: Schematic of planar and helical propulsion**

Ludwig [13] observed that a microorganism that waves rigid arms like oars is incapable of net motion. Sir Geoffrey Taylor explained hydrodynamics of swimming micro-/nanosized object in early 1951 [33]. The propulsion element flagellum was modeled as an infinite cylindrical filament executing small-amplitude planar and helical waves in an un-bounded fluid. The resulting stress and motion in the surrounding fluid was analyzed mathematically for progressive planar waves [34] as well as helical waves of smaller amplitudes and it was concluded by Taylor that the energy dissipated by two neighboring

flagellar waves beating in phase with each other is much less than the energy dissipated if they were beating out of phase.

Hancock [16] considered the line distribution of Stokeslets and doublets along the oscillating filament centerline. The strengths of these singularities were determined using boundary condition of no-slip on the flagellar surface, with the condition that the total energy of the induced velocity field remains finite. Gray and Hancock [15, 35] assumed that the head of the nanoswimmer travels along the axis of progression without oscillating from side to side and developed resistive force theory (RFT) for flagellar hydrodynamics. Gray and Hancock [15] explained spermatozoa propulsion by flagellar bending waves and obtained the propulsive speed of spermatozoon in terms of amplitude, wave length and frequency of waves passing down the tail of spermatozoon. The two approximations of tangential ($C_l$) and normal coefficients ($C_n$) of viscous resistance acting on the surface of a long thin cylindrical filament in motion through a viscous fluid of viscosity μ are being used to date in RFT,

$$C_l = -\frac{2\pi\mu}{\ln\left(\frac{b}{2\lambda}\right)+\frac{1}{2}},\ C_n = -\frac{4\pi\mu}{\ln\left(\frac{b}{2\lambda}\right)+\frac{1}{2}} \tag{2.1}$$

The parameters $b$ and $\lambda$ are the amplitude and wave length of the flagella, respectively. Machin [36] modeled wave propagation along an elastic filament and explained the passive and active elastic filaments. Machin [36] considered flagella to be made from contractile elements throughout its length in order to explain propagation mechanism. Chwang and Wu [37] compared the features of planar and helical waves, in terms of their propulsive velocities and power consumption. In a similar study, Blake [38] has shown that an infinite cylinder can propel itself through a viscous liquid at low Reynolds number if it has certain undulations on its surface. Berg and Anderson [39] considered a biological motor at the base of flagella [15]. Keller and Rubinow [41] assumed that the axis of flagellum makes a small angle with the axis of helical path and showed that the trajectory of the microorganism is a helix of small radius instead of a straight line and confirmed that non rigid body motion can propel itself headless. A combination of flagella filaments for *Spirillum sp.* bacteria was analyzed by Winet and Keller [42], and it was found that at least one of the bundles of the bacteria contributes to balanced force component and helps in swimming. de la Torre and Bloomfield [17] used the bead model to study helical flagella and replaced the helical flagellum by a discrete array of frictional

beads along its centerline. Lighthill [43] reviewed the slender body theory (SBT) and analyzed cell body-flagella interactions and derived solutions for the resistance coefficients $(C_l)$and $(C_n)$ as

$$C_l = \frac{4\pi\mu}{\ln\left(\frac{0.0324\lambda^2}{b^2}\right)-1}, C_n = \frac{8\pi\mu}{\ln\left(\frac{0.0324\lambda^2}{b^2}\right)+1} \tag{2.2}$$

Chwang and Wu [44-45] and Johnson [46], published on improved SBT. The seminal talk on "Life at low Reynolds number" by Purcell [47] led to further research in the field of modeling, simulation and parametric influence investigation for a nanoswimmer. Purcell conceptualized three possible mechanisms for propulsion in low Reynolds number swimming domain, namely, flexible oar, corkscrew swimmer, and three link swimmers. Further, Purcell concluded via symmetry arguments that the net displacement of a three link swimmer must follow a straight line, but the direction and other details of motion were not discussed. Purcell introduced an important property of swimming without inertia, namely; the scallop theorem. The low Reynolds number flows associated with microorganism propulsion and the hydromechanics of ciliary systems were reviewed by Brennen and Winet [48]. Rikmenspoel [49-50] considered flagellum as a thin tapered rod, which was clamped at the mid-piece and carried out the detailed observations of the tail movement of non-rotating and rotating bull spermatozoa and shown that the stiffness of the tail is most probably caused by collagen-like material in the fibrous sheath of the tail. Johnson and Brokaw [51] investigated the accuracy of the RFT, commonly used for hydrodynamic analysis of swimming flagella by comparing the distribution of forces, bending moments, and shear moments along the flagellum length calculated by the more accurate slender-body theory for large-amplitude, planar wave forms. RFT is better where the cell body is absent or very small. Next, Lowe et al. [52] explored the rapid rotations of the swimming bacteria and found that the bundle frequency (rotation rate) is closely correlated with swimming speed (except at higher viscosity) and that it decreases with increasing viscosity.

Shapere and Wilczek [53] studied the efficiencies of swimming motions due to small deformations of spherical and cylindrical bodies at low Reynolds number and determined optimal swimming strokes. In another study, Shapere and Wilczek [54] showed swimming motions for cylinders with a variety of cross-sections. The works on nanosized object swimming were reviewed by Sleigh [55].

The boundary element method (BEM) has been successfully applied to low Reynolds number domain, i.e., Stokes flow problem by many researchers such as Phan-Thein et al. [18], Ramia [56], Ramia et al. [57], Nasseri and Phan-Thein [58-59], Fujita and Kawai [60], and Trachtenberg et al. [72]. BEM is applicable to uniflagellated to multiflagellated organism and allows the variations in geometrical parameters. Further, discretization of boundary reduces the number of unknowns tremendously. Phan-Thein et al. [18] optimized the geometrical parameters to get maximum swimming speed for given power dissipation and input. Ramia [56] applied boundary element method to study the locomotion of a microorganism and predicted the instantaneous swimming velocity, counter-rotation angular velocity, and power dissipation of a given organism as functions of time and the geometry of the organism. Unlike previous approaches such as RFT and SBT, this method is not restricted to slender bodies, hence allows for the consideration of realistic organism geometries.

Ramia et al. [57] considered wall and neighbor element effects and applied boundary element method to study the locomotion of a microorganism and determined the optimal geometrical parameters to attain maximum swimming speed for a given power dissipation. The swimming of a spherical cell body, propelled by a single rotating flagellum near a plane boundary, midway between two plane boundaries or in the vicinity of another similar organism, was investigated. It was found that only a small increase (less than 10%) results in the mean swimming speed of an organism swimming near and parallel to another identical organism. Nasseri and Phan-Thein [58] used BEM to model the locomotion of micromachine with planer as well as helical rigid tails.

The necessity of tail shaping and elasticity of tail were observed to be the two key parameters to improve the efficiency of micromachines and were analyzed by a number of researchers. Further, Nasseri and Phan-Thein [59] in another work, modeled a micromachine with capsule-shaped head propelled by a rigid spiral tail using BEM and optimized geometrical parameters to attain highest translation velocity. Fujita and Kawai [60] calculated the optimum shape of a spiral flagellated microorganism using boundary element method and examined how the microorganism shape affects their motion. It was stated that eight parameters, namely, turn of flagellum, helical radius, length of magnified part, which was equal to helical wave number/magnification coefficient, radius of flagellum, length of flagellum, head aspect ratio, length ratio of front head to rear, flagellum ellipticity, affects the locomotion of microorganisms.

Andrietti and Bernardini [61] studied the swimming of flagellated microscopic organisms with a helical head and a helical pattern of flagellar beating, using a theoretical approach similar to Chwang and Wu [37]. The main finding of Andrietti and Bernardini [61] was that the helical shape of the head seems to increase the efficiency of propulsion of the spermatozoon when compared with the more commonly shaped spherical head.

Purcell [62] examined the relationships between external force (*F*) and external torque (*T*) applied on flagellum of a nanoswimmer as a function of translational velocity *v* and angular speed ω of flagellum to understand the nature of flagellar propulsion and concluded that the propulsion matrix of a propeller is proportional to the fluid viscosity μ and depend otherwise only on the shape and size of the propeller

$$F = Av + B\omega;\ T = Cv + D\omega \tag{2.3}$$

where A, B, C, D are the coefficient of propulsion matrix, also known as resistance matrix $\begin{pmatrix} A & B \\ C & D \end{pmatrix}$ and are proportional to fluid viscosity.

The works referred above did not consider the flagella elasticity issues in wave propagation. Wiggins and Goldstein [25] demonstrated the effect of elasticity on propulsion at low Reynolds number and determined the shape of tail using elastohydrodynamics and modeled as

$$\dot{y} = -\tilde{\nu} y'''' \tag{2.4}$$

where $\tilde{\nu}$ is hyper-diffusion constant and is defined as $\tilde{\nu} = A_a / C_n$ , and $\dot{y}$ and $y''''$ are the first derivative with respect to time and fourth derivative with respect to space, respectively. $A_a$ is the bending moment of elastic filament and $C_n$ is the normal drag coefficient.

Further, Wiggins et al. [63] explored elastohydrodynamics by coupling elasticity theory and overdamped viscous hydrodynamics of single semiflexible filaments executing the planar motion. Assuming small-amplitude deformations, Wiggins et al. obtained analytical solutions for the time-dependent shapes of moving polymers, one end of which was moved in an impulsive or oscillatory way. Camalet et al. [64] studied self-organised flagellar beating due to internally driven filaments and have

demonstrated that a pair of elastic filaments held together by an active, force-generating material, can induce wavelike patterns by a dynamic instability of the system. The resulting patterns of motion do not depend on the microscopic mechanism of the instability but only of the filament rigidity and hydrodynamic friction. Camalet et al. [64] suggested that the boundary conditions imposed at the ends select the type of beating pattern.

Wolgemuth et al. [65] studied the overdamped nonlinear dynamics of a rotationally forced filament with twist and bend elasticity, considering flagella as a shaft and studied about twist injection, twist diffusion, and writhing. It was found that at small rotating frequency, the shaft i.e., flagella, will remain straight but when the twist torque is comparable to filament buckling torque, flagella becomes unstable.

Koehler and Powers [66], studied effect of the twist on the deformation and torsional stress of a twisted elastic rod immersed in a viscous fluid of low Reynolds number neglecting Brownian effects and experimentally elucidated the interplay of viscous drag, twisting, and bending in the overdamped dynamics of twisted filaments immersed in a viscous fluid of low Reynolds number.

Camalet and Julicher [67] studied the dynamics of an elastic rod-like filament in two dimensions, driven by internally generated forces. The situation was motivated by cilia and flagella which contain an axoneme (cylindrical arrangement of nine doublets of parallel microtubules, and one pair of microtubules in the centre). Camalet and Julicher [67] discussed the effects of the boundary conditions and externally applied forces on the axonemal wave forms and calculated the swimming velocity for the case of free boundary conditions.

Goto et al. [68] analyzed the swimming motion of a monotrichously flagellated bacterium model using SBT and investigated the effects of the dimensions of the flagellum on the swimming speed and efficiency. Optimum shape for the fastest swimmer and the most efficient swimmer were calculated and compared with the flagellum existing on micro-organisms [69].

Lowe [69] described a method for simulating the inertia-less dynamics of a flexible filament immersed in a fluid and plotted the swimming speed and efficiency as a function of sperm number.

Lowe [69] proposed one dimensionless parameter Sperm number (*Sp*), which characterizes the relative magnitudes of the viscous and bending forces and was given as

$$Sp = \left( \frac{L^4 \omega C_n}{EI} \right)^{\frac{1}{4}} \tag{2.5}$$

where $L$ is the length of the filament, $EI$ is the bending rigidity, $\omega$ is the angular frequency, and $C_n$ is the perpendicular friction coefficient for the filament. A low value of sperm number implies that bending forces dominate, a high value that viscous forces dominate. At a sperm number (*Sp*) 2, both the swimming speed and efficiency (although not at exactly the same value) were find to be maximum.

For a precise and successful working of a nanoswimmer, it is quintessential that their moving mechanism should be properly designed. Researchers are trying to learn more and more from the nature and analyzing microorganisms in order to engineer nanorobot. Magariyama et al. [70] experimentally verified that the ratio of backward and forward swimming speeds of a *Vibrio alginolyticus* cell with a single polar flagellum was 1.5. The characteristics in speed of *Vibrio alginolyticus* were found to be different from the *E. Coli* characteristics. Later on, forward speed was found to be equal to the backward speed. Magariyama et al. mathematically developed the model given by Berg and Turner [4] using modified RFT. The modification includes introduction of two apparent viscosities in the existing RFT.

Woolley and Vernon [71] suggested that the ability of the flagellum to adapt planar or helical wave form depends upon environmental conditions. Raising the external viscosity or reducing the force of active sliding should increase the likelihood of helical waveform.

Powers [72], developed theory of bundle formation and demonstrated the importance of body rotation for flagellar filament bundling as it helps to propel the bacteria. Using RFT, Powers [72] had shown that the counter-rotation of the cell body necessary for torque balance is sufficient to wrap the filaments into a bundle, even in the absence of the swirling flows produced by each individual filament. Helical shape of the flagellar filament and the flows induced by the individual filaments were not taken into account.

The scale length [72] plays an important role in determining the rigidity or flexibility of a flagellum. The scale length (*l*) associated with bending and drag was defined as

$$l = \left( \frac{EI}{C_n \omega} \right)^{\frac{1}{4}} \tag{2.6}$$

where *EI* is the bending rigidity, $\omega$ is the angular frequency, and $C_n$ is the normal drag coefficient for the filament.

Trachtenberg et al. [73] analyzed the actual three dimensional reconstructions of bacterial flagellar filaments (propellers) rather than treating them as smooth, coiled cylinders or their center lines, as has been done in previous applications of the boundary element method and worked toward the role of flagella surface in flow transition. Flagella Surface complexity was found to be a crucial factor in formation and dispersion of flagellar bundles (key parameters in chemotaxi).

Takano and Goto [74] used RFT and Kirchhoff rod model for the numerical analysis of flexible helical flagellum of swimming bacteria. Propulsive speed of the bacteria was determined, taking deformation in account and demonstrated that the backward speed is slightly faster than the forward speed.

Edd et al. [75], worked on design aspects of a surgical microrobot and explained the four quadrant propulsion system for maneuvering and shown that use of carbon nanotubes as synthetic flagella is the possible tool of effective locomotion. The robot would be capable of traveling at almost 1mm/s with a 2% hydrodynamic efficiency for 1 nW of power, with 100 μm long filaments.

Becker et al. [76] using slender-body hydrodynamics in the inertialess limit, showed that the direction of net translation and the speed of the swimmer depend on the angular amplitude of the swimming strokes as well as on the relative length of the links.

Lagomarsino et al. [77] worked on large-amplitude motion and found that the dependence of the swimming speed on both sperm number and amplitude was significantly modified, relative to the small-amplitude case. To compare the efficiencies of different swimmers, Avron et al. [78] introduced a swimming drag coefficient which allowed for the ranking of swimmers at low Reynolds numbers. The smaller the swimming drag coefficient, the more efficient was the swimmer.

Kim and Powers [79] studied hydrodynamic interaction between rotating rigid helical flagella and used SBT to study bundling of flagella. Using numerical slender-body calculations and symmetry arguments, Kim and Powers [79] calculated the hydrodynamic forces and moments on nearby rotating helices at zero Reynolds number and showed that for two rigid helices rotating with zero phase difference, there was no time-averaged attractive or repulsive force between the helices.

The singly flagellated bacterium, *Vibrio alginolyticus*, moves forward and backward by alternating the rotational direction of its flagellum. When the cell swims close to a wall, the forward and backward speeds differ noticeably as was suggested in the work of Goto et al. [80]. This study detailed a boundary element model for the motion of a bacterium swimming near a rigid boundary and the results reveal that forward motion is more stable than backward motion with respect to pitching of the bacterium.

Flores et al. [81] presented computational model of the interaction of multiple bacterial flagella. Flores et al. [81] modeled the elasticity of the flagella with a network of elastic springs and found that the maximum swimming speed of single flagellum bacteria occurs at a certain value of the pitch of helical flagella irrespective of its length. Flores et al. also explained the bundling and tumbling in three flagella model and found that the counterclockwise rotation of all the flagella leads to bundling. With flagella motor rotating in opposite direction, the hydrodynamic interaction disturbs and leads to tumbling. Tumbling occurs in a faster time scale than bundling.

Behkam and Sitti [82] worked on various aspects of nanorobotic propulsion starting from *E. Coli* inspired propulsion based on RFT, modeling and testing of biomimetic flagellar propulsion method, and hybrid microrobot. Behkam and Sitti [82] introduced the biomimetic propulsion mechanism inspired by flagellar motion of bacteria. The key parameters such as velocity, distribution of force, and power requirements for different configurations of tail were determined by Behkam. Applying Buckingham's Pi theorem, a scaled-up model of the robot was constructed and tested in silicone oil. Another common method of propulsion among microorganisms is known as eukaryotic flagellar motion. Behkam and Sitti [83] further suggested that kinematic and dynamic analysis of this motion and comparison between the results of prokaryotic and eukaryotic flagellation would yield an effective design methodology for microscale swimming robots. The developed hydrodynamic models [83] were optimized for design parameters for each of two propulsion models i.e., prokaryotic and eukaryotic microorganisms. The

experiment was done for single flagella, and thrust force, torque, velocity, and efficiency were determined and compared with the scale- up model.

Behkam and Sitti [84] used following relations for the non-dimensional analysis of force, torque and velocity

$$\frac{M}{\mu\omega L^2} = f_M\left(\frac{A}{L},\frac{r_h}{L},\frac{\lambda}{L},\frac{d}{L}\right),\ \frac{F}{\mu\omega L^2} = f_{F_x}\left(\frac{A}{L},\frac{r_h}{L},\frac{\lambda}{L},\frac{d}{L}\right),\ \frac{U}{L\omega} = f_U\left(\frac{A}{L},\frac{r_h}{L},\frac{\lambda}{L},\frac{d}{L}\right) \quad (2.7)$$

where, $M$ is torque generated, $F$ is the propulsion force, $U$ is the forward velocity, $A$ is the amplitude of the helix, $r_h$ is the radius of head, $\lambda$ is the wavelength of the helix, $d$ is half the thickness of the tail filament and $L$ is the length of tail filament.

One of the issues in the work of Behkam and Sitti [84] was that thrust force and efficiency were calculated based on velocity component of larger amplitude wave, while the modeling was done with assumption of low amplitude wave. Majumdar et al. [85] made the appropriate corrections in the existing theory, and it was demonstrated that thrust force changes with viscosity of the medium as well and given as

$$F_x = \left[\lambda V_x - 2\frac{\pi^2 h^2}{\lambda} V_w\right] \frac{2\pi\mu}{\log\left(\frac{d}{2\lambda}\right) + \frac{1}{2}} \quad (2.8)$$

where, $F_x, \lambda, V_x, h, V_w$ and $d$ denote total thrust force, wavelength, velocity of flagellum in positive $x$-axis, amplitude of wave, wave speed, and filament thickness respectively.

The locomotion and manipulation dynamics of miniature robots are dominated by micro/nano-scale forces and the scaling effects. Manghi et al. [86] studied dynamics of rotating elastic filament and found a nonlinear relationship between applied torque and angular frequency in the presence of external load. Manghi et al. [86] had shown that rotation of elastic rod with constrained azimuthal angle give rise to forward thrust independent of sense of rotation. Chattopadhyay et al. [87] made use of optical tweezers and measured dynamic properties of bacteria such as torque and swimming speed of *E. coli*. Microscopic properties of the flagellar bundle [46] was estimated using the resistive force calculations for a helical coil. The propulsive efficiency, defined as the ratio of the propulsive power output to the rotary power input provided by the motors, was measured to be ≈ 1.7 %, which was consistent with the efficiency predicted theoretically for a rigid helical coil [46, 72].

Roper et al. [88] shown that the dynamics of magnetically driven micro-swimmers are an admixture of the gaits of a flagellum and of an elastic rod that is waggled from side to side. Recent advances in micro-machining allow very small cargos, such as single red blood cells, to be moved by outfitting them with tails made of micrometer-sized paramagnetic particles yoked together by polymer bridges. When a time-varying magnetic field is applied to such a filament, it bends from side to side and propels itself through the fluid, dragging the load behind it.

Yu et al. [89] experimentally investigated Purcell's flexible oar swimmer. A microswimmer was constructed and both tail shape and propulsive force were measured. Measurements of propulsive forces and time-varying shapes were in agreement with the results of resistive-force theory.

Sudo et al. [90], examined the wireless magnetic swimming mechanism for the development of medical micro robots working in human blood vessels. Locomotive characteristics of the swimming mechanism in a viscous liquid were analyzed by a high-speed video camera system. The effect of fluid viscosity on the locomotive characteristics of the magnetic swimming robot was also reported.

Lauga [91] presented an analytical treatment of the locomotion of an elastic swimmer in the limit of small amplitude actuation and characterized the geometry and performance of optimal swimmers. The efficiency range (typically 0.1% - 0.4% efficiency) reported for the most efficient elastic swimmers were comparable although smaller than the typical real swimming micro-organisms (usually 1% - 2% swimming efficiency). Swimming using multiple elastic filaments was also discussed for the better control on the swimming trajectories.

Researchers have proposed numerous microrobotic swimming methods, with the vast majority utilizing magnetic fields to wirelessly powered and controlled microrobots. Kosa et al. [92] worked toward the optimization of microactuators using mechanical-electrical-fluidic model and implement the same in the experiments using scaled-up model. It was shown that a 10 mm long tail was able to propel the swimming object with a velocity of 5cm/s. In another study, Kosa et al. [93] used piezoelastic swimming tail to generate planar waves and investigated the effect of head section presence on the swimming on a microrobot. Kosa et al. [93] found that propulsion velocity reduces to 50% when the ratio of volume of head to

volume of swimming tail reaches 12; i.e., velocity reduces as volume of head increases.

Nanoswimmers should help, through medical target identification, to improve diagnosis and provide new therapeutic procedures. In 2008, Cavalcanti et al. [94] addressed the control and the architecture design for developing practical molecular machines. Cavalcanti et al. [94] described a pathway towards an effective methodology to control nanoswimmers and advance nanotechnology as a valuable tool for medicine. Numerical analysis and computational simulation was adopted to illustrate the proposed nanoswimmer performance in a dynamic environment used as test-bed for medical instrumentation and drug delivery.

Earl et al. [95] modeled microscopic swimmers using numerical methods, which consist of Oseen tensor, lattice Boltzmann, and multiparticle collision dynamics. The model [95] consists of three spheres connected with each other and having movement in one dimension only. The expression for efficiency was the ratio of energy required by an external force to move the sphere by a distance to the work done to change the shape. The theory was generalized up to 200 spheres, and it was shown that a logarithmic ratio exist between the increment of spheres and the efficiency. The generalized model was able to turn and control its trajectory in three dimensions.

Alexander et al. [96] described the constraints imposed on the hydrodynamic scattering of two low Reynolds number swimmers by the time-reversal invariance of the Stokes equations.

Coq et al. [97] emphasized on the self induced helicity of elastic flagella for the driving of artificial swimmers. Coq et al. [97] showed that increasing the angular velocity, the filament undergoes a sharp but continuous shape transition from a linear to an helical shape tightly wrapped around the rotation axis. The argument in [97] was based on the rotation of single tilted flexible rod.

Keaveny and Maxey [98] described the dynamics of a chain of discrete paramagnetic beads bonded together by short flexible links to form a tail attached to a larger spherical particle or head. It has been demonstrated that the magnetic micro-swimmer introduced by Dreyfus et al. [19] with planar actuation can be used as a model to study a corkscrew form of swimming, driven by a rotating magnetic field. Further, for low-frequency

rotations, Keaveny and Maxey [98] predicted that the swimming speed (U) grows initially as $U \sim Sp^4$, where Sp is the sperm number [69].

Qian et al. [99] considered the deformation of a tilted elastic rod rotating in a viscous fluid and studied the shape transition when driven either at constant torque or at constant speed.

Lauga and Bartolo [100] demonstrated that two bodies with reciprocal deformation can exploit hydrodynamic interactions to obtain collective locomotion and effective long-range interactions. Normand and Lauga [101] derived the time-averaged forces acting on a tethered flapper in a polymeric fluid and demonstrated that the scallop theorem is not valid in polymeric fluids. Reciprocal movement cannot be used for locomotion at low Reynolds number in an infinite fluid or near a rigid surface but Trouilloud et al. [102] had shown that this limitation is relaxed for a body performing reciprocal motions near a deformable interface. Lauga and Powers [103] reviewed the biophysical and mechanical principles of locomotion at the small scales relevant to cell swimming and illustrated the theoretical framework necessary to understand biological and synthetic locomotion at low Reynolds number. Resistance matrices for solid bodies, flow singularities, and kinematic requirements for net translation were also emphasized in [103].

Some microorganisms, such as spermatozoa, synchronize their flagella when swimming in close proximity. Elfring and Lauga [104] showed that the time evolution of the phase difference between co-swimming cells depends only on the nature of the front-back geometrical asymmetry of their flagellar waveform and microorganisms can phase lock into conformations which minimize or maximize energy dissipation.

Subramanian et al. [105] developed an analytical model for propulsion attributed to generalized helical flagella. The linearly increasing amplitude helical model showed improved performance compared to the uniform amplitude model. Thus, a plausible design parameter for increased propagation of nanoswimmers is the helix profile. Apart from increment in velocity of nanoswimmer, the linear variation in amplitude reduces internal strains which may develop at the basal end of the flagella for constant amplitude helix.

In a recently study, the effects of bends on flagella and pitch angle were observed and optimized by Yang et al. [106]. Simultaneously optimizing the swimming efficiency with respect to inter-kink length and pitch angle, Yang et al. [106] found that the optimal

pitch angle is 35.5˚ and the optimal inter-kink length ratio is 0.338, which are in good agreement with experimental observations.

Coq et al. [107] studied theoretically and experimentally the periodic motion of a flexible filament immersed in a viscous fluid. They emphasized on the nonlinear force-torque relation resulting from the interplay between the linear elasticity of the rod and the linear Stokes flow. Coq et al. [107] showed that the characteristics of the propulsive force strongly depends on the actuation mode for a torque-driven beating.

Li et al. [108] proposed a dynamic model using RFT for the swimming microrobots with application for the controlled drug delivery inside the human body. The proposed microrobot had helical head and an elastic tail. It was shown that the microrobot performs better after the bifurcation in terms of speed and efficiency. Linear and angular velocities increase linearly with the driving torque applied by external magnetic field.

Wada and Netz [109] presented analytical and numerical studies on a self-propelling bi-stable helix as a model system for *Spiroplasma* bacterial motility. The effects of cell stiffness, viscosity and the thermal fluctuations on helical-shaped bacterial motility and its swimming speed were considered.

Magnetic fields are an attractive means to actuate ferro- and paramagnetic micro- and nano-structures in fluidic and biological environments. Ghosh and Fischer [21] described the construction and operation of one of the smallest artificial swimmers to date that can be navigated in water with micrometer-level precision using homogeneous magnetic fields. The propellers are typically 200-300 nm in width and about 1 to 2 $\mu$m long; are made of silicon dioxide ($SiO_2$).

Abbott et al. [22] compared three promising methods of microrobot swimming using magnetic fields, to rotate helical propellers that mimic bacterial flagella, to oscillate a magnetic head with a rigidly attached elastic tail, and pulling directly with magnetic field gradients. It was observed that helical propulsion will likely be the best choice for in vivo applications.

Artificial bacterial flagella (ABFs) consist of helical tails resembling natural flagella fabricated by the self-scrolling of helical nanobelts and soft-magnetic heads composed of Cr/Ni/Au stacked thin films. ABFs are controlled wirelessly using a low-strength rotating magnetic field. Zhang et al. [23] performed swimming tests of ABFs and investigated the influences of head size on swimming velocity and the lateral drift of an

ABF near a solid boundary. Inspired by monotrichous bacteria flagella, Zhang et al. [13] in another article, reported the fabrication and controlled swimming of artificial bacterial flagella (ABF), microsphere manipulation, and the thrust force generated by an ABF.

In a recent review, Fischer and Ghosh [110] discussed the construction, actuation, and operation in context of artificial micro-structure that can be controlled and propelled with homogenous magnetic fields. Peyer et al. [111] reported various magnetic helical micromachines that transforms a rotation around their helical axis into a translational motion along the helical axis and discussed the actuation, motion control, fabrication, and functionalization of helical micromachines for biomedical applications.

Previous analytical and computational models of flagellar propulsion has been dedicated to the fluid mechanics of flagella and cilia in Newtonian flows, only a few studies incorporated the non-Newtonian fluids. A variety of internal biological fluids have complex polymeric microstructures and exhibit non-Newtonian behavior. Inspired by this fact, Lauga [112] worked on the kinematics of locomotion and transport in complex biological fluids, wherein the fluid is non-Newtonian and observed that the transport kinematics in a viscoelastic fluid are also controlled by the mechanical properties of the fluid, such as fluid viscosity and relaxation time.

Many micro-organisms swim through gels and non-Newtonian fluids in their natural environments. Fu et al. [113] addressed how swimming velocities are affected in nonlinearly viscoelastic fluids and found that in general, nonlinear viscoelastic corrections decrease the swimming velocity relative to the Newtonian case. Fu et al. [113] assumed that the amplitude of deflection is small compared to both, the wavelength of deformations, and the radius of the cylinder. Design of a fastest swimming micro-swimmer requires tuning of material parameters and of the actuation frequency in order to maximize the dimensional swimming speed.

Viscoelasticity may have important effects on bacterial fluid dynamics. Smith et al. [114] modeled cilia-driven transport of biological fluids and applied the model to the large-amplitude motion of a single cilium in a linear Maxwell liquid. A test particle is propelled approximately one-fifth as quickly along the direction of cilia beating as in the Newtonian case.

For slender bodies in a Newtonian fluid, the ratio of normal to tangential drag coefficients is fully determined by the geometry and cannot exceed 2. Cohen and Boyle

[115] observed that, in non-Newtonian environments, the ratio of drag coefficients is a function of both the geometry and the medium. In addition to viscoelastic effects, biological fluids can also show shear-thinning viscosity as part of their non Newtonian behavior. In a recent study, Yim et al. [116], assessed the effect of varying viscosity with shear rate on the performance of swimming, experimentally. Experiments were conducted using two types of magnetically driven swimmers (oscillating flexible tail and rotating rigid coil devices) to test this effect. Velez-Cordero and Lauga [117] extended classical results of Taylor [33-34] to non-Newtonian fluids flow cases (i.e. shear thinning and shear thickening fluids) and addressed the role of shear-dependent viscosity on flagellar propulsion. It was shown that the shear-thinning fluids always decrease the cost of transport and yields the flow transport more efficient.

Engineered micro-/nanoswimmers must expend internal energy in order to produce the waves of deformation responsible for the motion. Spagnolie and Lauga [118] considered the regularization of Lighthill's sawtooth waveform while taking into account the additional energy costs of bending, sliding of the internal microtubules and internal viscous resistance. The shape of the flagellar wave which leads to the fastest swimming for a given energy expenditure was determined analytically and numerically. The optimal shapes of periodic, planar flagellar waves of both infinite and finite length were derived.

Rodenborn [119] determined the propulsive force, torque and drag on flagella with different biologically relevant geometries, determining the dependence of these forces and torques on both the wavelength and the axial length of the flagella. Swan et al. [120] modeled the hydrodynamic self-propulsion of microorganisms at low Reynolds number using Stokesian Dynamics simulations and represented the swimming body as an array of spheres. Lauga and Eloy [121] used internal energetic measure to derive computationally the optimal shape of an internally-forced periodic planar flagellum deforming as a travelling wave. The travelling-wave shape computed in [121] are the one which maximizes the swimming speed for a fixed energetic cost.

Berman et al. [122] studied the low-Reynolds-number locomotion of finite undulating filament propelled by a propagating sinusoidal wave using an approximate Resistive Force Theory (RFT). Berman et al. [122] assumed a local nature of hydrodynamic interaction between the filament and the surrounding liquid, and more accurate particle-based numerical computations taking into account the intra-filament hydrodynamic interaction.

The boundary-element method (BEM) is a reliable and accurate tool for studying the zero- Reynolds number hydrodynamics of motile microorganisms, especially in situations where the detailed geometry of the structure of the microorganism plays a role.

Symmetries in fluid-structure interaction problems have been used by some researchers to reduce the number of unknowns and as a result simplify numerical computation. Liu et al. [123] used modified boundary-element method utilizing symmetry concept in surface domain to model the motion of a bacterium propelled by a helical flagellum, and compute the swimming speed of a rotating helix subject to zero force. The chronological advancements in flagellar propulsion have been tabulated in Table 2.1.

**Table 2.1: Chronological advancements of flagellar propulsion**

| Year | Researcher | Work done |
|---|---|---|
| 1930 | Ludwig | Observed that rigid arms like oars is incapable of net motion in microorganisms. |
| 1951 | Taylor | Proposed RFT and modeled flagellum as an infinite cylindrical filament in an unbounded fluid. |
| 1953 | Hancock | Pioneered SBT and mathematically analyzed the propulsion and extended the study to realistic amplitudes |
| 1955 | Gray and Hancock | Studied the propulsion of spermatozoa using RFT |
| 1958 | Machin | Modeled wave propagation along an elastic filament |
| 1971 | Chwang and Wu | Compared the two modes of propulsion namely, planar wave and helical wave |
| 1974 | Chwang and Wu | Improved SBT |
| 1976 | Winet and Keller | Compared the RFT predictions with experimental observations on geometry of flagella |
| 1976 | Keller and Rubinow | Showed that trajectory of a microorganism is a helix instead of a straight line and confirmed that a non-rigid body motion can propel itself without a head |
| 1976 | Lighthill | Proposed the motion of a filament as the line distribution of Stokeslets and source dipole. Given more accurate normal $C_n$ and tangential coefficients $C_t$ of resistance. |
| 1977 | Brennen and Winet | Reviewed both SBT and RFT approaches |
| 1979 | Johnson and Brokaw | Compared RFT and SBT and suggested that SBT is better where cell body is present |

| Year | Researcher | Work done |
|---|---|---|
| 1980 | Johnson | Improved SBT |
| 1987 | Phan-Thein et al. | Optimized geometrical parameters for maximum swimming speed |
| 1991 | Ramia | Studied locomotion of a microorganism using BEM to predict propulsion characteristics |
| 1993 | Ramia et al. | Studied wall effects using BEM |
| 1996 | Nasseri and Phan-Thein | Modeled locomotion with planar and helical rigid tail |
| 1997 | Nasseri and Phan-Thein | Optimized a capsule shaped head propelled by a rigid spiral tail for maximum speed |
| 1998 | Wiggins and Goldstein | Determined the shape of the filament by balancing the visco-elastic forces using small amplitude deformations |
| 1999 | Camalet et al. | Studied inextensibility of the filament and the effect of boundary conditions imposed on beating pattern |
| 2000 | Goto et al. | Used SBT to understand swimming motion and calculate the optimal shapes for the fastest swimmer and the most efficient swimmer |
| 2001 | Magariyama et al. | Introduced two apparent viscosities in existing RFT |
| 2001 | Goto et al. | Studied cell body rotation of single flagellum bacterium |
| 2001 | Fujita and Kawai | Calculated optimal shape of a spiral flagellum |
| 2002 | Powers | Studied flagellar bundling and showed that the counter rotation of cell body is necessary for torque balance. |
| 2003 | Takano and Goto | Applied RFT for analysis of small flagellar deformations |
| 2003 | Edd et al. | Studied the design aspects of a surgical microrobot using RFT |
| 2003 | Trachtenberg et al. | Analyzed bacterial flagellar filaments and worked towards the role of flagella surface in flow transition. |
| 2004 | Behkam and Sitti | Studied *E.coli* inspired propulsion using RFT and tested the biomimetic flagellar propulsion |
| 2004 | Kim and Powers | Studied hydrodynamic interactions between rotating rigid flagella and their bundling |
| 2005 | Goto et al. | Studied the motion of bacterium near a rigid boundary |
| 2005 | Flores et al. | Modeled interaction of flagella in a multi flagellated swimmer |

| Year | Researcher | Work done |
|---|---|---|
| 2005 | Dreyfus et al. | First microscopic artificial nanoswimmer. Observed dependency of normalized velocity on sperm number. |
| 2006 | Chattopadhyay et al. | Validated RFT experimentally |
| 2007 | Lauga | Studied hydrodynamics of a rotating filament |
| 2009 | Coq et al. | Modeled the coupling with surrounding viscous fluids using local anisotropic friction coefficients. |
| 2009 | Li et al. | Proposed a dynamic model for swimming microbots for controlled drug delivery. |
| 2009 | Yang et al. | Numerically studied the *Spiroplasma* swimming using RFT |
| 2009 | Ghosh and Fischer | Smallest artificial nanoswimmer made till date. Demonstrated micron level precision in control using homogenous magnetic field. |
| 2009 | Zhang et al. | Studied the effect of solid boundaries on ABF. Observed that ABF cannot swim in a circle like a bacterium because head and tail do not counter rotate. |
| 2010 | Cohen and Boyle | Discussed the undulatory swimming in non-Newtonian fluid |
| 2010 | Spagnolie and Lauga | Discussed the optimal shapes of periodic and planar flagellar motion |
| 2011 | Swan et al. | Modeled hydrodynamic self propulsion of microorganism at low Reynolds number |
| 2012 | Rodenborn et al. | Studied propulsion of helical flagellum using SBT |
| 2013 | Berman et al. | Studied locomotion of finite undulating filament propelled by a sinusoidal wave |
| 2013 | Liu et al. | Modeled swimming of helically propelled bacterium subjected to zero force |

The continuous effort and work on realization of nanoswimmers is leading to ever growing published literature in the field. Still, the available literature has a vast gap between the realization of nanoswimmer as there are many assumptions in the theories developed and more so over limitation on fabrication technology in the nanodomain.

The available literature reported in this section pertains to the nanorobot locomotion via flagellar propulsion and the existing theories developed to model a nanoswimmer

propelled by a beating or a rotating elastic flagellum. Many researchers [15, 83, 90, 111] used RFT to estimate the forces acting on inelastic flagella moving at low Reynolds number and a few [71, 111] of them have also used elastohydrodynamic model in order to predict performance indexes of nanoswimmers. Mathematical models of the flagellated nanoswimmers show dependence of motion on multiple parameters like geometry and material of flagella, viscosity of surrounding medium, and the mode of actuation. Though the investigation of actuation modes has been done for uniform flagellated nanoswimmers, but its influence on tapered flagellated nanoswimmers is not yet addressed. This was first done by us and published [124, 125]. Material choice is another important and integral part of the design and must be explored for any device. Nanoswimmers are also no exemptions and needs suitable material for exploring the design perspective. Researchers proposed $SiO_2$ [21, 109], PDMS [126] and PEG-DA [127] as the biocompatible materials for flagella, but their adaptability as flagellar structure needs to be assessed with respect to parameters like flexural rigidity, and technical feasibility. We first proposed and published [128] the methodology for assessment of a material for its appropriateness as a material for flagella and assessed over 500 materials for their suitability as a material of choice for flagella.

Among above mentioned and many other gaps in existing theories on propulsion of nanoswimmer and actual nanoswimmer in nature, few of them have been addressed in the present thesis. Keeping in view the detailed literature presented in this section and assessed gaps in already attempted problems on propulsion of a nanoswimmer, the scope of the present thesis has been enlisted in the next section.

## 2.3 SCOPE OF THE PRESENT WORK

Based on the literature review done in previous section, the following issues have been considered and addressed:

1. Most of the researchers studied shapes and kinematics of flagellar propulsion assuming a particular flagella shape. Though the shape determination via elastohydrodynamics is attempted by some researchers but the effect of flagellar elasticity on nanoswimmer propulsion is largely uninvestigated. Does elasticity of flagella have something to do with efficiency of motion of nanoswimmer? Using RFT, the variation of nanoswimmer performance indexes i.e. propulsive

velocity, and propulsion efficiency as a function of elasticity and characteristic length ($l_o$) has been investigated in the present thesis and presented in Chapter 3.

2. In the vast literature available on modeling of flagellar propulsion, the flagellum is considered constant diameter whereas, the actual microorganism have tapered flagella. Why are microorganisms in nature designed with tapered flagellum? Is the taper of flagellum related to the efficiency of the nanoswimmer? Wave propagation through a tapered flagellum of a nanoswimmer for a given taper ratio needs to be studied in detail. The investigations on this has been done in the present work and the modeling, simulation, and analysis are presented in Chapter 4. The effect of flagellar elasticity on nanoswimmer propulsion by planar and helical motion of flagellum are investigated and reported in Chapter 4. The two modes of propulsion, namely planar wave and helical wave, have been compared for a tapered nanoswimmer based on their performance indexes (i.e., velocity and efficiency).
3. Though modeling of shape and size of nanoswimmers is investigated in literature, the material selection for the flagella needs to be assessed on the criteria like biocompatibility, physical properties and technological feasibility. The short listing of biocompatible materials is quintessential for attempts to engineer an artificial nanoswimmer. How can one design a nanoswimmer without a chosen material? Is it not imperative to propose a method to choose a material if we have to realize a nanoswimmer? The present study provides a methodology for assessing the candidature of a material for the fabrication of artificial flagella that shall have implant capabilities and shortlist the potential material and a survey of over 500 materials to qualify as a suitable candidate using the provided methodology. This has been presented in Chapter 5.
4. The performance of a uniform diameter nanoswimmer and the more realistic, tapered nanoswimmer using resistive force theory is investigated in Chapter 3 and Chapter 4, respectively. A systematic study is carried out with both planar and helical wave propagations through a uniflagellated nanoswimmer. The important results of the present study are summarized in Chapter 6.

**References**


1. Sharma NN, and Mittal RK (2008) Nanorobot Movement: Challenges and Biologically Inspired Solutions, Int. J. Smart Sensing and Intelligent Systems, 1 (1), pp. 87-109.
2. Requicha AAG (2003) Nanorobots, NEMS and Nanoassembly, Proc. IEEE, 91 (11), pp. 1922-1933.
3. Freitas RA Jr (1998) Exploratory Design in Medical Nanotechnology: A Mechanical Artificial Red Cell: Artificial Cells, Blood Design, and Immobility, Biotech, 26, pp. 441-430.
4. Berg HC, and Turner L (1979) Movement of Microorganisms in Viscous Environments, Nature, 278, pp. 349-351.
5. Cavalcanti A, and Freitas RA Jr. (2005) Nanorobotics Control Design: A Collective Behavior Approach for Medicine, IEEE Tr. Nanobioscience, 4(2), pp. 133-140.
6. Sitti M (2004) Micro and Nano-Scale Robotics, Proc. 2004 American Control Conference, Massachusetts, June 30 - July 2, pp. 1-8.
7. Siegel M (2001) Smart Sensors and Small Robots, Proc. IEEE Instrumentation and Measurement Technology Conference, Budapest, Hungary, May 21-23, pp. 303-308.
8. Freitas RA Jr. (1999) Nanomedicine, Volume I: Basic Capabilities, Landes Bioscience, Georgetown, TX; http://www.nanomedicine.com/NMI.htm
9. Sharma NN, Ganesh M, and Mittal RK (2004) Non-Brownian Motion of Nanoparticle: An Impact Process Model, IEEE Tr. Nanotechnology, 3(1), pp.180-186.
10. Sharma NN, Ganesh M, and Mittal RK (2005) Nano-Electromechanical System Impact Spectrum Modeling and Clubbing of Structural Properties, IE (I) Journal-MC, 85, pp. 188-193.
11. Sharma NN, and Mittal RK (2005) Brownian motion model of Nanoparticle Considering Non-Rigidity of Matter-A systems Modeling Approach, IEEE Tr. Nanotechnology, 4(2), pp. 180-186.

12. Lowe CP (2003) Dynamics of Filaments: Modelling of Dynamics of Driven Filaments, Philosophical Transactions: Biological Sciences, 358 (1437), pp. 1543-1550.
13. Ludwig W (1930) Zur Theorie der Flimmerbewegung (Dynamik, Nutzeffekt, Energiebalanz), J Comp Physiol A, 13, pp. 397-504.
14. Zhang L, Abbott JJ, Dong L, Bradley EK, Bell D, and Nelson BJ (2009) Artificial Bacterial Flagella: Fabrication and Magnetic Control, Applied Physics Letters, 94(064107), pp. 1-3.
15. Gray J, and Hancock GJ (1955) The Propulsion of Sea-Urchin Spermatozoa, J Exp Biol, 32, pp. 802-814.
16. Hancock G (1953) The Self-Propulsion of Microscopic Organisms through Liquids, Proc. of the Royal Society of London, Mathematical and Physical Sciences, 217, pp. 96-121.
17. de La Torre JG, and Bloomfield VA (1977) Hydrodynamic Theory of Swimming of Flagellated Microorganisms, Biophysical J, 20, pp. 49-64.
18. Phan-Thein N, Tran-Cong T, and Ramia M (1987) A Boundary Element Analysis of Flagellar Propulsion, J Fluid Mech, 184, pp. 533-549.
19. Dreyfus R, Baudry J, Roper ML, Fermigier M, Stone HA, and Bibette J (2005) Microscopic Artificial Swimmers, Nature, 437, pp. 862-865.
20. Kósa G, Shoham M, and Zaaroor M (2006) Analysis of a Swimming Micro Robot, The 1st IEEE/RAS-EMBS International Conference on Biomedical Robotics and Biomechatronics, Italy, pp. 131-135.
21. Ghosh A, and Fischer P (2009) Controlled Propulsion of Artificial Magnetic Nanostructured Propellers, Nano Letters, 9, pp. 2243-2245.
22. Abbott JJ, Peyer KE, Lagomarsino MC, Zhang L, Dong L, Kaliakatsos IK, and Nelson BJ (2009) How Should Microrobots Swim?", The International Journal of Robotics Research, 28, pp. 1434-1447.
23. Zhang L, Abbott JJ, Dong L, Peyer KE, Bradley EK, Zhang H, Bergeles C, and Nelson BJ (2009) Characterizing the Swimming Properties of Artificial Bacterial Flagella, Nano Letters, 9(10), pp. 3663-3667.

24. Iima M, and Mikhailov AS (2009) Propulsion Hydrodynamics of a Butterfly Micro-swimmer, A Letter Journal Exploring the Frontiers of Physics, 85(44001), pp.1-6.

25. Wiggins CH, and Goldstein RE (1998) Flexive and Propulsive Dynamics of Elastica at Low Reynolds Number, Phy Rev Lett, 80, pp. 3879-3882.

26. Cavalcanti A, Hogg T, and Shirinzadeh B (2006) Nanorobotics System Simulation in 3D Workspaces with Low Reynolds Number, IEEE-RAS MHS International Symposium on Micro-NanoMechatronics and Human Science, Nagoya, Japan, pp. 226-231.

27. Podaima BW, Vaseeharan T, and Gordon R (2004) Microscopic Dynamics of Cytobots, CCECE 2004 - CCGEI 2004, Niagara Falls, pp. 1527-1532.

28. Brey D (2001) Cell Movements: From Molecules to Motility, 2nd Ed, Garland Publishing Inc, NY.

29. Higdon JLL (1979) A Hydrodynamic Analysis of Flagellar Propulsion, J Fluid Mech, 90, pp. 685-711.

30. Adtani C, Das A, and Sharma NN (2009) Investigation of Hybrid Bio-mechanical Mechanism for Nanorobotic Propulsion, Int J Biomechatronics and Biomedical Robotics, 1(1), pp. 31-36.

31. Adtani C, Das A, and Sharma NN (2009) Modeling of Hybrid Bio-mechanical Mechanism for Nanorobotic Propulsion, Proc. 4th Int Conf on Autonomous Robots and Agents, 10-12 Feb., Wellington, New Zealand, pp.83-86.

32. Siva Kumar M, and Philominathan P (2009) The Physics of Flagellar Motion of E.coli during Chemotaxis, Biophys Rev, 2, pp. 13-20.

33. Taylor G (1951) Analysis of the Swimming of Microscopic Organisms, Proc of the Royal Society of London, Mathematical and Physical Sciences, 209, pp.447-461.

34. Taylor G (1952) The Action of Waving Cylindrical Tails in Propelling Microscopic Organisms, Proc. of the Royal Society of London, Mathematical and Physical Sciences, 211, pp. 225-239.

35. Gray J (1955) The Movement of Sea-Urchin Spermatozoa, J Exp Biol, 32, pp.775-801.

36. Machin KE (1958) Wave Propagation along Flagella, J Exp Biol, 35, pp.796-806.

37. Chwang AT, and Wu TY (1971) A note on Helical Movement of Microorganisms, Proc. Roy Soc Lond B, Biol Sci, 178 (52), pp. 327-346.

38. Blake JR (1971) Self Propulsion due to Oscillations on the Surface of a Cylinder at Low Reynolds Number, Bull Austral Math Soc, 1, pp. 255-264.

39. Berg HC, and Anderson RA (1973) Bacteria Swim by Rotating their Flagellar Filaments, Nature, 245, pp. 380-382.

40. Happel J, and Brenner H (1965) Low Reynolds Number Hydrodynamics, Prentice Hall, Englewood Cliffs, NJ.

41. Keller JB, and Rubinow SI (1976) Swimming of Flagellated Microorganisms, Biophys J, 16, pp. 151-170.

42. Winet H, and Keller SR (1976) Spirillum Swimming: Theory and Observations of Propulsion by the Flagellar Bundle, J Exp Biol, 65, pp. 577-602.

43. Lighthill J (1976) Flagellar Hydrodynamics, SIAM Rev, 18, pp. 161-173.

44. Chwang AT, and Wu TY (1974) Hydromechanics of Low Reynolds Number Flow. 1: Rotation of Axisymmetric Prolate Bodies, J Fluid Mech, 63, pp.607-622.

45. Chwang AT, and Wu TY (1975) Hydromechanics of Low-Reynolds Number Flow. 2: Singularity Method for Stokes Flows, J Fluid Mech, 67, pp. 787-815.

46. Johnson RE (1979) An Improved Slender Body Theory for Stokes Flow, J Fluid Mech, 99, pp. 411-431.

47. Prucell EM (1977) Life at low Reynolds Number, Amer J Phys, 45, pp. 3-11.

48. Brennen C, and Winet H (1977) Fluid Mechanics of Propulsion by Cilia and Flagella, Ann Rev Fluid Mech, 9, pp. 339-98.

49. Rikmenspoel R (1965) The Tail Movement of Bull Spermatozoa: Observation and Model Calculation, Biophysical J, 5, pp. 365-392.

50. Rikmenspoel R (1966) Elastic Properties of the Sea Urchin Sperm Flagellum, Biophysical J, 6, pp. 365-392.

51. Johnson RE, and Brokaw CJ (1979) Flagellar Hydrodynamics: A comparison between Resistive-Force Theory and Slender-Body Theory, Biophys J, 25, pp.113-127.

52. Lowe G, Meister M, and Berg HC (1987) Rapid Rotation of Flagellar Bundles in Swimming Bacteria, Nature, 325, pp. 637-640.

53. Shapere A, and Wilczek F (1989) Geometry of Self-propulsion at Low Reynolds Number, J Fluid Mech, 198, pp. 557-585.

54. Shapere A, and Wilczek F (1989) Efficiencies of Self-propulsion at Low Reynolds Number, J Fluid Mech, 198, pp. 587-599.

55. Sleigh MA (1991) Mechanisms of Flagellar Propulsion: A Biologist's View of the Relation Between Structure, Motion, and Fluid mechanics, Protoplasma, 164, pp.45-53.

56. Ramia M (1991) Numerical Model for the Locomotion of Spirilla, Biophys J, 60, pp. 1057-1078.

57. Ramia M, Tullock DL, and Phan-Thein N (1993) The Role of Hydrodynamic Interaction in the Locomotion of Microorganisms, Biophys J, 65, pp. 755-778.

58. Nasseri S, and Phan-Thein N (1996) On the Path and Efficiency of Two Micromachines with Rigid Tails, Computational Mechnanics, 18, pp. 192-199.

59. Nasseri S, and Phan-Thein N (1997) Geometric Optimization of a Micromachine with a Spiral Tail Immersed in Viscous Medium, Computational Mechnanics, 20, pp. 267-271.

60. Fujita T, and Kawai T (2001) Optimum Shape of a Flagellated Microorganism, JSME International Journal, 44, pp. 952-957.

61. Andrietti F, and Bernardini G (1994) The Movement of Spermatozoa with Helical Head: Theoritical Analysis and Experimental Results, Biophys J, 67, pp.1767-74.

62. Purcell EM (1997) The Efficiency of Propulsion by a Rotating Flagellum, Proc Natl Acad Sci: Biophysics, 94, pp. 11307-311.

63. Wiggins CH, Riveline D, Ott A, and Goldstein RE (2000) Trapping and Wiggling: Elastohydrodynamics of Driven Microfilaments, Biophys J, 74, pp.1043-1060.

64. Camalet S, Julicher F, and Prost J (1999) Self-Organized Beating and Swimming of Internally Driven Filaments, Phy Rev Lett, 82, pp. 1590-1593.

65. Wolgemuth CW, Powers TR, and Goldstein RE (2000) Twirling and Whirling: Viscous Dynamics of Rotating Elastic Filaments, Phy Rev Lett, 84, pp. 1623-1626.

66. Koehler SA, and Powers TR (2000) Twirling Elastica: Kinks, Viscous drag, and Torsional Stress, Phy Rev Lett, 85(22), pp. 4827-4830.

67. Camalet S, and Julicher F (2000) Generic Aspects of Axonemal Beating, New Journal of Physics, 2, pp. 24.1-24.23.

68. Goto T, Inaoka R, and Tokano Y (2000) Numerical Analysis of Bacterium Motion based on the Slender Body Theory, JSME International Journal, 43(4), pp. 875-881.

69. Lowe CP (2001) A Hybrid Particle/Continuum Model for Micro-organism Motility, Future Generation Computer Systems, 17, pp. 853-862.

70. Magariyama Y, Masuda S, Takano Y, Ohtani T, and Kudo S (2001) Difference between Forward and Backward Swimming Speeds of the Single Polar-flagellated Bacterium, FEMS Microbiology Letters, 205, pp.343-347.

71. Woolley DM, and Vernon GG (2001) A Study of Helical and Planar Waves on Sea Urchin Sperm Flagella, with a Theory of How They are Generated, The Journal of Experimental Biology, 204, pp. 1333-1345.

72. Powers TR (2002) Role of Body Rotation in Bacterial Flagellar Bundling, Phy Rev E, 65: 040903, pp. 1-4.

73. Trachtenberg S, Fishelov D, and Ben-Artzi M (2003) Bacterial Flagellar Microhydrodynamics: Laminar Flow over Complex Flagellar Filaments, Analog Archimedean Screws and Cylinders, and its Perturbations, Biophys J, 85, pp.1345-1357.

74. Takano Y, and Goto T (2003) Numerical Analysis of Small Deformation of Flexible Helical Flagellum of Swimming Bacteria, JSME International Journal, 46(4), pp. 1234-1240.

75. Edd J, Payen S, Rubinsky B, Stoller ML, and Setti M (2003) Biomimetic Propulsion for a Swimming Surgical Micro-robot, Proc of the 2003 IEEE/RSJ International Conference on the Intelligent Robots and Systems, pp. 2583-2588.

76. Becker LE, Koehler SA, and Stone HA (2003) On Self-propulsion of Micro-machines at Low Reynolds Number: Purcell's Three-link Swimmer, J Fluid Mech, 490, pp. 15-35.

77. Lagomarsino MC, Capuani F, and Lowe CP (2003) A Simulation Study of the Dynamics of a Driven Filament in an Aristotelian Fluid, Journal of Theoretical Biology, 224, pp. 215-224.

78. Avron JE, Gat O, and Kenneth O (2004) Optimal Swimming at Low Reynolds Numbers, Physical Review letters, 93(18), pp. 186001:1-4.

79. Kim MJ, and Powers TR (2004) Hydrodynamic Interactions between Rotating Helices, Phy Rev E, 69 (6): 061910, pp. 1-5.

80. Goto T, Nakata K, Baba K, Nishimura M, and Magariyama Y (2005) A Fluid-Dynamic Interpretation of the Asymmetric Motion of Singly Flagellated Bacteria Swimming Close to a Boundary, Biophys J, 89, pp. 3771-3779.

81. Flores H, Lobaton E, Mendez-Diez S, Tlupova S, and Cortez R (2005) A Study of Bacterial Flagellar Bundling, Bulletin of Mathematical Biology, 67, pp.137-168.

82. Behkam B, and Sitti M (2004) E. Coli Inspired Propulsion for Swimming Microrobots, In Proc of 2004 ASME, International Mechanical Engineering Congress, Anaheim, California, November 13-19, pp. 59621-59626.

83. Behkam B, and Sitti M (2005) Modeling and Testing of a Biomimetic Flagellar Propulsion Method for Microscale Biomedical Swimming Robots, Proc of 2005 IEEE/ASME, International Conference on Advanced Intelligent Mechatronics, Monterey, California, July 24-28, pp. 37-42.

84. Behkam B, and Sitti M (2006) Design Methodology for Biomimetic Propulsion of Miniature Swimming Robots, Journal of Dynamics Systems, Measurements, and Control, Transactions of the ASME, 128, pp. 36-43.

85. Majumdar R, Rathore JS, and Sharma NN (2009) Simulation of Swimming Nanorobots in Biological Fluids, Proc. 4th Int. Conf on Autonomous Robots and Agents (ICARA 2009), 10-12 Feb. Wellington, New Zealand, pp. 79-82.

86. Manghi M, Schlagberger X, and Netz RR (2006) Propulsion with a Rotating Elastic Nanorod, Phys Rev Lett, 96(068101), pp. 1-4.

87. Chattopadhyay S, Moldovan R, Yeung C, and Wu XL (2006) Swimming Efficiency of Bacterium E-Coli, Proc of the National Academy of Sciences, 103(37), pp. 13712-13717.

88. Roper M, Dreyfus R, Baudry J, Fermigier M, Bibette J, and Stone HA (2008) Do Magnetic Micro-swimmers Move like Eukaryotic Cells?, Proc R Soc A, 464, pp.877-904.

89. Yu TS, Lauga E, and Hosoi AE (2006) Experimental Investigations of Elastic Tail Propulsion at Low Reynolds Number, HML Report Number 06-P-01.

90. Sudo S, Segawa S, and Honda T (2006) Magnetic Swimming Mechanism in a Viscous Liquid, Journal of Intelligent Material Systems and Structures, 17, pp.729-736.

91. Lauga E (2007) Floppy Swimming: Viscous Locomotion of Actuated Elastica, Physical Review E, 75(041916), pp. 1-16.

92. Kosa G, Shoham M, and Zaaroor M (2007) Propulsion Method for Swimming Microrobots, IEEE Transactions on Robotics, 32(1), pp. 137-150.

93. Kosa G, Hata N, Jolesz F, Neubach Z, Shoham M, Zaaroor M, and Szekely G (2008) Flagellar Swimming for Medical Microrobots: Theory, Experiments and Application, Proc of 2nd Biennial IEEE/RAS-EMBS Int Conf on Biomedical Robotics and Biomechatronics, Scottsdale, USA, Oct 19-22, 2008, pp. 258-263.

94. Cavalcanti A, Shirinzadeh B, Freitas RA Jr., and Hogg T (2008) Nanorobot Architecture for Medical Target Identification, Nanotechnology, 19(15103), pp.1-15.

95. Earl DJ, Pooley CM, Ryder JF, Bredberg I, and Yeomans JM (2007) Modeling Microscopic Swimmers at Low Reynolds Number, Journal of Chemical Physics, 126(064703), pp. 1-10.

96. Alexander GP, Pooley CM, and Yeomans JM (2008) Scattering of Low Reynolds Number Swimmers, Physical Review E, 78(045302), pp. 1-4.

97. Coq N, Roure OD, Marthelot J, Bartolo D, and Fermigier M (2008) Rotational Dynamics of a Soft Filament: Wrapping Transition and Propulsive Force, Physics of Fluids, 20(051703), pp. 1-4.

98. Keaveny EE, and Maxey MR (2008) Spiral Swimming of an Artificial Micro-Swimmer, J Fluid Mech, 598, pp. 293-319.

99. Qian B, Powers TR, and Breuer KS (2008) Shape Transition and Propulsive Force of an Elastic Rod Rotating in a Viscous Liquid, Phys Rev Lett, 100(078101), pp. 1-4.

100. Lauga E, and Bartolo D (2008) No Many-Scallop Theorem: Collective Locomotion of Reciprocal Swimmers, Physical Review E, 78(030901), pp. 1-4.

101. Normand T, and Lauga E (2008) Flapping Motion and Force Generation in a Viscoelastic Fluid, Physical Review E, 78(061907), pp. 1-4.

102. Trouilloud R, Yu TS, Hosoi AE, and Lauga E (2008) Soft Swimming: Exploiting Deformable Interfaces for Low Reynolds Number Locomotion, Phys Rev Lett, 101(048102), pp. 1-4.

103. Lauga E, and Powers TR (2009) The Hydrodynamics of Swimming Microorganisms, Reports on Progress in Physics, 72(9), pp. 1-58.

104. Elfring GJ, and Lauga E (2009) Hydrodynamic Phase Locking of Swimming Microorganisms, Phys Rev Lett, 103(088101), pp. 1-4.

105. Subramanian S, Rathore JS, and Sharma NN (2009) Design and Analysis of Helical Flagella Propelled nanorobots, Proc. 4th Int IEEE Conf on Micro/Nano Engineered and Molecular Systems, 5-8 Jan. 2009, Shenzen, China, pp. 950-953.

106. Yang J, Wolgemuth CW, and Huber G (2009) Kinematics of the Swimming of Spiroplasma, Phys Rev Lett, 102 (218102), pp. 1-4.

107. Coq N, du Roure O, Fermigier M, and Bartolo D (2009) Helical Beating of an Actuated Elastic Filament, Journal of Physics: Condensed Matter, 21, pp.1-7.

108. Li H, Tan J, and Zhang M (2009) Dynamics Modeling and Analysis of a Swimming Microrobot for Controlled Drug Delivery, IEEE Transactions on Automation Science and Engg, 6, pp. 220-227.

109. Wada H, and Netz RR (2009) Hydrodynamics of Helical-Shaped Bacterial Motility, Physical Review E, 80(021921), pp.1-20.

110. Fischer P, and Ghosh A (2011) Magnetically Actuated Propulsion at Low Reynolds Numbers: Towards Nanoscale Control, Nanoscale, The Royal Society of Chemistry, 3, pp. 557-563.

111. Peyer KE, Tottori S, Qiu F, Zhang L, and Nelson B (2013) Magnetic Helical Micromachines, Chem. Eur. J., 19, pp. 28-38.

112. Lauga E (2007) Propulsion in a Viscoelastic Fluid, Physics of Fluids, 19, pp. 083104.

113. Fu HC, Wolgemuth CW, and Powers TR (2009) Swimming Speeds of Filaments in Nonlinearly Viscoelastic Fluids, Physics of Fluids, 21(033102), pp.1-10.

114. Smith DJ, Gaffney EA, and Blake JR (2009) Mathematical Modelling of Cilia-Driven Transport of Biological Fluids, Proc R Soc A, 465, pp. 2417-2439.

115. Cohen N and Boyle JH (2010) Swimming at Low Reynolds Number: A Beginners Guide to Undulatory Locomotion, Contemporary Physics, 51 (2), pp. 103-123.

116. Yim D, Cho J, Jin S, and Yoo JY (2012) Flow Visualization Study on the Near-Surface Motility of a Flagellar Propeller, http://meetings.aps.org/link/BAPS.2012.DFD.G17.10

117. Vélez-Cordero J R, and E Lauga (2013) Waving Transport and Propulsion in a Generalized Newtonian Fluid, Journal of Non-Newtonian Fluid Mechanics, 199, pp. 37-50.

118. Spagnolie SE, and Lauga E (2010) The Optimal Elastic Flagellum, Physics of Fluids 22(031901), pp. 1-15.

119. Rodenborn B, Chen CH, Swinney HL, and Zhang HP (2011) Propulsion of Microorganisms by a Helical Flagellum, 64th Annual Meeting of the APS Division of Fluid Dynamics, November 20-22, 2011, Baltimore, Maryland.

120. Swan JW, Brady JF, Moore RS, and ChE (2011) Modeling Hydrodynamic Self-propulsion with Stokesian Dynamics or Teaching Stokesian Dynamics to Swim, Physics of Fluids, 23, pp. 071901.

121. Lauga E, and Eloy C (2013), Shape of Optimal Active Flagella, J. Fluid Mech., 730, pp. R1-R11.

122. Berman RS, Kenneth O, Sznitman J, and Leshansky AM (2013) Undulatory Locomotion of Finite Filaments: Lessons from *C. elegans*, New Journal of Physics, 15, pp. 075022 (1-33).

123. Liu B, Kenneth SB, and Powers TR (2013) Helical Swimming in Stokes Flow using a Novel Boundary-Element Method, Phys. Fluids, 25, pp. 061902.

124. Rathore JS, Majumdar R, and Sharma NN (2012) Planar wave propagation through a tapered flagellated nanoswimmer, IEEE Transactions on Nanotechnology, 11(6), pp.1117-1121.

125. Kotesa RS, Rathore JS, and Sharma NN (2013) Tapered Flagellated Nanoswimmer: Comparison of Helical Wave and Planar Wave Propulsion. BioNanoScience, Springer, 3(4), pp. 343-347.

126. Evans BA, Shields AR, Lloyd Carroll R, Washburn S, Falvo MR, Superfine R (2007) Magnetically Actuated Nanorod Arrays as Biomimetic Cilia. Nanoletters, 7(5), pp. 1428-1434.

127. Klein F, Richter B, Striebel T, Franz CM, Freymann G, Wegener M, Bastmeyer M (2011) Two-component Polymer Scaffolds for Controlled Three-Dimensional Cell Culture. Adv. Mater., 23, pp. 1341-1345.

128. Majumdar R, Neha S, Rathore JS, and Sharma NN (2013) In Search of Materials for Artificial Flagella of Nanoswimmers. Journal of Materials Science, Springer, 48(1), pp.240-250.

Chapter 3

# Flagellar Propulsion and Resistive Force Theory

## 3.1 INTRODUCTION

In the previous chapter, literature review including various aspects such as modeling approaches, effect of body shape, importance of viscosity, wall and neighbor effect on swimming, and fabrication in context of realizing nanoswimmer have been presented chronologically. In the present chapter, the existing modeling theories of propulsion of nanoswimmer such as resistive force theory (RFT), slender body theory (SBT), boundary element method (BEM) and the bead model (BM) are discussed briefly. Advantages and limitations of RFT over other theories are outlined. Further using RFT, mathematical modeling and analysis is carried out for both planar wave propulsion (PWP) and helical wave propulsion (HWP) with uniform diameter nanoswimmer. The chapter includes determination of steady state shapes of flagellum using elastohydrodynamics and derivation of RFT model to include propulsion, thrust force and efficiency as explicit functions of characteristic length of flagellum. Variation in characteristic length is achieved by varying elastic modulus of the flagellum material.

As discussed in Chapter 1, section 1.2, locomotion strategies used at microscopic level in low Reynolds number regime is quite different than the strategies used at macroscopic level. Inertia drift no longer works at small Reynolds number ($\mathrm{Re} \leq 1$). The concept of performing half of the stroke at faster rate and the other half at slower rate i.e. Scallop concept, does not work in low Reynolds number domain, therefore to swim or propel, a nanoswimmer must have non-reciprocal propulsive mechanism.

In 1977, Purcell [1] in his landmark talk "Life at low Reynolds number" suggested two possible swimming strategies employed by nature that work at low Reynolds number, namely either by the planar beating of tail (flagella) i.e. 'the flexible oar' or by helical propulsion of tail (flagella) i.e. the 'corkscrew swimmer'. The two strategies are schematically shown in Figure 3.1. From Figure 3.1(a) and Figure 3.1(b) it can be seen that the motion of flagella in both cases is non-symmetric. The non-symmetric motion is shown by bold and dotted line, and the corresponding swim is part of cyclic motion.

To model and analyze the propulsion of flagellated nanoswimmer, following approaches have been proposed by researchers in available literature [2-22]

i Resistive force theory (RFT) [3]

ii Slender body theory (SBT) [4]

iii Boundary element method (BEM) [5]

iv Bead model (BM) [6]

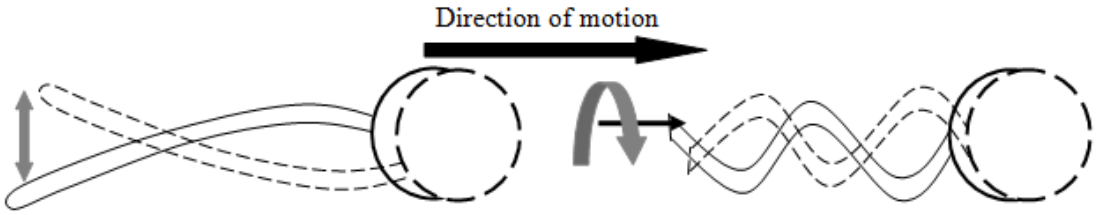


(a) (b)

**Figure 3.1: Planar (i.e. wiggling) and helical wave (i.e. corkscrew) propulsion**

RFT, the use of which was first pioneered by Gray and Hancock [3], has been shown to be highly effective in predicting the propulsion parameters for planar and helical waves corroborating observations from nature [3] as well as scaled up experiments [7-9]. RFT uses the linear Stokes flow assumption and considers the flagellum to be composed of a series of interconnected cylinders. The fluid resistance on each small cylinder is calculated by assuming that it is translating at its given orientation in the absence of neighboring cylinders.

The more rigorous slender body theory provides a systematic method of approximating the flow field and hence the forces on long and thin objects. The advantage of slender body theory is that solutions of desired accuracy can be obtained, and its disadvantage is that it can require tedious and involved computations. Slender body theory captures the hydrodynamic interactions between distant parts of a curved filaments more accurately. This interaction, which is not considered in resistive-force theory, is not so significant for small cell bodies, such as the heads of simple spermatozoa. For larger cell bodies, or cell bodies that have large amplitude motions transverse to the swimming direction, use of slender-body theory is required for accurate analysis. Slender body theory is based on the fundamental concepts of mass and momentum conservation at low Reynolds numbers, which result in a system of linear partial differential equations i.e. Stokes equations [10]. Slender Body Theory (SBT) was first formulated by Hancock [4] and firmed up by pioneers like Taylor [11], Cox [12], Batchelor [13], Higdon [14], Johnson [15], who

refined and brought this theory forward. Johnson and Brokaw [16] investigated the accuracy of the RFT and compared the distinctions between RFT and SBT. It was shown by Brokaw and other researchers that SBT is good for large-amplitude planar waves whereas RFT is better where the cell body is absent or very small.

Unlike previous approaches such as RFT and SBT, boundary element method (BEM) is not restricted to slender bodies, allow the modeling of realistic and complex geometries [17]. BEM is applicable to all, uniflagellated to multiflagellated nanoswimmer with the variations in geometrical parameters. BEM is a numerical technique to find the flow field and pressure around an elastic filament using Stokes equation. In boundary element method, forces on a flagellum and the resultant flow field can be found by discretizing a flagellum surface and assigning a Stokeslet to represent the fluid response to each surface element.

In another approach, called as bead model, few researchers [6, 18-22] divided linear elastic filaments (i.e. flagella) of nanoswimmer in discrete beads connected through stiff linkers. In 1977, de la Torre and Bloomfield [6] proposed the bead model approach for the study of hydrodynamics of microorganism, in which the helical flagellum is replaced by a discrete array of frictional beads along its center line. The beads were assumed to behave hydrodynamically like spheres whose radius is equal to that of the flagellum. In this approach, hydrodynamic behavior of spheres is determined by Stokes' law frictional coefficients and the hydrodynamic interaction tensors between them.

The literature available on modeling of locomotion at low Reynolds number for nanoswimmer reported shows the importance and popularity of RFT among researchers starting from early 1931 to till date. This is so because of simplicity and relative ease of application of RFT for obtaining results for uniflagellated nanoswimmers. Despite the limitation that RFT does not account for the interactions between the flagellum and the cell body or flow boundaries, it gives quite accurate and acceptable results for flagellated nanoswimmer with small head. Gray and Hancock validated resistive-force theory and their proposed resistive coefficients by comparing their model with the behavior of sea-urchin spermatozoa [3]. The difference in results obtained by RFT and actual sea-urchin spermatozoa was less than 1%. Embracement of the theory by the academic community followed with successful applications, other biological organisms have been modeled using RFT. In the next section, RFT approach is explained which is followed by sections on modeling of PWP and HWP with uniform diameter flagellum.

## 3.2 RESISTIVE FORCE THEORY

Resistive force theory (RFT) for modeling propulsion of a nanoswimmer was first proposed by Sir Geoffrey Taylor [2]. Gray and Hancock [3], Chwang and Wu [23], Lighthill [24] are the few pioneers, who refined and brought this theory forward. It was initially proposed for sea urchin spermatozoa. To estimate the forces on filaments moving at low Reynolds number, Gray and Hancock proposed a method in which local force components are linearly related to velocity components through corresponding drag coefficients and this method later in time became popularly known as resistive force theory (RFT). RFT is also known as local drag theory as it describes the hydrodynamic forces per unit length acting at a point on a filament in terms of velocity of the filament at that point. The researchers argued that as the flagellum undulates provided its radius of curvature is large compared to its diameter, the forces corresponding to the normal and tangential motion would be approximately given by the product of local flagellum velocity and the drag coefficients.

In RFT, the fluid is treated as a passive background material which responds negligibly to the motion of slender object. The theory is valid for the situation in which the inertial forces are negligible as compared to the viscous forces. Nanoswimmers present an ideal case of negligible inertia and RFT is suitably applied for its' modeling. The wave form for both i.e. PWP and HWP have been generated from first principles of balancing the viscous forces with the bending forces and presented in section 3.3 and section 3.4, respectively. In the following sub-section RFT is explained taking planar wave as an example.

## 3.3 SIMULATION OF PLANER WAVE PROPULSION (PWP) THROUGH A UNIFORM DIAMETER NANOSWIMMER (UDN)

In this section, the mathematical model for uniform diameter nanoswimmer (UDN) propelling by generating PWP has been presented. Although the RFT modeling has been reported in literature, it is derived in the next section for the sake of continuity. The developed mathematical model is further simulated for performance indexes of nanoswimmer namely swimming velocity and efficiency i.e. $V_x$ and $\eta$ in the next section.

### 3.3.1 Modeling PWP in UDN

Figure 3.2 shows a simple schematic of the nanoswimmer proposed to be propelled by a flagellar motion executing planar wave motion. The coordinates drawn are shown along with the flagellum. Coordinates origin is considered to be at head and tail joint as shown in Figure 3.2.

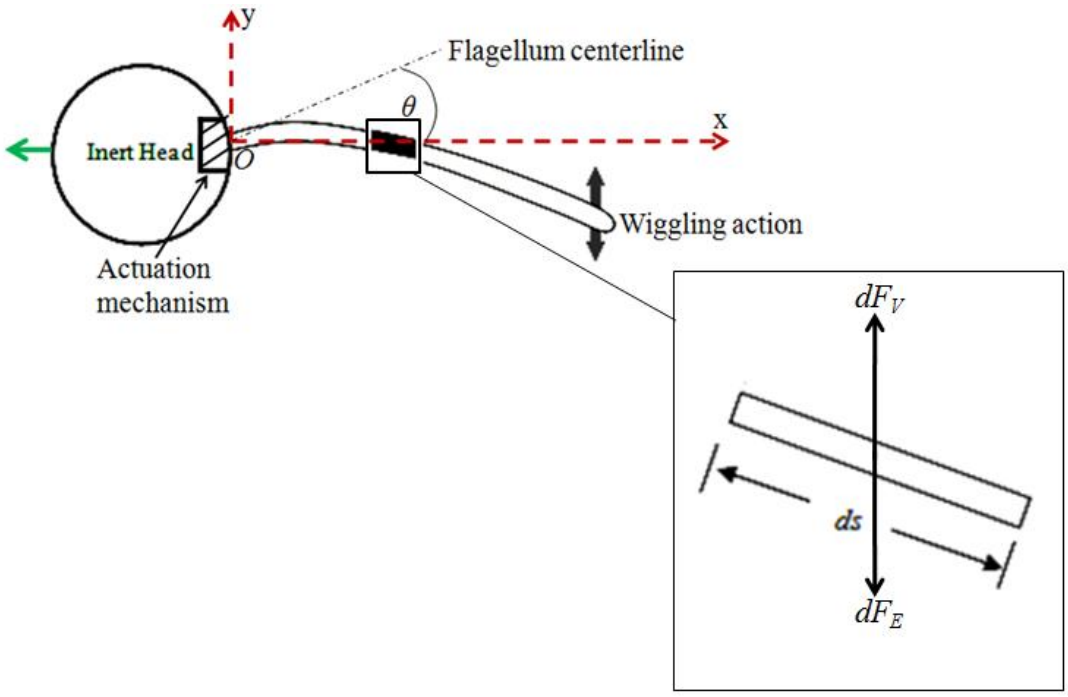


**Figure 3.2: Schematic diagram of a nanoswimmer whereby the wiggling of the elastic tail generates forward thrust**

The nanoswimmer is considered to be consisting of a head and an elastic tail part i.e. flagellum. The propulsive force is generated by the tail motion in a fluid. The nanoswimmer is considered to be surrounded by the fluid (shown in Figure 3.2 as white background) and its constraint boundary are supposed to be far away and therefore do not influence the motion of tail. Assessing the tail configuration provides the boundary conditions, the drag of a small element '*ds*' of the wiggling tail provides a thrust force perpendicular to the direction of actuation. This thrust force and a summation of all such thrust forces from all the elements constituting the tail, provide propulsion to the nanoswimmer with a velocity $V_x$ in *x*-direction. The head of the nanoswimmer is taken as sphere lying along negative *x* direction. The base angle ($\theta$) of flagella oscillates with a frequency ($\omega$) in two dimensions i.e. in *xy* plane by an actuating mechanism assumed to be present in the swimmer's head. The present thesis is focused on the design of flagella and we have assumed the presence of actuation mechanism responsible for either planar or

helical beating of flagella. The work models and investigates two aspects of flagellum design namely (1) determination of the steady state shape and (2) calculation of performance indexes namely swimming velocity ($V_x$) and efficiency of propulsion ($\eta$).

The inertia terms in the equation of motion are neglected, which is a valid assumption (also repeatedly emphasized in available literature) for a nanoswimmer as mass of the nanoswimmer is negligible. The flagellum is considered as a thin body, which is valid for $L/b$ from 50 to 500, where $L$ and $b$ are the length and cross-sectional radius of flagellum [29], respectively. Uniform elasticity and uniform circular cross section has been considered along the flagellum.

With the above mentioned considerations, two forces govern the motion of an element of flagellum, namely elastic forces ($dF_E$) that tend to straighten the flagellum and viscous forces ($dF_V$) that oppose the motion of each element through the fluid medium (Refer Figure 3.2.). The two forces determine the form and the rate of propagation of waves along flagella. At equilibrium of the two forces, force balance is used to derive the resultant governing equation of motion. Consider the forces acting on an element *ds* of the flagellum (Figure 3.2). The elastic force $dF_E$ is obtained by considering *ds* as an oscillating elastic beam and has been derived in [25]. The derivation of equation is given in Appendix-I for reference. The force $dF_E$ is given as [25]:

$$dF_E = EI \frac{\partial^4 y}{\partial x^4} ds \tag{3.1}$$

where, $E$ is the elasticity of the material of flagella, $I$ is the area moment of inertia and $y$ is the transverse displacement at any given position over length.

The viscous force $dF_V$ is product of drag coefficient acting on element *ds* and elemental velocity in *y* direction [26]. Considering drag coefficient as $C_n$ in normal direction and elemental velocity as $\frac{\partial y}{\partial t}$, the elemental viscous force $dF_V$ on element *ds* is

$$dF_V = -C_n \frac{\partial y}{\partial t} ds \tag{3.2}$$

where, $C_n$ is the normal resistive force coefficient, $y$ is the displacement of element *ds* in *y* direction, and $t$ is time, $\frac{\partial y}{\partial t}$ is the rate of change of displacement $y$ with respect to time.

At steady state of motion, equilibrium of forces results in force balance. A force balance on element *ds* of the tail is given by equating elastic forces ( $dF_E$ ) and viscous drag ( $dF_V$ ) and is obtained by equating equation (3.1) with equation (3.2) as:

$$EI\frac{\partial^4 y}{\partial x^4} = -C_n\frac{\partial y}{\partial t} \tag{3.3}$$

Equation (3.3) is Euler's beam equation and the solution of the equation (3.3) is obtained and given in [27]. The solution of equation (3.3) is assumed as a function of *x* and *t*, and is given as:

$$y(x,t) = y(x)e^{i\omega t} \tag{3.4}$$

where displacement *y* is a function of displacement in *x* direction and time *t*, and $\omega$ is frequency of oscillation of element. The first order time derivative and fourth order displacement derivative of equation (3.4) are obtained as:

$$\frac{\partial y}{\partial t} = y(x)i\omega e^{i\omega t} \tag{3.5}$$

$$\frac{\partial^4 y}{\partial x^4} = e^{i\omega t}\frac{d^4 y}{dx^4} \tag{3.6}$$

Substituting $\frac{\partial y}{\partial t}$ from equation (3.5) and $\frac{\partial^4 y}{\partial x^4}$ from equation (3.6), in equation (3.3) and rearranging the terms, we obtain

$$\frac{d^4 y}{dx^4} + i\frac{C_n\omega}{EI}y = 0 \tag{3.7}$$

Considering

$$l = \left(\frac{E\ I}{C_n\omega}\right)^{\frac{1}{4}} \tag{3.8}$$

where, *l* is the scale length associated with elastic forces and drag on the filament. The scale length plays an important role in determining the rigidity or flexibility of a flagellum. Equation (3.7) is written in terms of scale length as:

$$\frac{d^4 y}{dx^4} + \frac{i}{l^4}y = 0 \tag{3.9}$$

The characteristic equation (3.9) is written as:

$$m^4 + \frac{i}{l^4} = 0 \tag{3.10}$$

where $m^4 = \frac{d^4 y}{dx^4}$; is the fourth order space derivative of transverse displacement of the flagellum.

The general solution of the equation (3.3) is given as [28]

$$y(x,t) = e^{i\omega t}[A_1 e^{\frac{m_1}{l}x} + A_2 e^{\frac{m_2}{l}x} + A_3 e^{\frac{m_3}{l}x} + A_4 e^{\frac{m_4}{l}x}] \tag{3.11}$$

where $A_1$, $A_2$, $A_3$ and $A_4$ are the arbitrary constants, which are obtained from the boundary conditions given in equation (3.12) and $m_1$, $m_2$, $m_3$, and $m_4$ are the four roots of $(-i)^{\frac{1}{4}}$. In the next sub section, the boundary conditions are presented to obtain the complete solution of equation (3.11).

### 3.3.2 Modeling Performance Indexes in Planar Wave Propelled UDN

The actuation of the flagellum is at the proximal end (i.e. where $x = 0$) with the tail fixed to the head. Consider a time dependent slope having maxima as $G = \tan(\theta_{\max})$ at beating frequency of $\omega$. At the distal end (i.e. where $x = L$), the shear force and the bending moment vanishes. Hence for a spherical head attached to cylindrical tail of a nanoswimmer among many possibilities, the boundary conditions considered here are as follows

$$\text{Position at proximal end } y\big|_{x=0} = 0 \tag{3.12a}$$

$$\text{Slope at proximal end } y'\big|_{x=0} = Ge^{i\omega t} \tag{3.12b}$$

$$\text{Bending moment at distal end } y''\big|_{x=L} = 0 \tag{3.12c}$$

$$\text{Shear force at distal end } y'''\big|_{x=L} = 0 \tag{3.12d}$$

The four coefficients $A_1$, $A_2$, $A_3$ and $A_4$ are calculated by substituting the boundary conditions given in equation (3.12), in equation (3.11).

Substituting the boundary condition from equations (3.12a) in equation (3.11) we get

$$A_1 + A_2 + A_3 + A_4 = 0 \tag{3.13a}$$

Similarly substituting the second boundary condition from equations (3.12b) in equation (3.11) we get

$$A_1 \frac{m_1}{l} + A_2 \frac{m_2}{l} + A_3 \frac{m_3}{l} + A_4 \frac{m_4}{l} = G \tag{3.13b}$$

Similarly substituting the third boundary condition from equations (3.12c) in equation (3.11) we get

$$A_1 m_1^2 e^{\frac{m_1}{l}L} + A_2 m_2^2 e^{\frac{m_2}{l}L} + A_3 m_3^2 e^{\frac{m_3}{l}L} + A_4 m_4^2 e^{\frac{m_4}{l}L} = 0 \tag{3.13c}$$

Similarly substituting the fourth boundary condition from equations (3.12d) in equation (3.11) we get

$$A_1 m_1^3 e^{\frac{m_1}{l}L} + A_2 m_2^3 e^{\frac{m_2}{l}L} + A_3 m_3^3 e^{\frac{m_3}{l}L} + A_4 m_4^3 e^{\frac{m_4}{l}L} = 0 \tag{3.13d}$$

The equations (3.13a) to (3.13d) are combined and rewritten in form of matrix as

$$\begin{Bmatrix} 1 & 1 & 1 & 1 \\ m_1 & m_2 & m_3 & m_4 \\ m_1^2 e^{m_1 \frac{L}{l}} & m_2^2 e^{m_2 \frac{L}{l}} & m_3^2 e^{m_3 \frac{L}{l}} & m_4^2 e^{m_4 \frac{L}{l}} \\ m_1^3 e^{m_1 \frac{L}{l}} & m_2^3 e^{m_2 \frac{L}{l}} & m_3^3 e^{m_3 \frac{L}{l}} & m_4^3 e^{m_4 \frac{L}{l}} \end{Bmatrix} \begin{bmatrix} A_1 \\ A_2 \\ A_3 \\ A_4 \end{bmatrix} = \begin{bmatrix} 0 \\ G \times l \\ 0 \\ 0 \end{bmatrix} \tag{3.14}$$

where, $L/l$ (i.e. $l_o$) is the characteristic length, a dimensionless term, which characterizes the relative magnitudes of the viscous and bending forces and hence represents the overall effectiveness of a nanoswimmer. Equation (3.14) is used to obtain four coefficients $A_1$, $A_2$, $A_3$ and $A_4$. By substituting back them in equation (3.11) we obtain steady state shape of wave form. Characteristic length describes the length of flagellum scaled by characteristic distance over which undulations in flagellum settle down. Characteristic length is a key and fundamental parameter to evaluate the performance of a nanoswimmer and is defined as

$$l_o = \frac{L}{l} = \left( \frac{L}{\left( \frac{E\,I}{C_n \omega} \right)^{\frac{1}{4}}} \right) \tag{3.15}$$

A low value of characteristic length ($l_o$) indicates that bending forces dominate and a high value of characteristic length corresponds to higher viscous forces. Thus if $l_o \approx 1$ flagellum behaves like a rigid rod with only very small deflections while for $l_o \rangle\rangle 1$, flagellum is very sloppy. Characteristic length ($l_o$) is also known as Sperm number (*Sp*) and was proposed by researchers in 2003 [18-19].

Referring to Figure 3.2 again, the element *ds* is redrawn in Figure 3.3 more elaborately. Figure 3.3 shows the forces acting in normal and longitudinal directions on the element *ds* of the flagellum due to transverse velocity $V_y$ and forward velocity $V_x$. The element is oriented to the *x*-axis at an angle $\theta$ at an instance of time *t*. In Figure 3.3, the longitudinal direction *l* and the normal direction *n* are shown along and normal to the centroidal axis of the element *ds*.

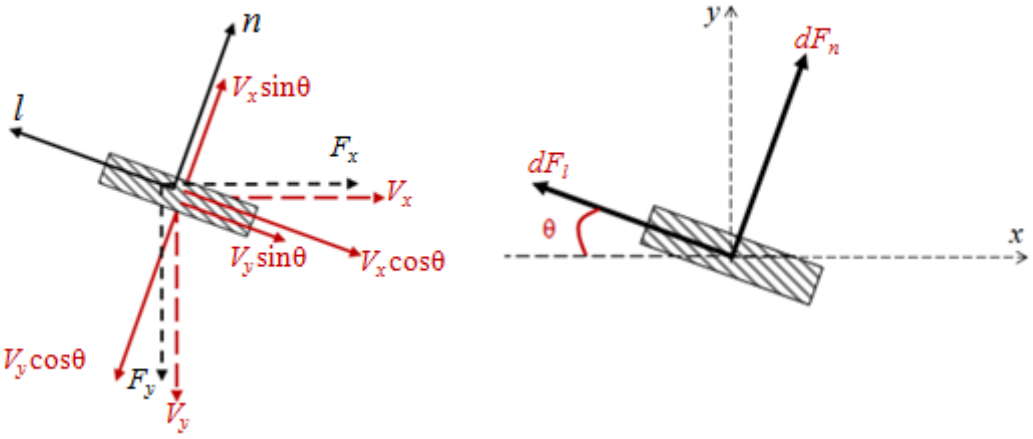


**Figure 3.3: Free body diagram of the element '*ds*' of the tail**

The drag force generated depends on the components of the velocity in the normal and the longitudinal directions. The resistance of the fluid to the flagellum's motion is computable if the local coefficient of drag for the element and its velocity component in normal and longitudinal directions are known. Usually, the coefficient of drag is expressed in terms of normal and tangential drag coefficients per unit length, $C_n$, and $C_l$, respectively. The total force in normal and longitudinal directions for any motion of the flagellum is found by an integration of the forces from each such small segment of the flagellum. For objects that are much longer than the cross sectional dimensions, the fluid force per unit length is conveniently split into a normal force ($dF_n$) and a longitudinal force ($dF_l$). These two components of force (i.e. $dF_n$ and $dF_l$) due to

transverse and forward displacements of the element are vectorial summation of components of drag forces and are given as

$$dF_n = C_n(V_y \cos\theta - V_x \sin\theta)ds \tag{3.16}$$

$$dF_l = C_l(V_x \cos\theta + V_y \sin\theta)ds \tag{3.17}$$

where, $V_x$ and $V_y$ are the velocity in *x* and *y*- directions, respectively, $V_x \sin\theta$ and $V_y \cos\theta$ are velocity components in *n*-direction and $V_x \cos\theta$ and $V_y \sin\theta$ are components in *l*-direction. These two formulae given in equations (3.16) and (3.17) constitute the basis of resistive force theory

$C_n$ and $C_l$ in equation (3.16) and (3.17) are the coefficients of normal and tangential drag per unit lengths. The velocity of wave propagation is correlated with the thrust force generated by the flagellum through these drag coefficients. Gray and Hancock [3] assumed the drag coefficient as a function of viscosity of medium, the wavelength and diameter of the flagellum. In 1958, Machin [28] modified it as a function of viscosity and Reynolds number. Later Wiggins et al. [29] proposed it to be a function of viscosity of the medium and length to radius ratio of the flagellum. Over the period of time this coefficient has changed its form for better approximation of the propulsion indexes of nanoswimmer. The more accepted and more used normal and tangential coefficients of drag $C_n$ and $C_{l,}$ is given as [3, 29-30]

$$C_n = \frac{4\pi\mu}{\ln\left(\frac{L}{b}\right) + 0.5} \tag{3.18}$$

$$C_l = \frac{2\pi\mu}{\ln\left(\frac{L}{b}\right) - 0.5} \tag{3.19}$$

where $\mu$ is the viscosity of the liquid medium, *L* is length of the flagellum and *b* is flagellum radius. The resultant forward thrust (i.e. net force in *x*-direction) and the resultant transverse force (i.e. net force in *y*-direction) on the element *ds* (refer Figure 3.3) is found out by taking components of normal and longitudinal forces along *x*- and *y*-directions, respectively and are given as

$$dF_x = dF_n \sin\theta - dF_l \cos\theta \tag{3.20}$$

$$dF_y = -dF_n \cos\theta - dF_l \sin\theta \tag{3.21}$$

Substituting the normal force $dF_n$ and longitudinal force $dF_l$ from equations (3.16) and (3.17), respectively, in equation (3.20), and rearranging gives the net forward thrust $dF_x$ as

$$dF_x = [(C_n - C_l)V_y \sin\theta\cos\theta - (C_n \sin^2\theta + C_l \cos^2\theta)V_x]ds \qquad (3.22)$$

Similarly, the net transverse force is obtained by substituting the normal force $dF_n$ and longitudinal force $dF_l$ from equations (3.16) and (3.17), respectively, in equation (3.21) and rearranging we get $dF_y$

$$dF_y = [(C_n - C_l)V_x \sin\theta\cos\theta - (C_n \cos^2\theta + C_l \sin^2\theta)V_y]ds \qquad (3.23)$$

Dividing numerator and denominator of equations (3.22) and (3.23) by $\cos^2\theta$

$$dF_x = \frac{[(C_n - C_l)V_y \sin\theta\cos\theta - (C_n \sin^2\theta + C_l \cos^2\theta)V_x]ds/\cos^2\theta}{1/\cos^2\theta} \qquad (3.24)$$

$$dF_y = \frac{[(C_n - C_l)V_x \sin\theta\cos\theta - (C_n \cos^2\theta + C_l \sin^2\theta)V_y]ds/\cos^2\theta}{1/\cos^2\theta} \qquad (3.25)$$

Now, using $\frac{1}{\cos^2\theta} = \sec^2\theta = 1 + \tan^2\theta$ in equation (3.24) and (3.25), and solving, we get

$$dF_x = \frac{[(C_n - C_l)V_y \tan\theta - (C_n \tan^2\theta + C_l)V_x]}{1 + \tan^2\theta}ds \qquad (3.26)$$

$$dF_y = \frac{[(C_n - C_l)V_x \tan\theta - (C_n + C_l \tan^2\theta)V_y]}{1 + \tan^2\theta}ds \qquad (3.27)$$

Length of the small element *ds* is given by $ds = \left(\sqrt{1 + \tan^2\theta}\right)dx$, where $dx$ is the projection of elemental length *ds* along *x*-axis and $\theta$ is the angle between element *ds* and *x*-axis. Substituting for $ds$ in terms of $dx$ and $\theta$ in equation (3.26) and equation (3.27) and considering for the low amplitude waves, $\theta$ very small $(\text{i.e. } \tan\theta \langle\langle 1)$ therefore neglecting terms with $\tan^2\theta$, the equations (3.26) and (3.27) reduce to

$$dF_x \approx [(C_n - C_l)V_y \tan\theta - C_l V_x]dx \qquad (3.28)$$

$$dF_y \approx [(C_n - C_l)V_x \tan\theta - C_n V_y]dx \qquad (3.29)$$

Now, substituting $\tan\theta = \frac{dy}{dx}$ and $V_y = \frac{dy}{dt}$ in equation (3.28) and substituting $y$ from equation (3.11) and integrating equation over the flagella length from 0 to $L$, gives the net thrust $F_x$ generated by the flagellum and is given as

$$F_x = \int_0^L dF_x = \int_0^L [(C_n - C_l)\frac{dy}{dt}\frac{dy}{dx} - C_l V_x]dx \tag{3.30}$$

The net thrust $(F_x)$ is used to overcome the drag due to the head by nanoswimmer to move forward. Under steady state conditions, the magnitude of the thrust force $F_x$ generated by the entire tail is equal to the drag experienced by the head. From Stokes' equation, drag due to a spherical head of radius $r_h$ in a viscous medium of viscosity $\mu$ is given as [31]

$$F_{head} = 6\pi\ \mu\ r_h V_x \tag{3.31}$$

Equating the net thrust force generated due to wiggling action of the flagellum from equation (3.30) to the drag due to spherical head from equation (3.31), we can calculate the forward velocity $V_x$ of the nanoswimmer. Equating (3.30) to with equation (3.31) we have

$$\int_0^L \left\{(C_n - C_l)\frac{dy}{dt}\frac{dy}{dx} - C_l V_x\right\}dx = 6\pi\ \mu\ r_h V_x \tag{3.32}$$

Rearranging equation (3.30), we obtained forward velocity $V_x$ of the nanoswimmer

$$V_x = \frac{\int_0^L \left\{(C_n - C_l)\frac{dy}{dt}\frac{dy}{dx}\right\}\ dx}{6\pi\mu\ r_h + C_l L} \tag{3.33}$$

Forward velocity $V_x$ is the first index to evaluate the performance of the nanoswimmer. Another index for performance investigation of a nanoswimmer is efficiency $(\eta)$ of a nanoswimmer which is defined as the ratio of useful power developed for forward motion along the $x$ axis to the total power needed for wiggling the tail. The power needed to wiggle the tail is the power comsumed in motion in the $x$ and $y$-directions and is calculated by integrating $dF_x V_x$ and $dF_y V_y$ over the flagella length.

Efficiency $(\eta)$ of the nanoswimmer is defined as

$$\eta = \frac{\int_0^L dF_x V_x}{\int_0^L dF_x V_x + \int_0^L dF_y V_y} \tag{3.34}$$

The developed mathematical model for performance measuring index of nanoswimmer namely velocity $(V_x)$ (refer equation 3.33), and efficiency $(\eta)$ (refer equation 3.34) are simulated in the next section using MATLAB®.

### 3.3.3 Simulation, Results and Discussion of Performance of Planar Wave Propelled UDN

The numerical simulations for the propulsion model developed for uniform flagella (refer equation 3.11, with substitution of four coefficients $A_1$, $A_2$, $A_3$ and $A_4$ from equation 3.14) in previous section are carried out using MATLAB®. The MATLAB code is given in Appendix-II. The parameters for simulation namely flagellum stiffness, viscosity of surrounding medium, flagellum length, cross-section radius of the flagellum, and radius of head are chosen based on prokaryotic microorganism and sea-urchin spermatozoa since they use planar wave propulsion. The parametric values used for simulations are listed in the Table 3.1.

The simulated shapes are obtained for a flagella of uniform diameter (cross-section radius 0.2 $\mu$m) and length $L$ = 50 $\mu$m. The fluid through which the nanoswimmer is swimming is assumed to be water with viscosity 0.001 Pa-s. The head radius considered is 0.5 $\mu$m. The values of flexural rigidity ($EI$) is chosen in the range of $10^{-24}$ Nm$^2$ - $10^{-18}$ Nm$^2$ [32-33]. The simulated range of values for $EI$ covers entire experimentally observed and simulated values in available literature. From observed values of beating frequency in nature [34], the range considered here varies from 25 Hz to 45 Hz. The values of surrounding medium viscosity, length of flagellum, and cross-section radius and radius of head are kept same for all simulation whereas flagellum stiffness is varied as parameter from $10^{-18}$ Nm$^2$ to $10^{-24}$ Nm$^2$ to understand the effect of flexural rigidity of flagellum on shapes and motion of the nanoswimmer.

**Table 3.1: List of parametric values (PWP)**

| S.No. | Parameter | Value [3, 32-34] (Sea-urchin spermatozoa) |
|---|---|---|
| 1 | Flagellum stiffness (*EI*) | $10^{-22}$ Nm$^2$ |
| 2 | Surrounding medium (water) viscosity $(\mu)$ | 0.001Pa.s |
| 3 | Flagellum length (*L*) | 50 μm |
| 4 | Cross section radius of flagellum (*b*) | 0.2 μm |
| 5 | Radius of head ( $r_h$ ) | 0.5 μm |

The variation in flagellum stiffness causes characteristic length $l_o$ (refer equation 3.15) to vary from 1 to 10. The simulations were carried out for different values of $l_o$ in this range i.e. 1 to 10. For simulation, the boundary conditions given in equation (3.12) were considered. The simulated shapes of the elastic flagella for five different characteristic lengths ($l_o$) 1, 2, 5, 7 and 10, respectively with a flagella beating frequency of 35 Hz [3] are shown in Figure 3.4 to Figure 3.8 at eight different time intervals. Figure 3.4 and Figure 3.5 shows the flagellum with smaller characteristic lengths i.e. when $l_o \approx 1$ and ($l_o \approx 2$). Figure 3.4 and Figure 3.5, illustrates that the flagellum with smaller characteristic lengths behave as a stiff filament, while those with larger characteristic lengths (Figure 3.6, 3.7 and 3.8) behave as a flexible filament. In case of smaller characteristic lengths, Figure 3.4, ($l_o \approx 1$) and Figure 3.5 ($l_o \approx 2$), bending forces dominate and flagella remain straight and, hence flagella behaves like a rigid filament. Since the kinematic reversibility in low Reynolds regime does not produce a net thrust and exhibits rigidity, hence reversibility of motion in a cycle (refer mode shapes in Figure 3.4 and Figure 3.5), no net forward motion is achieved in such designs of nanoswimmer for flagellum with small characteristic lengths.

The plots of the shape of elastic flagella (Figure 3.6) obtained for a flagella beating frequency of 35 Hz, are in accordance with those published in literature [6] and also corroborates to the damping distance (the distance wave travels before its amplitude falls to 1/*e* of its original value) of around 2.6 times the scale length in the waveform. It is

clearly observed from the plots (Figure 3.4 to Figure 3.8) that with increase in characteristic length, the flexibility of the flagellum increases.

Figure 3.7 ($l_o \approx 7$) and Figure 3.8 ($l_o \approx 10$) shows that the flagellum elements located at a distance larger than $l$ does not oscillate much and therefore do not contribute towards thrust. For the larger characteristic length, drag forces dominates and hence leads to insufficient propulsion as most of the filament length has small deflection with very little oscillation. The drag exist throughout the length of the flagellum contributes drag but there exist no thrust contribution over a substantial length in larger characteristic length nanoswimmer. The velocity of swimmer decreases and tends to become zero because of excess drag for larger characteristic length of nanoswimmer. For the values of characteristic length ($l_o \approx 10$), the maximum amplitude in $x$ direction is observed to occur at a distance less than 10% of total length. To take full advantage of drag and thrust based propulsion, characteristic length ($l_o$) of flagella should be optimal and that may be around 2.6.

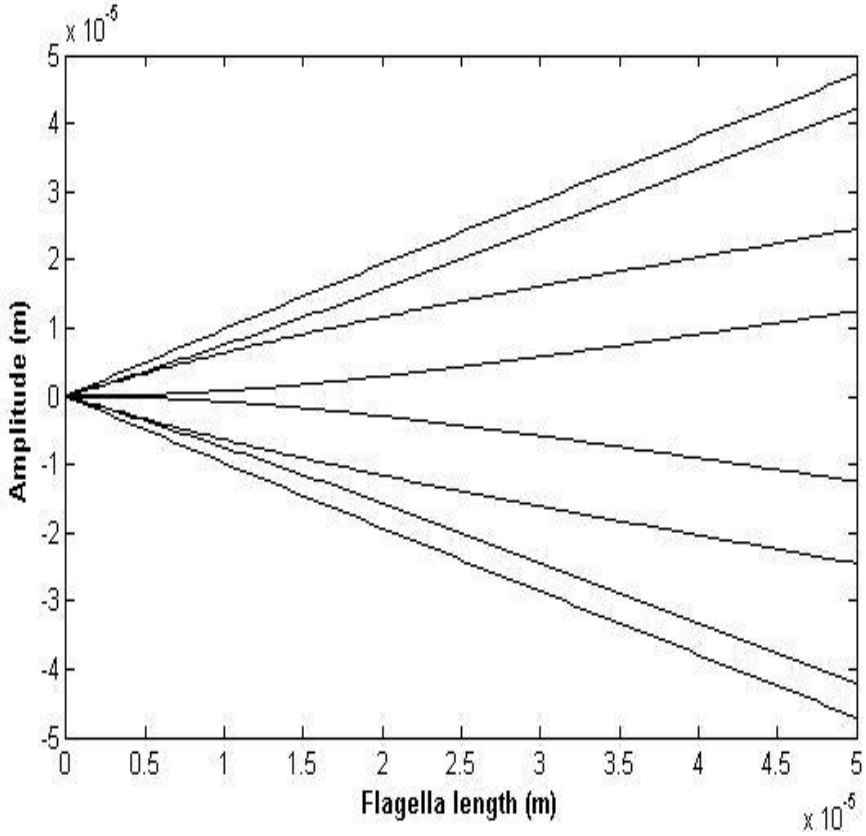


**Figure 3.4: Flagella projections are taken for $L$ equals to $l$ (i.e. $l_o \approx 1$) with flagellar beating frequency of 35 Hz at eight different time intervals**

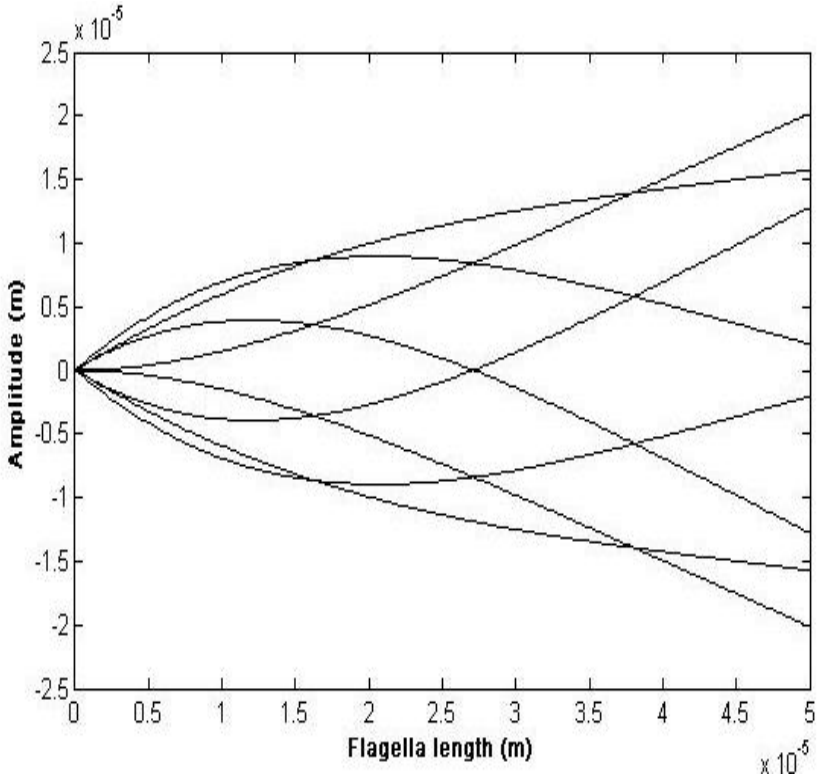


**Figure 3.5: Flagella projections are taken for *L* equals to 3*l* (i.e. $l_o \approx 3$) with flagellar beating frequency of 35 Hz at eight different time intervals**

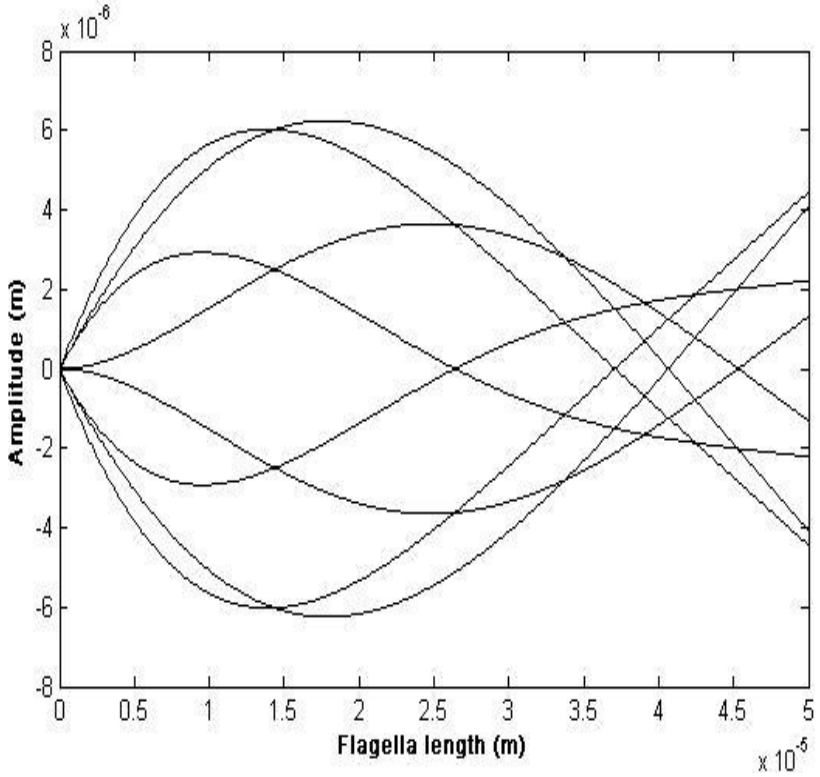


**Figure 3.6: Flagella projections are taken for *L* equals to 5*l* (i.e. $l_o \approx 5$) with flagellar beating frequency of 35 Hz at eight different time intervals**

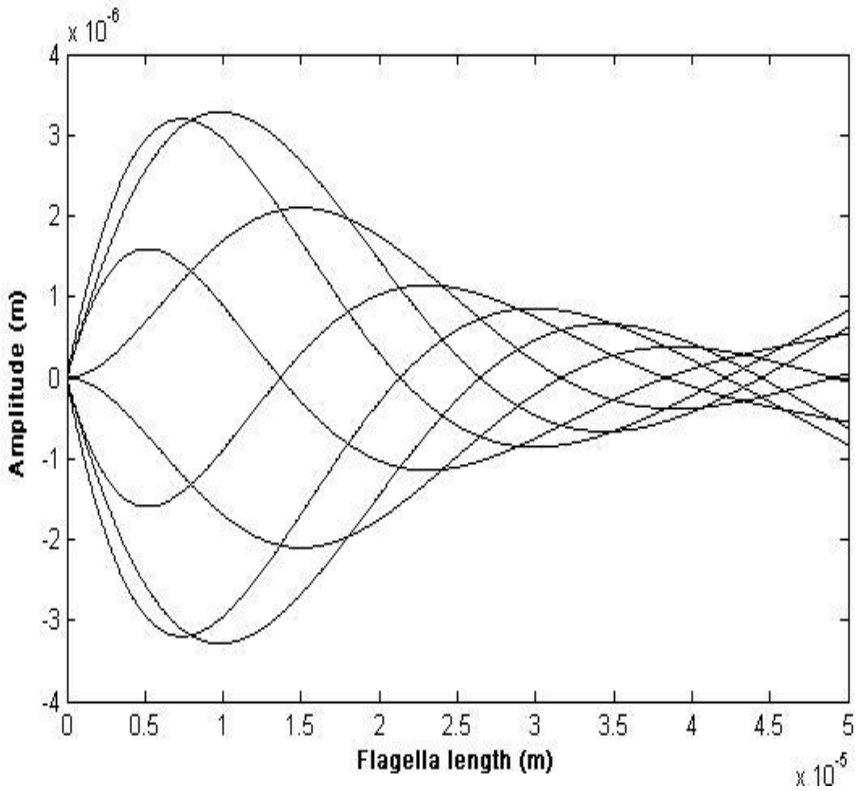


**Figure 3.7: Flagella projections are taken for *L* equals to 7*l* (i.e. $l_o \approx 7$) with flagellar beating frequency of 35 Hz at eight different time intervals**

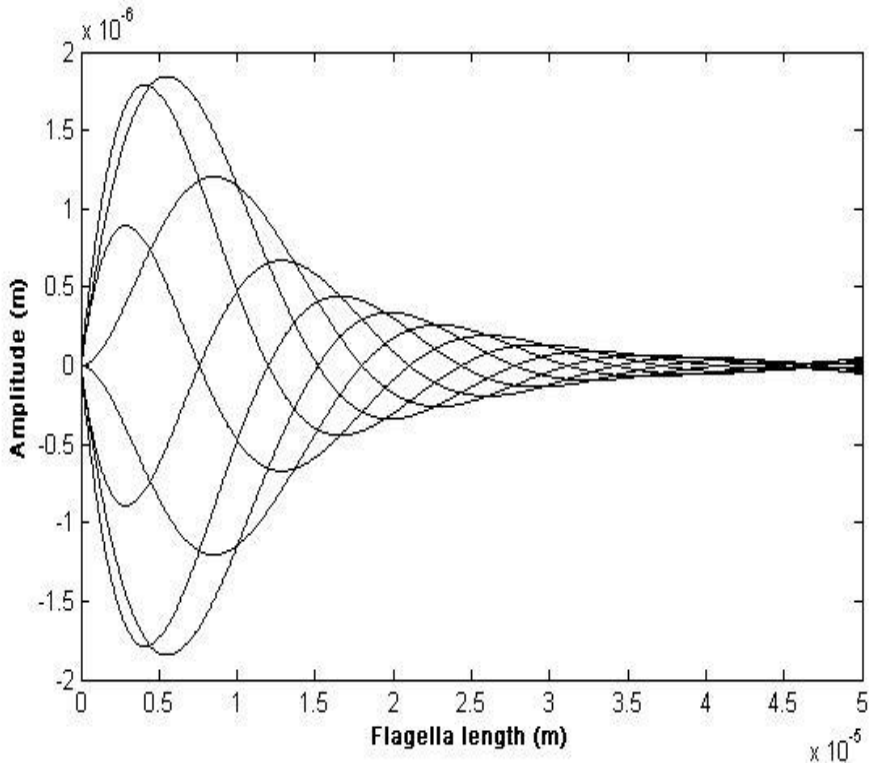


**Figure 3.8: Flagella projections are taken for *L* equals to 10*l*, (i.e. $l_o \approx 10$) with flagellar beating frequency of 35 Hz at eight different time intervals**

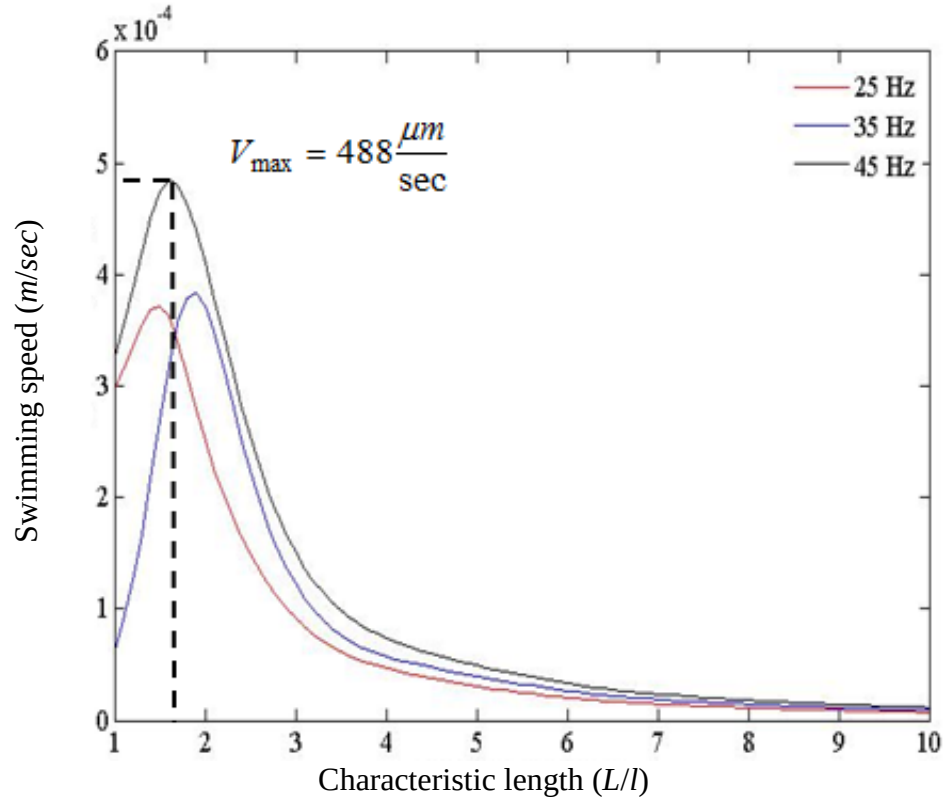


**Figure 3.9: Swimming speed variation with characteristic length $(L/l)$ for flagella beating frequency $\omega$ = 25, 35, 45 Hz**

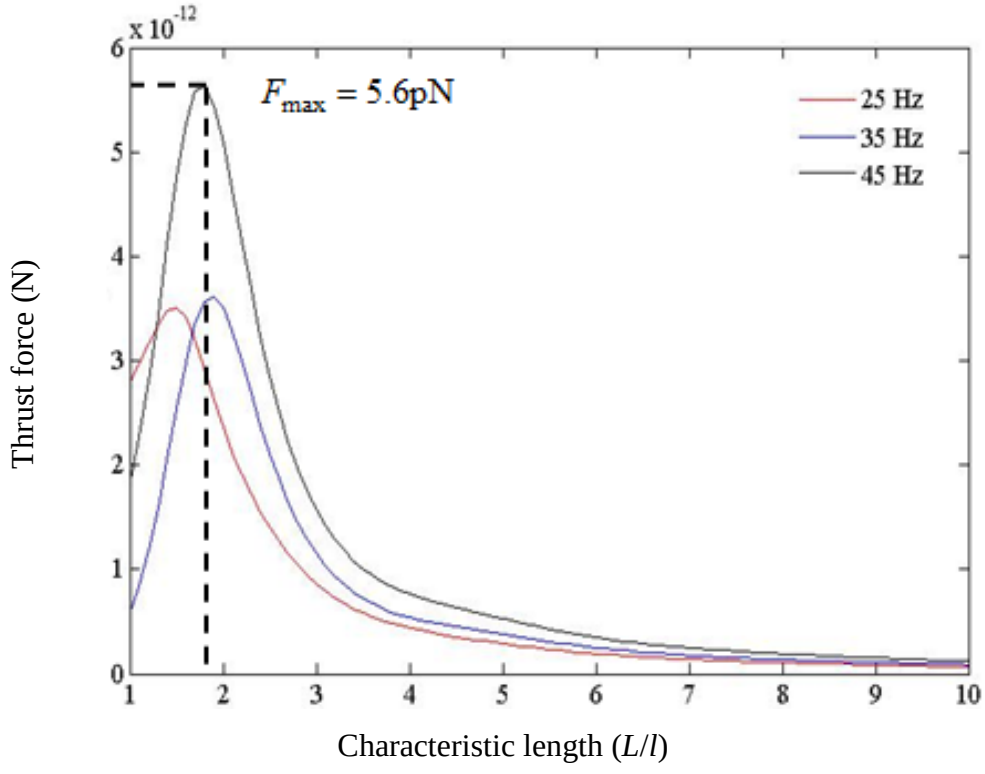


**Figure 3.10: Thrust force ( $F_x$ ) variation with characteristic length $(L/l)$ for flagella beating frequency $\omega$ = 25, 35, 45 Hz**

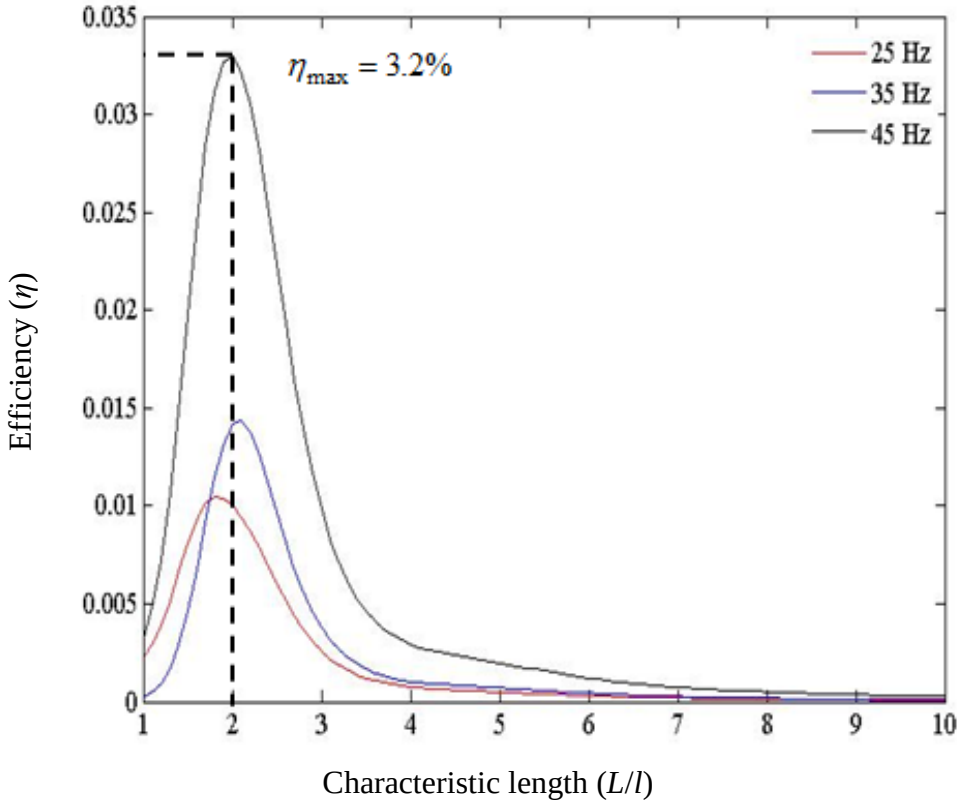


**Figure 3.11: Propulsive efficiency ($\eta$) Vs characteristic length $(L/l)$ for flagella beating frequency $\omega$ = 25, 35, 45 Hz**

Velocity of nanoswimmer which is mathematically modeled in equation (3.31) is simulated using parametric values as that used in simulations of mode shapes of nanoswimmer. The results of simulations are plotted in Figure 3.9. Figure 3.9 shows the variation of swimming speed with respect to characteristic length ($l_o$) for three different frequency values varied from 25 Hz to 45 Hz in steps of 10 Hz. From Figure 3.9, it can be observed that the swimming speed is maximum for $(L/l)$ near 2 and is optimal at 45 Hz.

The mathematical model of thrust force given by equation (3.30) and that for efficiency is given by equation (3.34) are also simulated for same parametric values used for simulation of mode shapes of the nanoswimmer. The results of simulations are plotted in Figure 3.10 and 3.11 respectively for thrust force $F_x$ and efficiency $\eta$. Maxima in swimming speed also corresponds to maxima in thrust force as is observed from Figure 3.10 and from efficiency plots, Figure 3.11. Further it can be observed that the

nanoswimmer generates higher thrust and, moves faster and efficiently at higher beating frequency values. The maximum swimming speed obtained at 45 Hz is 488 $\mu$m/s.
The maximum efficiency of nanoswimmer is found to occur at $\omega$ = 45 Hz, $L/l \approx 2$ and has a value of 3.2%. The maxima of both, the swimming speed (Figure 3.9) and propulsive efficiency (Figure 3.11) are in the range of $l_o \approx 2$.

The trend of variation of swimming speed, thrust force and efficiency is similar and is observed from Figure 3.9, Figure 3.10 and Figure 3.11, respectively. The values of $V_x$, $F_X$, $\eta$ increases as $L/l$, attains a maxima and then asymptotically reaches zero as $L/l \to \infty$. It is also observed from the plots that maxima of the nanoswimmer velocity $V_X$ occurs at beating frequency 45 Hz. For other frequencies, the shift in peak of $V_x$ is significantly visible. For $F_X$ and $\eta$, the highest value occurs at 45 Hz.

The resistive force theory has been applied to planar bending waves upto this point of investigation, but, helical wave propulsion has many advantages when fabrication and development of nanoswimmers is to be done artificially. In the planar bending wave model, elements of the flagella undergo opposite strains extremely often and hence it may be tough to create such a fiber on nanoscale. Nano springs made of carbon nanotubes are already existent [35] and hence the helical model may be the most easily artificially reproducible. In the planar bending waves, energy has to be generated locally for sustaining the same amplitude throughout the length of the tail which may be extremely tough for an artificial fiber. Therefore an investigation on helical wave propulsion is also carried out on similar lines as was done in the section for planar wave propulsion. Interestingly, despite its advantages mentioned above, such an analysis is not available in literature. The modeling and analysis was first reported by us in [36].

In the next section, mathematical modeling and analysis is carried out for helical wave propulsion with flagella of uniform diameter using RFT.

## 3.4 HELICAL WAVE PROPULSION (HWP) THROUGH A UNIFORM DIAMETER NANOSWIMMER (UDN)

In the previous section, mathematical modeling, simulation and analysis is performed for a nanoswimmer with flagella of uniform diameter, propelling itself by generating planar

wave. Performance of the nanoswimmer was evaluated in terms of forward velocity $V_x$ and propulsive efficiency $\eta$ using RFT.

In this section, mathematical model for UDN propelling itself by generating HWP has been done. The modeling has not been reported in earlier in literature and was first carried out by us with the boundary conditions given in section 3.4.2 and published in [36]. The developed mathematical model is simulated for performance indexes of nanoswimmer, namely, forward velocity $V_z$ and propulsive efficiency $\eta$.

### 3.4.1 Modeling HWP in UDN

Schematic of nanoswimmer performing helical wave motion through its flagella is shown in Figure 3.12. The coordinate system considered is also illustrated in Figure 3.12. The flagellar filament is taken with one end constrained to lie at the origin *O* and the other end is considered free. Initial unstressed shape of nanoswimmer is shown as a straight rod in Figure 3.12(a). $\theta$ denotes the angle made by the flagellum with the $z$-axis or axis of rotation. The base of the flagellum rotates along the $z$-axis, making the filament sweep out a cone of rotation along $z$-axis. Actuator inside the head is assumed to cause elastic deformation of the flagellum and take the shape of a helix with both pitch and amplitude varying along the $z$ direction as shown in Figure 3.12(b). The position vector of any point on the flagellum with respect to $z$-axis is considered as $\vec{r} = x\hat{i} + y\hat{j}$. The head of the nanoswimmer is taken as a sphere lying along the negative $z$-axis. The coordinate system along with the flagellum rotates with positive $z$-axis as axis of rotation at an angular velocity $\omega$ relative to a frame of reference situated on the head.

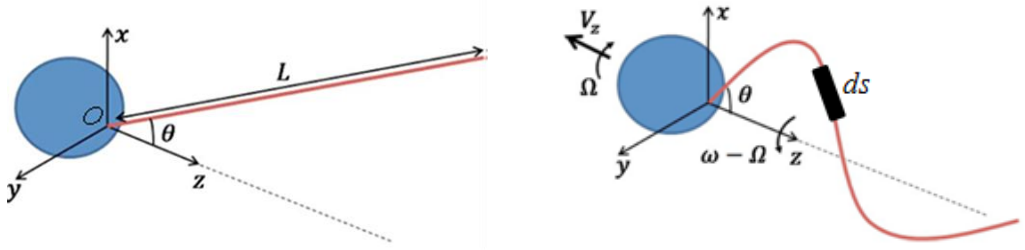


**Figure 3.12: Schematic of the nanoswimmer showing (a) initial non-deflected shape of the filament and (b) steady state deflected shape of the filament**

At steady state, transverse velocity of flagellum (i.e. velocity component perpendicular to flagellum centerline) relative to the fluid is

$$\vec{v}_{\perp} = \omega\hat{k} \times \vec{r} = -y\omega\,\hat{i} + x\omega\,\hat{j} \tag{3.35}$$

where, $\omega$ is angular velocity of flagellum with respect to head of nanoswimmer and $\hat{i}$, $\hat{j}$, $\hat{k}$ are the unit vectors in $x$, $y$ and $z$-direction, respectively.

The flagellum is both translating with respect to the fluid as well as rotating about its own centroidal axis. The rotation about centroidal axis causes a viscous torque tending to twist the flagellum about its own cross section. This torque ($\tau_v$) is order of $O(4\pi\mu\ b^2\omega r)$ [30] which is quite less for a flagellum with small diameter (in comparision to its length) and therefore the twist effect due to torque $\tau_v$ is neglected for estimating the shape.

For nanoswimmer, inertia force is negligible and steady state shape of flagellum is determined by a balance of elastic and viscous forces acting over the flagellum. The elastic bending force on an element of length *ds* for helical wave propulsion, $dF_E$, is given by replacing *y* with $\vec{r}$ and *x* with *z* in equation (3.1) and is obtained as equation (3.36)

$$dF_E = EI\left(\frac{\partial^4 \vec{r}}{\partial z^4}\right)ds \tag{3.36}$$

where, *E* is the elasticity of the material of flagella, *I* is the area moment of inertia and $\vec{r}$ is the position vector of the small element *ds* on flagellum.

The viscous forces ($dF_V$) on an element *ds* are well approximated by the resistive-force coefficients [30] and is given as

$$dF_V = -C_n \vec{v}_{\perp} ds \tag{3.37}$$

where, $C_n$ is the normal resistive force coefficient detailed subsequently and $\vec{v}_{\perp}$ is the velocity component perpendicular to flagellum centerline.

At steady state of motion, elastic bending force $dF_E$ (equation 3.36) and resistive force $dF_V$ (equation 3.37) balance each other on the element *ds*. Equating elastic and viscous forces on a small element *ds* of the flagellum gives

$$EI\left(\frac{\partial^4 \vec{r}}{\partial z^4}\right) = -C_n \vec{v}_{\perp} \tag{3.38}$$

Substituting for $\vec{r} = x\hat{i} + y\hat{j}$ and transverse velocity $(\vec{v}_{\perp})$of flagellum from equation (3.35), in equation (3.38), we obtain

$$EI\left(\frac{\partial^4 x}{\partial z^4}\hat{i} + \frac{\partial^4 y}{\partial z^4}\hat{j}\right) = -C_n\left(-y\omega\hat{i} + x\omega\hat{j}\right) \tag{3.39}$$

Equating $\hat{i}$ components on LHS and RHS in equation (3.39), we get

$$y = l^4\frac{\partial^4 x}{\partial z^4} \tag{3.40}$$

Similarly, equating $\hat{j}$ components on LHS and RHS in equation (3.39), we get

$$x = -l^4\frac{\partial^4 y}{\partial z^4} \tag{3.41}$$

where, $l = \left(\frac{EI}{C_n\omega}\right)^{\frac{1}{4}}$; $l$, is the scale length associated with elastic forces and drag on the flagellum and is same as given by equation (3.8) for PWP in section 3.3.1.

Further, substituting the value of $y$ from equation (3.40) in equation (3.41), we get

$$x = -l^4\frac{\partial^4}{\partial z^4}\left(l^4\frac{\partial^4 x}{\partial z^4}\right) \tag{3.42}$$

Solving we get $x$-$z$ wave form equation

$$x = -l^8\frac{\partial^8 x}{\partial z^8} \tag{3.43}$$

The characteristic equation (3.43) is written as:

$$m^8 + \frac{1}{l^8} = 0 \tag{3.44}$$

where $m^8 = \frac{d^8 x}{dz^8}$; is the eighth order space derivative of transverse displacement of the flagellum with respect to $z$.

The solution of equation (3.44) is a generalization of Machin's solution [28] and is given as

$$x(z) = \sum_{i=1}^{8} A_i e^{\frac{m_i z}{l}} \tag{3.45}$$

Substituting equation (3.45) back in equation (3.40) gives *y*-*z* wave form of flagellum

$$y(z) = \sum_{i=1}^{8} A_i (m_i)^4 e^{\frac{m_i z}{l}} \tag{3.46}$$

where eight constants $A_i$ ($i$ = 1 to 8) in equations (3.45) and (3.46) are obtained using boundary conditions which are presented in next section and $m_1$ to $m_8$ are the eight roots of $(-1)^{1/8}$. Using the boundary conditions, the mathematical models for forward velocity $V_z$, angular velocity $\Omega$, thrust force $F_z$, torque ($M_z$ and $L_z$; components of torque generated due to circumferential force acting on the flagellum element) and propulsive efficiency $\eta$ are developed in the next section.

### 3.4.2 Modeling Performance Indexes in Helical Wave Propelled UDN

For the UDN with the basal end of the tail attached at the axis of rotation and making an angle $\theta$ to the axis of rotation (Refer Figure 3.12 (a) and Figure 3.12 (b)), the boundary conditions considered are given as

$$x(z)\big|_{z=0}, y(z)\big|_{z=0} = 0 \tag{3.47a}$$

which means displacement positions *x* at $z = 0$ and *y* at $z = 0$ is zero.

$$\left.\frac{\partial x}{\partial z}\right|_{z=0} = \tan\theta, \left.\frac{\partial y}{\partial z}\right|_{z=0} = 0 \tag{3.47b}$$

which means slope at the base along *x* and *y* directions are tan $\theta$ and zero, respectively.

$$\left.\frac{\partial^2 x}{\partial z^2}\right|_{z=L} = 0, \left.\frac{\partial^2 y}{\partial z^2}\right|_{z=L} = 0 \tag{3.47c}$$

which means curvature at the distal end is zero.

$$\left.\frac{\partial^3 x}{\partial z^3}\right|_{z=L} = 0, \left.\frac{\partial^3 y}{\partial z^3}\right|_{z=L} = 0 \tag{3.47d}$$

which means shear force at the distal end is also zero.

The eight constants $A_i$ in equation (3.45) and equation (3.46), are calculated by substituting the above boundary conditions, i.e., equation (3.47), four for *x* direction and four for *y* direction, in equations (3.45) and (3.46). The eight constants $A_i$ ($i$ = 1 to 8) determine the shape of the wave in the flagellum.

Substituting the boundary condition from equations (3.47a) in equation (3.45) and (3.46) we get

$$\sum_{i=1}^{8} A_i = 0 \tag{3.48a}$$

$$\sum_{i=1}^{8} A_i (m_i)^4 = 0 \tag{3.48b}$$

Similarly substituting the second boundary condition from equations (3.47b) in equation (3.45) and (3.46) we get

$$\sum_{i=1}^{8} A_i \frac{m_i}{l} = \tan\theta \tag{3.48c}$$

$$\sum_{i=1}^{8} A_i \, m_i^5 = 0 \tag{3.48d}$$

Similarly substituting the third boundary condition from equations (3.47c) in equation (3.45) and (3.46) we get

$$\sum_{i=1}^{8} A_i \, m_i^2 e^{m_i \frac{L}{l}} = 0 \tag{3.48e}$$

$$\sum_{i=1}^{8} A_i \, m_i^6 e^{m_i \frac{L}{l}} = 0 \tag{3.48f}$$

Similarly substituting the fourth boundary condition from equations (3.48d) in equation (3.45) and (3.46) we get

$$\sum_{i=1}^{8} A_i \, m_i^3 e^{m_i \frac{L}{l}} = 0 \tag{3.48g}$$

$$\sum_{i=1}^{8} A_i \, m_i^7 e^{m_i \frac{L}{l}} = 0 \tag{3.48h}$$

The equations (3.48a) to (3.48h) are combined and rewritten in the form of a matrix as

$$[M][A] = [Z] \tag{3.49}$$

where

$$[M]=\begin{Bmatrix} 1 & 1 & 1 & 1 & 1 & 1 & 1 & 1 \\ m_1^4 & m_2^4 & m_3^4 & m_4^4 & m_5^4 & m_6^4 & m_7^4 & m_8^4 \\ m_1 & m_2 & m_3 & m_4 & m_5 & m_6 & m_7 & m_8 \\ m_1^5 & m_2^5 & m_3^5 & m_4^5 & m_5^5 & m_6^5 & m_7^5 & m_8^5 \\ m_1^2 e^{m_1\frac{L}{l}} & m_2^2 e^{m_2\frac{L}{l}} & m_3^2 e^{m_3\frac{L}{l}} & m_4^2 e^{m_4\frac{L}{l}} & m_5^2 e^{m_5\frac{L}{l}} & m_6^2 e^{m_6\frac{L}{l}} & m_7^2 e^{m_7\frac{L}{l}} & m_8^2 e^{m_8\frac{L}{l}} \\ m_1^6 e^{m_1\frac{L}{l}} & m_2^6 e^{m_2\frac{L}{l}} & m_3^6 e^{m_3\frac{L}{l}} & m_4^6 e^{m_4\frac{L}{l}} & m_5^6 e^{m_5\frac{L}{l}} & m_6^6 e^{m_6\frac{L}{l}} & m_7^6 e^{m_7\frac{L}{l}} & m_8^6 e^{m_8\frac{L}{l}} \\ m_1^3 e^{m_1\frac{L}{l}} & m_2^3 e^{m_2\frac{L}{l}} & m_3^3 e^{m_3\frac{L}{l}} & m_4^3 e^{m_4\frac{L}{l}} & m_5^3 e^{m_5\frac{L}{l}} & m_6^3 e^{m_6\frac{L}{l}} & m_7^3 e^{m_7\frac{L}{l}} & m_8^3 e^{m_8\frac{L}{l}} \\ m_1^7 e^{m_1\frac{L}{l}} & m_2^7 e^{m_2\frac{L}{l}} & m_3^7 e^{m_3\frac{L}{l}} & m_4^7 e^{m_4\frac{L}{l}} & m_5^7 e^{m_5\frac{L}{l}} & m_6^7 e^{m_6\frac{L}{l}} & m_7^7 e^{m_7\frac{L}{l}} & m_8^7 e^{m_8\frac{L}{l}} \end{Bmatrix}$$

$$[A]=\begin{bmatrix} A_1 \\ A_2 \\ A_3 \\ A_4 \\ A_5 \\ A_6 \\ A_7 \\ A_8 \end{bmatrix}, \text{ and } [Z]=\begin{bmatrix} 0 \\ 0 \\ \tan\theta \times l \\ 0 \\ 0 \\ 0 \\ 0 \\ 0 \end{bmatrix}$$

where, $L/l$ $(\text{i.e. } l_o)$ is the characteristic length and is same as given in equation (3.15).

Equation (3.49) is used to obtain coefficient matrix $[A]$ and is given as

$$[A]=[M]^{-1}[Z] \tag{3.50}$$

where $[M]^{-1}$ is the inverse of matrix $[M]$. By solving equation (3.49), we obtained eight constants (i.e. $A_1$ to $A_8$). A MATLAB code was written to calculate inverse of the matrix $[M]$. Using these eight constants, steady state shape of wave in flagellum is obtained. The steady state shapes obtained are general curves in space and are treated as helixes of variable amplitude and pitch. To evaluate instantaneous pitch angle, first we determine the projection of the helix on a plane. The projection of a vector (which is a small curved element of flagellum in our case) on a plane in 3D-space is found by the projection of the vector on the normal to plane and subtract this projection from the original vector [37]. From the obtained projections, the instantaneous amplitude and pitch angle of the curved flagellum element are obtained. Consider a general curve $d\vec{s}$ as a small element of helix in 3D-space, having instantaneous amplitude $\alpha(z)$ and pitch angle $\beta(z)$.

The position vector of a small element $d\vec{s}$ of the flagellum with respect to $z$-axis is considered as $\vec{r} = x\hat{i} + y\hat{j}$. The projection $(d\vec{s}_p)$ of a vector $d\vec{s}$ on a plane containing normal vector ($\hat{n}$) and is given by

$$d\vec{s}_p = d\vec{s} - (d\vec{s}.\hat{n})\hat{n} \tag{3.51}$$

where $d\vec{s} = dx\hat{i} + dy\hat{j} + dz\hat{k}$ is a curve in space and $\hat{n} = \dfrac{-x\hat{i} - y\hat{j}}{\sqrt{x^2 + y^2}}$ is the unit normal vector at a given $z$- location.

Substituting the $d\vec{s}$ and $\hat{n}$ in equation (3.51), we get

$$d\vec{s}_p = \left(dx\hat{i} + dy\hat{j} + dz\hat{k}\right) - \left[\left(dx\hat{i} + dy\hat{j} + dz\hat{k}\right).\left(\frac{-x\hat{i} - y\hat{j}}{\sqrt{x^2 + y^2}}\right)\right]\left(\frac{-x\hat{i} - y\hat{j}}{\sqrt{x^2 + y^2}}\right) \tag{3.52}$$

Solving equation (3.52), we get

$$d\vec{s}_p = \left(dx\hat{i} + dy\hat{j} + dz\hat{k}\right) - \left[\frac{(xdx + ydy)}{\sqrt{x^2 + y^2}}\right]\left(\frac{x\hat{i} + y\hat{j}}{\sqrt{x^2 + y^2}}\right) \tag{3.53}$$

Simplifying and rearranging *x*, *y* and *z* components in equation (3.53), we get

$$d\vec{s}_p = \left(\frac{y^2dx - xydy}{|\vec{r}|^2}\right)\hat{i} + \left(\frac{x^2dy - xydx}{|\vec{r}|^2}\right)\hat{j} + dz\hat{k} \tag{3.54}$$

where $|\vec{r}| = \sqrt{x^2 + y^2}$ is the amplitude of the vector $\vec{r}$.

The vector projection $d\vec{s}_p$ is approximately a straight line in the projected plane therefore the instantaneous pitch angle of the flagellum element is written as

$$\tan\beta(z) = \frac{\left|\left(\dfrac{y^2dx - xydy}{|\vec{r}|^2}\right)\hat{i} + \left(\dfrac{x^2dy - xydx}{|\vec{r}|^2}\right)\hat{j}\right|}{\left|dz\hat{k}\right|} \tag{3.55}$$

Simplyfing equation (3.55), we obtain

$$\tan\beta(z) = \frac{\sqrt{\dfrac{\left(y^2dx - xydy\right)^2 + \left(x^2dy - xydx\right)^2}{|\vec{r}|^4}}}{\left|dz\hat{k}\right|} \tag{3.56}$$

Further simplifying equation (3.56), we get

$$\tan\beta(z)=\frac{\sqrt{\frac{\left(y^2dx\right)^2+(xydy)^2-2\left(y^2dx\right)(xydy)+\left(x^2dy\right)^2+(xydx)^2-2\left(x^2dy\right)(xydx)}{|\vec{r}|^4}}}{\left|dz\hat{k}\right|} \quad (3.57)$$

Separating $dx^2$, $dy^2$ and $dxdy$ terms in equation (3.57) and rearranging the terms

$$\tan\beta(z)=\frac{\sqrt{\frac{y^2\left(x^2+y^2\right)dx^2+x^2\left(x^2+y^2\right)dy^2-2\left(x^2+y^2\right)(xy)(dxdy)}{|\vec{r}|^4}}}{\left|dz\hat{k}\right|} \quad (3.58)$$

Taking $\left(x^2+y^2\right)$ common and using $|\vec{r}|=\sqrt{x^2+y^2}$ in equation (3.58), we get

$$\tan\beta(z)=\frac{\sqrt{\left(x^2+y^2\right)}\frac{\sqrt{y^2dx^2+x^2dy^2-2(xy)(dxdy)}}{|\vec{r}|^2}}{\left|dz\hat{k}\right|} \quad (3.59)$$

Simplifying equation (3.59), gives

$$\tan\beta(z)=\frac{\frac{1}{|\vec{r}|^2}\sqrt{x^2+y^2}\left(ydx-xdy\right)}{dz} \quad (3.60)$$

From equation (3.60), the pitch angle $\beta(z)$ in terms of vector amplitude $\vec{r}$ and slopes along *x* and *y* direction is defined as

$$\tan\beta(z)=\frac{1}{\vec{r}}\left(y\left(\frac{dx}{dz}\right)-x\left(\frac{dy}{dz}\right)\right) \quad (3.61)$$

The amplitude $\alpha(z)$ of the flagellum element is given by

$$\alpha(z)=|\vec{r}|=\sqrt{x^2+y^2} \quad (3.62)$$

For an element of the flagellum $d\vec{s}$ at a distance of *z* from the base, the pitch angle $\beta(z)$ and the amplitude $\alpha(z)$ are evaluated using equations (3.61) and (3.62). The obtained instantaneous amplitude and pitch angle of the curved flagellum element are used to derive the propulsive dynamics of any arbitrary shape in space, applying equations (3.67) and (3.68).

Referring to Figure 3.12, Figure 3.13(a) is drawn to elaborately show the various forces and their directions along with velocity components acting on the element *ds*. Figure 3.13(b) shows magnified view of element *ds* with various forces.

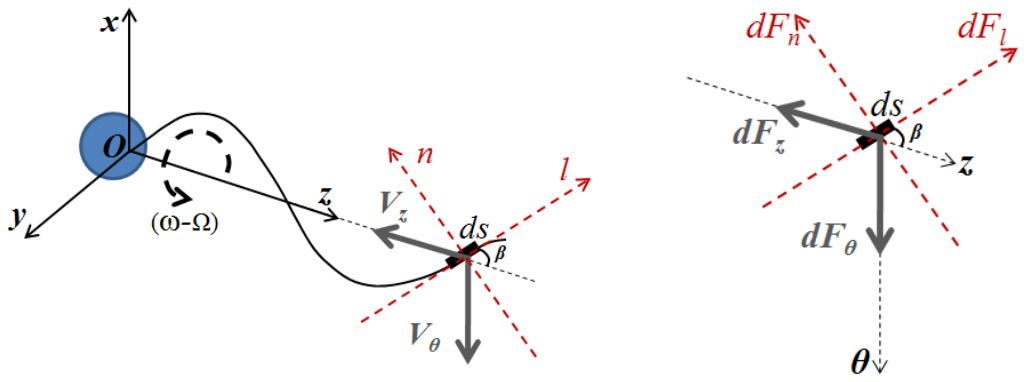


(a) (b)

**Figure 3.13: (a) Flagellum element *ds* , centerline making an angle ( $\beta$ ) with z-axis (b) Forces acting on a flagellum element *ds***

The forces acting in normal (*n*) and longitudinal (*l*) directions are proportional to the velocity of the element in the corresponding directions and the viscosity of the medium. Accordingly, if the normal and longitudinal component of velocity of flagellum element *ds* are $V_n$ and $V_l$ respectively, the normal $(dF_n)$ and longitudinal $(dF_l)$ viscous forces acting on element *ds* are:

$$dF_n = -C_n V_n ds \tag{3.63}$$

$$dF_l = -C_l V_l ds \tag{3.64}$$

where $C_n$, and $C_l$, are the resistive coefficients.

The velocity components of the element *ds* in *n* and *l* direction are obtained by taking components of $z$ and $\theta$ velocity components (i.e. $V_z$ and $V_\theta$) along normal and longitudinal directions and are given as

$$V_n = (V_z \sin\beta - V_\theta \cos\beta) \tag{3.65}$$

$$V_l = (V_z \cos\beta + V_\theta \sin\beta) \tag{3.66}$$

where, $V_z$ and $V_\theta$ are the swimming velocity in the negative $z$ and $\theta$ directions, respectively, $V_z \sin\beta$ and $V_\theta \cos\beta$ are velocity components in *n*-direction and $V_z \cos\beta$ and $V_\theta \sin\beta$ are velocity components in *l*-direction [refer Figure 3.13 (a)] and the

flagellum rotates counter-clockwise when viewed from positive $z$ axis. Substituting the normal velocity $V_n$ and longitudinal velocity $V_l$ from equations (3.65) and (3.66) respectively, in equations (3.63) and (3.64), the forces acting on element *ds* in normal (*n*) and longitudinal (*l*) directions with respect to flagellum centerline are given as

$$dF_n = C_n(V_z \sin\beta - V_\theta \cos\beta)ds \tag{3.67}$$

$$dF_l = C_l(V_z \cos\beta + V_\theta \sin\beta)ds \tag{3.68}$$

The rotation gives rise to a circumferential velocity of flagellum element $V_\theta = |\vec{r}|(\omega - \Omega)$, wherein $\Omega$ is the angular velocity of the head with respect to the ground reference frame xyz. $C_n$ is normal drag coefficient and $C_l$ is tangential drag coefficient and are given as in equation (3.18) and equation (3.19). The two drag coefficients are re-written for sake of ready reference and continuity.

$$C_n = \frac{4\pi\mu}{\ln\left(\frac{L}{b}\right) + 0.5}(\varepsilon) \tag{3.69}$$

$$C_l = \frac{2\pi\mu}{\ln\left(\frac{L}{b}\right) - 0.5}(\varepsilon) \tag{3.70}$$

where, $\mu$ is the viscosity of the surrounding medium, $L$ is the total length of the flagellum, and *b* is its radius of cross section. $\varepsilon$ is the modification factor suggested by Johnson and Brockaw [16] for HWP whose value is 1.35.

The propulsive forces on the flagellum element *ds* in the negative $z$ direction $(dF_z)$ and positive $\theta$ direction $(dF_\theta)$ [refer Figure 3.13 (b)] are determined by resolving components of normal $(dF_n)$ and longitudinal forces $(dF_l)$ along $z$ and $\theta$-directions, respectively. The component of $dF_n$ in z-direction is $dF_n \sin\beta$ and in $\theta$-direction is $dF_n \cos\beta$. Similarly the component of $dF_l$ in z-direction is $dF_l \cos\beta$ and in $\theta$-direction is $dF_l \sin\beta$. The vectorially summing these force components in $z$ and $\theta$-directions, we get

$$dF_z = -(dF_n \sin\beta + dF_l \cos\beta) \tag{3.71}$$

$$dF_\theta = (dF_l \sin\beta - dF_n \cos\beta) \tag{3.72}$$

Substituting normal and longitudianl force components from equations (3.67) and (3.68), in equation (3.71), the net thrust force $(dF_z)$ on the flagellum element is obtained

$$dF_z = -\{C_n(V_z \sin\beta - V_\theta \cos\beta)\sin\beta + C_l(V_\theta \sin\beta + V_z \cos\beta)\cos\beta\}ds \quad (3.73)$$

Similarly substituting normal and longitudianl force components from equations (3.67) and (3.68), in equation (3.72), the net circumferential force $(dF_\theta)$ on the flagellum element is obtained

$$dF_\theta = \{C_l(V_z \cos\beta + V_\theta \sin\beta)\sin\beta - C_n(V_z \sin\beta - V_\theta \cos\beta)\cos\beta\}ds \quad (3.74)$$

Further, the length of element $ds$ is given by

$$ds = \sqrt{1+\cos^2(dy/dx)^2}.dz/\cos\beta \quad (3.75)$$

For small amplitude gradients $\frac{dy}{dx}$, can be neglected and equation (3.75) is reduced to

$$ds = \sec\beta \; dz \quad (3.76)$$

Substituting $ds = \sec\beta \; dz$ (small amplitude assumption) from equation (3.76) in equations (3.73), the net thrust force $dF_z$ is given by

$$dF_z = -\{C_n(V_z \sin\beta - V_\theta \cos\beta)\tan\beta + C_l(V_\theta \sin\beta + V_z \cos\beta)\}dz \quad (3.77)$$

Similarly, substituting $ds = \sec\beta \; dz$ from equation (3.76) in equations (3.74), the net circumferential force $dF_\theta$ is given by

$$dF_\theta = \{C_l(V_z \cos\beta + V_\theta \sin\beta)\tan\beta - C_n(V_z \sin\beta - V_\theta \cos\beta)\}dz \quad (3.78)$$

The net circumferential force on the flagellum element causing torque about the axis of rotation has two components $(\text{i.e. } dM_z \text{ and } dL_z)$. The first of these arise due to rotation of the element about the axis of rotation i.e. $z$ axis $(dM_z)$ and is given as

$$dM_z = \vec{r} \times dF_\theta \quad (3.79)$$

Substituting circumferential force from equations (3.78) in equation (3.79), we obtain

$$dM_z = r\{C_l(V_z \cos\beta + V_\theta \sin\beta)\tan\beta - C_n(V_z \sin\beta - V_\theta \cos\beta)\}dz \quad (3.80)$$

The second torque component $(dL_z)$ is a result of rotation of the element about its own centerline and is given by [30]

$$dL_z = 4\pi\mu\ b^2(\omega - \Omega)\cos\beta dz \tag{3.81}$$

The drag force on a spherical head of radius $r_h$ moving in a medium with viscosity $\mu$ is given as [31]

$$F_{head} = 6\pi\mu\ r_h V_z \tag{3.82}$$

Also the torque experienced by a spherical head of radius $r_h$ rotating in a medium with viscosity $\mu$ is given as [31]

$$M_{head} = 8\pi\mu\ r_h^3\Omega \tag{3.83}$$

The head spin about its center at an angular velocity $\Omega$ in a direction opposite to that of the flagellum. This causes the flagellum to rotate at $(\omega - \Omega)$ with respect to the ground reference frame.

Under steady swimming conditions the velocity $V_z$ in $z$ - direction is constant. The total thrust force developed by the flagellum is equal to the drag experienced by the head. The total thrust force is obtained by integrating $(dF_z)$ over total length of flagellum from 0 to $L$. Equating that with drag force $F_{head}$ , we get

$$\int_0^L dF_z = F_{head} \tag{3.84}$$

Similarly, under steady swimming conditions, the net torque generated by the flagellum is equal in magnitude to the torque experienced by the head. The net torque is obtained by integrating $(dM_z + dL_z)$over total length of flagellum from 0 to $L$ and is equated to the torque experienced by head as

$$\int_0^L (dM_z + dL_z) = M_{head} \tag{3.85}$$

Substituting the $(dF_z)$ from equation (3.77) and $F_{head}$ from equation (3.82) in equation (3.84) and rearranging we get

$$-\int_0^L \{C_n(V_z\sin\beta - V_\theta\cos\beta)\tan\beta + C_l(V_\theta\sin\beta + V_z\cos\beta)\}dz - 6\pi\ \mu\ r_h V_z = 0 \tag{3.86}$$

Substituting circumferential velocity of flagellum element $V_\theta = |\vec{r}|(\omega - \Omega)$ in equation (3.86) and rearranging the $V_z$, $\omega$ and $\Omega$ terms separately

$$\begin{aligned} &-\int_0^L \{V_z(C_n \sin\beta + C_l \cos\beta)dz + 6\pi\ \mu\ r_h\} - \int_0^L \{(\Omega)(C_n - C_l)r\sin\beta\}\,dz \\ &+\int_0^L \{(\omega)(C_n - C_l)r\sin\beta\}\,dz = 0 \end{aligned} \tag{3.87}$$

Substituting the $(dL_z)$ and $(dM_z)$ from equations (3.80) and (3.81), respectively and $M_{head}$ from equation (3.83), in equation (3.85), we get

$$\begin{aligned} &\int_0^L r\{C_l(V_\theta \sin\beta + V_z \cos\beta)\tan\beta + C_n(V_\theta \cos\beta - V_z \sin\beta)\}dz \\ &+\int_0^L 4\pi\mu\ b^2(\omega - \Omega)\cos\beta dz = 8\pi\mu\ r_h^3\Omega \end{aligned} \tag{3.88}$$

With substitution of circumferential velocity of flagellum element $V_\theta = |\vec{r}|(\omega - \Omega)$ in equation (3.88) and separating $V_z$ , $\omega$ and $\Omega$ terms, we get

$$\begin{aligned} &\int_0^L V_z(C_l - C_n)r\sin\beta \\ &+\omega\left\{\int_0^L \left(C_l r^2 \sin\beta\tan\beta + C_n r^2\cos\beta + 4\pi\mu\ b^2\cos\beta\right)dz\right\} \\ &-\Omega\left\{\int_0^L \left(4\pi\mu\ b^2\cos\beta + C_l r^2\sin\beta\tan\beta + C_n r^2\cos\beta\right)dz + 8\pi\mu\ r_h^3\right\} = 0 \end{aligned} \tag{3.89}$$

Integrating equations (3.87) and (3.89) along the length of the flagellum and simplifying the resulting simultaneous equations, we get

$$V_z\{C_l I_4 + C_n I_5 + 6\pi\mu\, r_h\} + \Omega\ \{C_n - C_l\}I_1 = \omega\{C_n - C_l\}I_1 \tag{3.90}$$

$$\begin{aligned} &V_z\{C_l - C_n\}I_1 - \Omega\ \left\{4\pi\mu\, b^2 I_4 + C_l I_2 + C_n I_3 + 8\pi\mu\, r_h^3\right\} \\ &= -\omega\left\{C_l I_2 + C_n I_3 + 4\pi\mu\, b^2 I_4\right\} \end{aligned} \tag{3.91}$$

where the integrals $I_1$ to $I_5$ in equations (3.90) and (3.91) are defined as

$$I_1 = \int_0^L r\sin\beta\ dz, \qquad I_2 = \int_0^L r^2\sin\beta\tan\beta\ dz,$$

$$I_3 = \int_0^L r^2\cos\beta\ dz, \qquad I_4 = \int_0^L \cos\beta\ dz,$$

$$I_5 = \int_0^L \sin\beta \tan\beta \, dz$$

The equations (3.90) and (3.91) are rewritten in form of matrix as

$$\begin{Bmatrix} V_z \\ \Omega \end{Bmatrix} = [P]^{-1} \times [Q]\{\omega\} \tag{3.92}$$

where $[P] = \begin{bmatrix} (C_l I_4 + C_n I_5 + 6\pi\mu\, a) & (C_n - C_l) I_1 \\ -(C_n - C_l) I_1 & -\left(4\pi\mu\, b^2 I_4 + C_l I_2 + C_n I_3 + 8\pi\mu\, a^3\right) \end{bmatrix}$

and $[Q] = \begin{bmatrix} (C_n - C_l) I_1 \\ -\left(C_l I_2 + C_n I_3 + 4\pi\mu\, b^2 I_4\right) \end{bmatrix}$

Equation (3.92) is the mathematical model for performance index forward velocity $V_z$ and angular velocity $\Omega$ for helical wave propelled UDN. For obtaining steady state shape of the flagellum, the initial shape is predicted assuming head velocity $\Omega$ zero. Since the steady state shape is a function of, $\Omega$, the updated value is substituted back into the shape calculation model i.e. equations (3.45) and (3.46), iteratively to give a modified shape and consequently modified values of propulsion parameters. The iterations are carried out till a constant value of $\Omega$ and thus the steady shape is obtained. The values of $V_z$ and $\Omega$, obtained by solving equation (3.92), are used to calculate the efficiency of the nanoswimmer.

The efficiency ($\eta$) of the nanoswimmer is calculated as the ratio of useful power developed for forward motion along $z$ axis to total power needed for spinning the flagellum and head. Useful power developed is obtained by integrating the product of force $(dF_z)$ and velocity $V_z$ over flagellum length from 0 to $L$. Similarly the total power required to spin the flagellum and head is the sum of power required to overcome the rotational resistance of flagellum and head.

$$\eta = \frac{F_z V_z}{M_{flagellum}(\omega - \Omega) + M_{head}\,\Omega} \tag{3.93}$$

Equations (3.90), (3.91) and (3.93) are simulated in next section to investigate the performance of a nanoswimmer propelled by helical waves. The results obtained after simulations are analyzed and discussed in the following section.

### 3.4.3 Simulation, Results and Discussion of Performance of Helical Wave Propelled UDN

The simulations of the mathematical model developed for displacement shapes in equation (3.45) and (3.46), and thrust force $(F_z)$, forward velocity $(V_z)$ and efficiency $(\eta)$ in equations (3.77), (3.92) and (3.93) in previous section are carried out using MATLAB®. The MATLAB program is given in Appendix-III. The values of parameters for simulation are chosen as actual values in eukaryotic microorganism [34] and spermatozoa [3], both the eukaryotic microorganism [34] and spermatozoa performs helical wave based propulsion and therefore are appropriate choice for validation of model developed in previous section. For eukaryotic microorganism and spermatozoa, the stiffness of flagellum has been estimated to be in the range of $10^{-24}$ $Nm^2$ [32] to $10^{-18}$ $Nm^2$ [33]. Rigidity in the range mentioned for flagellum warrants a study of the deflection of filaments that are subjected to loading due to viscous drag. For microorganism with spherical heads, the effective head diameter varies from 0.5 $\mu$m to 6 $\mu$m. The parametric values considered for simulations are summarized in Table 3.2.

**Table 3.2: Parametric values for simulation (HWP)**

| S.No. | Parameter | Value (Eukaryotic microorganism) [34] |
|---|---|---|
| 1 | Filament stiffness (*EI*) | $10^{-22}$ $Nm^2$ |
| 2 | Surrounding medium (water) viscosity $(\mu)$ | 0.001 Pa.s |
| 3 | Length of filament (*L*) | 10 $\mu$m |
| 4 | Cross section radius of filament (*b*) | 0.2 $\mu$m |
| 5 | Radius of head ( $r_h$ ) | 0.5 $\mu$m |

The range is so chosen to include the values of parameters corresponding to *Eukaryotic* microorganisms because *Eukaryotic* microorganisms propels themselves through HWP. A flagellum of length $L$ = 10 $\mu$m and a circular cross section with radius 0.2 $\mu$m is considered. The fluid through which the nanoswimmer is swimming is assumed to be water with viscosity 1 *mPa-s*. From observed values of rotational frequency in nature [3, 34] for helical wave propelled nanoswimmers, the range considered here for simulations varies from 100 Hz to 500 Hz. The angle at the base of the flagellum is

varied from 10 deg to 70 deg in steps of 5 deg. The steady state shape is predicted based on the input parameters which in turn estimate performance parameters. The model developed here has been validated by deriving performance parameters for planar waves and comparing with those given in available literature [29].

Using boundary conditions given in equations (3.47), equation (3.45) and (3.46) representing the mathematical model for displacement, shapes are obtained whose projection on *xy*, *xz*, and *yz* planes are shown in Figure 3.14 through to Figure 3.16, respectively for four different characteristic length $l_o = L/l$ values i.e. ($l_o$) as 1.5, 2, 5, 10.

As seen in Figure 3.14, the shapes obtained are left handed helixes with the helical axis along positive $z$-direction. The shapes are obtained from simulating a filament driven counter clockwise when viewed from the positive *z*-direction. For a counterclockwise driven left handed helix, the thrust force is along negative *z*-direction. Reversing the direction of rotation changes the handedness of the helix and hence the direction of thrust force remains unaltered.

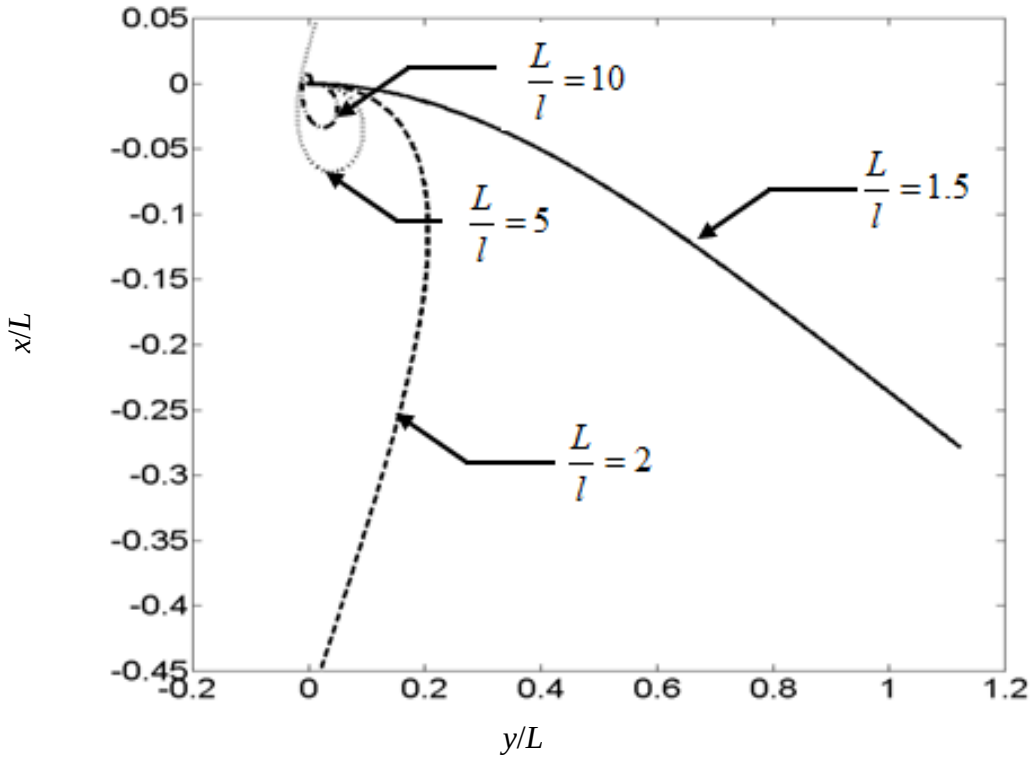


**Figure 3.14: Steady state shapes of the filament projected on *xy* plane for different values of characteristic length (*L*/*l*) for a rotation frequency 100 Hz and $\theta$ = 45 deg: (a) *L*/*l*=1.5 (solid), (b) *L*/*l*=2 (dotted), (c) *L*/*l*=5 (dashed) and (d) *L*/*l*=10 (dot dashed)**

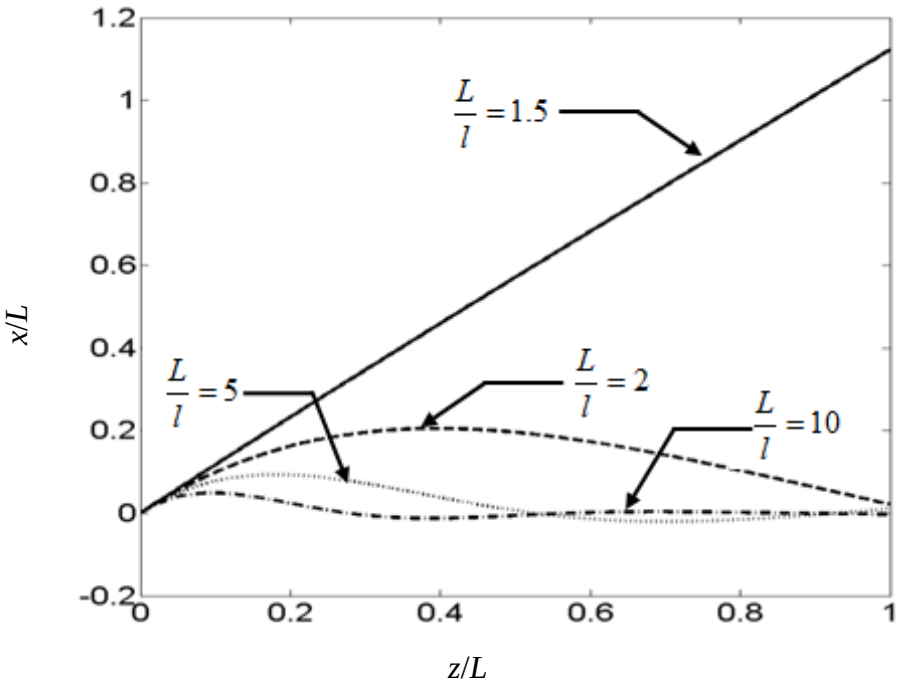


**Figure 3.15: Steady state shapes of the filament projected on *xz* plane for different values of characteristic length (*L*/*l*) for a rotation frequency 100 Hz and $\theta$ = 45 deg: (a) *L*/*l*=1.5(solid), (b) *L*/*l*=2 (dotted), (c) *L*/*l*=5 (dashed), and (d) *L*/*l*=10 (dot dashed)**

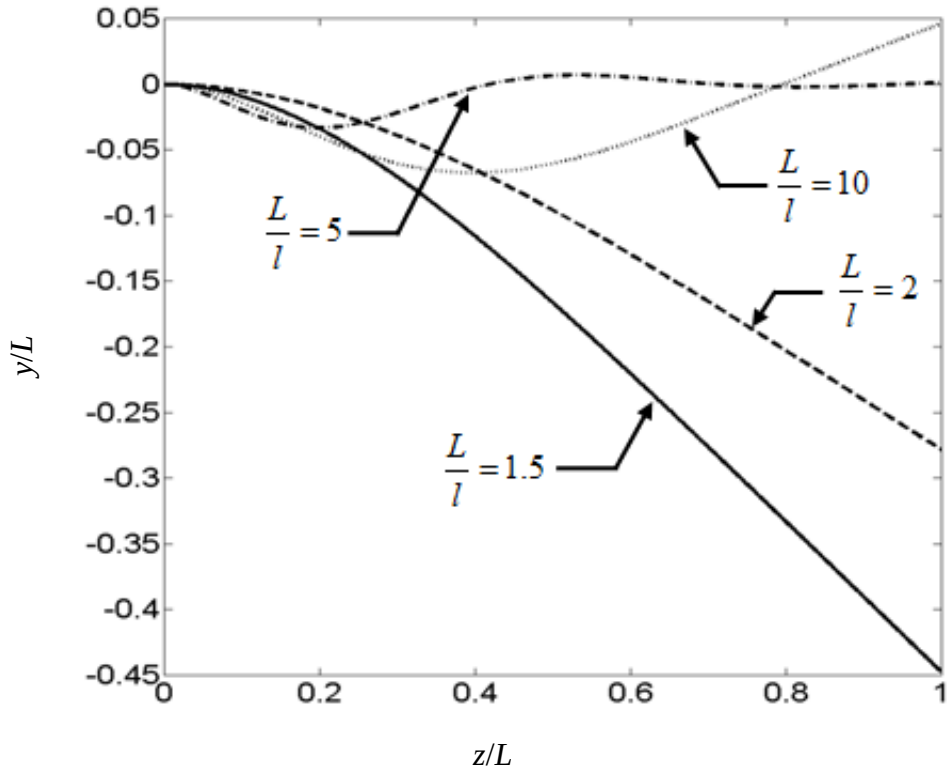


**Figure 3.16: Steady state shapes of the filament projected on *yz* plane for different values of characteristic length (*L*/*l*) for a rotation frequency 100 Hz and $\theta$ = 45 deg: (a) *L*/*l*=1.5(solid), (b) *L*/*l*=2 (dotted), (c) *L*/*l*=5 (dashed), and (d) *L*/*l*=10 (dot dashed)**

The steady state shapes plotted in Figure 3.14 through to Figure 3.16 show similarity to those obtained by Powers [30] for flagellar bundling. The results shown in Figure 3.14 to 3.16 are for rotation frequency ( $\omega = 100$ Hz ) and pitch angle ( $\theta = 45$ deg).

Figure 3.15 shows the projections of steady state shapes of flagellum on *xz* plane for four different characteristic lengths. The *x*-axis corresponds to the rotating amplitude given in dimensionless form i.e. (*x*/*L*). The *y*-axis gives the projection of flagellum on *yz* plane divided by flagellum length i.e. (*z*/*L*). As the values of characteristic length (*L*/*l*) increases from 1.5 to 10, the flagellum becomes more and more flexible. It is observed from Figure 3.15, for values of characteristic length *L*/*l* = 10, the maximum amplitude in *x*-direction is observed to occur at a distance less than 10% of the total length. Thus if *L*/*l* $\rangle\rangle$1 the flagellum behaves very sloppy and bending occurs near proximal end. Figure 3.16 shows the projections of steady state shapes of flagellum on *yz* plane for four different characteristic lengths at same values of rotational frequency and pitch angle i.e. 100 Hz and 45 deg, respectively.

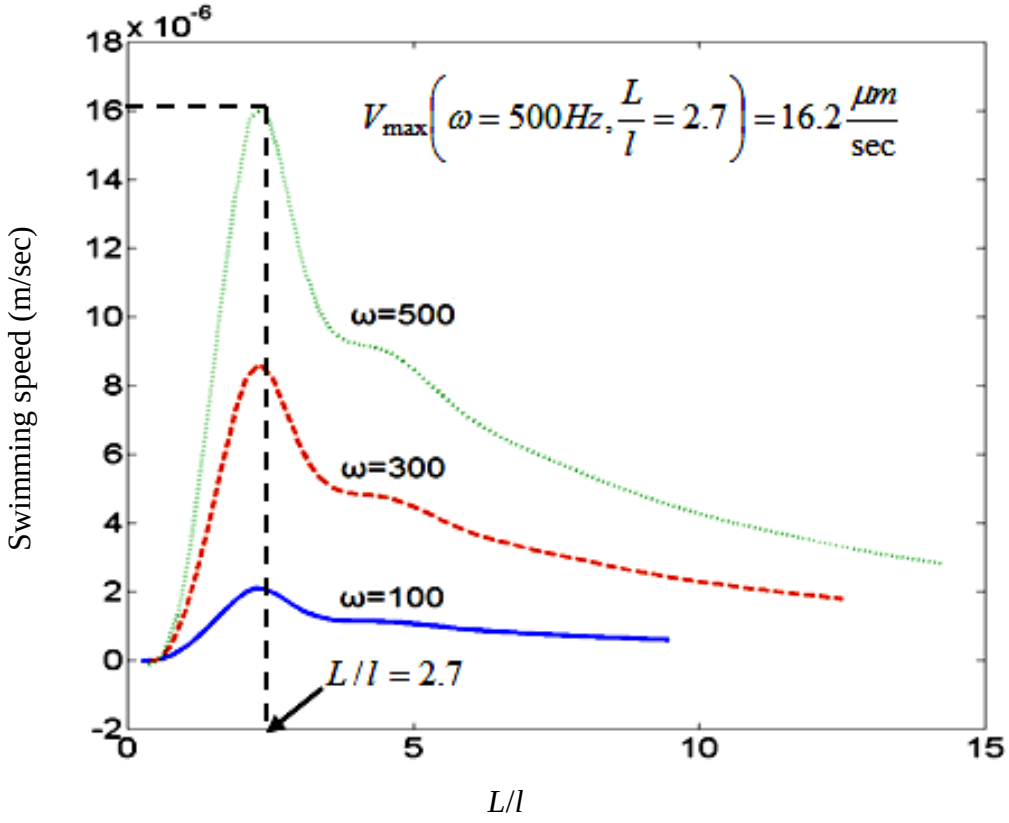


**Figure 3.17: Variation of swimming speed with characteristic length (*L*/*l*) for different driving frequencies**

The simulated results for swimming velocity ($V_z$) for variations in $L/l$ are plotted in Figure 3.17 for three frequency values i.e. 100 Hz, 300 Hz and 500 Hz. The $x$-axis corresponds to the characteristic length i.e. $L/l$. The $y$-axis gives the swimming speed ($V_z$) of flagellated nanoswimmer. As seen in Figure 3.17, the swimming speed is maximum for $L/l$ =2.7. For $L/l$ near 2.7, the amplitudes peak at the distal end. This can be inferred by comparing plots in Figure 3.15, hence allowing the entire length of the flagellum to contribute to the thrust force. At values of $L/l \rangle 2.7$ the maximum amplitude occurs near the proximal end i.e. $z = 0$ and in the remaining portion of the flagellum amplitudes quickly dies out, thus causing most of the part of the flagellum to contribute mainly to the drag without adding much thrust. The thrust force has a linear relation with the swimming speed (refer equation 3.59). For helical waves, the thrust force peak was obtained at $L = 2.7l$, whereas for planar waves, the maxima of thrust force was obtained at $L \approx 2l$ (refer section 3.3.3, Figure 3.10) which corroborates with results available in literature [29]. The simulation results of varying head radius were carried out and the effect of head radius on swimming speed is illustrated in Figure 3.18. The $x$-axis corresponds to the head radius given in dimensionless form i.e. $r_h/L$. The $y$-axis gives the swimming speed of nanoswimmer.

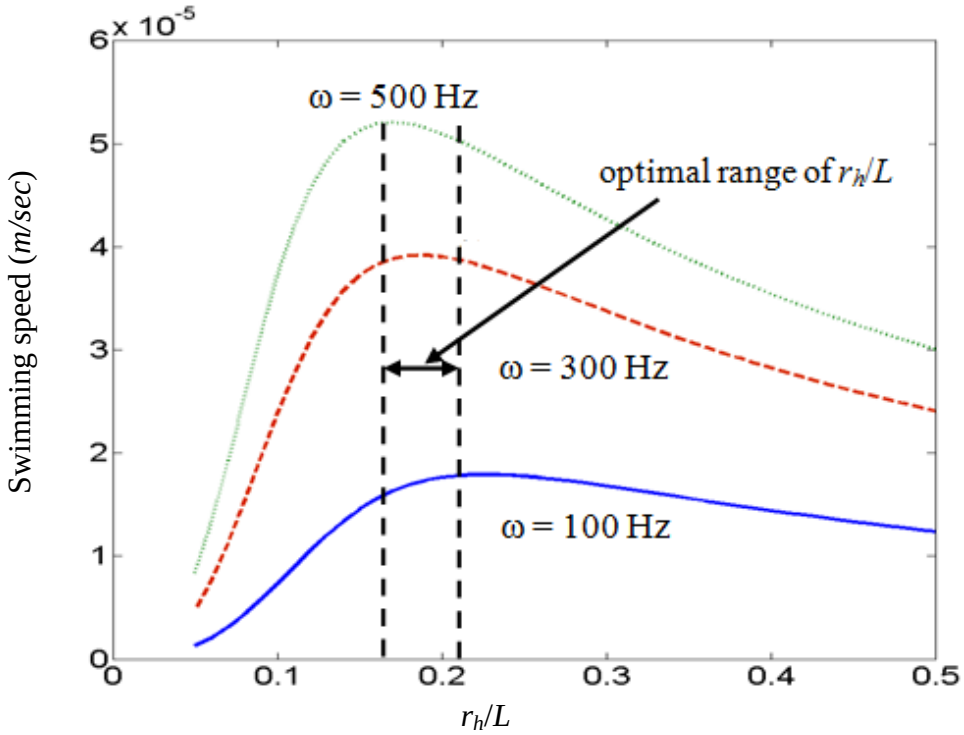


**Figure 3.18: Plot showing swimming speed variation with respect to $r_h/L$ for different driving frequencies**

As shown in Figure 3.18, for zero radius of the head, no waves propagate along the tail, thus causing zero swimming velocity which is also concluded by Behkam and Sitti [7]. In the range of simulation for $r_h/L$ varying from 0 to 0.5, swimming speed increases nonlinearly and reaches a maximum and then starts decreasing. The trend of swimming speed over head radius remains similar for three different frequency values considered i.e. 100 Hz, 300 Hz and 500 Hz. For values of head radius $(r_h)$ above optimal value, the translational drag increases linearly with $r_h$; therefore, helical wave propulsion becomes less efficient with low speeds i.e. 100 Hz for larger head sizes. The maximum swimming speed obtained is 52 $\mu$m/sec at higher rotational frequency i.e. 500 Hz as compared with 488 $\mu$m/sec for planar waves. This is mainly due to the fact that fraction of the power developed by the actuator in generating helical waves is consumed in rotating the head against viscous drag.

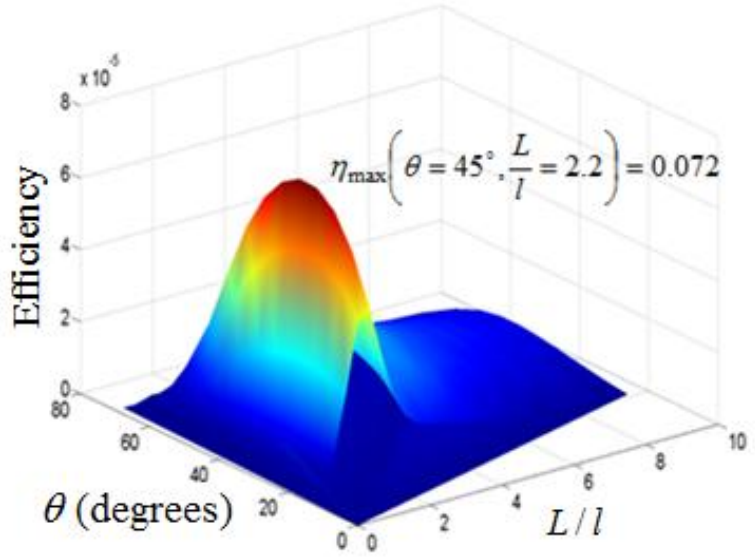


**Figure 3.19: Plot of efficiency with respect to *L*/*l* and $\theta$ at 100 Hz showing optimal band of both values**

In Figure 3.19, simulation results for efficiency $(\eta)$ are plotted with respect to characteristic length *L*/*l* of the flagellum and angle $(\theta)$ at the basal end of the flagellum as parameter from 0 to 70 deg. In the 3-dimension plot in Figure 3.19, it is seen that a region of high efficiency exists for $45\text{deg} < \theta < 55\text{deg}$. The maximum efficiency is found to occur at $\theta = 45$ deg, $L/l = 2.2$ and has value of 0.0072%. This efficiency peak also corresponds to peak in thrust force. This may be attributed to the large amplitudes developed near the proximal end of the tail at values of $\theta > 45$ deg, which offsets the

effects of decreasing amplitude along the length. Larger amplitude waves propagating along the tail have two counteracting effects on the net thrust developed: (1) initial increase in $\theta$ causes an increase in amplitude therefore leading to higher translational velocities for a given value of $\omega$ and a corresponding increase in thrust force (refer Figure 3.20); (2) moving beyond the optimal range, however, the increased moment acting on the head dominates, which increases head's angular velocity. The increase in angular velocity of head reduces the net absolute angular velocity of the flagellum and consequently the thrust force generated.

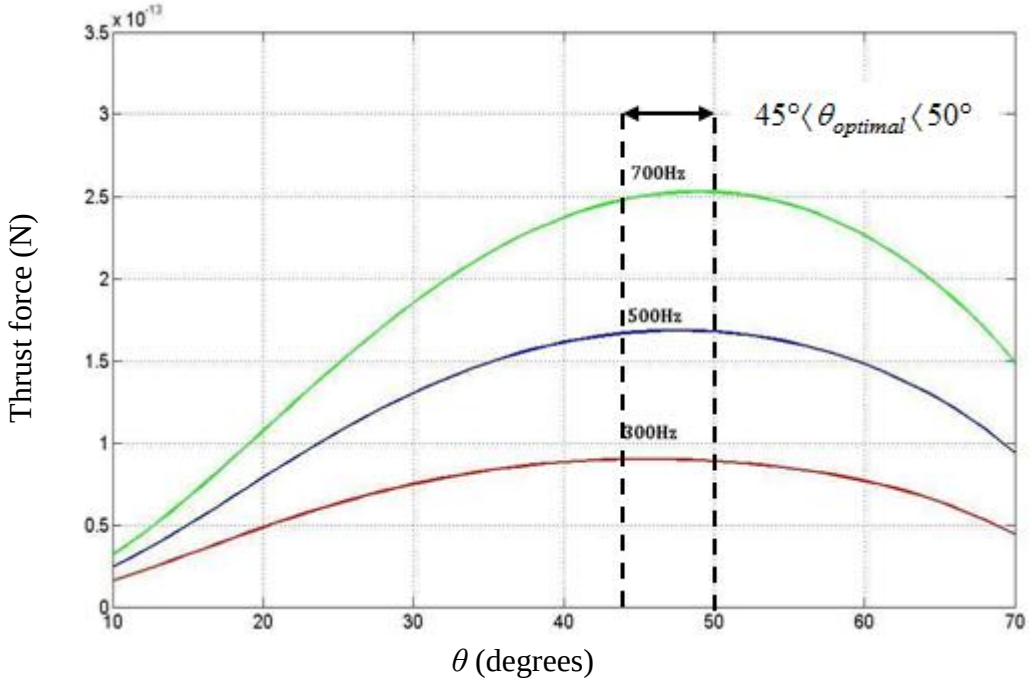


**Figure 3.20: Variation of thrust force with $\theta$ for different values of driving frequency**

In Figure 3.20, the effect of rotation frequency on the optimal basal angle can be observed. As the frequency of rotation increases so do the optimal angles ranging from $\theta = 45$ deg at 300 Hz to almost 50 deg at 700 Hz. This is explained by the viscous forces becoming more dominant as $\omega$ increases therefore requiring an increase in the basal angle $\theta$ to maintain the amplitude and thrust force.

In the present section, the mathematical model for the forces, velocity, and efficiency, was developed considering a case of the helical wave propelled UDN. The rotation of the helical flagella about the longitudinal axis, results in a net forward thrust, in viscous

domains, which propels the nanoswimmer forward. We compare propulsion of an UDN using a PWP and HWP modes in the next section.

In the quest to see the effect of flagella elasticity on swimming velocity and efficiency of motion of nanoswimmer, a dimensionless term, characteristic length $\left(\text{i.e. } l_o\right)$ is defined (refer equation 3.15). Characteristic length is a basic parameter to evaluate the performance of a nanoswimmer that accounts for the modulus of elasticity of flagellum material, area moment of inertia of flagellum cross-section, viscosity of the fluid medium and actuation frequency of flagellum. In practical situations, the value of $l_o$ is constrained by the modulus of elasticity of available bio-compatible materials; the width of the targeted area; the viscosity of the fluid medium, and the frequency of actuation. For smaller values of characteristics length $\left(l_o \approx 1\right)$ the flagellum behaves like a rigid rod while for higher values of characteristic length $\left(l_o \approx 10\right)$ the flagellum behaves very sloppy. Both these situations results in no net forward motion. The characteristics length for maximum velocity has been found out to be 1.7 for PWP (refer Figure 3.9) whereas it is 2.7 for HWP (refer Figure 3.17). The characteristics length for maximum efficiency has been found out to be 2 for PWP (refer Figure 3.11) whereas 2.2 for HWP (refer Figure 3.19).

## 3.5 CONCLUSIONS

Resistive force theory has been used from very early days till today and offers a very simple way of computing forces and the velocity. In the present chapter, we used RFT to develop a mathematical model for planar and helical wave propulsions. Propulsion characteristics of passive elastic flagellum propagating helical waves have been studied and the same compared to the case of propulsion using elastic flagellum propagating planar waves. An *ab-initio* approach is used where the steady state shape of the flagellum is predicted based on elastohydrodynamic equations using an iterative algorithm. A generalized propulsion model was developed to predict the propulsion characteristics of any shape. The model developed to study propulsion characteristics are given in equation (3.31) and equation (3.32) for PWP and in equation (3.84) and equation (3.85) for HWP is used to estimate swimming speed, thrust force, and efficiency of the nanoswimmer. From the analysis of simulated results it is seen that a planar wave propelled UDN performs better in the range of characteristic length $1.7l \le L \le 2l$

whereas a helical wave propelled UDN performs better in the range of $2.2l \leq L \leq 2.7l$. Swimmers with longer flagellum lead to an increase in the drag force and hence have a detrimental effect on the swimming speed and efficiency. Based on the efficiency and velocity parameters, a range of optimal values for head radius, flagellum radius, beating/rotating frequency, basal angle have been reported, which provide a starting point for designing a nanoswimmer. Studies simulated result on the radius of the head prove that helical waves cannot propagate as head size tends to zero. The propulsion via helical waves is better than the propulsion via planar waves, because, in the planar wave propulsion, elements of the flagellum undergo opposite strains often and energy has to be generated locally for sustaining the same amplitude throughout the length of the flagellum, whereas the reversible straining is less in case of helical flagellar propulsion mechanism. From the fabrication point of view also, mechanisms used to generate rotary motions are simpler as compared to that required for planar motions. The geometry, dimension and other parameteric values have been taken from [7-8, 28-29] to validate the results, and the discrepancy obtained is 5.32% in speed and 6.25% in the efficiency of a nanoswimmer propelling through HWP. This may be because the flagellum considered here is of uniform diameter unlike tapered as found in nature.

In the next Chapter, mathematical modeling and simulation results of a tapered flagellated nanoswimmer are explored.

## References


1. Purcell EM (1977) Life at low Reynolds Number, Am J Phys, 45(1), pp. 3-11.
2. Taylor G (1951) Analysis of the Swimming of Microscopic Organisms, Proc R Soc, Mathematical and Physical Sciences, 209, pp. 447-461.
3. Gray J, and Hancock GJ (1955) The Propulsion of Sea-Urchin Spermatozoa, J Exp Biol, 32, pp. 802-814.
4. Hancock G (1953) The Self-Propulsion of Microscopic Organisms through Liquids, Proc. of the Royal Society of London, Mathematical and Physical Sciences, 217, pp. 96-121.
5. Phan-Thein N, Tran-Cong T, and Ramia M (1987) A Boundary Element Analysis of Flagellar Propulsion, J Fluid Mech, 184, pp. 533-549.
6. de La Torre JG, and Bloomfield VA (1977) Hydrodynamic Theory of Swimming of Flagellated Microorganisms, Biophysical J, 20, pp. 49-64.
7. Behkam B, and Sitti M (2004) E. Coli Inspired Propulsion for Swimming Microrobots, Proc ASME, International Mechanical Engineering Congress, Anaheim, California, November 13-19, pp. 59621-59626.
8. Behkam B, and Sitti M (2006) Design Methodology for Biomimetic Propulsion of Miniature Swimming Robots, Journal of Dynamics Systems, Measurements, and Control, Transactions of the ASME, 128, pp. 36-43.
9. Yu TS, Lauga E, and Hosoi AE (2006) Experimental Investigations of Elastic Tail Propulsion at Low Reynolds Number, Phys Fluids, 18(091701), pp. 1-4.
10. Yates, G. T. (1986). How Microorganisms Move through Water, American scientist, 74(4), 358-365.
11. Taylor, G. I. (1969). Motion of axisymmetric bodies in viscous fluids. Problems of Hydrodynamics and Continuum Mechanics, SIAM Publ, 718-724.
12. Cox, R. G. (1970). The motion of long slender bodies in a viscous fluid. Part 1. General theory. J. Fluid Mech, 44(4), 791-810.
13. Batchelor, G. K. (1970). Slender-body theory for particles of arbitrary cross-section in Stokes flow. Journal of Fluid Mechanics, 44(03), 419-440.
14. Higdon JLL (1979) A Hydrodynamic Analysis of Flagellar Propulsion, J Fluid Mech, 90, pp. 685-711.

15. Johnson RE (1980) An Improved Slender Body Theory for Stokes Flow, J Fluid Mech, 99, pp. 411-431.
16. Johnson RE, and Brokaw CJ (1979) Flagellar Hydrodynamics: A comparison between Resistive Force Theory and Slender Body Theory, Biophys J, 25, pp.113-127.
17. Goto T, Nakata K, Baba K, Nishimura M, and Magariyama Y (2005) A Fluid-Dynamic Interpretation of the Asymmetric Motion of Singly Flagellated Bacteria Swimming Close to a Boundary, Biophys J, 89, pp. 3771-3779.
18. Lagomarsino MC, Capuani F, and Lowe CP (2003) A Simulation Study of the Dynamics of a Driven Filaments in an Aristotelian Fluid, J of Theoritical Biol, 224, pp. 215-224.
19. Lowe CP (2003) Dynamics of Filaments: Modelling the Dynamics of Driven Microfilaments, Phil Trans R Soc B, 358, pp. 1543-1550.
20. Najafi A, and Golestanian R (2005) Propulsion at Low Reynolds Number. Journal of Physics: Condensed Matter, 17(14), S1203.
21. Goubault C, Jop P, Fermigier M, Baudry J, Bertrand E, and Bibette J (2003) Flexible Magnetic Filaments as Micromechanical Sensors. Physical Review Letters, 91(26), pp. 260802.
22. Gauger E, and Stark H (2006) Numerical Study of a Microscopic Artificial Swimmer. Physical Review E, 74(2), pp. 021907.
23. Chwang AT, and Wu TY (1971) A note on Helical Movement of Microorganisms, Proc R Soc B Biol Sci, 178, pp. 327-346.
24. Lighthill J (1976) Flagellar Hydrodynamics, SIAM Rev 18(2), pp. 161-230.
25. Meirovitch L, Fundamentals of Vibrations, Tata McGraw-Hill, India, 2000.
26. Lamb H, Hydrodynamics, Cambridge University press, Cambridge, 1895.
27. M. Braun, Differential Equations and Their Applications. 4th ed., New York: Springer-Verlag, 1992, ch. 2.
28. Machin KE (1958) Wave Propagation along Flagella, J Exp Biol, 35, pp. 796-806.
29. Wiggins CH, and Goldstein RE (1998) Flexive and Propulsive Dynamics of Elastica at Low Reynolds Number, Phy Rev Lett, 80, pp. 3879-3882.
30. Powers TR (2002) Role of Body Rotation in Bacterial Flagellar Bundling, Phy Rev E, 65(4), pp. 040903.

31. Happel J, and Brenner H (1965) Low Reynolds Number Hydrodynamics, Prentice Hall, Englewood Cliffs, NJ.
32. Fujime S, Maruyama M, and Asakura S (1972) Flexural Rigidity of Bacterial Flagella Studied by Quasi-elastic Scattering of Laser Light, J Mol Biol, 68(2), pp.347-354.
33. Hoshikawa H, and Kamiya R (1985) Elastic Properties of Bacterial Flagellar Filaments: II. Determination of the Modulus of Rigidity, Biophys Chem, 22(3), pp.159-166.
34. Brennen C, and Winet H (1977) Fluid Mechanics of Propulsion by Cilia and Flagella, Ann Rev Fluid Mech, 9, pp. 339-98.
35. Lordi V and Yao N (1998) Radial Compression and Controlled Cutting of Carbon Nanotubes. Journal of Chemical Physics, 109 (6), pp. 2509-2512.
36. Deepak K, Rathore JS, and Sharma NN (2011) Nanorobot Propulsion using Helical Elastic Filamenst at Low Reynolds Numbers. J Nanotechnol Eng Med, Transactions of the ASME 2(1) 011009, pp. 1-6.
37. Randolph Pyle H (1961) The Projection of a Vector on a Plane, Mathematics Magazine, Mathematical Association of America, 34 (4), pp. 195-197.

# Chapter 4

# Tapered Flagellated Nanoswimmer

## 4.1 INTRODUCTION

In the previous Chapter, the mathematical modeling and analysis is carried out for both planar wave and helical wave propulsion with a uniform diameter flagellated nanoswimmer, using RFT. Steady state shapes of flagellum are determined including elastohydrodynamics and the developed mathematical model was simulated for performance indexes of nanoswimmer namely swimming velocity, thrust force and efficiency. Literature [1-11] is available where, the flagellum is considered as filament of a constant diameter with a value of few hundreds of nanometer propelling an inert spherical head. In almost all models available in literature the diameter of the flagellum is considered constant. But in nature, the actual profile of flagellum of a nanoswimmer is tapered and the head also is more of an oblate spheroid in shape. The debate therefore is to consider taper of flagellum and model elastohydrodynamic propulsion accordingly and hence investigate the effect of inclusion of the taper flagellum in the evaluation of shape, velocity and efficiency of a beating flagellum.

In this Chapter, the analytical design optimization of a tapered flagellated nanoswimmer for better performance has been studied. The chapter deals with the modeling and simulation of the planar as well as helical wave propulsion through a tapered flagellum and computes its performance indexes of swimming velocity and efficiency and are compared for different taper ratios of the flagellum. The output performance is measured in terms of velocity of propulsion and the efficiency of the nanoswimmer and the results are compared with the uniform diameter case. The parametric study highlights the optimum taper ratio of a tapering flagellum that generates minimum drag. The performance indexes as explicit functions of elastic modulus of the flagellum material and effect of beat frequency on performance indexes is also analyzed. The observations of the study are important conclusions towards designing artificial flagellum for nanoswimmers.

## 4.2 SIMULATION OF PLANER WAVE PROPULSION (PWP) THROUGH A TAPERED NANOSWIMMER (TN)

In this section, mathematical modeling for tapered nanoswimmer (TN) propelling through planar wave propulsion (PWP) using RFT has been presented. The modeling has not been reported in earlier in literature and was first attempted by us and published [12]. In this attempt, the boundary conditions used are same as given in section 3.3.2. The boundary conditions are kept same so as to compare the two designs of flagellum namely constant diameter and tapered diameter. The developed mathematical model is simulated for performance indexes of nanoswimmer namely forward velocity $V_x$, and propulsive efficiency $\eta$.

### 4.2.1 Modeling PWP in TN

Figure 4.1 schematically shows a TN of length *L* propelled by executing a planar wave motion. The TN consists of a flagellum few micro-meters long, which is tapered throughout the length, attached to a spherical or an elongated head. Coordinates origin is considered to be at head and flagellum joint as shown in Figure 4.1. TN is assumed to be surrounded by the fluid (not shown in Figure 4.1) and fluid flow is considered unbounded in order to avoid any wall effects. Assessing the tail configuration provides the boundary conditions, the drag of a small element *ds* of the wiggling tail provides a net thrust force perpendicular to the direction of actuation, propelling the nanoswimmer with velocity $V_x$ in *x*-direction. The head of the nanoswimmer is taken as sphere lying along negative *x* direction. The base of the flagellum oscillates with frequency $\omega$ in *xy* plane by an actuating mechanism assumed to be present in the swimmer's head.

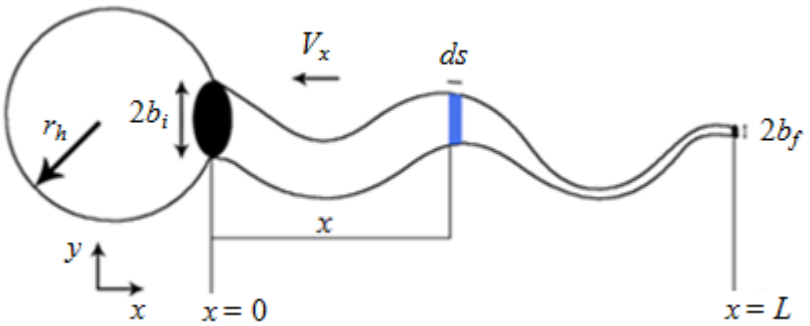


**Figure 4.1: Physical interpretation of tapered flagellum**

For a nanoswimmer, inertia forces are insignificant [7] as mentioned in section 1.2, Chapter 1 and the steady state shape of flagellum is determined by balancing elastic and viscous forces acting over the flagellum. Since in TN, radius of the flagellum cross-section is linearly varying along flagellum length therefore the moment of inertia $I$ (which was constant in UDN case) in equation (3.1) is also varying along *x* and is replaced with $I(x)$. The elastic bending force $dF_E$ is obtained by considering an element *ds* at a distance *x* from proximal end as an oscillating elastic beam with moment of inertia $I(x)$. Therefore $dF_E$ is obtained by replacing $I$ with $I(x)$ in equation (3.1) and is given as:

$$dF_E = E\frac{\partial^2}{\partial x^2}\left[I(x)\left(\frac{\partial^2 y}{\partial x^2}\right)\right]ds \tag{4.1}$$

where, *E* is the elasticity of the material of flagella, $I(x)$ is the area moment of inertia and *y* is the transverse displacement at any given position over length of flagellum.

The viscous forces ($dF_V$) is product of drag coefficient acting on element *ds* and elemental velocity in *y* direction. In TN, normal drag coefficient $C_n$ is not a constant and vary along the length of flagellum therefore replacing $C_n$ with $C_n(x)$ in equation (3.2), the elemental viscous force $dF_V$ on element *ds* is

$$dF_V = -C_n(x)\frac{\partial y}{\partial t}ds \tag{4.2}$$

where, $C_n(x)$ is the normal resistive force coefficient, *y* is the transverse displacement and $\frac{\partial y}{\partial t}$ is the rate of change of displacement *y* with respect to time.

At steady state of motion, elastic bending force $dF_E$ (equation 4.1) and viscous force $dF_V$ (equation 4.2) balances each other on element *ds*. Equating elastic and viscous forces on a small element *ds* of the flagellum gives the governing equation of the model as

$$E\frac{\partial^2}{\partial x^2}\left(I(x)\frac{\partial^2 y}{\partial x^2}\right) = -C_n(x)\frac{\partial y}{\partial t} \tag{4.3}$$

where, area moment of inertia $I(x)$, at any given position over length is obtained by replacing $b$ with $b(x)$ and given as

$$I(x) = \frac{\pi \ b(x)^4}{4} \tag{4.4}$$

Equation (4.3) is Euler's beam equation for a beam with varying cross-sectional area. Further simplifying equation (4.3), we get

$$I(x)\frac{\partial^4 y}{\partial x^4} + 2I'(x)\frac{\partial^3 y}{\partial x^3} + I''(x)\frac{\partial^2 y}{\partial x^2} = -\frac{C_n(x)}{E}\frac{\partial y}{\partial t} \tag{4.5}$$

where $I'(x)$ and $I''(x)$ are first and second order space derivatives of $I(x)$. The general solution of the equation (4.5) is

$$y(x,t) = y(x)e^{i\omega t} \tag{4.6}$$

where displacement *y* is a function of displacement in *x* direction and time *t*, and $\omega$ is frequency of oscillation of element. The time and displacement derivatives of equation (4.6) are obtained as:

$$\frac{\partial y}{\partial t} = y(x)i\omega e^{i\omega t} \tag{4.7}$$

$$\frac{\partial^2 y}{\partial x^2} = y''(x)e^{i\omega t} \tag{4.8}$$

$$\frac{\partial^3 y}{\partial x^3} = y'''(x)e^{i\omega t} \tag{4.9}$$

$$\frac{\partial^4 y}{\partial x^4} = y''''(x)e^{i\omega t} \tag{4.10}$$

Inserting space and time derivatives from equations (4.7) through to (4.10) in equation (4.5), the governing equation reduces to

$$I(x)y''''(x) + 2I'(x)y'''(x) + I''(x)y''(x) + i\left(\frac{C_n\omega}{E}\right)y(x) = 0 \tag{4.11}$$

In TN, radius of the flagellum cross-section is linearly varying over flagellum length (*L*) from $b_i$ (radius at *x* = 0) to $b_f$ (radius at *x* = *L*) as shown in Figure 4.2. The cross section radius $b(x)$, at any arbitrary section over the flagellum length (with linear taper assumption) at a distance *x* from the proximal end (actuated end) i.e. *x* = 0, is given as

$$b(x) = b_i(kx+1) \tag{4.12}$$

where, $b_i$ is the flagellum radius at $x = 0$ and $k = \left( \frac{b_f - b_i}{L\, b_i} \right)$ is the slope of linear taper.

Substituting $b(x)$ from equation (4.12) in equation (4.4)

$$I(x) = \frac{\pi\, b_i^4 (kx+1)^4}{4} = I_o (kx+1)^4 \tag{4.13}$$

where, $I_o = \frac{\pi\, b_i^{\,4}}{4}$, is the area moment of inertia at proximal end.

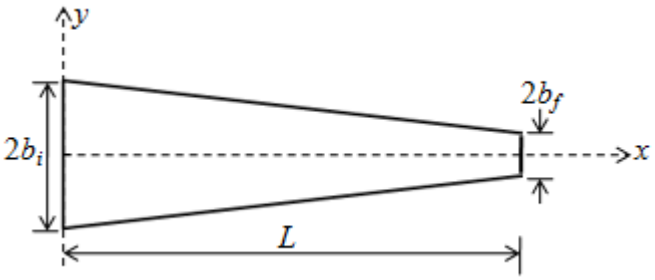


**Figure 4.2: Linearly varying tapered flagellum**

Differentiating $I(x)$ with respect to *x*, gives first order space derivative $I'(x)$ as

$$I'(x) = 4kI_o (kx+1)^3 \tag{4.14}$$

Differentiating equation (4.14) once again with respect to *x*, gives second order space derivative $I''(x)$ as

$$I''(x) = 12k^2 I_o (kx+1)^2 \tag{4.15}$$

Substituting $I(x)$, $I'(x)$ and $I''(x)$ from equations (4.13), (4.14) and (4.15) respectively in equation (4.11) and simplifying, we get

$$(kx+1)^4 y''''(x) + 8k(kx+1)^3 y'''(x) + 12k^2 (kx+1)^2 y''(x) + i\left( \frac{C_n \omega}{E\, I_o} \right) y(x) = 0 \tag{4.16}$$

Equation (4.16) is the general equation for a linear tapered flagella executing a planar motion. Equation (4.16) is a linear differential equation also commonly known as Legendre's linear equation, whose solution can be found by assuming another variable $\tau$ such that

$$\tau = \ln(kx+1) \tag{4.17}$$

Differentiating equation (4.17) with respect to *x* gives

$$\frac{d\tau}{dx} = \frac{k}{(kx+1)} \tag{4.18}$$

Multiplying numerator and denominator of equation (4.18) by *dy* and rewriting, we get

$$(kx+1)y' = k\frac{dy}{d\tau} = kDy \tag{4.19}$$

where $D = \frac{d}{d\tau}$ and $y' = \frac{dy}{dx}$ .

Further, differentiating equation (4.19) with respect to *x* to get second, third and fourth order space derivatives as given

$$(kx+1)^2 y'' = k^2 D(D-1)y \tag{4.20}$$

$$(kx+1)^3 y''' = k^3 D(D-1)(D-2)y \tag{4.21}$$

$$(kx+1)^4 y'''' = k^4 D(D-1)(D-2)(D-3)y \tag{4.22}$$

Substituting $y'', y'''$, and $y''''$ from equations (4.20) through to (4.22) in equation (4.16), we get characteristic equation

$$\left\{\begin{array}{l} k^4 D(D-1)(D-2)(D-3)y + 8k^4 D(D-1)(D-2)y \\ +12k^4 D(D-1)y + i\left(\frac{C_n\omega}{E\,I_o}\right)y \end{array}\right\} = 0 \tag{4.23}$$

The set of parameters, $\left(\frac{E\,I_o}{C_n\omega}\right)$, has length units and is replaced by $l^4$ in equation (4.23) for further simplification. As previously defined in equation (3.8) in section 3.3.1, the length parameter ($l$) is also known as scale length $l = \left(\frac{E\,I_o}{C_n\omega}\right)^{\frac{1}{4}}$. Simplifying characteristic equation (4.23), we get

$$\left\{\begin{array}{l} k^4\left(D^4 - 6D^3 + 11D^2 - 6D\right) \\ +8k^4\left(D^3 - 3D^2 + 2D\right) + k^4\left(12D^2 - 12D\right) + \frac{i}{l^4} \end{array}\right\} = 0 \tag{4.24}$$

Dividing equation (4.24) by $k^4$ and rearranging, we get

$$D^4 + 2D^3 - D^2 - 2D + \frac{i}{k^4 l^4} = 0 \tag{4.25}$$

The general solution of equation (4.3) is given as [13]

$$y = e^{i\omega t} \sum_{j=1}^{4} A_j (k'x + 1)^{m_j} \tag{4.26}$$

where, the four coefficients $A_j$ ($j$ = 1 to 4) are calculated by substituting the boundary conditions given in equation (4.27), $k'$ is product of the slope of the linear taper ($k$) and scale length ($l$) and $m_j$ are the four roots of the auxiliary equation (4.25).

### 4.2.2 Modeling Performance Indexes in Planar Wave Propelled TN

The boundary conditions considered for TN are same as previously defined in equation (3.12) in section 3.3.2 for UDN. i.e. the actuation of the flagellum is at the proximal end with the flagellum fixed to the head and with a time dependent slope having maxima as $G = \tan(\theta_{\max})$ at beating frequency of $\omega$. At the distal end, the shear force and the bending moment vanishes. Hence for a spherical head attached to cylindrical tapered flagellum, the boundary conditions considered are given as

$$\text{Position at proximal end } y\big|_{x=0} = 0 \tag{4.27a}$$

$$\text{Slope at proximal end } y'\big|_{x=0} = Ge^{i\omega t} \tag{4.27b}$$

$$\text{Bending moment at distal end } y''\big|_{x=L} = 0 \tag{4.27c}$$

$$\text{Shear force at distal end } y'''\big|_{x=L} = 0 \tag{4.27d}$$

The four coefficients $A_1$, $A_2$, $A_3$ and $A_4$ are calculated by substituting the boundary conditions given in equation (4.27), in equation (4.26).

Substituting the boundary condition from equations (4.27a) in equation (4.26) we get

$$\sum_{i=1}^{4} A_i = 0 \tag{4.28a}$$

Substituting the second boundary condition from equations (4.27b) in equation (4.26) we get

$$k' \sum_{i=1}^{4} A_i m_i = G \tag{4.28b}$$

Substituting the third boundary condition from equations (4.27c) in equation (4.26) we get

$$\sum_{i=1}^{4} A_i m_i (m_i - 1)(k'L + 1)^{m_i - 2} = 0 \tag{4.28c}$$

Similarly substituting the fourth boundary condition from equations (4.27d) in equation (4.26) we get

$$\sum_{i=1}^{4} A_i m_i (m_i - 1)(m_i - 2)(k'L + 1)^{m_i - 3} = 0 \tag{4.28d}$$

The equations (4.28a) to (4.28d) are combined and rewritten in form of matrix as

$$[M][A] = [Z] \tag{4.29}$$

where

$$M = \begin{Bmatrix} 1 & 1 \\ m_1 & m_2 \\ m_1(m_1 - 1)(k'L + 1)^{m_1 - 2} & m_2(m_2 - 1)(k'L + 1)^{m_2 - 2} \\ m_1(m_1 - 1)(m_1 - 2)(k'L + 1)^{m_1 - 3} & m_2(m_2 - 1)(m_2 - 2)(k'L + 1)^{m_2 - 3} \\ 1 & 1 \\ m_3 & m_4 \\ m_3(m_3 - 1)(k'L + 1)^{m_3 - 2} & m_4(m_4 - 1)(k'L + 1)^{m_4 - 2} \\ m_3(m_3 - 1)(m_3 - 2)(k'L + 1)^{m_3 - 3} & m_4(m_4 - 1)(m_4 - 2)(k'L + 1)^{m_4 - 3} \end{Bmatrix}$$

$$A = \begin{bmatrix} A_1 \\ A_2 \\ A_3 \\ A_4 \end{bmatrix}, \text{and } Z = \begin{bmatrix} 0 \\ \frac{G}{k'} \\ 0 \\ 0 \end{bmatrix}$$

Equation (4.28) is used to obtain coefficient matrix $[A]$ and is given as

$$[A] = [M]^{-1}[Z] \tag{4.30}$$

where $[M]^{-1}$ is the inverse of matrix $[M]$. A MATLAB code was written (given in Appendix-IV) to calculate coefficient matrix. The four coefficients $A_1$, $A_2$, $A_3$ and $A_4$ are substituted back in equation (4.26) to obtain the wave form of flagellum in *x*-*y* plane.

Figure 4.3 shows the forces acting in normal and longitudinal directions on the element *ds* of the flagellum due to transverse velocity $V_y$ and forward velocity $V_x$. The element is oriented to the *x*-axis at an angle $\theta$ at an instance of time *t*. The drag force generated depends on the components of the velocity in normal and longitudinal directions. The resistance of the fluid to the flagellum's motion is computed for known values of the

local coefficient of drag i.e. $C_n(x)$ and $C_l(x)$ for the element and its velocity component in normal and longitudinal directions.

Using RFT, the local normal i.e. $dF_n(x)$ and longitudinal components i.e. $dF_l(x)$ of the force on element '*ds*' due to forward and transverse displacements of the element are vectorial summation of components of forces in *x* and *y* direction and are given as

$$dF_n(x) = C_n(x)(V_y \cos\theta - V_x \sin\theta)ds \tag{4.31}$$

$$dF_l(x) = C_l(x)(V_x \cos\theta + V_y \sin\theta)ds \tag{4.32}$$

where, $V_x$ and $V_y$ are the velocity in *x* and *y*- directions, respectively, $V_x \sin\theta$ and $V_y \cos\theta$ are velocity components in *n*-direction and $V_x \cos\theta$ and $V_y \sin\theta$ are components in *l*-direction. $C_n(x)$ and $C_l(x)$ are the local normal and longitudinal drag coefficients for the cylindrical element and are widely accepted in research community as given in [14] and are written below for sake of convenience. With radius $b(x)$ at any *x* distance from origin and in a medium having viscosity $\mu$, $C_n(x)$ and $C_l(x)$ for the tapered profile are obtained by replacing $b$ with $b(x)$ in equation (3.18) and equation (3.19) and are given as

$$C_n(x) = \frac{4\pi\mu}{\ln\left(\frac{L}{b(x)}\right) + 0.5} \tag{4.33}$$

$$C_l(x) = \frac{2\pi\mu}{\ln\left(\frac{L}{b(x)}\right) - 0.5} \tag{4.34}$$

In the uniform diameter case, $C_n$ and $C_l$ are constant throughout the length of the flagellum as *b* is constant.

The resultant propulsive forces i.e. $dF_x(x)$ and transverse force i.e. $dF_y(x)$ on the flagellum element *ds* in the $x$ and $y$ direction are determined by resolving components of normal $dF_n(x)$ and longitudinal forces $dF_l(x)$ along $x$ and $y$-directions, and are given as

$$dF_x(x) = dF_n(x)\sin\theta - dF_l(x)\cos\theta \tag{4.35}$$

$$dF_y(x) = -dF_n(x)\cos\theta - dF_l(x)\sin\theta \tag{4.36}$$

Substituting the local normal $dF_n(x)$ and longitudinal forces $dF_l(x)$ from equations (4.31) and (4.32), in equation (4.35) and rearranging $V_x$ and $V_y$ terms separately, gives the net forward thrust $dF_x(x)$ as

$$dF_x(x) = \left[-\left(C_n(x)\sin^2\theta + C_l(x)\cos^2\theta\right)V_x + \left(C_n(x) - C_l(x)\right)V_y\sin\theta\cos\theta\right] ds \tag{4.37}$$

Similarly, the net transverse force $dF_y(x)$ is obtained by substituting the local normal $dF_n(x)$ and longitudinal forces $dF_l(x)$ from equations (4.31) and (4.32), in equation (4.36) and rearranging $V_x$ and $V_y$ terms separately and is given as

$$dF_y(x) = \left[\left\{C_n(x) - C_l(x)\right\}V_x\sin\theta\cos\theta - \left\{C_n(x)\cos^2\theta + C_l(x)\sin^2\theta\right\}V_y\right] ds \tag{4.38}$$

Dividing numerator and denominator of equations (4.37) and (4.38) by $\cos^2\theta$

$$dF_x(x) = \frac{\dfrac{\left[-\left\{C_n(x)\sin^2\theta + C_l(x)\cos^2\theta\right\}V_x + \left\{C_n(x) - C_l(x)\right\}V_y\sin\theta\cos\theta\right]}{\cos^2\theta}}{\dfrac{1}{\cos^2\theta}} ds \tag{4.39}$$

$$dF_y(x) = \frac{\dfrac{\left[\left\{C_n(x) - C_l(x)\right\}V_x\sin\theta\cos\theta - \left\{C_n(x)\cos^2\theta + C_l(x)\sin^2\theta\right\}V_y\right]}{\cos^2\theta}}{\dfrac{1}{\cos^2\theta}} ds \tag{4.40}$$

Using $\dfrac{1}{\cos^2\theta} = \sec^2\theta = 1 + \tan^2\theta$ in equation (4.39) and equation (4.40) and solving, we get

$$dF_x(x) = \frac{\left[-\left\{C_n(x)\tan^2\theta + C_l(x)\right\}V_x + \left\{C_n(x) - C_l(x)\right\}V_y\tan\theta\right]}{1 + \tan^2\theta} ds \tag{4.41}$$

$$dF_y(x) = \frac{\left[\left\{C_n(x) - C_l(x)\right\}V_x\tan\theta - \left\{C_n(x) + C_l(x)\tan^2\theta\right\}V_y\right]}{1 + \tan^2\theta} ds \tag{4.42}$$

Length of the small element *ds* is given by $ds = \left(\sqrt{1 + \tan^2\theta}\right) dx$, where *dx* is the projection of elemental length *ds* along *x*-axis and $\theta$ is the angle between element *ds*

and *x*-axis. Substituting for $ds$ in terms of $dx$ and $\theta$ in equation (4.41) and equation (4.42) and with consideration of low amplitude waves, $\theta$ is very small $(\text{i.e. } \tan\theta \langle\langle 1)$, the equations (4.41) and (4.42) reduce to

$$dF_x(x) \approx [-V_x C_l(x) + \{C_n(x) - C_l(x)\} V_y \tan\theta] dx \tag{4.43}$$

$$dF_y(x) \approx [\{C_n(x) - C_l(x)\} V_x \tan\theta - V_y C_n(x)] dx \tag{4.44}$$

Further, substituting $\tan\theta = \frac{dy}{dx}$ and $V_y = \frac{dy}{dt}$ in equation (4.43) and, taking $y$ from equation (4.26) and integrating the thrust force over length, we calculate the average thrust generated by the flagellum and is given as

$$F_x = \int_0^L dF_x = \int_0^L [-V_x C_l(x) + \{C_n(x) - C_l(x)\} \frac{dy}{dt} \frac{dy}{dx}] dx \tag{4.45}$$

Under steady state conditions, the net thrust force $F_x$ generated by flagellum balances the drag due to the head by TN.

From Stokes' equation, drag due to a spherical head of radius $r_h$ in a viscous medium of viscosity $\mu$ is given as

$$F_{head} = 6\pi \ \mu \ r_h V_x \tag{4.46}$$

Equating the net thrust force generated due to wiggling of flagellum from equation (4.45) to the drag due to spherical head from equation (4.46) we calculate the forward velocity $V_x$ of TN and is given as

$$\int_0^L [-V_x C_l(x) + \{C_n(x) - C_l(x)\} \frac{dy}{dt} \frac{dy}{dx}] dx = 6\pi \ \mu \ r_h V_x \tag{4.47}$$

Rearranging equation (4.47), we obtain forward velocity $V_x$ of the tapered flagellated nanoswimmer

$$V_x = \frac{\int_0^L \left[ \{C_n(x) - C_l(x)\} \frac{dy}{dt} \frac{dy}{dx} \right] dx}{6\pi \ \mu \ r_h + C_l(x) V_x L} \tag{4.48}$$

The forward velocity $V_x$ is first performance index to assess TN's performance. The propulsive efficiency ($\eta$) is the another index for performance investigation of TN. The

efficiency ($\eta$) of a nanoswimmer is defined as the ratio of useful power developed for forward motion along the *x*-axis to the total power needed for wiggling the tail. The power utilised in the *x* and *y*-directions can be calculated by integrating the terms $dF_x(x)V_x$ and $dF_y(x)V_y$ over the flagella length and therefore efficiency ($\eta$) of TN is given as

$$\eta = \frac{\int_0^L dF_x(x)V_x}{\int_0^L dF_x(x)V_x + \int_0^L dF_y(x)V_y} \tag{4.49}$$

where, $\mu$ is the viscosity of the medium, $L$ and $b$ are the length and radius of the flagellum, and $V_x$ and $V_y$ represents the forward and transverse movement of element *ds* of the flagellum.

The developed mathematical model for performance measuring index of TN namely velocity (refer equation 4.48), and efficiency (refer equation 4.49) are simulated in the next section using MATLAB®.

### 4.2.3 Simulation, Results and Discussion of Performance of Planar Wave Propelled TN

Numerical simulation of the propulsion model given by equation (4.26) for TN is carried out in MATLAB®. The MATLAB code is given in Appendix-IV. The tail is discretized in 100 elements around which the solution converges. A mesh grid is made to discretize the total time period also into 100 time steps. From the computed mode shapes of the planar wave, partial derivatives with respect to space and time are calculated using the gradient function. The mode shapes, velocity and efficiency are first obtained for uniform flagella of length 50 μm and cross section radius 200 nm. The fluid through which the TN is swimming is assumed to be water with viscosity 0.001 *Pa-s*. The head radius to flagellar length ratio is kept as 0.3 [14].

The flexural rigidity is considered in the range of $10^{-21}$ $Nm^2$ [15-16]. To compare the uniform diameter (case A) with the tapered geometry the volume of the flagellum is kept constant and two new cases are developed for a given ratio of initial and final diameter. In the first new case (case B) the length is kept equal to that of the uniform diameter flagellum study and in second new case (case C) the initial diameter is kept

equal to the diameter of the uniform case. For the given flexural rigidity and diameter of uniform flagellum the value of flexural modulus is calculated to be of the order of 1 MPa. The same modulus value is used for the tapered cases. The three possible designs corresponding to case A, case B and case C are tabulated in Table 4.1 alongside the parameters used in simulation.

**Table 4.1: Parameters for simulation (PWP)**

| | **Case A Constant Diameter** | **Case B Taper Diameter** (equal length as in Case A) | | **Case C Taper Diameter** (equal initial diameter as in Case A) | |
|---|---|---|---|---|---|
| Radius (nm) | 200 | Initial | 288.23 | Initial | 200 |
| | | Final | 96.07 | Final | 66.66 |
| Length (μm) | 50 | 50 | | 103.85 | |
| Head radius(μm) | 15 | 15 | | 15 | |
| Viscosity (Pa.s) | 0.001 | 0.001 | | 0.001 | |
| Frequency (Hz) | 35 | 35 | | 35 | |
| Elasticity (MPa) | 1 | 1 | | 1 | |

A specific case of uniform diameter flagellum is obtained for the input parameters as mentioned in second column of Table 4.1. Keeping volume constant, we generated the two other cases (B and C). For both the new cases i.e. case B and case C, a taper ratio of 3:1 considered as an input. The obtained initial and final radius of the tapered flagellum for case B and case C is mentioned in first row of the Table 4.1.

The mode shapes of all three cases are plotted in Figure 4.3. The output velocity and efficiency are noted in Table 4.2. The mode shape of case A is similar to those obtained by Lauga in [14]. For case B the amplitude is higher than that of case A. Analyzing the performance parameters, case B shows both higher velocity and efficiency compared to case A (Refer to the velocity and efficiency in column 2 and 3 of Table 4.2), while in case C the efficiency falls drastically compared to both cases A and B (Refer column 4 in Table 4.2 and compare them with the corresponding values in column 2 and 3 in the same table), as the flagellum length is greater and a considerable part of it exhibits no oscillations, produces larger drag and almost no thrust.

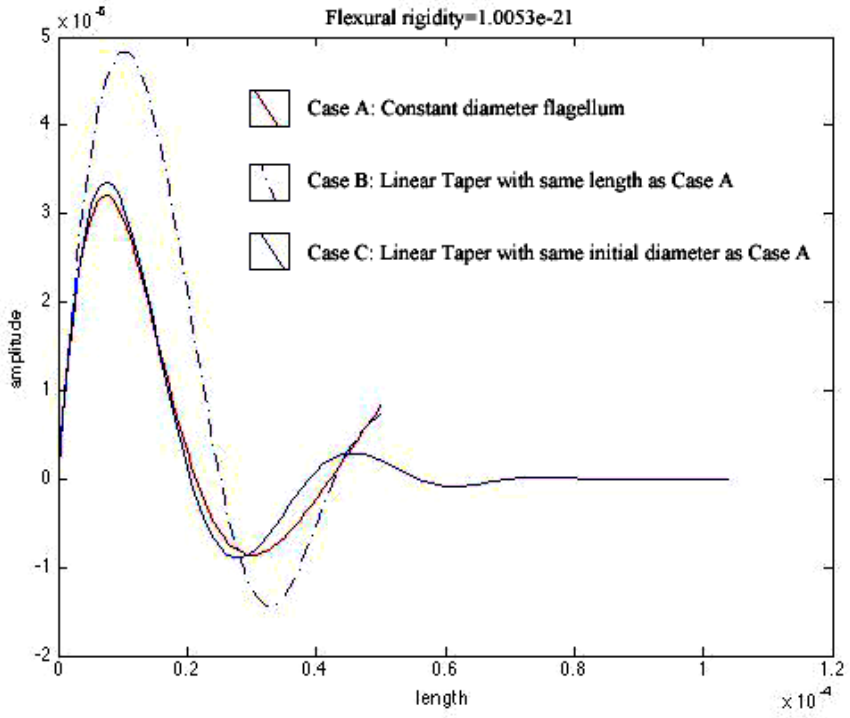


**Figure 4.3: Mode shapes of planar wave propulsion in different cases i.e., case A, case B and case C.**

The efficiency in case C is significantly low with a value of $0.642\times10^{-2}$ %. The value of efficiency obtained for case B is 0.1% which is also observed in natural nanoswimmer like Eukaryotic cells [3, 5]. Case C with lower efficiency is neglected for further parametric studies. Cases A and B are analyzed for varying elasticity and frequency. The results obtained are given in the next section.

**Table 4.2: Results - Comparison of three cases**

| | **Case A Constant Diameter** | **Case B Taper Diameter** (equal length as in Case A) | **Case C Taper Diameter** (equal initial diameter as in Case A) |
|---|---|---|---|
| Velocity (μm/s) | 3.604 | 9.804 | 3.427 |
| Thrust Force (pN) | 1.018 | 2.772 | 0.969 |
| Efficiency ($10^{-2}$ %) | 3.029 | 10 | 0.642 |

As projected in Table 4.2 the calculated velocity is in the order of 10μm/s. Actually observed velocity in the microorganisms are around 100μm/s or higher [15]. In order to match the velocity attained by naturally occurring nanoswimmer, a better design by parametric variation is investigated for better performance.

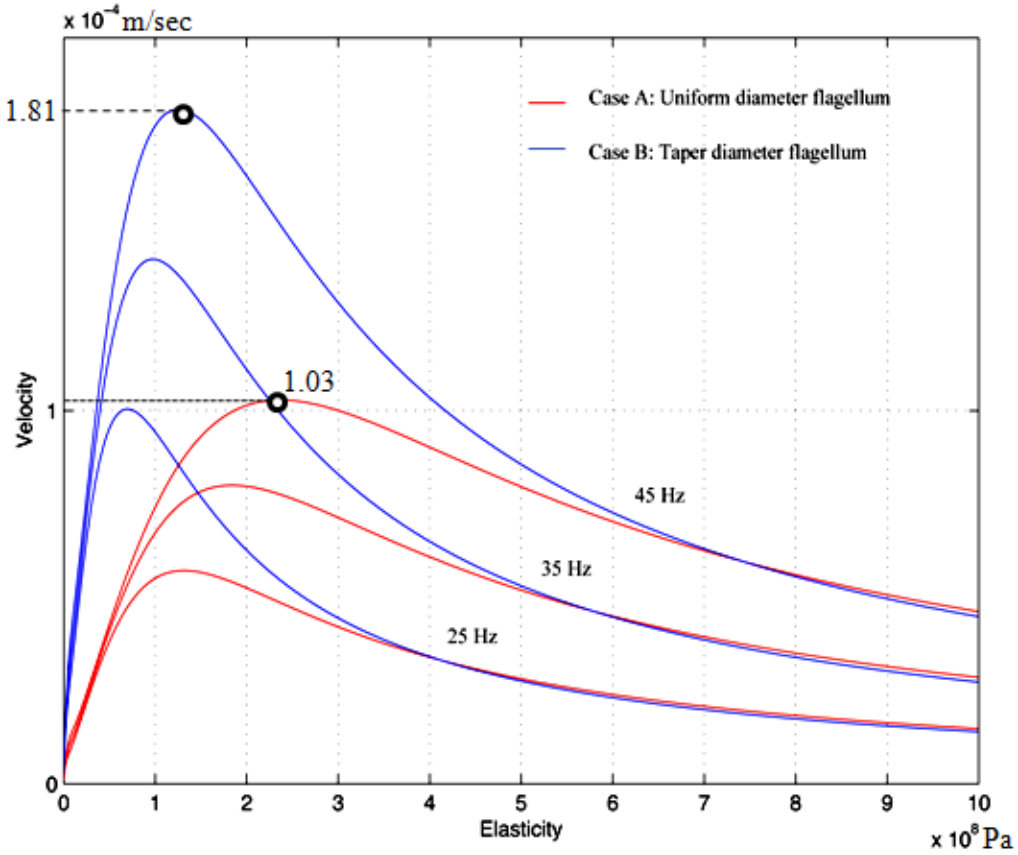


**Figure 4.4: Velocity over parametric variation of Elasticity**

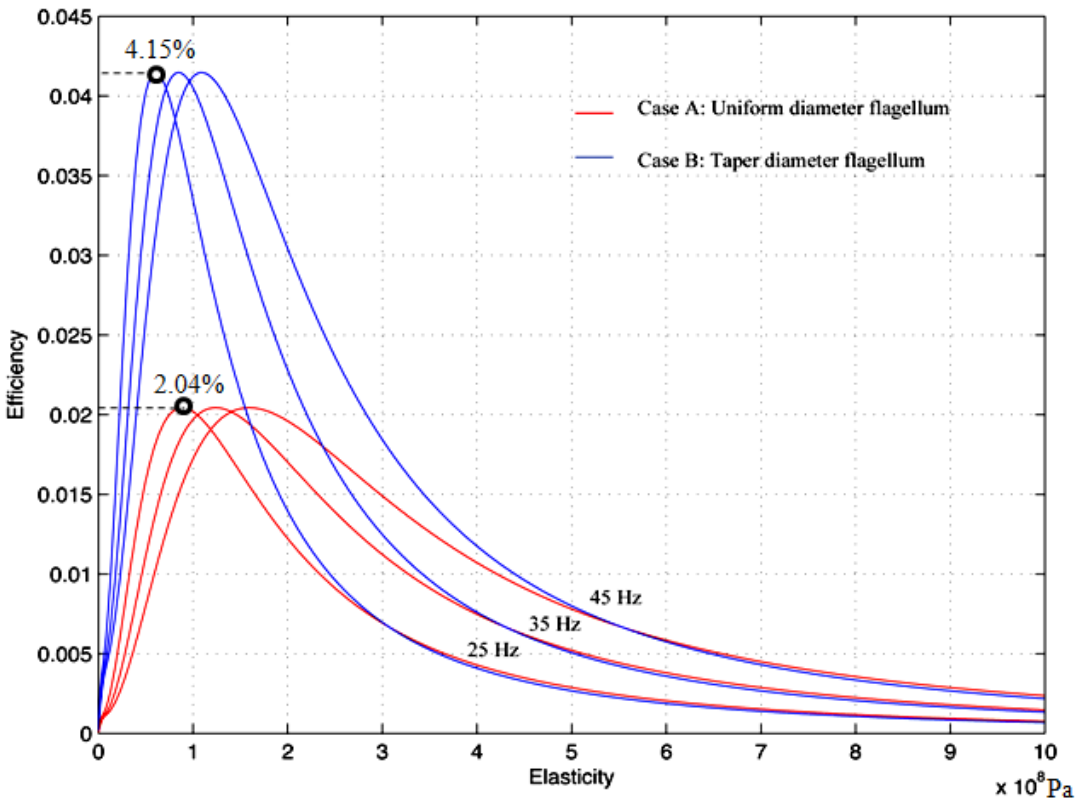


**Figure 4.5: Efficiency over parametric variation of Elasticity**

The explicit formulation of the propulsion model including elastic modulus is important for choice of flagellum material. Elasticity of flagella and beating frequency are important parameters in nanoswimmer design and were also shown to significantly affect performance indexes of uniform diameter nanoswimmer in Chapter 3. By choosing appropriate elasticity of material and beating frequency of the flagellum we can achieve the velocity attained and observed in nanoswimmers existing in nature.

The elasticity of the parameter is varied from 0.1 MPa to 1 GPa. Keeping geometric parameters as stated in Table 4.1, Figure 4.4 illustrates the variation velocity verses variation elasticity over a range from 0.1 MPa to 1 GPa. A family of plots of velocity for increasing frequency from 25 Hz to 45 Hz in steps of 10 Hz is plotted. As seen from the plotted curves in Figure 4.4, a consistent increase in velocity is observed as frequency increases and this is true for both cases of uniform diameter and tapered diameter. For uniform diameter, the model of velocity used for simulation is given in equation (3.33) in section 3.3.2, chapter 3 and tapered diameter flagellum design the model used for simulation is given in equation (4.48). For the uniform diameter case (case A) a maximum velocity of 103 μm/s is observed at a frequency of 45 Hz when elasticity is around 240 MPa, while the maxima of velocity for the taper diameter case (case B) is 181 μm/s, which is achieved at a lower elasticity of around 125 MPa and at the same beating frequency of 45 Hz.

For both case A and B, Figure 4.5 illustrates the variation of efficiency over elasticity for three different frequencies. The tapered diameter case (case B) gives a higher maximum efficiency of 4.15% for the material with lower elasticity of 60 MPa at a lower frequency of 25 Hz, while the maximum efficiency of uniform diameter case (case A) is only 2.04% which is achieved at a elasticity of around 88.1 MPa for a beating frequency of 25 Hz.

Figure 4.6 and Figure 4.7 shows the variation of the ratio of velocity i.e. ($V_{taper}$ / $V_{uniform}$) and efficiency ratio i.e. ($\eta_{taper}$ / $\eta_{uniform}$) over wide range of elasticity for a tapered diameter nanoswimmer with that of uniform diameter nanoswimmer. It can be observed from Figure 4.6 that, for a given frequency, the velocity ratio for the taper to uniform case go as high as 3.2. Similarly, from Figure 4.7, it is observed that efficiency ratio for the taper to uniform diameter nanoswimmer go as high as 3.75.

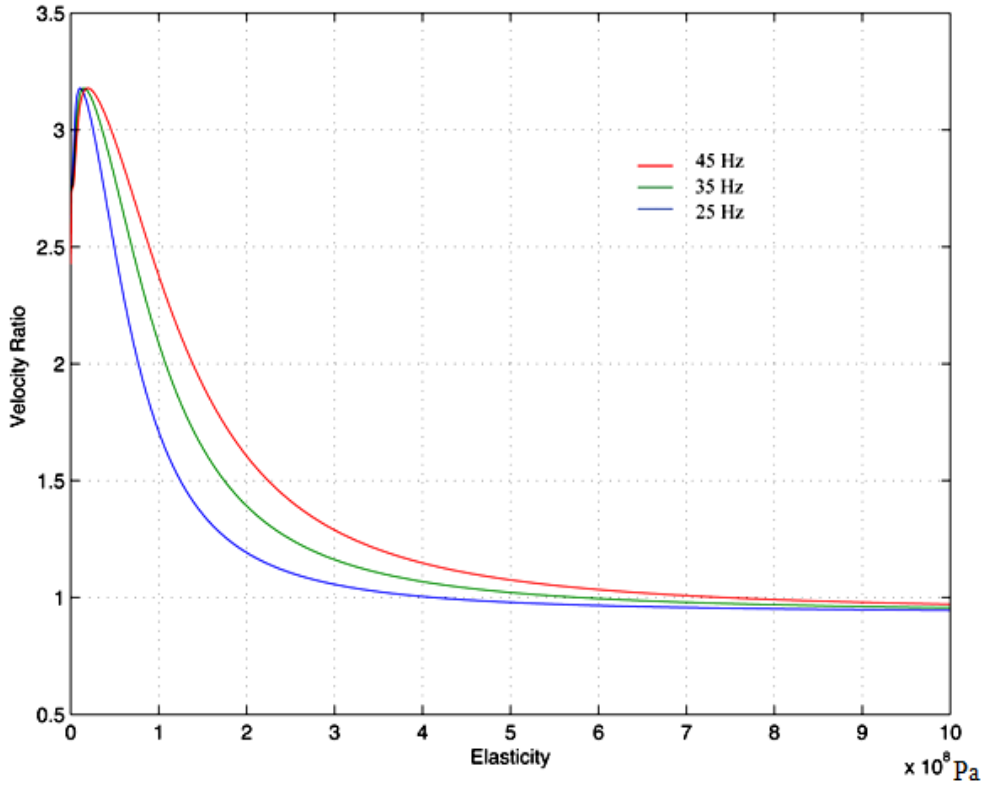


**Figure 4.6: Velocity ratio over parametric variation of Elasticity**

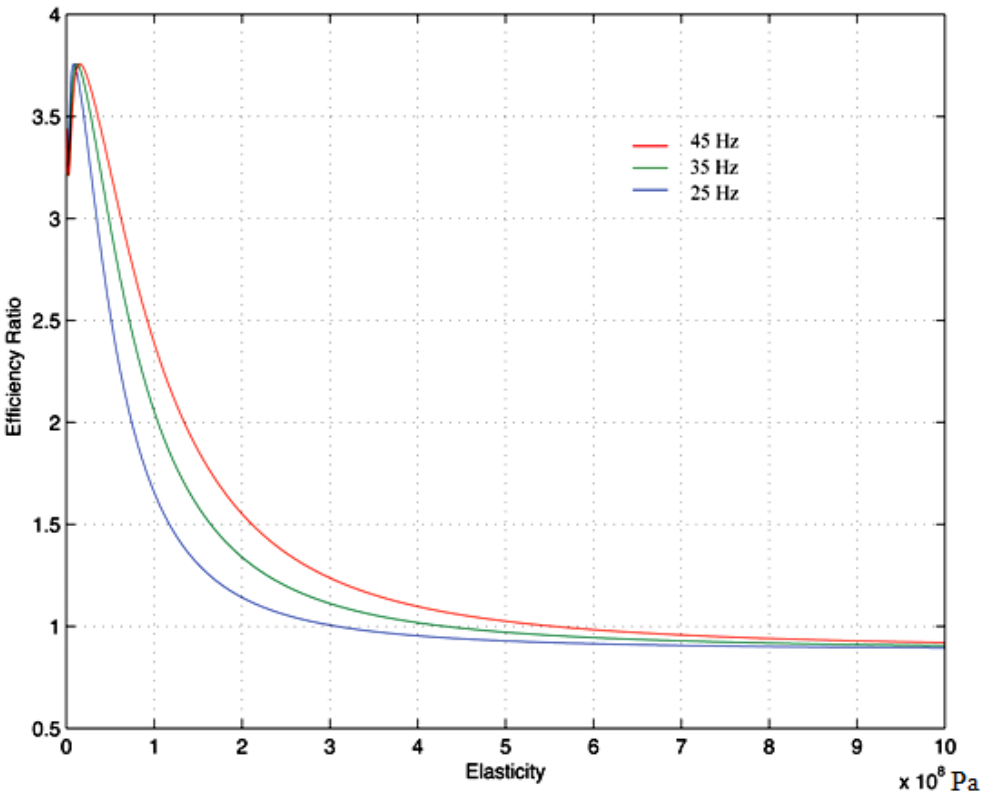


**Figure 4.7: Efficiency ratio over parametric variation of Elasticity**

In microorganisms, the beating frequency is observed to be 35 Hz [3]. For 35 Hz beating frequency, from Figure 4.6, it is observed that the value of the velocity for the tapered case is almost three times the velocity for corresponding uniform case. On the basis of improved velocity (refer Figure 4.6) and efficiency (refer Figure 4.7), with a given amount (mass) of flagellum material, the taper flagellum is a better approximation of the observation made in actual microorganisms.

Further, the parametric variation of the slope $k$ is carried on to check variation of the mode shape of the flagellum and later influence on velocity and efficiency. The findings are highlighted in Figure 4.8. Taking the optimum value (refer Figure 4.8, i.e. the value corresponding to $b_i : b_f = 18$) we set the parameters used for the study as given in Table 4.3.

**Table 4.3: Simulation Parameters**

| | **Case A**<br>**Constant Diameter** | **Case B**<br>**Taper Diameter**<br>(equal length as in Case A) | |
|---|---|---|---|
| Radius (nm) | 200 | Initial | 336.68 |
| | | Final | 18.70 |
| Length (μm) | 50 | 50 | |
| Viscosity (Pa.s) | 0.001 | 0.001 | |
| Frequency (Hz) | 35 | 35 | |
| Elasticity (MPa) | 200 | 200 | |

The taper ratio of the tail ($k$) and its effect on the velocity and efficiency is illustrated in Figure 4.8 as the variation of the ratio of performance in the taper case to the uniform constant diameter case.

Keeping physical parameters as stated in Table 4.3, Figure 4.8 illustrates the effects of variation of taper ratio ($b_i/b_f$) over a range from 2 to 50. The velocity increases as the taper ratio increases but efficiency reaches a maxima when $b_i : b_f$ is around 18.

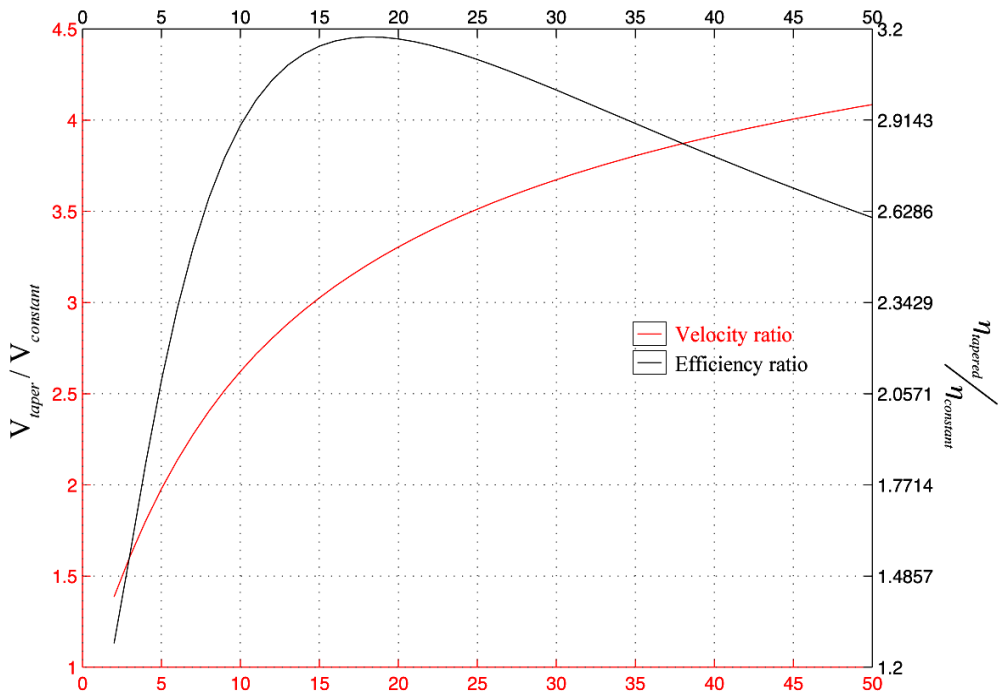


**Figure 4.8: Performance ratio over parametric variation of taper ratio**

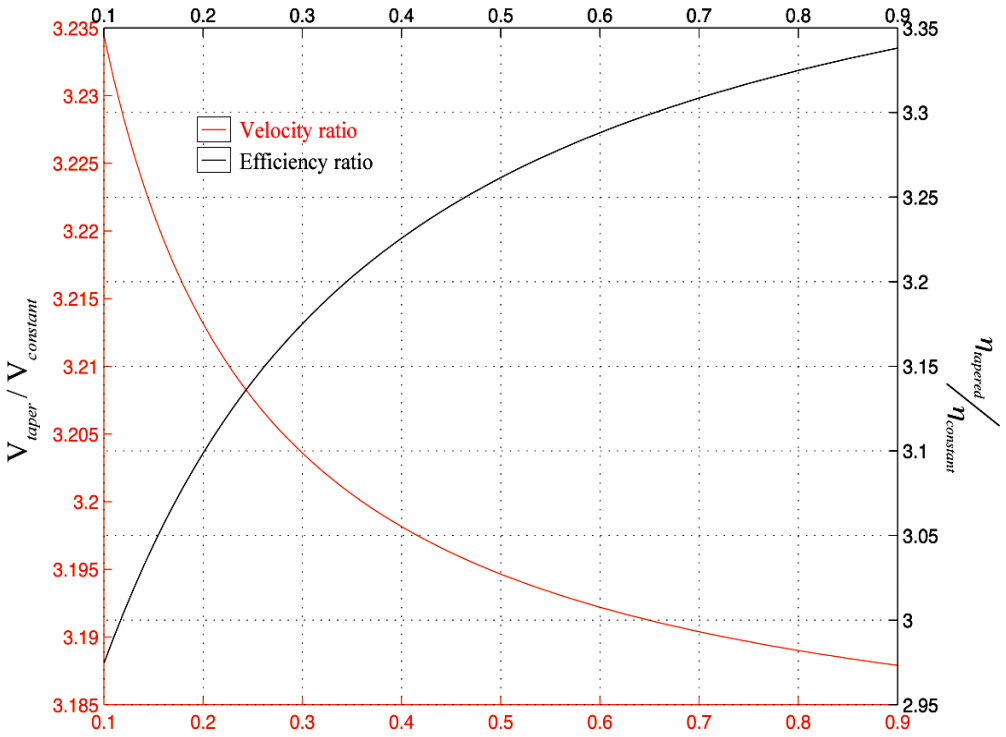


**Figure 4.9: Performance ratio over parametric variation of head radius to tail length**

Considering a spherical head, the variation of the head radius to flagellum length ratio ($r_h$:$L$) also has effect on performance of nanoswimmer. The velocity ratio and the efficiency ratio between the tapered case and constant diameter case over variation of $r_h$:$L$ are illustrated in Figure 4.9. Figure 4.9 shows that, for a spherical head, as head size increases the drag increases leading to decrease in the velocity. Moreover the dissipation of the power due to transverse motion is also lowered at low axial velocity. This in turn increases the efficiency of the swimmer with increase in head size.

The propulsion characteristics of a tapered flagellum propagating planar waves have been studied and the same is compared to the case of uniform flagellum. Mode shapes of a tapered flagellum are predicted based on elastohydrodynamic equations. Keeping the flagellum volume constant, two new cases are developed for a given ratio of initial and final diameter. Results obtained from simulations have plotted in Figure 4.4 through Figure 4.9. From the Figure 4.4 and Figure 4.5, it is observed that the linearly tapered flagellum planar model (case B) showed improved performance higher velocity and efficiency compared to the uniform flagellum model. For a given frequency, the velocity and efficiency ratio for the taper to uniform case can go as high as 3.2 and 3.4 respectively, as seen from Figure 4.6 and Figure 4.7. The maximum efficiency of the taper case is almost three times the maximum efficiency of the uniform diameter case at 35 Hz beating frequency.

Based on the simulation results reported above propulsion through a taper flagellum is more efficient and faster than the uniform diameter flagellum attached to same size spherical head. The optimum taper ratio ($b_i$ : $b_f$ ) is around 18 for a TN. The $r_h$ : $L$ is the deciding factor which has to trade off between the velocity and the efficiency. For a given flagellum length, any increase in head size leads to increase in drag which in turn decreases the velocity.

## 4.3 SIMULATION OF HELICAL WAVE PROPULSION (HWP) THROUGH A TAPERED NANOSWIMMER (TN)

In the previous section, performance indexes, i.e., forward velocity ($V_x$) and propulsive efficiency ($\eta$) for a tapered nanoswimmer propelling itself through planar wave propulsion are obtained. It has been shown that the planar wave propulsion through a tapered flagella facilitates higher efficiency and velocity as compared to

the uniform diameter case. In this section, mathematical modeling and simulation is carried out for a TN propelling through HWP. The optimal size and shape parameters are found for two cases - the fastest swimmer and the most efficient swimmer. The performance parameters are computed for helical wave propagation and compared with planar wave propagation for TN [12]. The comparison between PWP and HWP based on forward velocity ($V_x$) and propulsive efficiency ($\eta$) is given in section 4.3.3 and published in [17].

The shape and the flexural rigidity of the flagella greatly affect the motility of the locomotor efficiency [20-25]. In tapered flagella, the flexural rigidity of the material and the drag force reduces at the distal end, thereby increasing the thrust force [16-17], [25]. In order to predict the shape form, forward speed and propulsive efficiency of tapered helical flagella, the mathematical model is developed using the resistive force theory (RFT) [3] as was done for earlier cases of uniform diameter nanoswimmer in Chapter 3 and tapered diameter nanoswimmer in the previous section. Using RFT, the forces corresponding to the normal and tangential motion of flagella would be approximately given by the local flagellum velocity and the drag coefficients in normal and tangential direction. The net force can be found out by integrating these forces over the length.

### 4.3.1 Modeling HWP in TN

Figure 4.10 shows the schematic of the tapered flagellated nanoswimmer of length $L$ with a head of radius $r_h$. The coordinate system chosen is at the base of the flagellum. The base of the flagellum rotates along the $z$-axis, making the filament sweep out a cone of rotation along $z$-axis. Actuator inside the head is assumed to cause elastic deformation of the flagellum and take the shape of a helix with both pitch and amplitude varying along the $z$ direction as shown in Figure 4.10. The head of the nanoswimmer is taken as a sphere lying along the negative $z$-axis. The coordinate system along with the flagellum rotates with positive $z$-axis as axis of rotation at an angular velocity $\omega$ relative to a frame of reference situated on the head.

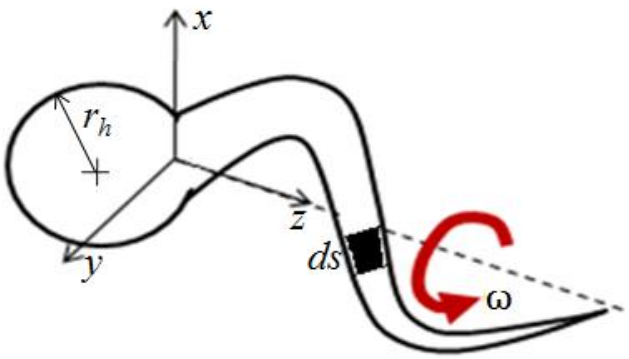


**Figure 4.10: Schematic of nanoswimmer with a tapered flagellum**

For a tapered flagellated nanoswimmer, steady state shape of flagellum is determined by a balance of elastic and viscous forces acting over the flagellum. The elastic bending force on an element of length *ds* for helical wave propagation, $dF_E$ is given by replacing *y* with $\vec{r}$ and *x* with *z* in equation (4.1) and is obtained as equation (4.50) :

$$dF_E = E\frac{\partial^2}{\partial z^2}\left\{I(z)\left(\frac{\partial^2 \vec{r}}{\partial z^2}\right)\right\}ds \tag{4.50}$$

where, *E* is the elasticity of the material of flagella, $I(z)$ is the area moment of inertia and $\vec{r}$ is the position vector of the small element *ds* on flagellum. The position vector of any point on the flagellum with respect to z-axis is considered as $\vec{r} = x\hat{i} + y\hat{j}$ .

The viscous forces ($dF_V$) is product of drag coefficient acting on element *ds* and elemental velocity component perpendicular to flagellum centerline. The viscous force on an element of length *ds* for helical wave propulsion, $dF_V$ is given by replacing *y* with $\vec{r}$ and *x* with *z* in equation (4.2) and is obtained as equation (4.51) :

$$dF_V = -C_n(z)\vec{v}_\perp ds \tag{4.51}$$

where, $C_n(z)$ is the local normal drag coefficient and $\vec{v}_\perp$ is the transverse velocity of the fluid relative to flagellum.

At steady state, the transverse velocity of the fluid relative to flagellum is given by equation (3.35) defined in section 3.4.1 as

$$\vec{v}_\perp = \omega\hat{k} \times \vec{r} = -y\omega\hat{i} + x\omega\hat{j} \tag{4.52}$$

where, where, $\omega$ is angular velocity of flagellum with respect to head of nanoswimmer and $\hat{i}$, $\hat{j}$, $\hat{k}$ are the unit vectors in $x$, $y$ and $z$ -direction, respectively.

With the same assumptions made in section 3.4.1, the viscous torque ($\tau$) tending to twist the flagellum about its own cross section is considered to be small and is of the order $O(4\pi\mu\ b^2\omega r)$ [26]. The twist effect due to torque $\tau$ is neglected for estimating the shape since the diameter of the flagellum is small compared to its length $L$.

At steady state swimming conditions, elastic bending forces $dF_E$ (equation 4.50) and viscous forces $dF_V$ (equation 4.51) balances each other on element *ds*. Equating elastic and viscous forces on a small element *ds* of flagellum gives

$$E\frac{\partial^2}{\partial z^2}\left(I(z)\frac{\partial^2\vec{r}}{\partial z^2}\right) = -C_n(z)\vec{v}_\perp \tag{4.53}$$

where, $I(z)$ is the area moment of inertia of any arbitrary cross-section and given as

$$I(z) = \frac{\pi b(z)^4}{4} \tag{4.54}$$

where, $b(z)$ is the radius of the cross section.

Simplifying equation (4.53), and substituting transverse velocity of flagellum from equation (4.52), in equation (4.53), gives

$$E\left\{I(z)\frac{\partial^4\vec{r}}{\partial z^4} + 2I'(z)\frac{\partial^3\vec{r}}{\partial z^3} + I''(z)\frac{\partial^2\vec{r}}{\partial z^2}\right\} = C_n(z)\left[y\omega\hat{i} - x\omega\hat{j}\right] \tag{4.55}$$

Substituting for $\vec{r} = x\hat{i} + y\hat{j}$ in equation (4.55) and separating $\hat{i}$ and $\hat{j}$ terms, we get

$$\begin{aligned} &E\left\{I(z)\frac{\partial^4 x}{\partial z^4} + 2I'(z)\frac{\partial^3 x}{\partial z^3} + I''(z)\frac{\partial^2 x}{\partial z^2}\right\}\hat{i} + E\left\{I(z)\frac{\partial^4 y}{\partial z^4} + 2I'(z)\frac{\partial^3 y}{\partial z^3} + I''(z)\frac{\partial^2 y}{\partial z^2}\right\}\hat{j} \\ &= C_n(z)\left[y\omega\hat{i} - x\omega\hat{j}\right] \end{aligned} \tag{4.56}$$

Equating $\hat{i}$ components on LHS and RHS in equation (4.56) and dividing it by $C_n(z)\omega$, we get

$$y = \frac{E}{C_n(z)\omega}\left\{I(z)\frac{\partial^4 x}{\partial z^4} + 2I'(z)\frac{\partial^3 x}{\partial z^3} + I''(z)\frac{\partial^2 x}{\partial z^2}\right\} \tag{4.57}$$

Similarly, equating $\hat{j}$ components on LHS and RHS in equation (4.56) and simplifying, we get

$$x = -\frac{E}{C_n(z)\omega}\left\{I(z)\frac{\partial^4 y}{\partial z^4} + 2I'(z)\frac{\partial^3 y}{\partial z^3} + I''(z)\frac{\partial^2 y}{\partial z^2}\right\} \tag{4.58}$$

where $I'(z)$ and $I''(z)$ in equations (4.57) and (4.58) are the first and second order space derivatives of $I(z)$.

Substituting, $x$ from equation (4.58) in equation (4.57), we get

$$y = -\left(\frac{E}{C_n(z)\omega}\right)^2 \left[\begin{array}{l} I(z)\frac{\partial^4}{\partial z^4}\left\{I(z)\frac{\partial^4 y}{\partial z^4} + 2I'(z)\frac{\partial^3 y}{\partial z^3} + I''(z)\frac{\partial^2 y}{\partial z^2}\right\} \\ + 2I'(z)\frac{\partial^3}{\partial z^3}\left\{I(z)\frac{\partial^4 y}{\partial z^4} + 2I'(z)\frac{\partial^3 y}{\partial z^3} + I''(z)\frac{\partial^2 y}{\partial z^2}\right\} \\ + I''(z)\frac{\partial^2}{\partial z^2}\left\{I(z)\frac{\partial^4 y}{\partial z^4} + 2I'(z)\frac{\partial^3 y}{\partial z^3} + I''(z)\frac{\partial^2 y}{\partial z^2}\right\} \end{array}\right] \tag{4.59}$$

Further simplifying equation (4.59), we get

$$y = -\left(\frac{E}{C_n(z)\omega}\right)^2 \left[\begin{array}{l} I^2(z)\frac{\partial^8 y}{\partial z^8} + 8I(z)I'(z)\frac{\partial^7 y}{\partial z^7} \\ + \left\{16I(z)I''(z) + 10I'^2(z)\right\}\frac{\partial^6 y}{\partial z^6} \\ + \left\{24I'(z)I''(z) + 20I(z)I'''(z)\right\}\frac{\partial^5 y}{\partial z^5} \\ + \left\{15I(z)I''''(z) + 20I'(z)I'''(z) + 6I''^2(z)\right\}\frac{\partial^4 y}{\partial z^4} \\ + \left\{10I'(z)I''''(z) + 4I''(z)I'''(z)\right\}\frac{\partial^3 y}{\partial z^3} \\ + I''(z)I''''(z)\frac{\partial^2 y}{\partial z^2} \end{array}\right] \tag{4.60}$$

In TN, radius of the flagellum cross-section is linearly varying over flagellum length ($L$) from $b_i$ (radius at $z = 0$) to $b_f$ (radius at $z = L$). The cross section radius $b(z)$, at any arbitrary section over the flagellum length (with linear taper assumption) at a distance $z$ from the proximal end (actuated end) i.e. $z = 0$, is given as

$$b(z) = b_i(kz + 1) \tag{4.61}$$

where, $b_i$ is the flagellum radius at $z = 0$ and $k = \left( \frac{b_f - b_i}{L\, b_i} \right)$ is the slope of linear taper. Substituting $b(z)$ from equation (4.61) in equation (4.54)

$$I(z) = \frac{\pi\, b_i^4 (kz+1)^4}{4} = I_o (kz+1)^4 \tag{4.62}$$

where, $I_o = \frac{\pi\, b_i^{\,4}}{4}$, is the area moment of inertia at proximal end. The cross-section radius at proximal and distal end of flagella are $b_i$ and $b_f$, respectively.

Differentiating $I(z)$ with respect to *z*, gives first order space derivative $I'(z)$ as

$$I'(z) = I_o (4k)(kz+1)^3 \tag{4.63}$$

Similarly, second $I''(z)$, third $I'''(z)$ and fourth order $I''''(z)$ space derivatives of equation (4.62), respectively are given as

$$I''(z) = I_o \left(12k^2\right)(kz+1)^2 \tag{4.64}$$

$$I'''(z) = I_o \left(24k^3\right)(kz+1) \tag{4.65}$$

$$I''''(z) = I_o \left(24k^4\right) \tag{4.66}$$

Substituting $I(z)$, $I'(z)$, $I''(z)$, $I'''(z)$ and $I''''(z)$ from equations (4.62), (4.63), (4.64), (4.65) and (4.66) respectively in equation (4.60) and simplifying, we get

$$y = -\left( \frac{EI_o}{C_n(z)\omega} \right)^2 \left[ \begin{array}{l} (kz+1)^8 \dfrac{\partial^8 y}{\partial z^8} + 32k(kz+1)^7 \dfrac{\partial^7 y}{\partial z^7} \\ + 352k^2(kz+1)^6 \dfrac{\partial^6 y}{\partial z^6} + 1632k^3(kz+1)^5 \dfrac{\partial^5 y}{\partial z^5} \\ + 3144k^4(kz+1)^4 \dfrac{\partial^4 y}{\partial z^4} + 2112k^5(kz+1)^3 \dfrac{\partial^3 y}{\partial z^3} \\ + 288k^6(kz+1)^2 \dfrac{\partial^2 y}{\partial z^2} \end{array} \right] \tag{4.67}$$

Equation (4.67) is the general equation for a linear tapered flagella executing a helical motion. Equation (4.67) is a variation of Legendre's linear equation, whose solution can be found by assuming another variable $\tau$ such that

$$\tau = \ln(kz+1) \tag{4.68}$$

Differentiating equation (4.68) with respect to *z* gives

$$\frac{d\tau}{dz} = \frac{k}{(kz+1)} \tag{4.69}$$

Multiplying numerator and denominator of equation (4.69) by *dy* and rewriting, we get

$$(kz+1)\frac{\partial y}{\partial z} = k\frac{dy}{d\tau} = kDy \tag{4.70}$$

where $D = \frac{d}{d\tau}$.

Further, differentiating equation (4.70) with respect to *z* to get second, third, fourth, fifth, sixth, seventh and eighth order space derivatives, we get

$$(kz+1)^2\frac{\partial^2 y}{\partial z^2} = k^2 D(D-1)y \tag{4.71}$$

$$(kz+1)^3\frac{\partial^3 y}{\partial z^3} = k^3 D(D-1)(D-2)y \tag{4.72}$$

$$(kz+1)^4\frac{\partial^4 y}{\partial z^4} = k^4 D(D-1)(D-2)(D-3)y \tag{4.73}$$

$$(kz+1)^5\frac{\partial^5 y}{\partial z^5} = k^5 D(D-1)(D-2)(D-3)(D-4)y \tag{4.74}$$

$$(kz+1)^6\frac{\partial^6 y}{\partial z^6} = k^6 D(D-1)(D-2)(D-3)(D-4)(D-5)y \tag{4.75}$$

$$(kz+1)^7\frac{\partial^7 y}{\partial z^7} = k^7 D(D-1)(D-2)(D-3)(D-4)(D-5)(D-6)y \tag{4.76}$$

$$(kz+1)^8\frac{\partial^8 y}{\partial z^8} = k^8 D(D-1)(D-2)(D-3)(D-4)(D-5)(D-6)(D-7)y \tag{4.77}$$

Substituting $\frac{\partial^2 y}{\partial z^2}, \frac{\partial^3 y}{\partial z^3}, \frac{\partial^4 y}{\partial z^4}, \frac{\partial^5 y}{\partial z^5}, \frac{\partial^6 y}{\partial z^6}, \frac{\partial^7 y}{\partial z^7}$ and $\frac{\partial^8 y}{\partial z^8}$ from equations (4.71) through to (4.77) in equation (4.67), we get characteristic equation

$$y = -\left(\frac{EI_o}{C_n(z)\omega}\right)^2 k^8\left[D^8 + 4D^7 + 2D^6 - 8D^5 - 7D^4 + 4D^3 + 4D^2\right]y \tag{4.78}$$

Dividing equation (4.78) with $\left(\frac{EI_o}{C_n(z)\omega}\right)^2 k^8$, we get

$$\frac{y}{\left(\frac{EI_o}{C_n(z)\omega}\right)^2 k^8} = -\left[D^8 + 4D^7 + 2D^6 - 8D^5 - 7D^4 + 4D^3 + 4D^2\right]y \qquad (4.79)$$

Further simplification of equation (4.79) gives

$$D^8 + 4D^7 + 2D^6 - 8D^5 - 7D^4 + 4D^3 + 4D^2 + \frac{1}{\left(\frac{EI_o}{C_n(z)\omega}\right)^2 k^8} = 0 \qquad (4.80)$$

Eight roots of auxiliary equation (4.80) is determined and the general solution of equation (4.67) is given as

$$y(z) = \sum_{i=1}^{8} A_i (kz+1)^{m_i} \qquad (4.81)$$

Substituting equation (4.81) back in equation (4.58), we get

$$x = -\frac{E}{C_n(z)\omega}\left[\begin{array}{l} I(z)\frac{\partial^4}{\partial z^4}\left\{\sum_{i=1}^{8} A_i (kz+1)^{m_i}\right\} \\ +2I'(z)\frac{\partial^3}{\partial z^3}\left\{\sum_{i=1}^{8} A_i (kz+1)^{m_i}\right\} \\ +I''(z)\frac{\partial^2}{\partial z^2}\left\{\sum_{i=1}^{8} A_i (kz+1)^{m_i}\right\} \end{array}\right] \qquad (4.82)$$

Substituting $I(z)$, $I'(z)$ and $I''(z)$ from equations (4.62), (4.63) and (4.64) respectively in equation (4.82) and simplifying, we get

$$x = -\frac{E}{C_n(z)\omega}\left[\begin{array}{l} I_o (kz+1)^4\left\{\sum_{i=1}^{8} A_i m_i (m_i-1)(m_i-2)(m_i-3)(kz+1)^{m_i-4}\right\} \\ +8I_o k(kz+1)^3\left\{\sum_{i=1}^{8} A_i m_i (m_i-1)(m_i-2)(kz+1)^{m_i-3}\right\} \\ +12I_o k^2 (kz+1)^2\left\{\sum_{i=1}^{8} A_i m_i (m_i-1)(kz+1)^{m_i-2}\right\} \end{array}\right] \qquad (4.83)$$

Further simplifying equation (4.83), we get *x*-*z* wave form of tapered flagellum executing helical wave

$$x(z) = -k^4 \left( \frac{EI_o}{C_n(z)\omega} \right) \sum_{i=1}^{8} A_i (m_i)(m_i - 1)(m_i + 1)(m_i + 2)(kz + 1)^{m_i} \qquad (4.84)$$

where, the eight coefficients $A_i$ ($i$ = 1 to 8) in equations (4.81) and (4.84) are calculated by substituting the boundary conditions given in next section and $m_1$ to $m_8$ are the eight roots of the auxiliary equation (4.80). Using boundary condition stated in equation (4.85), the mathematical models for performance indexes i.e. forward velocity $V_z$, angular velocity $\Omega$, thrust force $F_z$, torque $(M_z$ and $L_z)$ and propulsive efficiency $\eta$ of TN propelling through helical wave are developed in next section.

### 4.3.2 Modeling Performance Indexes in Helical Wave Propelled TN

For a helical wave propelled tapered flagellated nanoswimmer with the proximal end of the tail attached at the axis of rotation and rotating with a time dependent slope having maxima as $G$ at an angular frequency of ω (refer Figure 4.11, section 4.3.1), the boundary conditions considered are given as,

$$\text{Position } (x, y)\big|_{z=0} = (0,0) \qquad (4.85a)$$

which means displacement positions $x$ at $z = 0$ and $y$ at $z = 0$ is zero.

$$\text{Slope } \left( \frac{\partial x}{\partial z}, \frac{\partial y}{\partial z} \right)\Bigg|_{z=0} = (G\sin\omega t, G\cos\omega t) \qquad (4.85b)$$

Equation (4.85b) means slope at the base along $x$ and $y$ directions are $G\sin\omega t$ and $G\cos\omega t$, respectively. In equation (4.85b), $G$ is the measure of slope of helix.

$$\text{Bending moment } \left( \frac{\partial^2 x}{\partial z^2}, \frac{\partial^2 y}{\partial z^2} \right)\Bigg|_{z=L} = (0,0) \qquad (4.85c)$$

$$\text{Shear force } \left( \frac{\partial^3 x}{\partial z^3}, \frac{\partial^3 y}{\partial z^3} \right)\Bigg|_{z=L} = (0,0) \qquad (4.85d)$$

Equation (4.85c) and equation (4.85d) means that at the distal end the shear force and the bending moment vanishes, respectively.

The eight constants $A_i$, corresponding to equations (4.81) and (4.84), are calculated by substituting the boundary conditions given in equations (4.85), in equations (4.81) and (4.84), respectively. Substituting the boundary condition from equations (4.85a) in equation (4.81) and (4.84) we get

$$\sum_{i=1}^{8} A_i = 0 \tag{4.86a}$$

$$\sum_{i=1}^{8} A_i (m_i)(m_i - 1)(m_i + 1)(m_i + 2) = 0 \tag{4.86b}$$

Similarly substituting the second boundary condition from equation (4.85b) in equations (4.81) and (4.84) we get

$$\sum_{i=1}^{8} A_i m_i = \frac{G \cos \omega t}{k} \tag{4.86c}$$

$$\sum_{i=1}^{8} A_i (m_i^2)(m_i - 1)(m_i + 1)(m_i + 2) = \frac{G \sin \omega t}{k^5 \left( \frac{EI_o}{C_n(z)\omega} \right)^4} \tag{4.86d}$$

Similarly substituting the third boundary condition from equations (4.85c) in equation (4.81) and (4.84) we get

$$\sum_{i=1}^{8} A_i \, m_i (m_i - 1)(kL + 1)^{m_i - 2} = 0 \tag{4.86e}$$

$$\sum_{i=1}^{8} A_i (m_i^2)(m_i - 1)^2 (m_i + 1)(m_i + 2)(kL + 1)^{m_i - 2} = 0 \tag{4.86f}$$

Similarly substituting the fourth boundary condition from equations (4.85d) in equation (4.81) and (4.84) we get

$$\sum_{i=1}^{8} A_i \, m_i (m_i - 1)(m_i - 2)(kL + 1)^{m_i - 3} = 0 \tag{4.86g}$$

$$\sum_{i=1}^{8} A_i (m_i^2)(m_i - 1)^2 (m_i + 1)(m_i + 2)(m_i - 2)(kL + 1)^{m_i - 3} = 0 \tag{4.86h}$$

The equations (4.86a) to (4.86h) are combined and rewritten in form of matrix as

$$[M][A] = [Z] \tag{4.87}$$

where

$$[M]=\begin{Bmatrix} \sum_{i=1}^{8}1 \\ \sum_{i=1}^{8}(m_i)(m_i-1)(m_i+1)(m_i+2) \\ \sum_{i=1}^{8}m_i \\ \sum_{i=1}^{8}(m_i^2)(m_i-1)(m_i+1)(m_i+2) \\ \sum_{i=1}^{8}m_i(m_i-1)(kL+1)^{m_i-2}=0 \\ \sum_{i=1}^{8}(m_i^2)(m_i-1)^2(m_i+1)(m_i+2)(kL+1)^{m_i-2}=0 \\ \sum_{i=1}^{8}m_i(m_i-1)(m_i-2)(kL+1)^{m_i-3}=0 \\ \sum_{i=1}^{8}(m_i^2)(m_i-1)^2(m_i+1)(m_i+2)(m_i-2)(kL+1)^{m_i-3} \end{Bmatrix}$$

$$[A]=\begin{bmatrix} A_1 \\ A_2 \\ A_3 \\ A_4 \\ A_5 \\ A_6 \\ A_7 \\ A_8 \end{bmatrix}, \text{ and } [Z]=\begin{bmatrix} 0 \\ 0 \\ \frac{G\cos\omega t}{k} \\ \frac{G\sin\omega t}{k^5\left(\frac{EI_o}{C_n(z)\omega}\right)^4} \\ 0 \\ 0 \\ 0 \\ 0 \end{bmatrix}$$

Equation (4.87) is used to obtain coefficient matrix $[A]$ and is given as

$$[A]=[M]^{-1}[Z] \tag{4.88}$$

where $[M]^{-1}$ is the inverse of matrix $[M]$. By solving equation (4.88), we obtained eight constants (i.e. $A_1$ to $A_8$). A MATLAB code was written to calculate inverse of the matrix $[M]$. Using these eight constants, steady state shape of wave in flagellum is obtained. On obtaining the steady state shape by solving equations (4.81) and (4.84) in *x* and *y*, imposing the boundary conditions, the propulsion parameters are estimated using RFT. The steady state shapes obtained are arbitrary curves in space and are helixes of variable amplitude and pitch. The method developed in section 3.4.2 to evaluate the instantaneous pitch angle and amplitude of these curves and can be utilized to derive the propulsive dynamics of any arbitrary shape in space.

The instantaneous pitch angle $\beta(z)$ and amplitude $\alpha(z)$ are defined in equations (3.61) and (3.62), and rewritten here for continuity sake

$$\tan\beta(z) = \frac{1}{\vec{r}}\left| x.\frac{dy}{dz} - y.\frac{dx}{dz} \right| \tag{4.89}$$

$$\alpha(z) = |\vec{r}| = \sqrt{x^2 + y^2} \tag{4.90}$$

For an element of the tail of length '$ds$' at a distance of $z$ from the base, the pitch angle and amplitude are evaluated using equations (4.89) and (4.90), respectively. The local normal i.e. $dF_n(z)$ and longitudinal components i.e. $dF_l(z)$ of the force on such an element due to forward and transverse displacements of the element are vectorial summation of components of forces and are obtained by replacing $C_n$ and $C_l$ in equations (3.67) and (3.68), respectively with $C_n(z)$ and $C_l(z)$ and are given as

$$dF_n(z) = C_n(z)\left(V_z \sin\beta - V_\theta \cos\beta\right) ds \tag{4.91}$$

$$dF_l(z) = C_l(z)\left(V_z \cos\beta + V_\theta \sin\beta\right) ds \tag{4.92}$$

where, $C_n(z)$ and $C_l(z)$ are the local normal and tangential drag coefficients and $V_z$ and $V_\theta$ are the swimming velocity in the $z$ and $\theta$ directions, respectively, $V_z \sin\beta$ and $V_\theta \cos\beta$ are velocity components in *n*-direction and $V_z \cos\beta$ and $V_\theta \sin\beta$ are velocity components in *l*-direction. The flagellum rotates counter-clockwise when viewed from positive $z$ axis.

For the cylindrical element with radius $a(z)$ in a medium having viscosity $\mu$, the local normal and longitudinal drag coefficients, $C_n(z)$ and $C_l(z)$ respectively, are obtained from equation (4.33) and equation (4.34) by replacing $C_n(x)$ with $C_n(z)$; $C_l(x)$ with $C_l(z)$; and $b(x)$ with $b(z)$ and are given as

$$C_n(z) = \frac{4\pi\mu}{\ln\left(\frac{L}{b(z)}\right) + 0.5} \tag{4.93}$$

$$C_l(z) = \frac{2\pi\mu}{\ln\left(\frac{L}{b(z)}\right) - 0.5} \tag{4.94}$$

These coefficients are constant throughout the length for a flagellum with uniform diameter as $a$ is constant, whereas in case of a tapered flagellum, the cross-section radius $b$ is varying along flagellum length and is function of $b(z)$.

When the tail moves with an angular velocity of $\omega$, the reaction of fluid gives rise to an angular velocity $\Omega$ in the opposite direction [27]. This rotation gives rise to a linear velocity of $V_\theta = |\vec{r}|(\omega - \Omega)$, $\Omega$ is the angular velocity of the head with respect to the ground. The propulsive forces on the flagellum element *ds* in $z$-direction i.e. $dF_z(z)$ and $\theta$-direction i.e. $dF_\theta(z)$ are determined by using equations (3.71) and (3.72), and are given as

$$dF_z(z) = -\left[dF_n(z)\sin\beta + dF_l(z)\cos\beta\right] \tag{4.95}$$

$$dF_\theta(z) = \left[dF_l(z)\sin\beta - dF_n(z)\cos\beta\right] \tag{4.96}$$

Substituting normal and longitudianl force components, $dF_n(z)$ and $dF_l(z)$ respectively from equations (4.91) and (4.92), in equation (4.95), the net thrust force i.e. $dF_z(z)$ on the flagellum element is obtained and is given as

$$dF_z(z) = -\left[C_n(z)(V_z\sin\beta - V_\theta\cos\beta)\sin\beta + C_l(z)(V_\theta\sin\beta + V_z\cos\beta)\cos\beta\right]ds \tag{4.97}$$

Similarly substituting normal and longitudianl force components from equations (4.91) and (4.92), in equation (4.96), the net circumferential force i.e. $dF_\theta(z)$ on the flagellum element is obtained and is given as

$$dF_\theta(z) = \left[C_l(z)(V_z\cos\beta + V_\theta\sin\beta)\sin\beta - C_n(z)(V_z\sin\beta - V_\theta\cos\beta)\cos\beta\right]ds \tag{4.98}$$

The length of element $ds$ is given by

$$ds = \frac{\sqrt{1+\cos^2\beta\left(\frac{dy}{dx}\right)^2}}{\cos\beta}dz \tag{4.99}$$

For small amplitudes, $\left(\frac{dy}{dx}\right)^2$, can be neglected and equation (4.99) is reduced to

$$ds = \sec\beta\ dz \tag{4.100}$$

Substituting $ds = \sec\beta\ dz$ from equation (4.100) in equation (4.97) and equation (4.98), the net thrust force $dF_z(z)$ and the net circumferential force $dF_\theta(z)$ on flagellum element is given as

$$dF_z(z) = -\begin{Bmatrix} C_n(z)(V_z \sin\beta - V_\theta \cos\beta)\sin\beta \\ + C_l(z)(V_\theta \sin\beta + V_z \cos\beta)\cos\beta \end{Bmatrix} \sec\beta\, dz \qquad (4.101)$$

$$dF_\theta(z) = \begin{Bmatrix} C_l(z)(V_z \cos\beta + V_\theta \sin\beta)\sin\beta \\ - C_n(z)(V_z \sin\beta - V_\theta \cos\beta)\cos\beta \end{Bmatrix} \sec\beta\, dz \qquad (4.102)$$

Simplifying equation (4.101) and equation (4.102), we get

$$dF_z(z) = -\{C_n(z)(V_z \sin\beta - V_\theta \cos\beta)\tan\beta + C_l(z)(V_\theta \sin\beta + V_z \cos\beta)\}dz \qquad (4.103)$$

$$dF_\theta(z) = \{C_l(z)(V_z \cos\beta + V_\theta \sin\beta)\tan\beta - C_n(z)(V_z \sin\beta - V_\theta \cos\beta)\}dz \qquad (4.104)$$

The net circumferential force on the flagellum element causes torque about the axis of rotation and has two components $(\text{i.e. } dM_z(z) \text{ and } dL_z(z))$. The first of these arise due to rotation of the element about the axis of rotation i.e. $z$ axis i.e. $dM_z(z)$ and is given as

$$dM_z(z) = \vec{r} \times dF_\theta(z) \qquad (4.105)$$

Substituting circumferential force from equations (4.104) in equation (4.105), we obtain

$$dM_z(z) = \alpha(z)\{C_l(z)(V_z \cos\beta + V_\theta \sin\beta)\tan\beta - C_n(z)(V_z \sin\beta - V_\theta \cos\beta)\}dz \qquad (4.106)$$

The second torque component i.e. $dL_z(z)$ is a result of rotation of the element about its own centerline and is given by

$$dL_z(z) = 4\pi\mu\ b(z)^2(\omega - \Omega)\cos\beta\, dz \qquad (4.107)$$

The drag force on a spherical head of radius $r_h$ moving in a medium with viscosity $\mu$ is given as

$$F_{head} = 6\pi\ \mu\, r_h\, V_z \qquad (4.108)$$

Also the torque experienced by a spherical head of radius $r_h$ rotating in a medium with viscosity $\mu$ is given as

$$M_{head} = 8\pi\mu\ r_h{}^3\ \Omega \qquad (4.109)$$

Under steady swimming conditions the velocity $V_z$ is constant. The total thrust force developed by the flagellum is equal to the drag experienced by the head. The total thrust

force is obtained by integrating i.e. $dF_z(z)$ over total length of flagellum from 0 to $L$. Equating that with drag force $F_{head}$ for steady state motion, we get

$$\int_0^L dF_z(z) - F_{head} = 0 \tag{4.110}$$

Similarly, under steady swimming conditions, the net torque generated by the flagellum is equal in magnitude to the torque experienced by the head. The net torque is obtained by integrating $[dM_z(z) + dL_z(z)]$ over total length of flagellum from 0 to $L$ and is given by

$$\int_0^L \{dM_z(z) + dL_z(z)\} = M_{head} \tag{4.111}$$

Substituting the $dF_z(z)$ from equation (4.103) and $F_{head}$ from equation (4.108) in equation (4.110), we get

$$-\int_0^L \begin{Bmatrix} C_n(z)(V_z \sin\beta - V_\theta \cos\beta)\tan\beta \\ + C_l(z)(V_\theta \sin\beta + V_z \cos\beta) \end{Bmatrix} dz - 6\pi\,\mu\, r_h\, V_z = 0 \tag{4.112}$$

Substituting the $dL_z(z)$ and $dM_z(z)$ from equations (4.106) and (4.107), respectively and $M_{head}$ from equation (4.109), in equation (4.111), we get

$$\int_0^L \alpha(z) \begin{Bmatrix} C_l(z)(V_z \cos\beta + V_\theta \sin\beta)\tan\beta \\ - C_n(z)(V_z \sin\beta - V_\theta \cos\beta) \end{Bmatrix} dz + 4\pi\mu\, a(z)^2(\omega - \Omega)\cos\beta dz = 8\pi\mu\, r_h{}^3\Omega \tag{4.113}$$

Substituting $V_\theta = |\vec{r}|(\omega - \Omega)$ in equation (4.112) and separating $V_z$, $\omega$ and $\Omega$ terms, we get

$$\begin{aligned} &-V_z \int_0^L [C_n(z)\sin\beta\tan\beta + C_l(z)\cos\beta + 6\pi\,\mu\, r_h]dz \\ &+\omega \int_0^L [\{C_n(z) - C_l(z)\} r \sin\beta]dz - \Omega \int_0^L [\{C_n(z) - C_l(z)\} r \sin\beta]dz = 0 \end{aligned} \tag{4.114}$$

Similarly substituting $V_\theta = |\vec{r}|(\omega - \Omega)$ in equation (4.113) and separating $V_z$, $\omega$ and $\Omega$ terms, we get

$$
\begin{aligned}
&-\int_0^L \alpha(z)\sin\beta\{C_n(z)-C_l(z)\}V_z\,dz \\
&-\int_0^L \begin{Bmatrix} \alpha^2(z)\ C_l(z)\sin\beta\tan\beta+\alpha^2(z)\ C_n(z)\cos\beta \\ +4\pi\mu\, a^2(z)\cos\beta+8\pi\mu\, r_h{}^3 \end{Bmatrix}\Omega\,dz \\
&-\int_0^L \{\alpha^2(z)\ C_l(z)\sin\beta\tan\beta+\alpha^2(z)\ C_n(z)\cos\beta+4\pi\mu\, a^2(z)\cos\beta\}\omega\,dz=0
\end{aligned}
\tag{4.115}
$$

Integrating equations (4.114) and (4.115) along the length of the flagellum and simplifying the resulting simultaneous equations, we get

$$V_z[I_5+I_6-6\pi\mu\, r_h]+\Omega[I_1]=\omega[I_1] \tag{4.116}$$

$$V_z[-I_1]+\Omega[I_2+I_3+I_4-8\pi\mu\, r_h{}^3]=\omega[I_2+I_3+I_4] \tag{4.117}$$

where the integrals $I_1$ to $I_6$ in equations (4.116) and (4.117) are defined as

$$I_1=\int_0^L[\{C_n(z)-C_l(z)\}\alpha(z)\sin(\beta)]\,dz,$$

$$I_2=\int_0^L C_l(z)\left(-\alpha^2(z)\sin\beta\tan\beta\right)dz,$$

$$I_3=\int_0^L -\left(C_n(z)\alpha^2(z)\cos\beta\right)dz,$$

$$I_4=\int_0^L\left(-4\pi\mu\, a^2(z)\cos\beta\right)dz,$$

$$I_5=\int_0^L -C_n(z)\sin\beta\tan\beta\,dz,$$

$$I_6=\int_0^L -C_l(z)\cos\beta\,dz$$

Rewriting equations (4.116) and (4.117) in form of matrix, we get

$$\begin{Bmatrix} I_5+I_6-6\pi\mu\, r_h & I_1 \\ -I_1 & I_2+I_3+I_4-8\pi\mu\, r_h^3 \end{Bmatrix}\begin{bmatrix} V_z \\ \Omega \end{bmatrix}=\omega\begin{bmatrix} I_1 \\ I_2+I_3+I_4 \end{bmatrix} \tag{4.118}$$

Equation (4.118) is the mathematical model for performance index forward velocity $V_z$ and angular velocity $\Omega$ for helical wave propelled TN. The values of $V_z$ and $\Omega$, obtained by taking inverse and solving equation (4.118), are used to calculate the efficiency of the nanoswimmer.

The efficiency ($\eta$) of the nanoswimmer is calculated as the ratio of useful power developed for forward motion along $z$ axis to total power consumed by the nanoswimmer for transverse and forward motion. Useful power developed is obtained by integrating the product of force $(dF_z)$ and velocity $V_z$ over flagellum length. Similarly the total power dissipated by the swimmer is power required to overcome the rotational resistance of tapered flagellum.

$$\eta = \frac{\int_0^L dF_z V_z}{M_{head}\,\Omega + \int_0^L dM_z \omega} \tag{4.119}$$

Equations (4.118) and (4.119) are simulated in next section to investigate the performance of TFN propelled by helical waves. The results obtained after simulations are analyzed and discussed in the following section.

### 4.3.3 Simulations, Results and Discussion of Performance of Helical Wave Propelled TN

The simulations of the mathematical model developed for displacement shapes (refer Figure 4.11) in equation (4.81) and (4.84), and, forward velocity $(V_z)$ and efficiency $(\eta)$ in equations (4.118) and (4.119) for tapered flagellated nanoswimmer (TN) is carried out in MATLAB®. The MATLAB code is given in Appendix-V.

The tail is discretized in 100 elements around which the solution converges. The values of parameters chosen for the simulation are similar to that of *E coli* as these microorganisms use helical wave propulsion methods. The length of the flagellum is $10\,\mu m$, the frequency of helical wave is varied from 100 Hz – 500 Hz, and the viscosity of the medium $\mu$ is 0.001 *Pa-s*. The proximal end diameter $2b_i$ is 30 nm and $2b_f$ is varied from 0 to $2b_i$ in order to find the optimum value. Characteristic length (i.e. *L*/*l*) is varied from 1 to 10 by varying the modulus of elasticity, E from 0.01 - 200 GPa. In real life situations, the value of characteristic length is constrained by the elasticity of available bio-compatible [28] materials; the diameter of flagella is governed by the width of the targeted area inside the body, the blood viscosity inside our body and the frequency of motor can be adjusted to meet the optimum values of characteristic length.

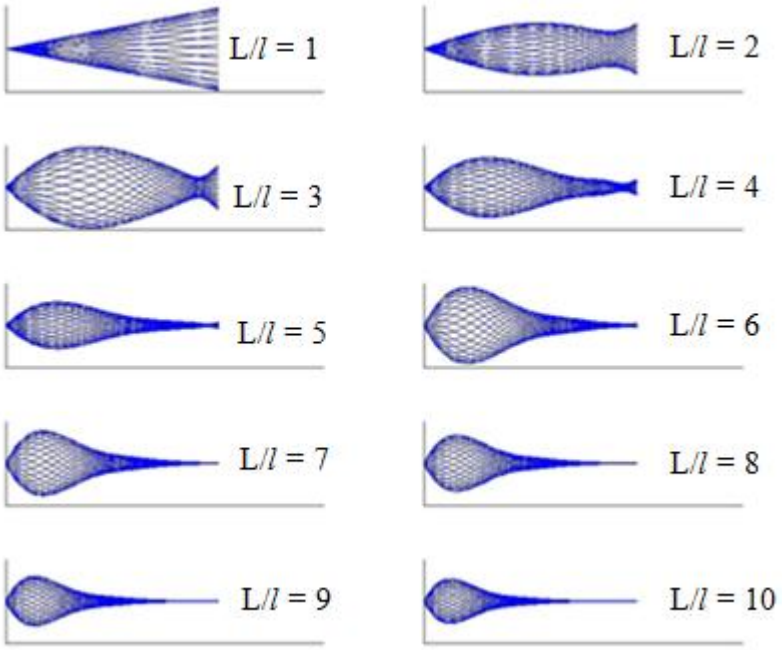


**Figure 4.11: Displacement shapes with respect to characteristic length (*L*/*l*)**

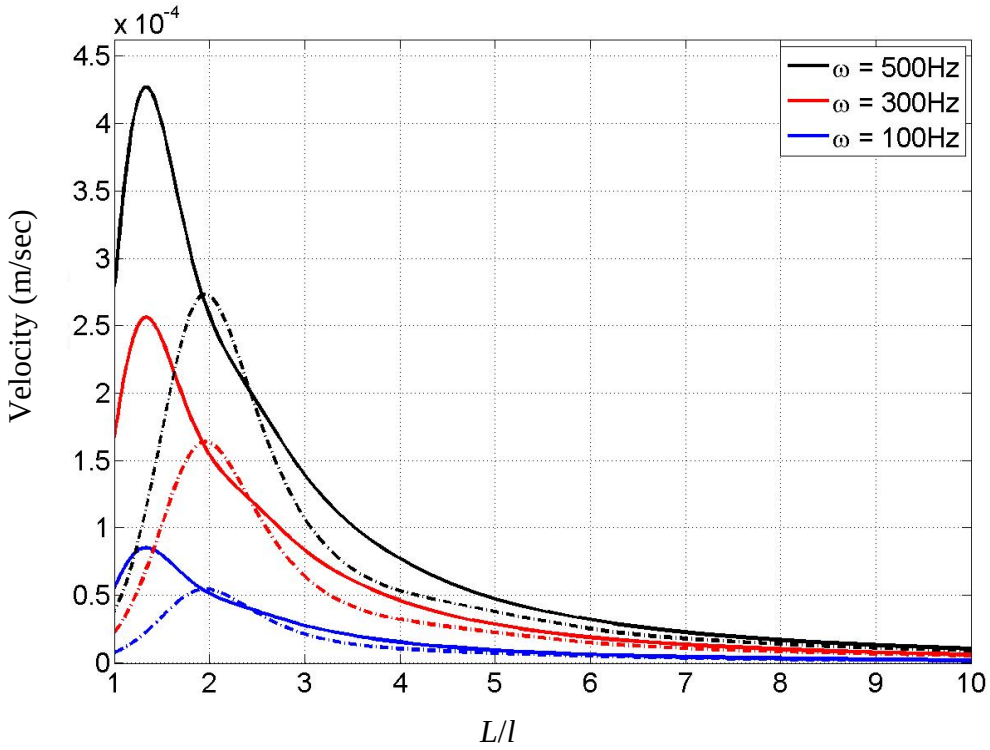


**Figure 4.12: Variation of velocity over $L/l$ ratio for different frequencies. The dotted lines correspond to uniform diameter flagellum case and the solid lines correspond to the tapered flagellum.**

Equation (4.118) is simulated for parameters given in Table 3.2, section 3.4.3 and the results obtained are plotted in Figure 4.12. Figure 4.12 illustrates the swimming velocity ($V_z$) variation over ($L/l$) ratio for three different actuation frequencies i.e. 100 Hz, 300 Hz and 500 Hz. It shows consistent increase in velocity as frequency increases and compares the swimming velocity of TN with UDN. For ($r_h/L$) = 0.34, a tapered flagellum with a taper ratio ($b_i/b_f$) = 5.88 shows higher velocity values as compared with uniform diameter flagellum. Similar trends have been observed for uniform diameter flagellum [29-30]. It shows, for TN swimming velocity is maximum for ($L/l$)~1.33, whereas the maxima of velocity is shifted for UDN and maximum swimming velocity occurs at $(L/l) \approx 1.8$, irrespective of flagella actuation frequency. The peak velocity increases linearly with increase in flagellum actuation frequency and a maximum velocity of 427.4 $\mu m$/sec is observed at a higher actuation frequency of 500Hz (refer Figure 4.12). The maximum velocity generated increases five times from 85.45 $\mu m/\sec$ at 100 Hz to 427.4 $\mu m/\sec$ at 500 Hz. It is observed that as the ratio ($L/l$) increases, the length of the active filament reduces which results in a greater passive length. As passive length does not contribute to total thrust generated by flagellum but instead contribute in drag force, a better design of nanoswimmer is to have ($L/l$) ratio in between 1.33 to 1.8. For longer filaments, i.e., at higher values of ($L/l$), the velocity approaches to zero.

The variation of velocity with variation in parameters like $b_i/b_f$, $r_h/L$ and $L/l$ are plotted in Figure 4.13. The maximum velocity obtained is 85.45 $\mu m/\sec$ and is found at $L/l$ ~1.33, $r_h/L$~ 0.34 and a taper ratio $b_i/b_f$ ~5.88. In Figure 4.13-A, contour plot of variation of velocity with respect to variation in $r_h/L$ and $L/l$ is plotted for $b_i/b_f$ = 5.88. Variation of $L/l$ is plotted on $x$-axis and $r_h/L$ is varied on $y$-axis. The family of curves for velocity are obtained by simulation of equation (4.116) and found closed contour as shown in Figure 4.13-A. The innermost contour represents a range of $r_h/L$ and $L/l$ corresponding to maximum velocity. It is observed that the velocity remains close to maximum for variation of $r_h/L$ from 0.26 to 0.42 whereas for a UDN, the maxima of velocity is observed at $r_h/L$~ 0.3 [24]. The range of $L/l$ corresponding to maximum velocity is from 1.33 to 1.72.

In Figure 4.13-B, contour plot of variation in velocity is plotted for variation of $b_i/b_f$ and $L/l$ ratio for $r_h/L$ = 0.34. Variation of $L/l$ is plotted on $x$-axis and $b_i/b_f$ is varied on $y$-axis. The innermost contour represents a range of $b_i/b_f$ and $L/l$ corresponding to maximum velocity.

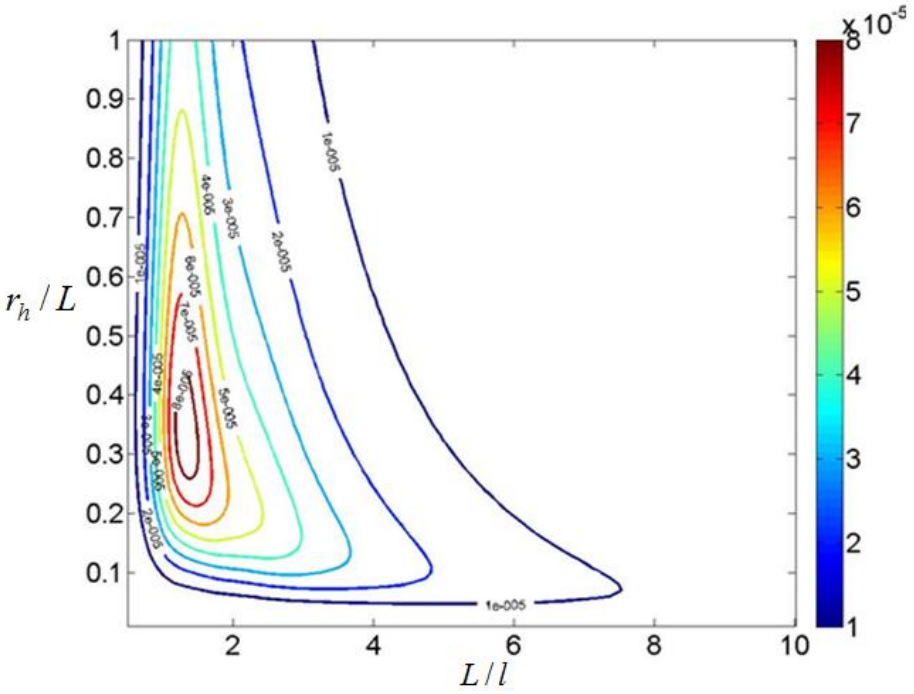


**Figure 4.13-A: Contour plot of velocity with variation in $r_h/L$ and L/$l$ ratio at $b_i/b_f$ = 5.88. The inner most contour represents the optimal range of $r_h/L$ and L/$l$ ratio for higher velocity.**

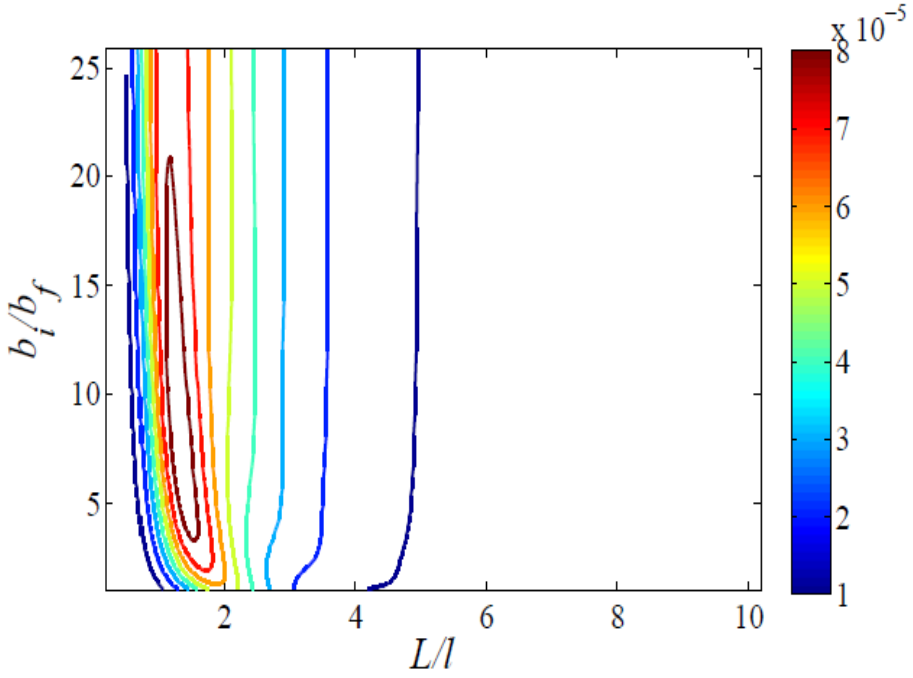


**Figure 4.13-B: Contour plot of velocity with variation in $b_i/b_f$ and L/$l$ ratio at $r_h/L$ = 0.34. The inner most contour represents the optimal range of $b_i/b_f$ and L/$l$ ratio for higher velocity.**

The inner most contour in Figure 4.13-B illustrates that the velocity remains close to maximum for $b_i/b_f$ varying from 2.7 to 21.2 and corresponding range of $L/l$ is from 1.33 to 1.72. The contour plots of velocity show that for $L/l > 2$, the velocity is observed to be maximum for a taper ratio ~0 (i.e. pointed end). The maximum velocity observed for a pointed end (i.e. flagellum with taper ratio ~0) is 64.59 $\mu m/\sec$ at $L/l$ = 1.33 whereas for a taper ratio~1, i.e. uniform diameter flagellum, the velocity observed 54.6μm/s at $L/l$ ratio ~ 2 [21, 24].

The variation of efficiency with variation in parameters like $b_i/b_f$, $r_h/L$ and $L/l$ are plotted in Figure 4.14. The maximum efficiency obtained is 0.58% and is found at $L/l$ ~1.85, $r_h/L$ ~ 0.28 and taper ratio $b_i/b_f$ ~3.57.

In Figure 4.14-A, contour plot of variation of efficiency with respect to variation in $r_h/L$ and $L/l$ is plotted for $b_i/b_f$ = 3.57. Variation of $L/l$ is plotted on $x$-axis and $r_h/L$ is varied on $y$-axis. The family of curves for efficiency are obtained by simulation of equation (4.119) and found closed contour as shown in Figure 4.14-A. The innermost contour represents a range of $r_h/L$ and $L/l$ corresponding to maximum efficiency. It is observed that the efficiency remains close to maximum for variation of $r_h/L$ from 0.25 to 0.45. The range of $L/l$ corresponding to maximum efficiency is from 1.33 to 1.72.

Figure 4.14-B illustrates the effect of taper ratio ($b_i/b_f$) and characteristic length ($L/l$) on the efficiency of nanoswimmer. The efficiency is close to maximum for the variation of taper ratio ($b_i/b_f$) from 2.3 to 5.4. The maximum efficiency observed for a pointed end (i.e. taper ratio ~0) is 0.51% at $L/l$ = 2.38, as compared to 0.36% at $L/l$ ratio ~ 2.5 for uniform diameter flagellum (i.e. taper ratio ~1).

In order to obtain an optimum taper ratio, distal end diameter $2b_f$ is varied from 0 to proximal end diameter, $2b_i$. The variation of velocity and efficiency over taper ratio $b_i/b_f$ for different characteristic lengths $L/l$ are shown in Figure 4.13 and Figure 4.14, respectively. The velocity is found to be maximum at $L/l \approx 1.4$ for $b_i/b_f \approx 5.88$, whereas the maxima of efficiency lies at $L/l \approx 1.8$ for $b_i/b_f \approx$ 3.57 with a head radius 3 $\mu m$.

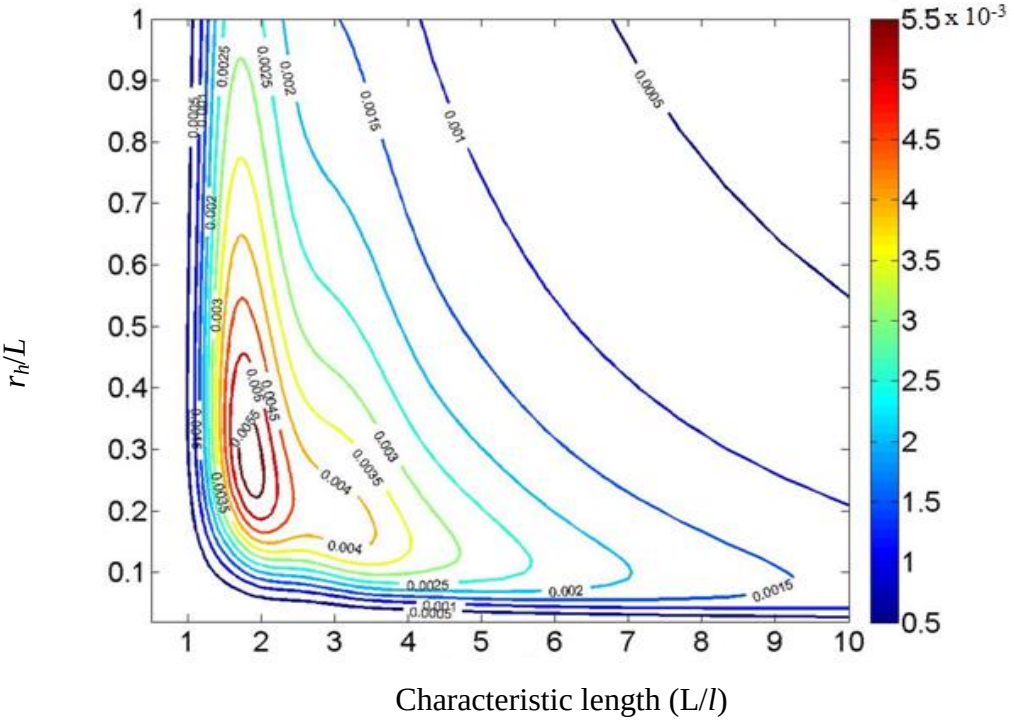


**Figure 4.14-A: Contour plot of efficiency with variation in $r_h/L$ and L/$l$ ratio at $b_i/b_f$ = 3.57. The inner most contour represents the optimal range of $r_h/L$ and L/$l$ ratio for higher efficiency.**

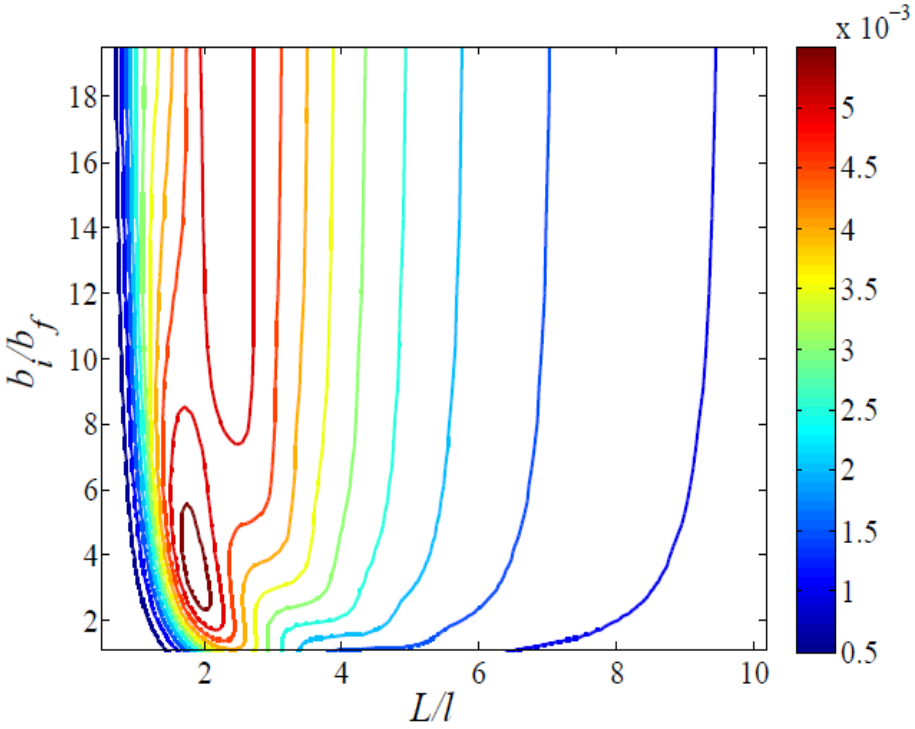


**Figure 4.14-B: Contour plot of efficiency with variation in $b_i/b_f$ and L/$l$ ratio at $r_h/L$ = 0.34. The inner most contour represents the optimal range of $b_i/b_f$ and L/$l$ ratio for higher efficiency.**

It can be seen from the Figure 4.13 and Figure 4.14 that the velocity and efficiency for $b_f \sim b_i$ i.e. uniform flagellated nanoswimmer, are small compared to the maximum values that can be obtained by having a taper. The optimal range of taper ratio for a fastest nanoswimmer lies between 2.7 to 21.2 (refer Figure 4.13-B) and for the most efficient swimmer the taper ratio lies in between 2.3 to 5.4 (refer Figure 4.14-B). Thus, a tapered flagellum is faster and efficient than the uniform diameter.

Velocity and efficiency is plotted against characteristic length (L/*l*) with varying head sizes in Figure 4.13 and Figure 4.14 and this corroborates the findings of Chwang and Wu [31]. As observed from the plots, single helically waving flagellum cannot swim unless it is attached to a head that moves relative to it. It is observed from Figure 4.14-B that the velocity is maximum for head size of $r_h/L$ = 0.33 at L/*l* =1.4 while the efficiency is maximum for head size of $r_h/L$ = 0.37 at L/*l* =1.8. The maximum velocity and the maximum efficiency values observed are 84.5 $\mu$m/sec and 0.57%, respectively. The optimum parameters for both the cases (i.e. the fastest swimmer and the most efficient swimmer) obtained at frequency of 100 Hz are enlisted in Table 4.4.

In the present section, the mathematical model for the forces, velocity, and efficiency, was developed considering a case of the helical wave propelled TN. The next section gives conclusion on propulsion of a TN using a PWP and HWP modes.

**Table 4.4: Results - Velocity and Efficiency**

| | ***Tapered Diameter*** | | ***Uniform Diameter*** | |
|---|---|---|---|---|
| **Parameters** | **Fastest swimmer** | **Efficient swimmer** | **Fastest swimmer** | **Efficient swimmer** |
| $b_i/b_f$ | 5.88 | 3.7 | 1 | 1 |
| $2b_i$ **(nm)** | 30 | 30 | 30 | 30 |
| $2b_f$ **(nm)** | 5.1 | 8.1 | 30 | 30 |
| $L/l$ | 1.4 | 1.8 | 2 | 2.5 |
| $V$ **(µm/s)** | 84.5 | 69.9 | 55.4 | 40.1 |
| **Efficiency** $(\eta)$ | 0.46% | 0.57% | 0.24% | 0.38% |

## 4.4 TAPERED NANOSWIMMER: COMPARISON OF PLANAR WAVE AND HELICAL WAVE PROPULSION MODES

For propulsion of a nanoswimmer, the elastic flagellum is subjected to either a planar wave or a helical wave by varying the mode of propulsion. The quest that still needs to be investigated is which of the two propulsion modes should be preferred for a tapered nanoswimmer. In the present section, the two modes of propulsion, namely planar wave and helical wave, have been compared for a tapered nanoswimmer based on their performance indexes (i.e., velocity and efficiency).

The simulations of the mathematical model developed for forward velocity and efficiency in equations (4.48) and (4.49) for tapered nanoswimmer (TN) propelled through planar wave propulsion, and in equations (4.118) and (4.119) for tapered nanoswimmer propelled through helical wave propulsion is carried out in MATLAB®. The simulation parameters chosen are listed in Table 4.1, section 4.2.3.

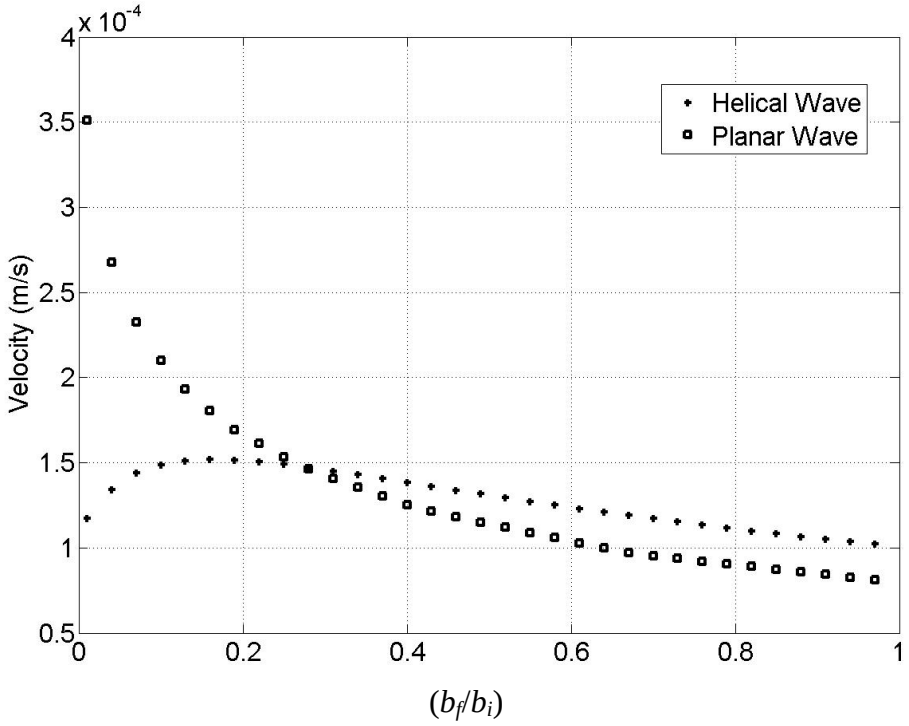


**Figure 4.15: Plot of velocity for planar and helical wave propulsion modes obtained for different taper ratio**

The length of the flagellum, $L$ is 50 µm, the proximal end diameter, $2b_i$ is 400 nm, the frequency of actuation is 35Hz and the viscosity of the medium $\mu$ is taken as 0.001 *Pa.s*. The ratio of head radius to flagellar length, $r_h/L$ is assumed to be 0.3 [14].

Figure 4.15 shows the effect of taper ratio on velocity for planar and helical wave propulsions. It has been observed that for a taper ratio less than 3.34 (i.e., $b_i / b_f \langle 3.34$), the helical wave propulsion outperforms the planar wave propulsion, whereas beyond this point, the planar wave propulsion is faster than the helical wave propulsion.

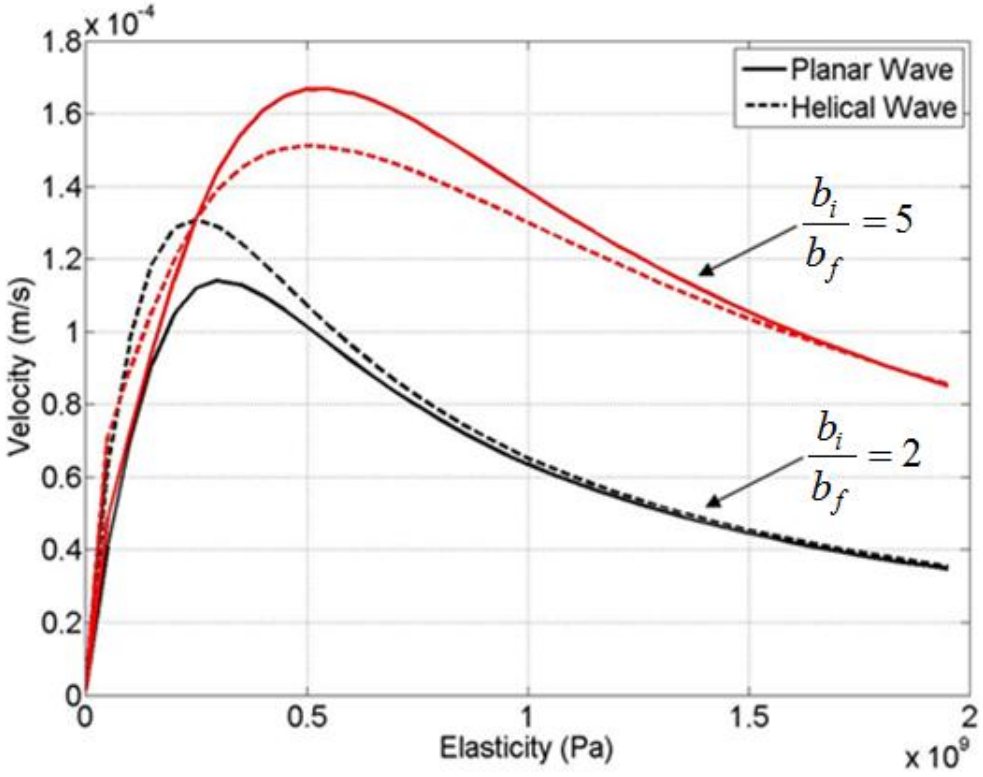


**Figure 4.16: Velocity over parametric variation of elasticity as a function of taper ratio and propulsion modes**

Keeping the geometric parameters same, the variation of velocity and efficiency over flagella elasticity for planar wave and helical wave propulsion has been plotted in Figure 4.16 and Figure 4.17, respectively. The maximum velocity of tapered nanoswimmer with the planar wave propulsion is found to be 166.8μm/s whereas the maximum velocity for the helical wave propulsion is found to be 151.9μm/s at a larger taper ratio of 5.

Figure 4.17 illustrates the variation of efficiency over elasticity for a taper ratio of 5. In the range of simulation for $E$ varying from 0.1MPa to 2GPa, efficiency of a nanoswimmer propelling through planar wave is always greater than the one propelling through helical wave.

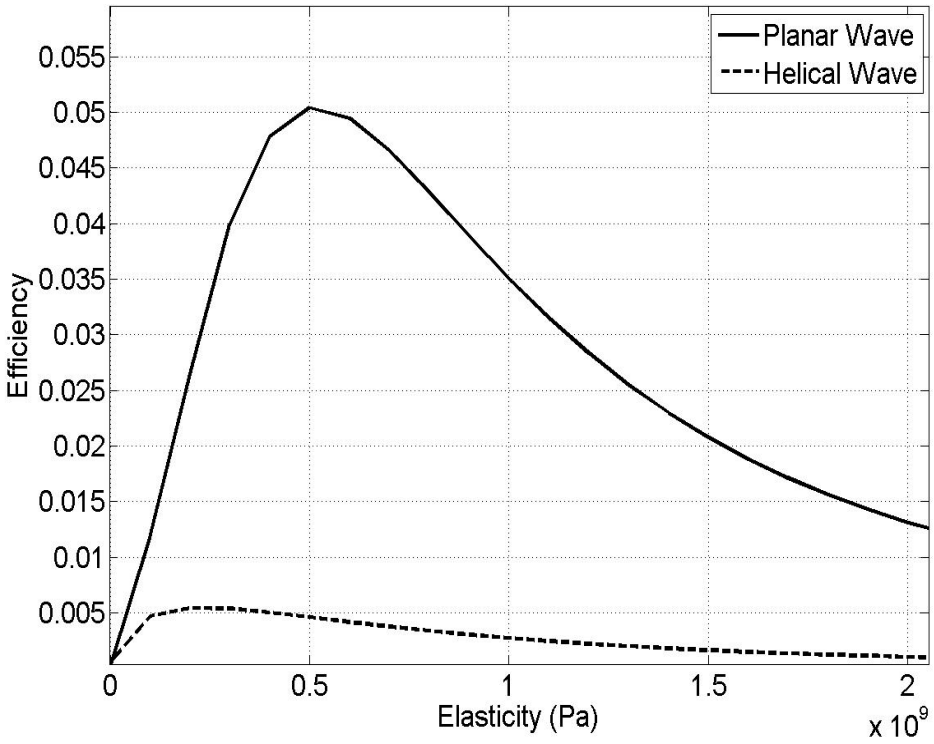


**Figure 4.17: Efficiency over parametric variation of elasticity as a function of propulsion modes for taper ratio $b_i/b_f$ = 5**

Planar wave propulsion gives a higher value of maximum efficiency ~5.01% when elasticity is around ~ 500MPa, while the maximum efficiency of helical wave propulsion is only ~0.55%, which is obtained at lower elasticity ~200MPa. The efficiency values are in agreement with previously reported values for a uniform flagellum [11], [14].

**Table 4.5: Comparison of planar wave propulsion with helical wave propulsion**

| | **Planar wave propulsion** | | **Helical wave propulsion** | |
|---|---|---|---|---|
| Taper ratio ( $b_i / b_f$ ) | 5 | 2 | 5 | 2 |
| $2b_i$ (nm) | 400 | 400 | 400 | 400 |
| $r_h/L$ | 0.3 | 0.3 | 0.3 | 0.3 |
| Maximum velocity (μm/s) | 166.8 | 114.1 | 151.9 | 128.8 |
| Maximum efficiency ($\eta$) | 5.01% | 3.33% | 0.55% | 0.50% |

## 4.5 CONCLUSIONS

In this Chapter, planar wave propulsion (PWP) and helical wave propulsion (HWP) with tapered nanoswimmer (TN) are modeled and simulated. The propulsion characteristics in terms of swimming speed and efficiency have been optimized for the fastest swimmer and for the efficient swimmer. The results were compared to that of a UDN and velocity and efficiency results show that the TN is a better choice than the UDN.

Mode shapes of a planar wave propelled TN are predicted based on elastohydrodynamic equations. Keeping the flagellum volume constant, two new cases are developed for a given ratio of initial and final diameter. Results indicate that for a given frequency, the velocity and efficiency ratio for TN to UDN propelled through planar wave can go as high as 3.2 times and 3.75 times respectively. The maximum efficiency of the taper case is almost double the maximum efficiency of the uniform diameter case. Considering this the tapered flagellum gives a more realistic value of the performance indicators that has not been shown or attempted in literature.

The maximum velocity of a helical wave propelled TN is 85.45μm/s as compared to 55.65μm/s for a uniform diameter flagellum. The maximum efficiency observed is 0.57% for a tapered flagellum and 0.38% for a uniform diameter flagellum. The optimal taper ratio and head size are found for both the fastest swimmer and the most efficient swimmer. The velocity is found to maximum at L/$l$~1.33, $r_h$/L ~0.34 and at a taper ratio ~5.88 whereas the efficiency is found maximum at L/$l$~1.85, $r_h$/L ~ 0.28 and taper ratio ~3.57. From the results, it is seen that the optimal range for head radius, characteristic length and taper ratio are (0.3-0.4), (1.33-2.1) and (3.57-5.88), respectively for a TN propelling itself through HWP. The maximum velocity and efficiency observed for tapered flagellated nanoswimmer through helical wave propagation are $85.45\,\mu m/\sec$ and 0.57%, respectively.

Tapered flagellated nanoswimmer propelling through a helical wave has been also compared with a planar wave. Results indicate that a tapered flagellated nanoswimmer propelling though planar wave is more efficient than the one propelling through helical wave for all taper ratios. At an actuation frequency of 35 Hz, the efficiency of planar wave is nearly ten times larger than that of helical wave. However, the simulation results for velocity show that for a taper ratio less than 3.34 (i.e., $b_i / b_f \langle 3.34$), the helical wave propulsion is faster, whereas beyond this point, the planar wave propulsion is superior.

**References**


1. Requicha AAG (2003) Nanorobots, NEMS, and Nanoassembly, Proc. IEEE, 91 (11), pp. 1922-1933.
2. Freitas RA Jr. (1999) Nanomedicine, Vol. I: Basic Capabilities, Landes Bioscience, 1999, http://www.nanomedicine.com.
3. Gray J, and Hancock GJ (1955) The Propulsion of Sea-Urchin Spermatozoa, J Exp Biol, 32, pp. 802-814.
4. Machin KE (1958) Wave Propagation along Flagella, J Exp Biol, 35, pp.796-806.
5. Brennen C, and Winet H (1977) Fluid Mechanics of Propulsion by Cilia and Flagella, Ann Rev Fluid Mech, 9, pp. 339-98.
6. Wiggins CH, and Goldstein RE (1998) Flexive and Propulsive Dynamics of Elastica at Low Reynolds Number, Phy Rev Lett, 80, pp. 3879-3882.
7. Lauga E, and Powers TR (2009) The Hydrodynamics of Swimming Microorganisms, Reports on Progress in Physics, 72(9), pp. 1-58.
8. Majumdar R, Rathore JS, and Sharma NN (2009) Simulation of Swimming Nanorobots in Biological Fluids, Proc 4th International Conference on Autonomous Robots and Agents (ICARA 2009), 10-12 Feb. Wellington, New Zealand, pp. 79-82.
9. Rathore JS, and Sharma NN (2010) Engineering Nanorobot: Chronology of Modeling Flagellar Propulsion. J Nanotechnol Eng Med, Transactions of the ASME 1(3) 031001, pp. 1-6.
10. Hoshikawa H, and Kamiya R (1985) Elastic Properties of Bacterial Flagellar Filaments: II. Determination of the Modulus of Rrigidity, Biophys Chem, 22(3), pp. 159-166.
11. Behkam B, and Sitti M (2006) Design Methodology for Biomimetic Propulsion of Miniature Swimming Robots, Journal of Dynamics Systems, Measurements, and Control, Transactions of the ASME, 128, pp. 36-43.
12. Rathore JS, Majumdar R, and Sharma NN (2012) Planar wave propagation through a tapered flagellated nanoswimmer, IEEE Transactions on Nanotechnology, 11(6), pp.1117-1121.
13. Braun M (1992) Differential Equations and Their Applications. 4th Ed., New York: Springer-Verlag, ch. 2.

14. Lauga E (2007) Floppy Swimming: Viscous Locomotion of Actuated Elastica, Physical Review E, 75(041916), pp.1-16.

15. Daniel ST (2008) Motion at low Reynolds number. Dissertation, Massachusetts Institute of Technology, Cambridge.

16. Rikmenspoel R (1965) The Tail Movement of Bull Spermatozoa: Observation and Model Calculation, Biophys J, 5, pp. 365-392.

17. Kotesa RS, Rathore JS, and Sharma NN (2013) Tapered Flagellated Nanoswimmer: Comparison of Helical Wave and Planar Wave Propulsion. BioNanoScience, Springer, 3(4), pp. 343-347.

18. Leifson E (1960) Atlas of Bacterial Flagellation, *Academic Press, New York and London*.

19. Gauthier M, Truchon D, and Rainville S (2008) Taking Control of the Flagellar Motor" La Physique AU Canada, 64(3), pp. 135-137.

20. Ammar ED, Fulton D, Meulia X, Bai T, and Hogenhout SA (2004) An attachment tip and pili-like structures in insect- and plant-pathogenic spiroplasmas of the class Mollicutes, Arch Microbiol, 181:97–105, DOI 10.1007/s00203-003-0630-8.

21. Tam LW, Dentler WL, and Lefebvre PA (2003) Defective flagellar assembly and length regulation in LF3 null mutants in Chlamydomonas, The Journal of Cell Biology, 163(3), pp.597-607.

22. Fawcett DW (1981) The Cell, 2nd Edition, W B Saunders Company, Ch 14.

23. Gaffney EA, Gadˆelha1 H, Smith DJ, Blake JR, and Kirkman-Brown JC (2011) Mammalian sperm motility: Observation and theory, annual reviews of fluid mechanics, 43, pp.501-28.

24. Riedel-Kruse IH, Hilfinger A, Howard J, and Jülicher F (2007) How molecular motors shape the flagellar beat, 1 (3), pp.192-208.

25. Lindemann C (1996) Functional significance of the outer dense fibers of mammalian sperm examined by computer simulations with the geometric clutch model, Cell Motil. Cytoskeleton 34(4), pp. 258-270.

26. Powers TR (2002) Role of Body Rotation in Bacterial Flagellar Bundling, Phy Rev E, 65: 040903, pp. 1-4.

27. Wooley DM, and Vernon GG (2001) A study of helical and planar waves on sea urchin sperm flagella, with a theory of how they are generated, The Journal of Experimental Biology, 204, pp.1333-1345.

28. Majumdar R, Neha S, Rathore JS, and Sharma NN (2013) In Search of Materials for Artificial Flagella of Nanoswimmers. Journal of Materials Science, Springer, 48(1), pp.240-250.

29. Lowe CP (2003) Dynamics of Filaments: modeling the dynamics of driven microfilaments, Phil. Trans. R. Soc. Lond., 358, pp. 1543-1550.

30. Lagomarsino MC, Capuani F, and Lowe CP (2003) A Simulation Study of the Dynamics of a Driven Filament in an Aristotelian Fluid, Journal of Theoritical Biology, 224, pp. 215-224.

31. Chwang AT, and Wu TY (1971) A Note on Helical Movement of Microorganisms, Proc. R. Soc. London, Ser. B, 178, pp.327-346.

# Chapter 5

# Flagella Material Selection

## 5.1 INTRODUCTION

Biomedical applications of nanoswimmer are revolutionary with potential use in localized drug delivery [1]. Nanoswimmers are propulsion mechanisms of nanorobots, where intense engineering research is going on to bio-mimic flagellar microorganisms consisting of a head and flagella. Propulsion models for such nanoswimmers are developed which contributes to the study of its dynamics and efficiency [2-6]. The model assumes the flagella generating the propulsive force either by executing a planar or by a helical wave motion. In Chapter 3 and Chapter 4, we have developed various models of planar and helical wave propulsion for uniform diameter and tapered diameter flagellum design. To evaluate the performance of a nanoswimmer, researchers [7-8] proposed a dimensionless parameter, Sperm number (*Sp*), which characterizes the relative magnitudes of the viscous and bending forces. Scaled-up validation of the model using Sperm number is also done [9-10], but attempts to actual fabrication of nanoswimmers reported in literature are very few [11-14].

In previous chapters (i.e. Chapter 3 and 4), mathematical modeling and analysis is carried out for both planar wave and helical wave propulsion with uniform diameter nanoswimmer (UDN) in Chapter 3 and more realistic tapered nanoswimmer (TN) in Chapter 4, using RFT. In the present chapter, motivated by targeted drug delivery system with the help of nanoparticles [15] and the intricacies of biology inspired nano-engineering [16-17], we search for materials that can be used for the practical realization of flagellar nanoswimmers. Material choice is an important and integral part of the design and must be explored for any device. Nanoswimmers are also no exemptions and needs suitable material for exploring the design perspective. Although [18] proposed plexiglas or rigid plastics as candidates, the proposed materials had no basis to screen for biocompatibility or check if nanostructures can be manufactured from it. Although researchers in [19-20] proposed PDMS and PEG-DA as the biocompatible materials for flagella, their adaptability as flagellar structure needs to be assessed with respect to other parameters like flexural rigidity too. Based on the modeling of

nanoswimmer carried out in Chapter 3 and 4, in this chapter, a methodology is proposed for assessing the candidature of any material for the fabrication of artificial flagella, which shall have implant capabilities *in vivo* and shortlist the potential material for a feasible design of nanoswimmer. To manufacture a bio-mimicked nanoswimmer, the physical properties of the biological organism are studied. Based on the derived values, engineering materials having properties in the said range are screened. Keeping in mind *in vivo* medical applications, biocompatibility study of the material is an essential part of screening that has been done. Thereafter, looking at the possible manufacturing techniques, fabrication feasibility of such biocompatible materials as nanostructure is presented in section 5.2. The methodology has not been reported in earlier in literature and was first proposed by us and published in [21].

## 5.2 METHODOLOGY

The present section proposes materials suitable for making the flagellum of a nanoswimmer. The findings in this chapter are based on the approach of screening hierarchy in context to flexure modulus followed by hemocompatibility and later technology feasibility. A literature review of the various stages of the framework discussed in the methodology is carried out leading to chosen material for design. We start with more than 500 materials given in Springer's materials handbook [22] and categorized them as metals, composites and polymers. Out of 500 materials given in materials handbook, 237 materials are found relevant in present context, which are enlisted in Appendix-VI. Around 36 engineering materials in the flexural modulus range ($E$ = 0.01 MPa to 10 GPa) is sorted out from the listed 237 materials (see Appendix-VI). The flexural modulus range under consideration is from $10^{-24}$ to $10^{-21}$ $Nm^2$. In the second-stage biocompatibility, specifically hemocompatibility, of the screened 36 materials was evaluated based on available literature. Finally, looking at the present set of manufacturing processes, fabrication feasibility of screened/shortlisted materials was assessed.


**Figure 5.1: Framework for material selection**

The like criteria for selection of material for fabrication of nanoswimmer are based on a three-stage screening process. The framework for selection specific to nanoswimmer is described in a flowchart as given in Figure 5.1. The conditions for acceptance with respect to these three stages, viz., physical property, biocompatibility, and technical feasibility of any particular material are elaborated below.

### 5.2.1 Physical Properties

The mathematical model in literature models the flagella as a beam. The model takes the flexural rigidity (*EI*) as the physical parameter of the beam. The value is in the range of $10^{-24}$ to $10^{-21}$ $Nm^2$ [18], [23]. Considering the microorganism that has flagellar diameter around 200 nm [1] the flexural modulus of the material is obtained in the range of 0.01 MPa to 10 GPa.

Given the range of modulus values, shortlisting was done for all the enlisted materials in Appendix-VI [22]. Mostly, polymers appeared in the shortlisting. Metal-alloys are not included in this study as their flexural moduli vary with respect to the composition of constituents. For polymers, flexure modulus was available, and for the rest elastic modulus was considered for screening the initial list.

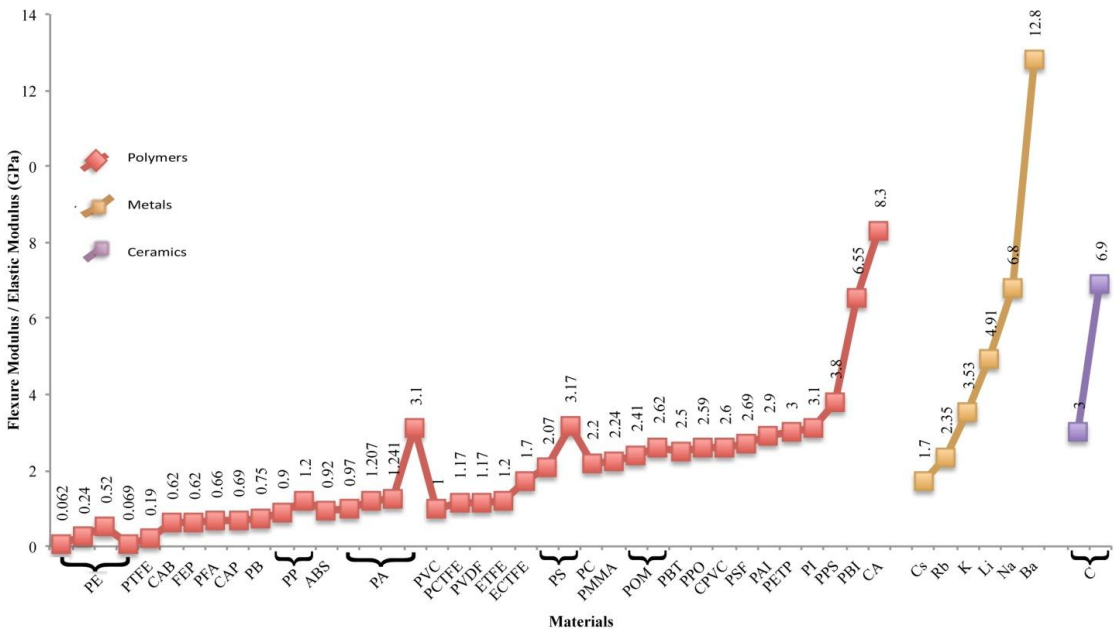


**Figure 5.2: Flexural/Elastic modulus of materials after stage 1 screening**

The screened materials are shown in Figure 5.2 where *x*-axis enlists the abbreviation of the common name (elaborately written in Table 5.1) of the material, and *y*-axis indicates the flexural or elastic modulus of the corresponding material. A few ceramics and metals also quantifies as potential material of choice for fabrication of nanoswimmer. Various grades and isomers of particular polymers are separately considered in Figure 5.2 and are clubbed together in Table 5.1. The screened 36 materials are enlisted in Table 5.1 in increasing order of their elastic modulus. The selection of these 36 materials are marked with ✓in Appendix-VI.

**Table 5.1: 36 materials screened after stage 1**

| S.No. | Materials | S.No. | Materials | S.No. | Materials | S.No. | Materials |
|---|---|---|---|---|---|---|---|
| **1** | POLYETHYLENE (PE) | **10** | POLYAMIDE NYLON 6 (PA) | **19** | POLYOXYMETHYLENE (POM) | **28** | POLYBENZENE-IMIDAZOLE (PBI) |
| **2** | POLYTETRAFLUROETHYLENE (PTFE) | **11** | POLYVINYL CHLORIDE (PVC) | **20** | POLYBUTADIENE TEREPHTALATE (PBT) | **29** | CELLULOSE ACETATE (CA) |
| **3** | CELLULOSE ACETATE-BUTYRATE (CAB) | **12** | POLYTRIFLUOROCHLOROETHYLENE (PCTFE) | **21** | POLYPHENYLENE OXIDE (PPO) | **30** | CESIUM (Cs) |
| **4** | FLUORINATED ETHYLENE PROPYLENE (FEP) | **13** | POLYVINYLIDENE FLUORIDE (PVDF) | **22** | CHLORINATED POLYVINYL CHLORIDE (CPVC) | **31** | RUBIDIUM (Rb) |
| **5** | PERFLUORINATED ALKOXY (PFA) | **14** | ETHYLENE TETRAFLUOROETHYLENE (ETFE) | **23** | POLYSULFONE (PSF) | **32** | POTASSIUM (K) |
| **6** | CELLULOSE ACETATE-PROPIONATE (CAP) | **15** | ETHYLENE CHLOROTRIFLUOROETHYLENE (ECTFE) | **24** | POLYAMIDE-IMIDE (PAI) | **33** | LITHIUM (Li) |
| **7** | POLYBUTYLENE (PB) | **16** | POLYSTYRENE (PS) | **25** | POLYETHYLENE TEREPHTALATE (PETP) | **34** | SODIUM (Na) |
| **8** | POLYPROPYLENE (Isotactic/Atactic) (PP) | **17** | POLYCARBONATE (PC) | **26** | POLYIMIDE (PI) | **35** | BARIUM (Ba) |
| **9** | ACRYLONITRILE BUTADIENE STYRENE (ABS) | **18** | POLYMETHYL METHACRYLATE (PMMA) | **27** | POLYPHENYLENE SULFIDE (PPS) | **36** | GRAPHITE (C) |

The shortlisted 36 materials with their properties are tabulated in Table 5.2. These 36 materials should next pass the test of bio (hemo) compatibility as the nanoswimmer objective may be to swim inside the body in blood. This is carried out in next section.

### 5.2.2 Biocompatibility

Biocompatibility deals with the study of any material's characteristics and its form and function, while it interacts with another biological system. There are various standards to ensure the acceptability of the results of the study performed on the material [24]. One of them is "The standard for biological evaluation of medical devices - ISO 10993," which deals with the various biocompatibility aspects. Although reports of the biocompatibility test conducted according to ISO 10993 [25], were not available in compiled form in any single publication for the screened materials, a thorough literature survey throws enough light on issues of their biocompatibility and medical usage. The findings are tabulated in Table 5.2. The column titled "Biocompatibility Test Protocol" discusses the type of testing protocol, carried out by researchers and available in different publication viz., *in vitro or in vivo* followed during biocompatibility assessment. The materials that qualify *in vivo* tests become more favorable candidates of choice for material for fabrication of nanoswimmer. Another major issue, is the fabrication feasibility even if the material passes the flexural rigidity and biocompatibility criteria of selection. Table 5.2 includes the possibility of fabrication with the chosen material. This is further discussed in next section.

### 5.2.3 Technology Feasibility

There are established technologies to produce nanowires and similar nanostructure [26-27]. The methods used for producing flagellar nanostructures of the above-screened materials are also looked into the literature and reported under column entitled "Technology Feasibility". The observations are compiled and commented in Table 5.2.

**Table 5.2: Biocompatibility and Technology Feasibility of various materials**

| S.No. | Materials | Biocompatibility Test Protocol | | | Technology Feasibility | | Remarks |
|---|---|---|---|---|---|---|---|
| | | *In vivo* | *In vitro* | Reference | Process used and Reference | Dia(nm) | |
| 1 | POLYETHYLENE (PE) | ✓ | ✓ | Belanger and Marois 2001[28] | Electrospinning<br>Rein et al. 2007 [29] | 250 -12000 | • LDPE (Low Density Polyethylene) biocompatibility is studied as suitable reference materials<br>• High Molecular Weight PE can be electrospun. |
| 2 | POLYTETRAFLUROETHYLENE (PTFE) | - | ✓ | Risbud MV et al. 2001[30]<br>Ainslie et al. 2006[31] | Jet Blown fibrils<br>Borkar et al. 2006 [32] | 20-30 | • PTFE /wollastonite composite (90:10) static incubation assay contact did not lead to hemolysis thus exhibiting preliminary haemocompatibility. |

| S.No. | Materials | Biocompatibility Test Protocol | | | Technology Feasibility | | Remarks |
|---|---|---|---|---|---|---|---|
| | | *In vivo* | *In vitro* | Reference | Process used and Reference | Dia(nm) | |
| | | | | | | | • Application in areas which require high rigidity and are subject to elevated temperatures. |
| 3 | CELLULOSE ACETATE-BUTYRATE (CAB) | ✓ | ✓ | Ocular Inserts Nilay et al. 2008[33], Mucoadhesivity Miyazaki et al. 2002 [35] | Twin-screw extruder Polyester/CAB immiscible polymer blends used Li et al. 2010 [36] | 179 | • Mostly used as microcapsules for drug delivery[33].<br>• Haemocompatibility not tested.<br>• The diameters of nanofibers obtained by twin-screw extruder are smaller than those via electrospinning.<br>• The blend would have different physical properties than CAB hence cross verification of the flexure rigidity of the blend needs to be checked. |
| 4 | FLUORINATED ETHYLENE PROPYLENE (FEP) | - | - | Not available | Melt blending and Melt spinning. Chen et al. 2006 [37] | 10-20 | • Haemocompatibility not tested.<br>• Used as coating<br>• Nanocomposite fibers based on Flourinated Multiwalled CNT (carbon nano tube) and a FEP copolymer. |
| 5 | PERFLUORINATED ALKOXY (PFA) | - | - | Not available | | | |
| 6 | CELLULOSE ACETATE-PROPIONATE (CAP) | - | ✓ | Gomes et al. 2007 [38] | Not available | | • Titanium coated with CAP was assessed as a low cost substitute for surface modification to make it an attractive substrate for cell and protien adhesion<br>• Grafted material would have different physical property than CAP. |
| 7 | POLYBUTYLENE (PB) | - | - | Not available | Twin-screw extruder Xiao et al. 2010 [39] Grafting Ramos et al. 2011 [40] | 137 | • Haemocompatibility not tested.<br>• PB/CNF (Carbon Nanofibres) potential applications as smart (electrorheological) fluids<br>• Polybutylene Terephthalate(PBT)/CAB immiscible polymer blends used for twin screw extrusion<br>• The blend and compound would have different physical properties than PB<br>• Polybutylene oxide grafted on CNF. |

| S.No. | Materials | Biocompatibility Test Protocol | | | Technology Feasibility | | Remarks |
|---|---|---|---|---|---|---|---|
| | | *In vivo* | *In vitro* | Reference | Process used and Reference | Dia(nm) | |
| 8 | POLYPROPYLENE (Isotactic/Atactic) (PP) | - | ✓ | Contreras-García et al. 2011 [401] | Twin-screw extruder<br>Wang et al. 2007 [42] | 75-375 | • improve the hemocompatibility and elution of antimicrobial agents for medical devices, N,N′-dimethylacrylamide (DMAAm) and N-isopropylacrylamide (NIPAAm) were sequentially grafted onto PP<br>• functionalized PP has potential as hemo- and cyto-compatible materials<br>• Isotactic polypropylene (iPP) Nano fiber |
| 9 | ACRYLONITRILE BUTADIENE STYRENE (ABS) | - | - | Not available | | | |
| 10 | POLYAMIDE NYLON 6 (PA) | - | ✓ | Risbud and Bhonde 2001 [43] | Electrospinning Bagheri et al. 2010 [44] | 100-200 | • Biocompatibility test data demonstrates it favourable for tissue engineering.<br>• Priliminary blood compatibility observes no detectable hemolysis in static incubation assay.<br>• solid phase microextraction (SPME) fiber was fabricated |
| 11 | POLYVINYL CHLORIDE (PVC) | - | ✓ | Rhodes et al. 1996 [45]<br>Balakrishnan and Jayakrishna 2000 [46] | Electrospinning<br>Lee et al. 2002 [47]<br>template based fabrication<br>Martín et al. 2012 [48] | | • Blood profusion model made to investigate platelet activation, granulocyte secretion, complement activation and contact phase activation of silicone, PVC and Nylon.<br>• PVC was the most platelet compatible material but caused most contact phase activation.<br>• PEGylated (Polyethyelene Glycol) PVC improves haemocompatibility |
| 12 | POLYTRIFLUORO CHLOROETHYLE NE (PCTFE) | - | - | Not available | | | |
| 13 | POLYVINYLIDEN E FLUORIDE (PVDF) | ✓ | ✓ | *In vivo*<br>Laroche et al. 1995[49]<br>*In vitro*<br>Chang et al. 2011[50] | Electrospinning<br>Choi et al. 2003 [51] | 250 | • identified the effects of various manufacturing processes on the crystalline microstructure, mechanical properties, and biocompatibility of PVDF |

| S.No. | Materials | Biocompatibility Test Protocol | | | Technology Feasibility | | Remarks |
|---|---|---|---|---|---|---|---|
| | | *In vivo* | *In vitro* | Reference | Process used and Reference | Dia(nm) | |
| | | | | | | | • *in vivo* thoracoabdominal bypass in a series of dogs.<br>• hemocompatible nature of grafted PEGylated polymers by controlling grafting structures gives them great potential in the molecular design of antithrombogenic membranes for use in human blood |
| 14 | ETHYLENE TETRAFLUOROETHYLENE (ETFE) | - | - | Not available | | | |
| 15 | ETHYLENE CHLOROTRIFLUOROETHYLENE (ECTFE) | ✓ | - | *In vivo* Wortman et al. 1983 [52] | Not available | | • Results indicate that cell adherence varies according to the type of material. |
| 16 | POLYSTYRENE (PS) | ✓ | ✓ | *In vitro and in vivo* Molugu et al. 2006 [53]<br>*In vivo* Anderson et al. 2010 [54] | Vacuum assisted infiltration<br>McCarthy et al. 2011 [55] | 200 | • Ocular and skin sensitivity, oral ingestion and inhalation studies done.<br>• nanoparticles may be safe for use as antibacterial agents<br>• Fluorescence Imaging of mouse<br>• Fluorescent magnetic PS nanowire produced |
| 17 | POLYCARBONATE (PC) | - | ✓ | Schohn et al. 1986 [56] | Lithography-assisted template bonding<br>Yoon et al. 2008 [57]<br>Novel electrospinning<br>Liao et al. 2011 [58] | 50000<br>221-1536 | • Haemodialysis treatments<br>• During dialysis with the polycarbonate membrane hypoxemia does not occur and the pulmonary vascular resistances and pulmonary arterial pressure remain stable.<br>• Template directed methods guide the nanostructure growth; in addition, they offer low temperature processing conditions such as electrochemical deposition in a liquid phase for specific applications.<br>• Bisphenol A polycarbonate has superior mechanical properties |
| 18 | POLYMETHYL METHACRYLATE (PMMA) | ✓ | ✓ | Thomson et al. 1992 [59] | Electrospinning<br>Czaplewski et al. 2003 [60]<br>Vapor Deposition Polymerization (VDP) | 85-350<br>100 | • Biocompatibility of PMMA as bone cement evaluated by exposing to human synovial fibroblasts and mouse peritoneal macrophages |

| S.No. | Materials | Biocompatibility Test Protocol | | | Technology Feasibility | | Remarks |
|---|---|---|---|---|---|---|---|
| | | *In vivo* | *In vitro* | Reference | Process used and Reference | Dia(nm) | |
| | | | | | Lee et al. 2006 [61]<br>radical-mediated dispersion polymerization<br>Kong and Jang 2008 [62] | | • Inflammatory potential noted from *in vitro* experiments but *in vivo* intra-articular injection of the particles into mouse knee joints well torlerated.<br>• Ag/PMMA nanofiber had an excellent biocidal potential against Gram-positive bacteria (*S. aureus*) as well as Gram-negative bacteria (*E. coli*)<br>• Haemocompatibility needs to be checked.<br>• organic-dye embedded PMMA by VDP<br>• Ag/PMMA Nanofibre by radical mediated dispersion polymerization |
| 19 | POLYOXYMETHYLENE (POM) | - | ✓ | Vitral Farinazzo et al. 2010 [63] | Electrospinning<br>Kongkhlang et al. 2008 [64] | | • Nanoporous structure gives high specific surface area<br>• Control parameter for desired fibre diameter and nanoporosity is discussed.<br>• Increase in tensile strength might make it unuseful for flagellar material<br>• study of nitric oxide (NO) cellular production for evaluating cytotoxic potential |
| 20 | POLYBUTADIENE TEREPHTALATE (PBT) | - | - | Not available | | | |
| 21 | POLYPHENYLENE OXIDE (PPO) | - | - | Not available | | | |
| 22 | CHLORINATED POLYVINYL CHLORIDE (CPVC) | - | - | Not available | High voltage electrospinning<br>Sang et al. 2007 [65] | | • CPVC nonwoven mat is used for water purification. |
| 23 | POLYSULFONE (PSF) | - | ✓ | Khang et al. 1995[66] | Electrospining<br>Zhibin et al. 2008 [67] | | • Platelet adhesion experiments on surface treated PSF films were carried out<br>• Chinese hamster ovary in vivo test highlights surface wettability of PSF as very important parameter for cell adhesion and growth<br>• Haemocompatibility not tested.<br>• PSF used for stiffening agent for carbon fibre epoxy composit |

| S.No. | Materials | Biocompatibility Test Protocol | | | Technology Feasibility | | Remarks |
|---|---|---|---|---|---|---|---|
| | | *In vivo* | *In vitro* | Reference | Process used and Reference | Dia(nm) | |
| 24 | POLYAMIDE-IMIDE (PAI) | - | ✓ | Imai et al. 1983 [68] | Novel electrospinning Lee et al. 2009 [69] | 200-1000 | • Structure - biocompatibility relationship of condensation polymers studied by cell culture method.<br>• *In vivo* heamocompatibility needs to be done |
| 25 | POLYETHYLENE TEREPHTALATE (PETP) | - | ✓ | De Brito Alves et al. 2003 [70] | Electrospinning Nanofiber mats prepapred Ma et al. 2004 [71] | 200-600 | • computer vision coupled with SEM was used to monitor the platelet adhesion and activation onto blood-contacting materials<br>• surface modification of PETP nanomats to mimic the fibrous proteins in native extracellular matrix towards constructing a biocompatible surface for endothelial cells |
| 26 | POLYIMIDE (PI) | - | ✓ | Richardson Jr. et al. 1993 [72] | Electrospinning Fukushima et al. 2010 [73] | 33±5 | • evaluated in vitro using a selected battery of levels I and II testing protocols<br>• good candidates for further testing as encapsulants for implantable biosensors.<br>• ultrafine beadfree nanofibers |
| 27 | POLYPHENYLENE SULFIDE (PPS) | - | - | Not available | | | |
| 28 | POLYBENZENE-IMIDAZOLE (PBI) | - | - | Not available | | | |
| 29 | CELLULOSE ACETATE (CA) | ✓ | - | Zhou et al. 2011 [74] | Electrospinning Zhang et al. 2008 [75] | 10-1000 | • chitosan/cellulose acetate microsphere (CCAM) was tested for blood compatibility<br>• implanted CCAM had no hepatotoxicity, no renal toxicity and no hemolytic effect in SD rats. |
| 30 | CESIUM (Cs) | - | - | Not available | | | |
| 31 | RUBIDIUM (Rb) | - | - | Not Biocompatible | Not available | | |
| 32 | POTASSIUM (K) | - | ✓ | Yumin et al. 2007 [76] | Not available | | • Potassium titanate biological thin film studied using simulated body fluid cultivation, kinetic clotting of blood and osteoblast cell cultivation experiments<br>• better biocompatibility and bioactivity than Ti-15Mo-3Nb |

| S.No. | Materials | Biocompatibility Test Protocol | | | Technology Feasibility | | Remarks |
|---|---|---|---|---|---|---|---|
| | | *In vivo* | *In vitro* | Reference | Process used and Reference | Dia(nm) | |
| | | | | | | | • Elemental potasium is difficult to test for biocompatibility and to make nanowire |
| 33 | LITHIUM (Li) | - | ✓ | Oh et al. 2004 [77] | Zhang et al. 2012 [78] | | • Influence of Lithium Flouride on biocompatibility and bioactivity of calcium aluminate+PMMA composite cement<br>• Lithium alloy / carbon nano composite |
| 34 | SODIUM (Na) | - | - | Not available | | | Anticoagulant |
| 35 | BARIUM (Ba) | - | - | Not available | Electrospinning He et al. [79] | 80-200 | $BaTiO_3$ nanofiber is fabricated by electrospinning. |
| 36 | GRAPHITE (C) | ✓ | - | Zhang et al. 2010 [80] | Powder metallurgy Jang and Han 2007 [81] | | • Graphene oxide (GO) is a promising material for targeted drug delivery to the lung<br>• Toxicity needs to be assessed |

## 5.3 MATERIALS FOR DESIGN OF NANOSWIMMER

We have followed a three-stage screening process to assess the candidature of the engineering materials as artificial flagella suitable for implant in the body. Figure 5.2 highlights the materials that are in the range of flexural modulus satisfying the mathematical model of the nanoswimmer propulsion derived in Chapter 3 and 4. There are 36 materials that qualify at this stage.

In stage 2, biocompatibility of the stage 1-screened material is assessed from the available literature. All the grades and isomers of any particular material are considered under a single category of the parent material at this stage, and 36 such sets of materials are evaluated for their hemocompatibilities. There is no relevant literature available for 15 materials out of 36 in context of hemocompatibility. For the sake of clarity, they are rewritten in Table 5.3 below. Among remaining 21 materials, the study results of 18 *in vitro* and 8 *in vivo* tests done on 21 materials have been published in the literature. We have rewritten these materials in Table 5.2 with a column on "Biocompatibility Test Protocol" below.

The 21 materials are further assessed for manufacturability i.e. for permissible existing technology for their fabrication. Various researchers explored electrospinning, twin-screw extrusion, powder metallurgy, and other novel methods to manufacture nanowires of polymers, metals and ceramics. It is enlisted in Table 5.2 under the "Technology feasibility".

The possibilities under technology feasibility are rewritten in Table 5.4 below. The corresponding diameter of the nanostructure synthesized is also highlighted.

**Table 5.3: Materials with nonavailability of literature on biocompatible issues**

| S.No. | Materials |
|---|---|
| 1 | FLUORINATED ETHYLENE PROPYLENE (FEP) |
| 2 | PERFLUORINATED ALKOXY (PFA) |
| 3 | POLYBUTYLENE (PB) |
| 4 | ACRYLONITRILE BUTADIENE STYRENE (ABS) |
| 5 | POLYTRIFLUOROCHLOROETHYLENE (PCTFE) |
| 6 | ETHYLENE TETRAFLUOROETHYLENE (ETFE) |
| 7 | POLYBUTADIENE TEREPHTALATE (PBT) |
| 8 | POLYPHENYLENE OXIDE (PPO) |
| 9 | CHLORINATED POLYVINYL CHLORIDE (CPVC) |
| 10 | POLYPHENYLENE SULFIDE (PPS) |
| 11 | POLYBENZENE-IMIDAZOLE (PBI) |
| 12 | CESIUM (Cs) |
| 13 | RUBIDIUM (Rb) |
| 14 | SODIUM (Na) |
| 15 | BARIUM (Ba) |

**Table 5.4: Possible existing technologies for fabrication**

| S.No. | Technology Feasibility (Process used) | Materials |
|---|---|---|
| 1 | Electrospinning | POLYETHYLENE (PE)<br>POLYAMIDE NYLON (PA)<br>POLYVINYL CHLORIDE (PVC)<br>POLYVINYLIDENE FLUORIDE (PVDF)<br>POLYMETHYL METHACRYLATE (PMMA)<br>POLYOXYMETHYLENE (POM)<br>POLYSULFONE (PSF)<br>POLYIMIDE (PI)<br>CELLULOSE ACETATE (CA)<br>BARIUM (Ba) |
| 2 | Jet Blown fibrils | POLYTETRAFLUROETHYLENE (PTFE) |
| 3 | Twin-screw extruder | CELLULOSE ACETATE-BUTYRATE (CAB)<br>POLYBUTYLENE (PB)<br>POLYPROPYLENE (Isotactic/Atactic) (PP) |
| 4 | Melt blending and Melt spinning. | FLUORINATED ETHYLENE PROPYLENE (FEP) |
| 5 | Vacuum assisted infiltration | POLYSTYRENE (PS) |
| 6 | Lithography-assisted template bonding | POLYCARBONATE (PC) |
| 7 | Powder metallurgy | GRAPHITE (C) |

Comments on the biocompatibility test done so far on the enlisted materials and their processing highlights if any are extracted from literature and also discussed in the "Remarks" column of Table 5.2.

The selection criteria is set such that the biocompatibility test data is available for *in vivo* studies conducted and it is feasible to process into nano-structure of diameter around 400 nm.

Amongst the 36 materials screened at stage 1, ten (S. No. 5, 9, 12, 14, 20, 21, 27, 28, 30 and 34 in Table 5.2) neither had any relevant data regarding biocompatibility nor seemed technically feasible to form nanostructures with the present day technology. There are 5 (S. No. 4, 7, 15, 22 and 31 in Table 5.2) other materials like FEP, which can be used only as coating material [82], which enhances the bioactivity or the biocompatibility of the device, coated with it. But independent structure or device formations by these 5 materials are not assessed yet. Further, nanowires from pristine materials like lithium and barium (S. No. 33 and 35) is not formed. Moreover the compounds, composites or the copolymers of the shortlisted material during stage 1, which may form nano-structures, often need flexural rigidity check. Normally as they are metal composites or oxides whose flexural rigidity values are higher than that derived in stage 1 hence they are rejected.

Amongst remaining 19 materials, *in vitro* testing of some materials for cytotoxicity, bioactivity and hemodialysis treatment are reported in literature but specific *in vitro* study with whole blood or *in vivo* hemocompatibility is not assessed. There are 7 materials out of 19 materials that can form nanowires and have succeeded in *in vivo* biomedical applications like ocular implant, bone cement and compatibility with skin, lungs and its mucoadhesivity is assessed positive but hemocompatibility is yet to be verified. CAB, PS, PMMA and Graphite (S. No. 3, 16, 18 and 36 in Table 5.2) are important candidates in this category. The National Heart, Lung, and Blood Institute (NHLBI), USA used polyethylene as reference material for biocompatibility testing [28]. Rein et al. [29] also carry out nanowire preparation of High Molecular Weight Polyethylene (HMWPE) (S. No. 1, Table 5.2) by electrospinning. It was also found that PVDF has favorable mechanical properties. Laroche et al. [49] proposed PVDF (S. No. 13, Table 5.2) as a suture for cardiovascular surgery. Thus PVDF shows good blood compatibility. The nanowires formed also can have controlled dimensions favorable for bio-mimicking flagella. *In vivo* testing of CA on SD rats had no hemolytic effect [74].

CA (S. No. 29, Table 5.2) is also electrospun to produce membranes and felts for conducting bio-separation studies by Zhang et al. [75].

With the data available at this stage we screened 3 materials out of 7 materials vis-à-vis Polyethylene (PE), Polyvinylidenefluoride (PVDF), Cellulose acetate (CA) that satisfied all the conditions. The details of their flexural modulus range, biocompatibility test asserted in literature and nanostructure dimension and process of manufacturing is highlighted in Table 5.5.

Based on the optimum Sperm number [7-8], a range of beating frequency is also suggested for the three proposed materials for maximum swimming efficiency, which is given in Table 5.5. A low value of Sperm number indicates that bending forces dominate and a high value of Sperm number corresponds to higher viscous forces.

**Table 5.5: Details of proposed materials**

| **Materials** | **Flexural Modulus (GPa)** | **Biocompatibility Test Protocol** | | **Technology Feasibility** | | **Optimal beating frequency range* (for Sp = 2)** [7] |
|---|---|---|---|---|---|---|
| | | ***In vivo*** | ***In vitro*** | **Process** | **Diameter (nm)** | |
| Polyethylene (HMWPE) | 0.52 - 0.97 | ✓ | ✓ | Electrospinning | 250 -12000 | • 9-16.5 Hz |
| Polyvinylidene Fluoride (PVDF) | 1.17 - 8.3 | ✓ | ✓ | Electrospinning | 250 | • 20-138 Hz |
| Cellulose Acetate (CA) | 8.3 - 27.6 | ✓ | - | Electrospinning | 10-1000 | • 138-460 Hz |

*****The parametric values of flagella length and diameter considered for calculating beating frequency are 50μm and 200 nm respectively.

The mathematical model developed for a TN propelling through HWP in section 4.3.1 is further simulated for three proposed materials in next section.

## 5.4 OPTIMAL FLAGELLUM DIAMETER FOR BIO-COMPATIBLE MATERIALS

Numerical simulation of the mathematical model developed for forward velocity $(V_z)$ and efficiency $(\eta)$ for tapered nanoswimmer in section 4.3.2 is carried out in MATLAB® and variation of both these indexes with respect to proximal diameter of flagellum are shown in Figure 5.3 and Figure 5.4. Figure 5.3 illustrates the variation of the velocity

over variation of proximal diameter of a helical wave propelled TN for three proposed bio-compatible artificial flagellar materials in section 5.3. Figure 5.3 shows the change in proximal diameter does not affect the peak velocity values significantly.

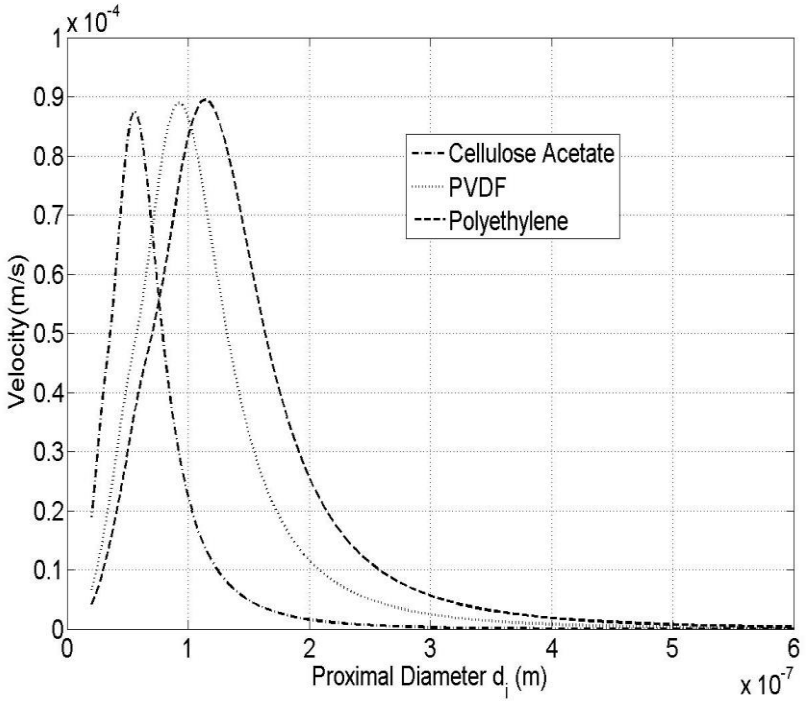


**Figure 5.3: Proximal flagellum diameter ($d_i$) for the fastest swimmer**

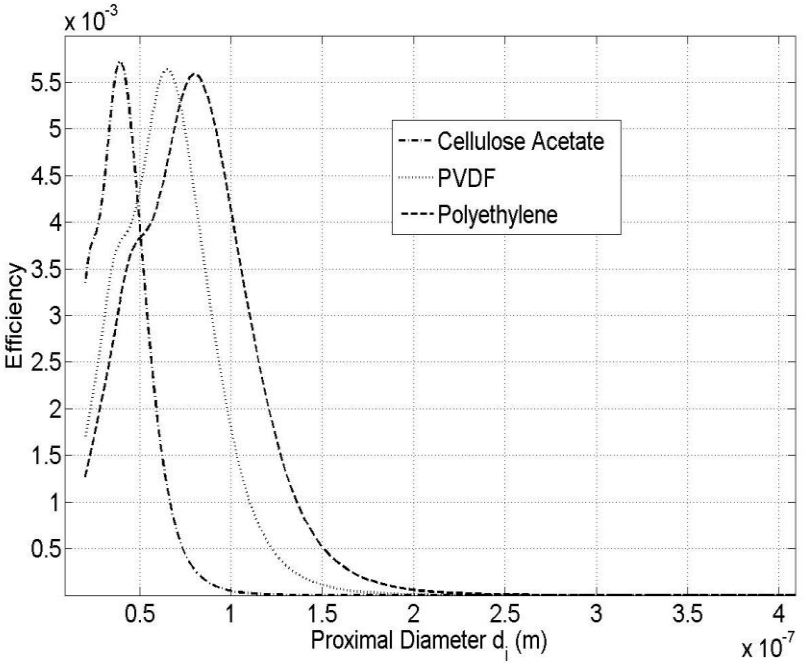


**Figure 5.4: Proximal flagellum diameter ($d_i$) for the most efficient swimmer**

Keeping the same taper ratio, the peak velocity increases from 85.4 μm/s (for Cellulose Acetate) to 90.4 μm/s (for Polyethylene) with variation in proximal diameter from 30 nm to 115 nm as shown in Figure 5.3. As the elasticity of the material decreases, the peak velocity shifts towards the larger diameter.

Figure 5.4 illustrates the variation of the efficiency over proximal diameter of a helical wave propelled TN for three proposed bio-compatible materials. It is observed from Figure 5.4 that the peak efficiency is decreased marginally with increase in diameter. Figure 5.4 shows that the maximum efficiency observed is 0.58% for a tapered flagellum made of Cellulose Acetate. However the peak efficiency values decrease as elasticity decreases. A range of optimal diameter for the fastest and the most efficient swimmer with the proposed materials at ω = 100Hz is listed in Table 5.6.

**Table 5.6: Proximal diameter for selected biocompatible materials for maximum velocity and efficiency**

| **Material** | **E (GPa)** | **Proximal diameter (nm)** | |
|---|---|---|---|
| | | *Fastest swimmer* | *Efficient swimmer* |
| Polyethylene[83] | 0.52-0.97 | 100-115 | 68-80 |
| PVDF[29] | 1.17-8.3 | 55-90 | 40-65 |
| Cellulose Acetate[76] | 8.3-27.6 | 40-55 | 30-40 |

## 5.5 CONCLUSIONS

The present chapter proposes a three-stage screening framework for assessing the candidature of any material for the fabrication of artificial flagella, which shall have implant capabilities *in vivo*. Based on the flexural modulus data collected for more than 500 materials and screening them according to the proposed framework there are three materials (Polyethylene, PVDF and Cellulose Acetate) that qualifies in all the criteria. In addition to these screened materials, researchers in [9], [19-20] have also found materials like $SiO_2$, PDMS and PEG-DA as suitable candidates for fabricating micro swimmers.

Comparison of fastest and most efficient nanoswimmer for three proposed biocompatible materials is carried out for the future design of nanoswimmer. The variation in

performance indexes of nanoswimmer namely swimming velocity and efficiency (i.e. $V_x$ and $\eta$) with respect to proximal diameter of flagellum for a helical wave propelled tapered nanoswimmer is obtained. The peak velocity increases from 85.4 μm/s (for Cellulose Acetate) to 90.4 μm/s (for Polyethylene) with variation in proximal diameter from 30 nm to 115 nm. The maximum efficiency observed is 0.58% for a tapered flagellum made of Cellulose Acetate.

## References


1. Requicha AAG (2003) Nanorobots, Nems, and Nanoassembly. Proc of the IEEE, 91(11), pp.1922-1933.
2. Gray J, Hancock GJ (1955) The Propulsion of Sea-urchin Spermatozoa. J. of Experimental Biol, 32, pp.802-814.
3. Lauga E, Powers TR (2009) The Hydrodynamics of Swimming Microorganisms. Reports on Prog in Phys, 72(9), pp.1-52.
4. Majumdar R, Rathore JS, Sharma NN (2009) Simulation of Swimming Nanorobots in Biological Fluids. Proc 4th International Conference on Autonomous Robots and Agents, Wellington, New Zealand, 10-12 February 2009, pp.79-82.
5. Subramanian S, Rathore JS, Sharma NN (2009) Design and Analysis of Helical Flagella Propelled Nanorobots. Proc of the 4th IEEE International Conference on Nano/Micro Engineered and Molecular Systems, Shenzhen, China, 5-8 January 2009, pp. 931-934.
6. Rathore JS, Sharma NN (2010) Engineering Nanorobot: Chronology of Modeling Flagellar Propulsion. J Nanotechnol Engineering Med, Transactions of the ASME, 1(3) 031001, pp.1-6.
7. Lowe CP (2003) Dynamics of Filaments: Modelling the Dynamics of Driven Microfilaments. Phil. Trans.R. Soc. Lond. B, (358), pp.1543-1550.
8. Lagomarsino MC, Capuani F, Lowe CP (2003) A Simulation Study of the Dynamics of a Driven Filament in an Aristotelian Fluid. J of Theoretical Biol, 224, pp. 215-224.
9. Behkam B, Sitti M (2006) Design Methodology for Biomimetic Propulsion of Miniature Swimming Robots. J of Dynamics Systems, Measurements, and Control, Transactions of the ASME, 128, pp. 36-43.
10. Yu TS, Lauga E, Hosoi AE (2006) Experimental Investigations of Elastic Tail Propulsion at Low Reynolds Number. Phys. Fluids, 18 (091701), pp. 1-4.
11. Ghosh A, Fischer P (2009) Controlled Propulsion of Artificial Magnetic Nanostructured Properties. Nano Letters, 9(6), pp. 2243-2245.

12. Abbott JJ, Lagomarsino MC, Zhang L, Dong, Nelson BJ (2009) How should Microrobots Swim?. The International J of Robotics Research, 28, pp.1434-1447.
13. Mutlu R, Alici G, Li W (2011) Kinematic Modeling for Artificial Flagellum of a Robotic Bacterium based on Electroactive Polymer Actuators. Proc IEEE/ASME International Conference on Advanced Intelligent Mechatronics, Budapest, Hungary, 3-7 July 2011, pp. 440-445.
14. Dreyfus R, Baudry J, Roper ML, Fermigier M, Stone HA, Bibette J (2005) Microscopic Artificial Swimmers. Nature, 437, pp. 862-865.
15. Faraji AH, Wipf P (2009) Nanoparticles in Cellular Drug Delivery. Bioorganic & Medicinal Chemistry, 17, pp. 2950-2962.
16. Sharma NN, Mittal RK (2007) Nanorobot Movement: Challenges and Biologically Inspired Solutions. Proc. 4th International Conference on Computational Intelligence, Robotics and Autonomous Systems, Palmerston North, New Zealand, 28-30 November 2007, pp. 19-25.
17. Peteu SF (2010) Micro- to Nano- Biosensors and Actuators Integrated for Responsive Delivery of Countermeasures. IEEE International Semiconductor Conference (CAS), 11-13 October 2010, pp. 179-190.
18. Gittes F, Mickey B, Nettleton J, Howard J (1993) Flexural Rigidity of Microtubules and Actin Filaments Measured from Thermal Fluctuations in Shape. The J of Cell Biology 120(4), pp.923-934.
19. Evans BA, Shields AR, Lloyd Carroll R, Washburn S, Falvo MR, Superfine R (2007) Magnetically Actuated Nanorod Arrays as Biomimetic Cilia. Nanoletters, 7(5), pp. 1428-1434.
20. Klein F, Richter B, Striebel T, Franz CM, Freymann G, Wegener M, Bastmeyer M (2011) Two-component Polymer Scaffolds for Controlled Three-Dimensional Cell Culture. Adv. Mater., 23, pp. 1341-1345.
21. Majumdar R, Neha S, Rathore JS, and Sharma NN (2013) In Search of Materials for Artificial Flagella of Nanoswimmers. Journal of Materials Science, Springer, 48(1), pp. 240-250.
22. Cardarelli F (2000) Materials Handbook: A Concise Desktop Reference. Springer.

23. Hoshikawa H, Kamiya R (1985) Elastic Properties of Bacterial Flagellar Filaments II: Determination of the Modulus of Rigidity. Biophysical Chemistry, 22, pp.159-166.

24. Helmus MN, Gibbons DF, Cebon D (2008) Biocompatibility: Meeting a Key Functional Requirement of Next-generation Medical Devices. J Toxicologic Pathology, 36(1), pp. 70-80.

25. Seyfert UT, Biehl V, Schenk J (2002) In vitro Hemocompatibility Testing of Biomaterials according to the ISO 10993-4. Biomolecular Engineering, 19, pp.91-96.

26. Teo WE, Ramakrishna S (2006) A Review on Electrospinning Design and Nanofibre Assemblies. Nanotechnology, 17, pp. 89-106.

27. Teo WE, Inai R, Ramakrishna S (2011) Technological Advances in Electrospinning of Nanofibers. Science and Technology of Advanced Materials, 12(013002), pp. 1-19.

28. Belanger MC, Marois Y (2001) Hemocompatibility, Biocompatibility, inflammatory and *in vivo* Studies of Primary Reference Materials Low-Density Polyethylene and Polydimethylsiloxane: A review. J of Biomedical Materials Research, 58(5), pp. 467-477.

29. Rein DM, Shavit-hadar L, Khalfin RL, Cohen Y, Shuster K, Zussman E (2007) Electrospinning of Ultrahigh-Molecular-Weight Polyethylene Nanofibers. J of Polymer Science: Part B: Polymer Physics, 45, pp. 766-773.

30. Risbud MV, Hambir S, Jog J, Bhonde RR (2001) Biocompatibility Assessment of Polytetrafluoroethylene/wollastonite Composites using Endothelial Cells and Macrophages. J Biomater Sci Polym Ed., 12(11), pp. 1177-1189.

31. Ainslie KM, Bachelder EM, Borkar S, Zahr AS, Sen A, Badding JV, Pishko MV (2007) Cell Adhesion on Nanofibrous Polytetrafluoroethylene (nPTFE). Langmuir, 23(2), pp. 747-754.

32. Borkar S, Gu B, Dirmyer M, Delicado R, Sen A, Jackson BR, Badding JV (2006) Polytetrafluoroethylene Nano/Microfibers by Jet Blowing. Polymer, 47(25), pp. 8337-8343.

33. Fundueanu G, Constantin M, Esposito E, Cortesi R, Nastruzzi C, Menegatti E (2005) Cellulose Acetate Butyrate Microcapsules Containing Dextran Ion-exchange Resins as Self-propelled Drug Release System. Biomaterials, 26, pp. 4337-4347.

34. Nilay S, Patil UA, Dinesh BM, Desai BG (2008) Drug-loaded Cellulose Acetate and Cellulose Acetate Butyrate Films as Ocular Inserts. East and Central African J of Pharmaceutical Sciences, 11(1), pp. 9-15.

35. Miyazaki Y, Ogihara K, Yakou S, Nagai T, Takayamab K (2003) In vitro and in vivo Evaluation of Mucoadhesive Microspheres consisting of Dextran Derivatives and Cellulose Acetate Butyrate. International Journal of Pharmaceutics, 258, pp. 21-29.

36. Li M, Xiao R, Sun G (2012) Preparation of Polyester Nanofibers and Nanofiber yarns from Polyester/Cellulose Acetate Butyrate Immiscible Polymer Blends. J of Applied Polymer Science, 124(1), pp. 28-36.

37. Chen X et al (2006) In-situ x-ray Deformation Study of Fluorinated Multiwalled Carbon Nanotube and Fluorinated Ethylene Propylene Nanocomposite Fibers. Macromolecules, 39, pp. 5427-5437.

38. Gomes GS et al (2007) Cellulose Acetate Propionate Coated Titanium: Characterization and Biotechnological Application. Materials Research, 10(4), pp. 469-474.

39. Xiao R, Li M, Sun G (2011) Nanofiber Formation in and Morphology Development of Immiscible Polymer Blends. Society for Plastic Engineers, Plastic Research Online. http://www.4spepro.org/view.php?source=003615-2011-07-11.

40. Ramos CT, Thapa R, Lozano K, Chipara M, Ferrer D, Gutierrez JJ (2011) Synthesis and Characterization of Poly(butylene oxide) Grafted Carbon Nanofibers. J of Nanoscience and Nanotechnology, 11(5), pp. 3965-3969.

41. Contreras-García A, Bucio E, Concheiro A, Alvarez-Lorenzo C (2011) Surface Functionalization of Polypropylene Devices with Hemocompatible DMAAm and NIPAAm Grafts for Norfloxacin Sustained Release. J of Bioactive and Compatible Polymers, 26(4), pp. 405-419.

42. Wang D, Sun G, Chiou BS, Hinestroza JP (2007) Controllable Fabrication and Properties of Polypropylene Nanofibers. Polymer Engineering & Science, 47(11), pp. 1865-1872.
43. Risbud MV, Bhonde RR (2001) Polyamide 6 Composite Membranes: Properties and in vitro Biocompatibility Evaluation. J Biomater Sci Polym Ed., 12(1), pp. 125-136.
44. Bagheri H, Aghakhani A, Baghernejad M, Akbarinejad A (2010) Novel Polyamide-based Nanofibers Prepared by Electrospinning Technique for Headspace Solid-phase Microextraction of Phenol and Chlorophenols from Environmental Samples. Analytica Chimica Acta, 716, pp.34–39.
45. Rhodes NP, Kumary TV, Williams DF (1996) Influence of Wall Shear Rate on Parameters of Blood Compatibility of Intravascular Catheters. Biomaterials, 17(20), pp. 1995-2002.
46. Balakrishnan B, Jayakrishna A (2000) Chemical Modification of Poly (vinyl chloride) using Poly (ethylene glycol) to Improve Blood Compatibility**.** Trends in Biomaterials & Artificial Organs, 18(2), pp. 230-236.
47. Lee KH, Kim HY, La YM, Lee DR, Sung NH (2002) Influence of a Mixing Solvent with Tetrahydrofuran and N,N-dimethylformamide on Electrospun Poly(vinyl chloride) Nonwoven Mats. J of Polymer Science, Part B: Polymer Physics, 40, pp. 2259-2268.
48. Martín J, Maiz J, Sacristan J, Mijangos C (2012) Tailored Polymer-based Nanorods and Nanotubes by "Template Synthesis": From preparation to Applications. Polymer, 53, pp. 1149-1166.
49. Laroche G, Marois Y, Guidoin R, King MW, Martin L, How T, Douvill Y (1995) Polyvinylidene Fluoride (PVDF) as a Biomaterial: From Polymeric Raw Material to Monofilament Vascular Suture. J Biomed Mater Res, 29(12), pp. 1525-1536.
50. Chang Y, Shih YJ, Ko CY, Jhong JF, Liu YL, Wei TC (2011) Hemocompatibility of Poly (Vinylidene Fluoride) Membrane Grafted with Network-like and Brush-like Antifouling Layer Controlled via Plasma-induced Surface PEGylation. Langmuir, 27, pp. 5445-5545.

51. Choi SW, Jo SM, Lee WS, Kim YR (2003) An Electrospun Poly (Vinylidene Fluoride) Nanofibrous Membrane and its Battery Applications. Advanced Materials, 15(23), pp. 2027-2032.

52. Wortman RS, Merritt K, Brown SA (1983) The use of the Mouse Peritoneal Cavity for Screening for Biocompatibility of Polymers. Artificial Cells, Blood Substitutes and Biotechnology, 11(1), pp. 103-114.

53. Molugu S, Qu L, Lin Y, Sun YP, Tzeng TR, Stutzenberger FJ, Latour RA (2006) In vitro and in vivo Biocompatibility of Mannosylated Polystyrene Nanoparticles. J of Biomedical Nanotechnology, 2(1), pp. 1-10.

54. Anderson DG et al (2010) Rapid Biocompatibility Analysis of Materials via in vivo Fluorescence Imaging of Mouse Models. PLOSONE 5(4), e10032. Available: http://www.plosone.org/article/info:doi%2F10.1371%2Fjournal.pone.0010032

55. McCarthy JE, Prina-Mello A, Rakovich T, Volkov Y, Gun'ko YK (2011) Fabrication and Characterization of Multimodal Magnetic-Fluorescentpolystyrene Nanowires as Selective Cell Imaging Probes. J of Materials Chemistry, 21(37), pp. 14219-14225.

56. Schohn DC, Jahn HA, Eber M, Hauptmann G (1986) Biocompatibility and Hemodynamic Studies during Polycarbonate Versus Cuprophane Membrane Dialysis. Blood Purif, 4(1-3), pp. 102-111.

57. Yoon H, Deshpande DC, Ramachandran V, Varadan VK (2008) Aligned Nanowire Growth using Lithography-assisted Bonding of a Polycarbonate Template for Neural Probe Electrodes. Nanotechnology, 19(2), pp. 025304-025312.

58. Liao CC, Wang CC, Shih KC, Chen CY (2011) Electrospinning Fabrication of Partially Crystalline Bisphenol a Polycarbonate Nanofibers: Effects on Conformation, Crystallinity, and Mechanical Properties. European Polymer J, 47(5), pp. 911-924.

59. Thomson LA, Law FC, James KH, Matthew CA, Rushton N (1992) Biocompatibility of Particulate Polymethylmethacrylate Bone Cements: a Comparative Study in vitro and in vivo. Biomaterials, 13(12), pp. 811-818.

60. Czaplewski D, Kameoka J, Craighead HG (2003) Nonlithographic Approach to Nanostructure Fabrication using a Scanned Electrospinning Source. J of Vacuum Science & Technology B, 21(6), pp. 2994:2997.

61. Lee KJ, Oh JH, Kim Y, Jang J (2006) Fabrication of Photoluminescent-dye Embedded Poly (methyl methacrylate) Nanofibers and Their Fluorescence Resonance Energy Transfer Properties. Adv. Mater., 18, pp. 2216-2219.

62. Kong H, Jang J (2008) Antibacterial Properties of Novel poly (methyl methacrylate) Nanofiber Containing Silver Nanoparticles. Langmuir, 24, pp. 2051-2056.

63. Vitral RWF, Ferreira AP, De Souza MA, Fraga MR, Vitral JCA (2010) In-vitro Study of Cellular Viability and Nitric Oxide Production by J774 Macrophages Stimulated by Interferon Gamma with Ceramic, Polycarbonate, and Polyoxymethylene Brackets. American J of Orthodontics and Dentofacial Orthopedics, 137(5), pp. 665-670.

64. Kongkhlang T, Kotaki M, Kousaka Y, Umemura T, Nakaya D, Chirachanchai S (2008) Electrospun Polyoxymethylene: Spinning Conditions and its Consequent Nanoporous Nanofiber. Macromolecules, 41, pp. 4746-4752.

65. Sang Y, Li F, Gu Q, Liang C, Chena J (2008) Heavy Metal-Contaminated Groundwater Treatment by a Novel Nanofiber Membrane. Desalination, 223, pp. 349-360.

66. Khang G, Jeong BJ, Lee HB, Park JB (1995) Biocompatibility of polysulfone II. Platelet adhesion and cho cell growth. Bio-Medical Materials and Engineering, 5(4), pp. 259-273.

67. Zhibin H, Gang L, Peng L, Yunhua YU, Haiyang L, Xiaolong J, Xiaoping Y (2008) Preparation and Properties of Carbon Fiber/Epoxy Composite Toughened by Electrospun Polysulfone Nanofibers**.** Acta Materiae Compositae Sinica 5: doi: CNKI:SUN:FUHE.0.2008-05-006

68. Imai Y, Watanabe A, Masuhara E, Imai Y (1983) Structure - Biocompatibility Relationship of Condensation Polymers. J of Biomedical Materials Research, 17(6), pp. 905-912.

69. Lee SH, Kim SY, Youn JR, Seong DG, Jee SY, Choi JI, Lee JR (2010) Processing of Continuous Poly (amide-imide) Nanofibers by Electrospinning. Polymer International, 59(2), pp. 212-217.

70. De Brito AS, De Queiroz AA, Higa OZ (2003) Digital Image Processing for Biocompatibility Studies of Clinical Implant Materials. Artif Organs, 27(5), pp. 444-446.

71. Ma Z, Kotaki M, Yong T, He W, Ramakrishna S (2005) Surface Engineering of Electrospun Polyethylene Terephthalate (PET) Nanofibers Towards Development of a New Material for Blood Vessel Engineering. Biomaterials, 26(15), pp. 2527-2536.

72. Richardson Jr RR, Miller JA, Reichert WM (1993) Polyimides as Biomaterials: Preliminary Biocompatibility Testing. Biomaterials, 14(8), pp. 627-635.

73. Fukushima S, Karube Y, Kawakami H (2010) Preparation of Ultrafine Uniform Electrospun Polyimide Nanofiber. Polymer J, 42, pp. 514-518.

74. Zhou HY, Zhou DJ, Zhang WF, Jiang LJ, Li JB, Chen XG (2011) Biocompatibility and Characteristics of Chitosan/Cellulose acetate Microspheres for Drug Delivery. Frontiers of Materials Science, 5(4), pp. 367-378.

75. Zhang L, Menkhaus TJ, Fong H (2008) Fabrication and Bioseparation Studies of Adsorptive Membranes/felts made from Electrospun Cellulose Acetate Nanofibers. J of Membrane Science, 319(1-2), pp. 176-184.

76. Yumin Q, Yun H, Chunxiang C, Shuangjin L, Huifen W (2007) Fabrication and Biocompatibility in vitro of Potassium Titanate Biological Thin Film/Titanium alloy Biological Composite. Frontiers of Materials Science in China, 1(3), pp. 252-257.

77. Oh SH, Choi SY, Lee YK, Kim KN (2004) The Influence of Lithium Fluoride on in vitro Biocompatibility and Bioactivity of Calcium Aluminate-PMMA Composite Cement. J of Material Science: Materials in Medicine, 15, pp.25-33.

78. Zhang X, Fedkiw PS, Khan SA (2012) Lithium Alloy Carbon Composite Nanofibers and Methods of Fabrication. U.S. Patents 2012/0034512 A1.

79. He Y, Zhang T, Zheng W, Wang R, Liu X, Xia Y, Zhao J (2010) Humidity Sensing Properties of BaTiO3 Nanofiber Prepared via Electrospinning. Sensors and Actuators-B, 146, pp. 98-102.

80. Zhang X, Yin J, Peng C, Hu W, Zhu Z, Li W, Fan C, Huang Q (2011) Distribution and Biocompatibility Studies of Graphene Oxide in Mice after Intravenous Administration. Carbon, 49(3), pp. 986-995.

81. Jang JH, Han KS (2007) Fabrication of Graphite Nanofibers Reinforced Metal Matrix Composites by Powder Metallurgy and Their Mechanical and Physical Characteristics. J of Composite Materials, 41(12), pp. 1431-1443.

82. Mao C, Qiu Y, Sang H, Zhu HMA, Shen J, Lin S (2004) Various Approaches to Modify Biomaterial Surfaces for Improving Hemocompatibility. Advances in Colloid and Interface Science, 110(1-2), pp. 5-17.

83. Mary C, Marois Y, King MW, Laroche G, Douville Y, Martin L, and Guidoin R (1998) Comparison of the in vivo Behavior of Polyvinylidene Fluoride and Polypropylene Sutures used in Vascular Surgery. ASAIO Journal, 44(3), pp. 199-206.

Chapter 6

# Overall Conclusions and Future Scope of Work

## 6.1 OVERALL CONCLUSIONS

The performance of a uniform diameter nanoswimmer (UDN) and more realistic, a tapered nanoswimmer (TN) using resistive force theory was investigated. A systematic study was carried out with both planar and helical wave propagations through a uniflagellated nanoswimmer. The important results of present study are summarized in the following paragraphs.

1. In Chapter 3, a generalized propulsion model was developed to predict the propulsion characteristics of elastic uniform flagella. The model is used to estimate swimming speed, thrust force, and efficiency of the nanoswimmer. From the results of simulation of generalized propulsion model, it is seen that in case of passive filaments it is advantageous to use short tail lengths. Longer tail lengths lead to an increase in the drag force and hence have a detrimental effect on swimming speed and efficiency. Boundary conditions such as the angle of the tail at the base are varied and optimized for helical wave propelled UDN. From the analysis of simulated results it is seen that a planar wave propelled UDN performs better in the range of characteristic length $1.7l \le L \le 2l$ whereas a helical wave propelled UDN performs better in the range of $2.2l \le L \le 2.7l$.

2. In Chapter 3, it has been shown that the HWP model is better than the PWP model due to practical aspects. The limitation of the planar bending wave model is that it is a 2D model and hence may never be able to conclude anything about performing turns in 3D. All parts for a helical model similar to the one in *E. Coli* are available today.

3. The propulsion characteristics of a planar wave propelled TN have been studied and the same is compared to the case of UDN. Mode shapes of a tapered flagellum are predicted based on elastohydrodynamic equations. Keeping the flagellum volume constant, two new cases are developed for a given ratio of

initial and final diameter. Results indicate that the linearly tapered flagellum planar model (case B) showed improved performance higher velocity and efficiency compared to the uniform flagellum model. For a given frequency, the velocity and efficiency ratio/fraction for the taper to uniform case can go as high as 3.2 times and 3.75 times respectively. The maximum efficiency of the taper case is almost double the maximum efficiency of the uniform diameter case. Considering this the tapered flagellum gives a more realistic value of the performance indicators that has not been shown or attempted in literature.

4. Based on the analysis done in Chapter 4, a TN is more efficient and faster than the UDN. The optimum taper ratio ($b_i$ : $b_f$) is around 18. The $r_h$ : $L$ is the deciding factor which has to trade off between the velocity and the efficiency.

5. In Chapter 4, helical wave propelled TN is also modeled and simulated. From the results, it is seen that the optimal range for head radius to flagellum length ratio, characteristic length and taper ratio are (0.3-0.4), (1.33-2.1) and (3.57-5.88), respectively. The maximum velocity and efficiency observed for tapered flagellated nanoswimmer through helical wave propagation are 84.5μm/sec and 0.57%, respectively.

6. The maximum velocity of a helical wave propelled TN is 85.45μm/s as compared to 55.65μm/s for a uniform diameter flagellum. The maximum efficiency observed is 0.57% for a tapered flagellum and 0.38% for a uniform diameter flagellum. The optimal taper ratio and head size are found for both the fastest swimmer and the most efficient swimmer. The velocity is found to maximum at L/$l$~1.33, $r_h$/L ~0.34 and at a taper ratio ~5.88 whereas the efficiency is found maximum at L/$l$~1.85, $r_h$/L ~ 0.28 and taper ratio ~3.57.

7. It has been observed that for a taper ratio less than 3.34 (i.e., $b_i / b_f \langle 3.34$), the helical wave propulsion outperforms the planar wave propulsion, whereas beyond this point, the planar wave propulsion is faster than the helical wave propulsion. Planar wave propulsion gives a higher value of maximum efficiency ~5.01% when elasticity is around ~ 500MPa, while the maximum efficiency of helical wave propulsion is only ~0.55%, which is obtained at lower elasticity ~200MPa. The efficiency values are in agreement with previously reported values for a uniform flagellum.

8. The Chapter 5 proposes a three-stage screening framework for assessing the candidature of any material for the fabrication of artificial flagella, which shall have implant capabilities *in vivo*. Based on the flexural modulus data collected for more than 500 materials and screening them according to the proposed framework there are three materials (Polyethylene, PVDF and Cellulose Acetate) that qualifies in all the criteria. In addition to these screened materials, researchers have also found materials like $SiO_2$, PDMS and PEG-DA as suitable candidates for fabricating nanoswimmers.
9. Comparison of fastest and most efficient nanoswimmer for three proposed biocompatible materials is carried out for the future design of nanoswimmer. The variation in performance indexes of nanoswimmer namely swimming velocity and efficiency with respect to proximal diameter of flagellum for a helical wave propelled tapered nanoswimmer is obtained. The peak velocity increases from 85.4μm/s (for Cellulose Acetate) to 90.4μm/s (for Polyethylene) with variation in proximal diameter from 30 nm to 115 nm. The maximum efficiency observed is 0.58% for a tapered flagellum made of Cellulose Acetate.

## 6.2 FUTURE SCOPE OF WORK

No research concludes with an absolute end. There is enough scope for further investigations in the area of "Dynamics and Design of the Nanoswimmers". The research in this topic will find a milestone when it will be first realized. From the perspective of present work, the following aspects can be studied and investigated further.

1. Scaled-up experiments to evaluate steady shapes of passive elastic filaments and their propulsive characteristics are needed to validate these theoretical results. Another direction for future work lies in developing materials for the tail, which while not actively generating bending moments, maintain constant amplitude along their length. Notwithstanding the challenges this study shows that passive filaments can be considered as a good starting point in the design and fabrication of nanoswimmers.
2. Effective ways of controlling nanoswimmers inside the human body is an important term in realization of an autonomous nanoswimmer which is yet to be addressed. Increasing the number of flagella will enhance both the speed and the

efficiency of nanoswimmers. The optimum design of a multi-flagella system in terms of number of flagella and spacing is yet to be investigated.

3. For nanomachines working in fluids, thermal agitation around the machine influences its movement to a greater degree which has not been investigated till date. Further, the thermal and chemical changes affect the low Reynolds number. The environment parametric variations need to be incorporated in hydrodynamic modeling of nanoswimmers.
4. Despite many attempts, no feasible design with on-board powering of a nanoswimmer has been proposed. Though researchers have proposed and investigated several techniques to locomote and control nanoswimmer but on-board actuation scheme of nanoswimmer have yet to be conducted to confirm their credibility.

## THE MOMENT-CURVATURE RELATION

For a symmetrical, linearly elastic beam element subjected to pure bending, the relation between the curvature $(1/\rho)$ of the neutral axis and applied bending moment ($M_b$) is given by equation (I.1)

$$\frac{1}{\rho} = \lim_{\Delta s \to 0} \frac{\Delta\phi}{\Delta s} = \frac{d\phi}{ds} = \frac{M_b}{EI} \tag{I.1}$$

where $\Delta\phi$ is change in the slope angle between two points on the neutral axis at a distance $\Delta s$, $E$ is modulus of elasticity, and $I$ is the moment of inertia of the cross-sectional area.

The curvature $(1/\rho)$ in terms of derivatives of deflection is given by equation (I.2)

$$\frac{d\phi}{ds} = \frac{\dfrac{d^2y}{dx^2}}{\left[1+\left(\dfrac{dy}{dx}\right)^2\right]^{\frac{3}{2}}} \tag{I.2}$$

where $y$ is the deflection of the neutral axis, and $\dfrac{dy}{dx}$ is the slope of deflection curve i.e. neutral axis.

Substituting equation (I.2) into (I.1), we get $y$ as a function of $M_b$ and is given as

$$\frac{M_b}{EI} = \frac{\dfrac{d^2y}{dx^2}}{\left[1+\left(\dfrac{dy}{dx}\right)^2\right]^{\frac{3}{2}}} \tag{I.3}$$

With small slope assumption $\left(\dfrac{dy}{dx} \langle\langle 1\right)$, equation (I.3) is simplified as

$$M_b = EI\frac{d^2y}{dx^2} \tag{I.4}$$

Differentiating equation (I.4) twice with respect to *x*, we get transverse load per unit length as a function of $y$

$$dF_E = EI\frac{\partial^4 y}{\partial x^4}ds \tag{I.5}$$

## MATLAB coding for obtaining performance indexes in UDN through Planar wave propulsion

```
% Calculates steady state shape for planar waves
clear
% G=input('Enter vale of amplitude: ');
G=1;
% f=input('Enter value of frequency: ');
% l0=input('Enter value of dimensionless length: ');
f=100;
L=35e-6;
n=1;
% for L=0.5e-6:0.1e-6:30e-6;
%-------------------------------------------------------------
k1=0.38+0.92i;       %fourth roots of -i
k2=-.92+.38i;
k3=-.38-.92i;
k4=0.92-.38i;
%-------------------------------------------------------------
A=1e-22;             %Typical value of stiffness reported in literature
u=0.001;             %fluid viscosity
r=0.2e-6;
cl=2*pi*u/(log(L/r)-0.5);     % drag coefficient
cn=4*pi*u/(log(L/r)+0.5);     % drag coefficient
cl=cl*1.35;
cn=cn*1.35;
ra=0.5e-6;                    % radius of head
l=(A/(cn*2*pi*f))^(1/4);      % scale length
l0=L/l;
%-----------------------------------------------------------------
h=.01;                        % discretization size
tl=1/f;
x=[0:h:l0];
m=length(x);
ht=tl/(m-1);
[t,x]=meshgrid(0:ht:tl,0:h:l0);          %mesh of time and space domain
a=[ 1 1 1 1; k1 k2 k3 k4; k1^2*exp(k1*l0) k2^2*exp(k2*l0)
k3^2*exp(k3*l0) k4^2*exp(k4*l0); k1^3*exp(k1*l0) k2^3*exp(k2*l0)
k3^3*exp(k3*l0) k4^3*exp(k4*l0)];
b=[0 G*l 0 0];
coeff=inv(a)*b';
y1=coeff(1)*exp(k1*x)/L;
y2=coeff(2)*exp(k2*x)/L;
y3=coeff(3)*exp(k3*x)/L;
y4=coeff(4)*exp(k4*x)/L;
yx=(y1+y2+y3+y4)*L;
[V(n),Fx(n),l01(n)]=prop1(t,x,yx,f,L,ht,ra);%Swimming speed
n=n+1;
% end
plot(l01,V);
function v=propL(x,yx,f,l,l0)
% clear
% F=quad('sshape',0,5);
tl=1/f;
w=2*pi*f;
```

```
cl=3.34e-3;
u=0.001;            % viscosity of water
a=1e-6;
L=l*l0;
h=x(2)-x(1);
j=1;
t=0;
yd=diff(yx)/h;
k=length(yd);
yd(k+1)=yd(k);
A1=(yx.*yd);
yd2=yd.^2;
for t=0:.0001:tl
    A2=1+exp(2*i*w*t)*yd2;
    I1=A1./(A2.^(0.5));
    I2=A2.^(0.5);
    F1=trapezoid(x,I1,h);
    F2=trapezoid(x,I2,h);
    Vx(j)=cl*(l^2)*i*w*exp(2*i*w*t)*F1/(cl*l*F2+6*pi*u*a);
    j=j+1;
end
v=real(sum(Vx)/(tl/.0001));

% Propulsion parameters for planar waves
function [V,Fx,l0]=prop1(t,x,yx,f,L,ht,a)
%-----------------------------------------------------
% physical parameters
A=1e-22;            % Typical value of stiffness reported in literature
u=0.001;            % fluid viscosity
r=0.2e-6;
w=2*pi*f;
cl=1.35*2*pi*u/(log(L/r)-0.5);     % drag coefficient
cn=1.35*4*pi*u/(log(L/r)+0.5);     % drag coefficient
l=(A/(cn*w))^(1/4);                % scale length
l0=L/l;
%-----------------------------------------------------
% shape definition
tl=1/f;
h=.01;
x=l*x;
h=l*h;

y=real(exp(1i*w*t).*yx); % final shape function (time dependent)
%-----------------------------------------------------------
[fx,ft]=gradient(y,h,ht);

F1=abs(((1+fx.^2).^0.5));

F=((ft.*fx)./F1);
F2=((cl+(fx.^2)*cn)./F1);
I2=trapezoid(x,F,h,ht)/tl;
I1=trapezoid(x,F2,h,ht)/tl;
% I2=integral(x,ft,h);
V=-((cn-cl)*I2/(I1+6*pi*u*a));
% Fy=abs(V*I1-2*I2);
Fx=6*pi*u*a*V;
% Integral with respect to space and time using trapezoidal rule
function intgnd=trapezoid(x,yx,h,ht)
k=length(x);
f(1:k)=0;
```

```
intgnd=0;
for j=1:k-1

    for i=1:k-1
        f(j)=f(j)+0.5*(yx(i,j)+yx(i+1,j))*h;
    end
end
for j=1:k-1
     intgnd=intgnd+0.5*(f(j)+f(j+1))*ht;
end
```

## MATLAB coding for obtaining performance indexes in UDN through helical wave propulsion

```
% Derivation of steady state shape for helical waves
function [x,y,z]=helical_shape(L,f,st)
% Helical waves mathematical model
% l0=input('Enter value of dimensionless length: ');
% b0=input('Enter value for radius of rotation: ');
% f=input('Enter value of forcing frequency: ');
A=1e-22;            % Typical value of stiffness reported in literature
u=0.001;            % fluid viscosity
cl=2*pi*u/(log(L/r)-0.5);
cl=cl+0.35*cl;      % drag coefficient
cn=4*pi*u/(log(L/r)+0.5);     % drag coefficient
cn=cn+0.35*cn;
ra=5e-6;                      % radius of head
l=(A/(cn*2*pi*f))^(1/4);      % scale length
l0=L/l
b0=L/10;
z=[0:.05:l0];
n=1;
for i=1:2:15
    k(n)=exp(j*pi*i/8);
    n=n+1;
end
% Evaluating coefficients
for n=1:8
    a(1,n)=1;
    a(2,n)=k(n)^4;
    a(3,n)=k(n)^2;
    a(4,n)=k(n)^6;
    a(5,n)=(k(n)^2)*exp(k(n)*l0);
    a(6,n)=(k(n)^6)*exp(k(n)*l0);
    a(7,n)=(k(n)^3)*exp(k(n)*l0);
    a(8,n)=(k(n)^7)*exp(k(n)*l0);
end
b=[b0 0 0 0 0 0 0 0];
coeff=inv(a)*b';
X1=coeff(1)*exp(k(1)*z);
X2=coeff(2)*exp(k(2)*z);
X3=coeff(3)*exp(k(3)*z);
X4=coeff(4)*exp(k(4)*z);
X5=coeff(5)*exp(k(5)*z);
X6=coeff(6)*exp(k(6)*z);
X7=coeff(7)*exp(k(7)*z);
X8=coeff(8)*exp(k(8)*z);
Y1=-coeff(1)*(k(1)^4)*exp(k(1)*z);
Y2=-coeff(2)*(k(2)^4)*exp(k(2)*z);
Y3=-coeff(3)*(k(3)^4)*exp(k(3)*z);
Y4=-coeff(4)*(k(4)^4)*exp(k(4)*z);
Y5=-coeff(5)*(k(5)^4)*exp(k(5)*z);
Y6=-coeff(6)*(k(6)^4)*exp(k(6)*z);
Y7=-coeff(7)*(k(7)^4)*exp(k(7)*z);
Y8=-coeff(8)*(k(8)^4)*exp(k(8)*z);
```

```
x=(X1+X2+X3+X4+X5+X6+X7+X8);
y=(Y1+Y2+Y3+Y4+Y5+Y6+Y7+Y8);
figure(1);
plot(x/L,y/L,st);
hold on;
figure(2);
plot(z/l0,y/L,st);
hold on;
figure(3);
plot(z/l0,x/L,st);
hold on;
[V(p),wv(p),Fx(p),M(p),Mt(p)]=prophelix2(x,y,z,f,l,l0);

% [V(p),wv(p),Fx(p),M(p),Mt(p)]=prophelix(x,y,z,f,l,l0);
wv(p);
w1=w-wv(p);
f=(w1/(2*pi));
end
% figure(1);
% plot(x/l,y/l,st);
% hold on;
% figure(2);
% plot(z/l0,x/l,st);
% hold on;
% figure(3);
% plot(z/l0,y/l,st);
% hold on;
% figure(4);
% plot3(x/l,y/l,z/l0,'r-');
V1=V(p);
wv1=wv(p);
Fx1=Fx(p);
M1=(M(p));
Mt1=(Mt(p));
eff1=Fx1*V1/(Mt1*(w-wv1)+M1*wv1);
% p=1:100;
% plot(p,wv);

% Propulsion parameters for helical waves
function [V,wv,Fx,M,Mt]=prophelix(x,y,z,f,l,l0)
L=l*l0;
u=0.001;            % water as fluid
b=.2e-6;            % diameter of tail
a=0.5e-6;           % radius of head
w=2*pi*f;
cn=4*pi*u/(log(L/b)+.5);
cl=2*pi*u/(log(L/b)-.5);
%---------------------------------------
r=abs(sqrt(x.^2+y.^2));
r2=r.^2;
z=l*z;
hz=z(2)-z(1);
yd=diff(y);
n=length(yd);
yd(n+1)=yd(n);
xd=diff(x);
xd(n+1)=xd(n);
yd=yd/hz;
xd=xd/hz;
bt=atan(abs(y.*xd-x.*yd)./r);
```

```
bt(1)=0;
%----------------------------------------
f1=r.*sin(bt);
f2=r2.*sin(bt).*tan(bt);
f3=r2.*cos(bt);
f4=cos(bt);
f5=sin(bt).*tan(bt);
I1=integral(z,f1,hz);
I2=integral(z,f2,hz);
I3=integral(z,f3,hz);
I4=integral(z,f4,hz);
I5=integral(z,f5,hz);
A=[cl*I1-cn*I1  4*pi*u*b^2*I4+8*pi*u*a^3-cl*I2-cn*I3; cl*I4+cn*I5-
6*pi*u*a  cn*I1-cl*I1];
B=[-w*(cl*I2+cn*I3) cn*I1*w-cl*I1*w];
sol=inv(A)*B';
V=sol(1);
wv=sol(2);
Fx=(6*pi*u*a*V);
M=8*pi*u*a^3*wv;
Mt=V*(cl*I1-cn*I1)+wv*(4*pi*u*b^2*I4-cl*I2-cn*I3)+w*(-
4*pi*u*b^2*I4+cl*I2+cn*I3);

% Propulsion parameters for helical waves
function [V,wv,Fx,M,Mt]=prophelix2(x,y,z,f,l,l0,a)
L=l*l0;
u=0.001;              % water as fluid
r=0.2e-6;             % radius of tail
% a=0.5e-6;           % radius of head
w=2*pi*f;             % Angular velocity if tail wrt head
cn=4*pi*u/(log(L/r)+.5);    % Normal
cl=2*pi*u/(log(L/r)-.5);    % Tangential drag coefficients
cl=1.35*cl;
cn=1.35*cn;
%---------------------------------------
x=real(x);
y=real(y);
r1=abs(sqrt(x.^2+y.^2));     % Calculating instantaneous amplitude
r2=r1.^2;
z=l*z;
hz=z(2)-z(1);
% Evalutaing differentials----------------
yd=diff(y);
n=length(yd);
yd(n+1)=yd(n);
xd=diff(x);
xd(n+1)=xd(n);
yd=yd/hz;
xd=xd/hz;
%----------------------------------------
% Calculating instantaneous pitch angle(radians)
bt=atan(abs(y.*xd-x.*yd)./(r1+1e-22));
m=1:n+1;
bt(1)=0;

%Propulsion model-----------------------------------------
f1=r1.*sin(bt);
f2=r2.*sin(bt).*tan(bt);
f3=r2.*cos(bt);
```

```
f4=cos(bt);
f5=sin(bt).*tan(bt);
I1=integral(z,f1,hz);
I2=integral(z,f2,hz);
I3=integral(z,f3,hz);
I4=integral(z,f4,hz);
I5=integral(z,f5,hz);
A(1,1)=I1*(cl-cn);
%(Calculation of angular speed of head and swimming velocity)
A(1,2)=-(4*pi*u*r^2*I4+8*pi*u*a^3+cl*I2+cn*I3);
A(2,1)=cl*I4+cn*I5+6*pi*u*a;
A(2,2)=I1*(cn-cl);

B=[-w*(cl*I2+cn*I3+4*pi*u*r^2*I4) w*I1*(cn-cl)];
% Modified for axial joint between motor and flagellum
sol=inv(A)*B';
V=sol(1);                        % swimming speed
wv=sol(2);                       % angular velocity of head
Fx=(6*pi*u*a*V);
M=8*pi*u*a^3*wv;
Mt=V*(cl*I1-cn*I1)+wv*(-4*pi*u*r^2*I4-cl*I2-
cn*I3)+w*(4*pi*u*r^2*I4+cl*I2+cn*I3);
```

MATLAB coding for obtaining performance indexes in TN through Planar wave propulsion

```
clc; clear all
%     parameters for simulations
%-----------------------------------------------------------
%     for parametric variation
L=50e-6;
rc=200e-9;
rh=15e-06;
vol=L*pi*rc^2;
u=0.001;
count=100;  %     no of elements
n=1;        %     to initialize variation of first parameter array
index
for E=0.1e6:1e6:1e9
elasticity(n)=E;
s=1;
for f=[25 35 45]
w=2*pi*f;
T=1/f;
%     case A - Constant diameter
%-------------------------------------------------------------
Ic=(pi/4)*(rc^4);
cnc=4*pi*u/(log(L/rc)+0.5);
cl_c=2*pi*u/(log(L/rc)-0.5);
sclenc=((E*Ic)/(cnc*w))^0.25;
flexr(n)=E*Ic;
scalelen(n,s)=L/sclenc;
%     Taper diameter
ratio=1/3;
%     case B - length remaining same
%-------------------------------------------------------------
x=linspace(0,L,count);
25
26 matlab codes
ri=sqrt(vol/((pi/3)*L*(1+ratio^2+ratio)));
rf=ri*ratio;
r=ri-((ri-rf)/L).*x;
I=(pi/4)*r.^4;
cn=4*pi*u./(log(L./r)+0.5);
cl=2*pi*u./(log(L./r)-0.5);
sclen=((E*I)./(cn*w)).^0.25;
%     case C - distal end diameter remaining same
%-------------------------------------------------------------
Lt=3*vol/(pi*(rc^2)*(1+ratio^2+ratio));
xx=linspace(0,Lt,count);
rix=rc;
rfx=rix*ratio;
rx=rix-((rix-rfx)./Lt)*xx;
Ix=(pi/4)*rx.^4;
cnx=4*pi*u./(log(Lt./rx)+0.5);
clx=2*pi*u./(log(Lt./rx)-0.5);
sclenx=((E*Ix)./(cnx*w)).^0.25;
```

```
%
-------------------------------------------------------------------------
%     PROPULSION OUTPUT PARAMETERS
%
-------------------------------------------------------------------------
%     propulsion calculation for case A
[tc yc hc htc]=ypro_const(x,sclenc,L,1,T);
[Vc,Fxc,Fyc,effc]=prop_planar_const(L,rc,tc,x,yc,hc,htc,rh,f,u);
%     propulsion calculation for case B
[t yx h ht]=ypro(x,sclen(1),L,1,T,ri,rf);
[V,Fx,Fy,eff]=propulsion(t,x,yx,h,ht,rh,L,cn,cl,count,f,u);
%     propulsion calculation for case C
%     [tx yxx hx htx]=ypro(xx,sclenx(1),Lt,1,T,rix,rfx);
A.1 main function module 27
%
      [Vx,Fxx,Fyx,effx]=propulsion(tx,xx,yxx,hx,htx,rh,Lt,cnx,clx,count
,f,u);
%     Velocity(n,:)=[Vc V V_Icn V_r];
%     efficiency(n,:)=[effc eff eff_Icn eff_r];
Velocity(n,s,:)=[Vc V ];      %Vx];
efficiency(n,s,:)=[effc eff ];      %effx];
thrust(n,s,:)=[Fxc Fx];
velfrac(n,s,:)=[V/Vc ]; %Vx/Vc];
efffrac(n,s,:)=[eff/effc ];   %effx/effc];
%     ti=num2str(E*Ic);
%     subplot(1,1,n)
%     if(E==190.8e6)
%     plot(x,real(yc));hold on;%,'-r',x,real(yx),'-.b',xx,real(yxx),'-
b');
%      ylabel('amplitude');xlabel('length');
%     end
%     Title(ti);
%     plot3(frac,rh_L,Vc,'xr',frac,rh_L,V,'ob',frac,rh_L,Vx,'xb');
hold on;
%     ylabel('Velocity for unit length');xlabel('tail radius to length
fraction');
%     figure (1);plot3(E,f,Vc,'xr');hold on; grid on;
%     figure (2);plot3(E,f,V,'ob');hold on; grid on;
%     xlabel('Elasticity');ylabel('Frequency')
%     figure(1);
%     plot(E,Vc,'xr',E,V,'ob',E,Vx,'xb');hold on;
%     grid on; ylabel('Velocity for unit length');xlabel('Elasticity');
%
%     figure(2);
%     plot(E,effc,'xr',E,eff,'ob',E,effx,'xb');hold on;
%     grid on; ylabel('Efficiency for unit
length');xlabel('Elasticity');
%     figure(1);
%      subplot(121)
%     plot(f,Vc,'xr',f,V,'ob',f,Vx,'xb');hold on;
%     ylabel('Velocity for unit length');xlabel('Frequency');
%     grid on;
%
%      subplot(122)
%     plot(f,V/Vc,'*r',f,Vx/Vc,'*b');hold on;
%     ylabel('Velocity ratio');xlabel('Frequency');
%     grid on;
%
%     figure(2);
%     plot(f,effc,'xr',f,eff,'ob',f,effx,'xb');hold on;
```

```
%     ylabel('Efficiency for unit length');xlabel('Frequency');

%     grid on;
freq(s)=f;
s=s+1;
end
n=n+1;
end
%     figure(1)
%     plot(scalelen,Velocity(:,2,1),scalelen,Velocity(:,2,2))
%     grid on;ylabel('Velocity');xlabel('L/scale length');
%     figure(2)
%
      plot(flexr,Velocity(:,1,1:2),'r',flexr,Velocity(:,2,1:2),'g',flex
r,Velocity(:,3,1:2),'')
%      grid on;ylabel('Velocity');xlabel('Flexural rigidity');
figure(1)
plot(elasticity,Velocity(:,:,1),'r',elasticity,Velocity(:,:,2),'b')
%     ,elasticity,Velocity(:,2,3),'g')
grid on;ylabel('Velocity');xlabel('Elasticity');
figure(2)
plot(elasticity,efficiency(:,:,1),'r',elasticity,efficiency(:,:,2),'b')
grid on;ylabel('Efficiency');xlabel('Elasticity');
figure(3)
plot(elasticity,velfrac(:,:,1))
grid on;ylabel('Velocity Fraction');xlabel('Elasticity');
figure(4)
plot(elasticity,efffrac(:,:,1))
grid on;ylabel('Efficiency Fraction');xlabel('Elasticity');
figure(5)
plot(elasticity,thrust(:,:,1),'r',elasticity,thrust(:,:,2),'b')
grid on;ylabel('Thrust Force');xlabel('Elasticity');
%
      plot(elasticity,efffrac(:,:,1),'r',elasticity,efffrac(:,:,2),'g')
;
a.2 profile module : uniform flagellum
Listing 4: Profile of Uniform Flagellum
function [t yx h ht] = ypro_const(x,sclen,L,G,T)
%     fourth roots of -i
k=roots([1 0 0 0 1i]);
%-------------------------------------
l=L/sclen;
a=[ 1 1 1 1; ...
k(1) k(2) k(3) k(4);...
A.3 profile module : tapered flagellum 29
k(1)^2*exp(k(1)*l) k(2)^2*exp(k(2)*l) k(3)^2*exp(k(3)*l) k(4)
^2*exp(k(4)*l);...
k(1)^3*exp(k(1)*l) k(2)^3*exp(k(2)*l) k(3)^3*exp(k(3)*l) k(4)
^3*exp(k(4)*l)];
b=[0; G*sclen; 0; 0];
coeff=inv(a)*b;
%-------------------------------------------------------------
%     x=linspace(0,L);
h=x(2)-x(1);
m=length(x);
ht=T/(m-1);
[t,x]=meshgrid(0:ht:T,0:h:L); %     mesh of time and space domain
%-------------------------------------------------------------
y1=coeff(1)*exp(k(1)*x/sclen);
y2=coeff(2)*exp(k(2)*x/sclen);
```

```
y3=coeff(3)*exp(k(3)*x/sclen);
y4=coeff(4)*exp(k(4)*x/sclen);
yx=(y1+y2+y3+y4);
```

_

a.3 profile module : tapered flagellum

Listing 5: Profile of Tapered Flagellum

```
function [t yx h ht]=ypro(x,scl,L,G,T,di,df)
%     function yx = ypro_lin(scl,L,G,T,di,df)
%-----------------------------------------------
%     calculate roots of auxiliary equation
%-----------------------------------------------
k=(df-di)/(L*di);
c=1i/(k*scl)^4;
z=[1 2 -1 -2 c];
m=roots(z);
m1=m(1);m2=m(2);m3=m(3);m4=m(4);
%-----------------------------------------------
h=x(2)-x(1);
p=length(x);
ht=T/(p-1);
[t,x]=meshgrid(0:ht:T,0:h:L); %     mesh of time and space domain
%-----------------------------------------------
M=[1 1 1 1;...
m(1) m(2) m(3) m(4);...
m(1)*(m(1)-1)*((df/di)^(m(1)-2)) m(2)*(m(2)-1)*((df/di)^(m(2)
-2)) m(3)*(m(3)-1)*((df/di)^(m(3)-2)) m(4)*(m(4)-1)*((df/
di)^(m(4)-2));...
m(1)*(m(1)-1)*(m(1)-2)*((df/di)^(m(1)-3)) m(2)*(m(2)-1)*(m(2)
-2)*((df/di)^(m(2)-3)) m(3)*(m(3)-1)*(m(3)-2)*((df/di)^(m
(3)-3)) m(4)*(m(4)-1)*(m(4)-2)*((df/di)^(m(4)-3))];...
30 matlab codes
der=[0;G/k;0;0];
A1= M\der;
%-----------------------------------------------
y1=A1(1)*(k*x+1).^m(1);
y2=A1(2)*(k*x+1).^m(2);
y3=A1(3)*(k*x+1).^m(3);
y4=A1(4)*(k*x+1).^m(4);
yx=(y1+y2+y3+y4);
end
```

a.4 output module : uniform flagellum

Listing 6: Output meseaurements for uniform flagellum

```
%     Propulsion parameters for planar waves
function[V,Fx,Fy,eff]=prop_planar_const(L,rc,t,x,yx,h,ht,a,f,u)
%-----------------------------------------------------
%     variables_lin_taper;
%     u=0.001;
w=2*pi*f;
T=1/f;
cn=4*pi*u/(log(L/rc)+0.5);
cl=2*pi*u/(log(L/rc)-0.5);
y=real(exp(1i*w*t).*yx); %    final shape function (time dependent)
%-----------------------------------------------------
[fx,ft]=gradient(y,h,ht);
F=ft.*fx;
F2=ft.*ft;
I1_temp=ht*trapz(F);
I1=h*trapz(I1_temp)/T;
I2_temp=ht*trapz(fx);
I2=h*trapz(I2_temp)/T;
```

```
I3_temp=ht*trapz(ft);
I3=h*trapz(I3_temp)/T;
I4_temp=ht*trapz(F2);
I4=h*trapz(I4_temp)/T;
V=abs(((cn-cl)*I1)/((L*cl)+(6*pi*u*a)));
Fx=6*pi*u*a*V;
Fy=abs(((cn-cl)*V*I2)-(cn*I3));
FynVy=abs(((cn-cl)*V*I1)-(cn*I4));
eff=(Fx*V)/((FynVy)+(Fx*V));
end
```

A.5 output module: tapered flagellum 31

a.5 output module: tapered flagellum

Listing 7: Output meseaurements for tapered flagellum

```
%     Propulsion parameters for planar waves
function[V,Fx,Fy,eff]=propulsion(t,x,yx,h,ht,a,L,cnx,clx,count,f,u)
%-----------------------------------------------------
w=2*pi*f;
T=1/f;
%      u=0.001;
%     cn=mean(cnx);cl=mean(clx);
for i=1:1:count
cn(:,i)=cnx;
cl(:,i)=clx;
end
y=real(exp(1i*w*t).*yx); %    final shape function (time dependent)
%     plot3(x,t,y);
%-----------------------------------------------------
[fx,ft]=gradient(y,h,ht);
F=(cn-cl).*ft.*fx;
%      I1=trapezoid(x,F,h,ht)/T;
I1_temp=h*trapz(F);
%     I1=ht*trapz(I1_temp);
I1=ht*trapz(I1_temp)/T;
%     I5=trapezoid(x,cl,h,ht)/T;
I5_temp=h*trapz(cl);
%     I5=ht*trapz(I5_temp);
I5=ht*trapz(I5_temp)/T;
cfx=(cn-cl).*fx;
%     I2=trapezoid(x,cfx,h,ht)/T;
I2_temp=h*trapz(cfx);
%     I2=ht*trapz(I2_temp);
I2=ht*trapz(I2_temp)/T;
cft=cn.*ft;
%     I3=trapezoid(x,cft,h,ht)/T;
I3_temp=h*trapz(cft);
%     I3=ht*trapz(I3_temp);
I3=ht*trapz(I3_temp)/T;
F2=cn.*ft.*ft;
%     I4=trapezoid(x,F2,h,ht)/T;
I4_temp=h*trapz(F2);
%     I4=ht*trapz(I1_temp);
32 matlab codes
I4=ht*trapz(I4_temp)/T;
V=abs((I1)/(I5+(6*pi*u*a)));
Fx=6*pi*u*a*V;
Fy=((V*I2)-(I3));
FynVy=abs((V*I1)-(I4));
eff=(Fx*V)/((FynVy)+(Fx*V));
end
```

MATLAB coding for obtaining performance indexes in TN through helical wave propulsion

```
%-------------------Parametric variation of distal end diameter--------
format long
L=10e-6;                %Length (m)
eta=1;                        %Extent
di=200e-9;              %Initial Diameter(m)
 I=pi*(di^4)/64;        %Moment of Inertia(m^4)
k=(df-di)/(L*di);
 Mu=0.001;              %Viscoscity(Pa.s)
R_sphere=3e-6;          %Radius of head(m)
% b=1e-6;

omega=100*2*pi;         %Angular Velocity(rad/s)
C_drag=4*pi*Mu/(log(2*L/di)+0.5);
dz=L/100;               %Length element(m)
t=0.2;                        %Time (s)
t_step=0.01;            %Time step(s)
scl=(EI/(omega*C_drag))^0.25
loop=0;
counter=0;
scl=L/1.8;
scl=L/1.4;

%-----------------ROOTS OF EQUATION-------------------
for df=0.1e-9:0.5e-9:di-0.5e-9
k=(df-di)/(L*di);
EQ=[ 1, 4, 2, -8, -7, 4, 4, 0,(1/(scl*k)^8)];
m=roots(EQ);

counter=counter+1;
for i=1:8
    C(i)=m(i)*(m(i)-1)*(m(i)+1)*(m(i)+2);
    R(i)=C(i)*m(i)*(m(i)-1)*(((k*L)+1)^(m(i)-2));
    P(i)=m(i)*(m(i)-1)*(((k*L)+1)^(m(i)-2));
    Q(i)=C(i)*m(i)*(m(i)-1)*(m(i)-2)*(((k*L)+1)^(m(i)-3));
    S(i)=m(i)*(m(i)-1)*(m(i)-2)*(((k*L)+1)^(m(i)-3));
 end
%-----------------MATRIX for A(i)--------------------------
M=[C(1) C(2) C(3) C(4) C(5) C(6) C(7) C(8);...
   1 1 1 1 1 1 1 1;...
   C(1)*m(1) C(2)*m(2) C(3)*m(3) C(4)*m(4) C(5)*m(5) C(6)*m(6)
C(7)*m(7) C(8)*m(8);...
   m(1) m(2) m(3) m(4) m(5) m(6) m(7) m(8);...
   R(1) R(2) R(3) R(4) R(5) R(6) R(7) R(8);...
   P(1) P(2) P(3) P(4) P(5) P(6) P(7) P(8);...
   Q(1) Q(2) Q(3) Q(4) Q(5) Q(6) Q(7) Q(8);...
   S(1) S(2) S(3) S(4) S(5) S(6) S(7) S(8)];

n=0;
for t=0:t_step:t
n=n+1;
```

```
der(1:8,n)=[0;0;-
eta*sin(omega*t)/((k^5)*(scl^4));eta*cos(omega*t)/k;0;0;0;0];
% der=[0;0;0.05;0.0866;0;0;0;0];
A1(1:8,n)= M\der(1:8,n);

i=0;
for z=0:dz:L
    i=i+1;

y1=A1(1,n)*(k*z+1)^m(1);
y2=A1(2,n)*(k*z+1)^m(2);
y3=A1(3,n)*(k*z+1)^m(3);
y4=A1(4,n)*(k*z+1)^m(4);
y5=A1(5,n)*(k*z+1)^m(5);
y6=A1(6,n)*(k*z+1)^m(6);
y7=A1(7,n)*(k*z+1)^m(7);
y8=A1(8,n)*(k*z+1)^m(8);
yz(i,n)=(y1+y2+y3+y4+y5+y6+y7+y8);

x1=-((k*scl)^4)*C(1)*A1(1,n)*((k*z+1)^m(1));
x2=-((k*scl)^4)*C(2)*A1(2,n)*((k*z+1)^m(2));
x3=-((k*scl)^4)*C(3)*A1(3,n)*((k*z+1)^m(3));
x4=-((k*scl)^4)*C(4)*A1(4,n)*((k*z+1)^m(4));
x5=-((k*scl)^4)*C(5)*A1(5,n)*((k*z+1)^m(5));
x6=-((k*scl)^4)*C(6)*A1(6,n)*((k*z+1)^m(6));
x7=-((k*scl)^4)*C(7)*A1(7,n)*((k*z+1)^m(7));
x8=-((k*scl)^4)*C(8)*A1(8,n)*((k*z+1)^m(8));
xz(i,n)=(x1+x2+x3+x4+x5+x6+x7+x8);

end
j=1;
z=0:dz:L;
Amp(1,n)=0;
M11=0;
M12=0;
M21=0;
M22=0;
dl_O=0;
dl_w=0;
C1=0;
C2=0;
for a=0:dz:L
j=j+1;
    C_n(j-1,n)=4*pi*Mu/(log(2*L*exp(0.5)/(di*(k*z(j-1)+1))));
    C_l(j-1,n)=2*pi*Mu/(log(2*L*exp(-0.5)/(di*(k*z(j-1)+1))));
end
j=1;
for a=dz:dz:L
    j=j+1;
    Amp(j,n)=(xz(j,n)^2+yz(j,n)^2)^0.5;
    beta_angle(j,n)=atan(abs((xz(j,n)*(yz(j,n)-yz(j-1,n))-
(yz(j,n)*(xz(j,n)-xz(j-1,n))))/(z(j)-z(j-
1)))/(xz(j,n)^2+yz(j,n)^2)^0.5);
    b=di*(k*z(j-1)+1)/2;
    %---------------Coefficient of Fz----------------------
   M11=M11+(-C_n(j-1,n)*sin(beta_angle(j,n))*tan(beta_angle(j,n))-
C_l(j-1,n)*cos(beta_angle(j,n)))*dz;
   M12=M12+((Amp(j,n)*sin(beta_angle(j,n)))*(C_l(j-1,n)-C_n(j-
1,n)))*dz;
```

```
   C1=C1+(omega*(Amp(j,n)*sin(beta_angle(j,n))*(-C_l(j-1,n)+ C_n(j-
1,n))))*dz;
    %---------------Coefficient of Mz-----------------------
   M21=M21+ (Amp(j,n)*sin(beta_angle(j,n))*(C_l(j-1,n)-C_n(j-1,n)))*dz;
   M22=M22+ (-Amp(j,n)*Amp(j,n)*(C_l(j-
1,n)*sin(beta_angle(j,n))*tan(beta_angle(j,n))+C_n(j-
1,n)*cos(beta_angle(j,n)))-4*pi*Mu*b*b*cos(beta_angle(j,n)))*dz;
   dl_O=dl_O+(4*pi*Mu*b*b*cos(beta_angle(j,n)))*dz;
   dl_w=dl_w+(omega*4*pi*Mu*b*b*cos(beta_angle(j,n)))*dz;
   C2=C2+ (omega*(Amp(j,n)*Amp(j,n)*(C_l(j-
1,n)*sin(beta_angle(j,n))*tan(beta_angle(j,n))+C_n(j-
1,n)*cos(beta_angle(j,n)))+4*pi*Mu*b*b*cos(beta_angle(j,n))))*dz;
end
M31=M11-(6*pi*Mu*R_sphere);
M32=M22-(8*Mu*pi*(R_sphere^3));
Matr=[M31 M12;...
    M21 M32];
RHS=[-C1;-C2];
X=Matr\RHS;
Fz=M11*X(1)+M12*X(2)+C1;
Mz=M21*X(1)+(M22+dl_O)*X(2)+C2-dl_w;
Efficiency=Fz*X(1)/(Mz*omega);
V1(counter)=X(1);
V(counter)=Efficiency;
V2(counter)=Fz;
% Rat(counter)=df/di;
Rat(counter)=df/di;
hold on
%---------------PLOTTING-----------------------------------------------
%           subplot(5,1,counter)
%           plot(z,yz(1:i,n),'black')
%           hold on
%           subplot(3,3,2)
%     figure(2)
%           plot(z,xz(1:i,n))
%           title('XZ');
%           hold on
%           subplot(3,3,3)
%     figure(3)
%           plot3(z,xz,yz)
%           title('3D');
%           hold on
%           subplot(3,3,4)
%           plot(z,beta_angle(1:i,n))
%           title('BETA ANGLE');
%           hold on
%           subplot(3,3,5)
%     figure(4)
%           plot(z,Amp(1:i,n))
%           title('AMPLITUDE');
%           hold on
%           subplot(3,3,6)
%           plot(z,C_n(1:i,n))
%           title('C_n');
%           hold on
%           subplot(3,3,7)
%           plot(z,C_l(1:i,n))
%           title('C_l');
%           hold on
end
```

```
end
figure(1)
plot(Rat,V,'black')
hold on
figure(2)
plot(Rat,V1,'black')
hold on
figure(3)
plot(Rat,V2,'black')
hold on
[g,I]=max(V);
%     text(Rat(I),V(I),'\leftarrow a=')
%     text(Rat(I),V(I),'\leftarrow a=5.0 \mu m',...
%           'HorizontalAlignment','left')
%      V=X(1)
%     O=X(2)/(2*pi)
%     Fz
%     Mz
%     Efficiency*100
%     EI
%     scl
```

Materials list used for flagellum material selection

| S.No. | Material | E(GPa) | Selection |
|---|---|---|---|
| 1 | GRAPHITE | 3-12 | ✓ |
| 2 | PYROLITIC CARBON | 16-30 | × |
| 3 | DIAMOND | 900 | × |
| 4 | VITREOUS CARBON (Treated @ 1000C) | 28 | × |
| 5 | VITREOUS CARBON (Treated @ 2500C) | 22 | × |
| 6 | BORON | 320 | × |
| 7 | CHROMIUM DIBORIDE | 211 | × |
| 8 | HAFNIUM DIBORIDE | 500 | × |
| 9 | LANTHANUM HEXABORIDE | 479 | × |
| 10 | MOLYBDENUM BORIDE | 672 | × |
| 11 | NIOBIUM MONOBORIDE | 637 | × |
| 12 | TANTALUM DIBORIDE | 257 | × |
| 13 | THORIUM TETRABORIDE | 148 | × |
| 14 | TITANIUM DIBORIDE | 372-551 | × |
| 15 | URANIUM TETRABORIDE | 440 | × |
| 16 | VANADIUM DIBORIDE | 268 | × |
| 17 | ZIRCONIUM DIBORIDE | 343-506 | × |
| 18 | BERYLLIUM CARBIDE | 314.4 | × |
| 19 | BORON CARBIDE | 440-470 | × |
| 20 | CHROMIUM CARBIDE | 386 | × |
| 21 | DIAMOND | 930 | × |
| 22 | GRAPHITE | 6.9 | × |
| 23 | HAFNIUM MONOCARBIDE | 424 | × |

| S.No. | Material | E(GPa) | Selection |
|---|---|---|---|
| 24 | MOLYBDENUM HEMICARBIDE | 221 | × |
| 25 | MOLYBDENUM MONOCARBIDE | 197 | × |
| 26 | SILICON MONOCARBIDE (ALPHA) | 386-414 | × |
| 27 | SILICON MONOCARBIDE (BETA) | 262-468 | × |
| 28 | TANTALUM MONOCARBIDE | 364 | × |
| 29 | TITANIUM MONOCARBIDE | 310-462 | × |
| 30 | TUNGSTEN HEMICARBIDE | 421 | × |
| 31 | TUNGSTEN MONOCARBIDE | 710 | × |
| 32 | URANIUM CARBIDE | 179-221 | × |
| 33 | URANIUM MONOCARBIDE | 172.4 | × |
| 34 | VANADIUM MONOCARBIDE | 614 | × |
| 35 | ZIRCONIUM MONOCARBIDE | 345 | × |
| 36 | ALUMINIUM NITIDE | 346 | × |
| 37 | BORON MONONITRIDE | 85.5 | × |
| 38 | SILICON NITRIDE(BETA) | 55 | × |
| 39 | SILICON NITRIDE(ALPHA) | 304 | × |
| 40 | TITANIUM MONONITRIDE | 248 | × |
| 41 | URANIUM MONONITRIDE | 149 | × |
| 42 | MOLYDBENUM DISILICATE | 407 | × |
| 43 | URANIUM SILICIDE | 77.9 | × |
| 44 | ALUMINIUM SESQUIOXIDE (Al, corundum, sapphire) | 365-393 | × |
| 45 | BERYLLIUM MONOXIDE | 296.5-345 | × |
| 46 | CERIUM DIOXIDE | 181 | × |
| 47 | HAFNIUM DIOXIDE | 57 | × |
| 48 | GADOLINIUM OXIDE | 124 | × |

| S.No. | Material | E(GPa) | Selection |
|---|---|---|---|
| 49 | MAGNESIUM MONOXIDE | 303.4 | × |
| 50 | SAMARIUM OXIDE | 183 | × |
| 51 | SILICIUM DIOXIDE | 72.95 | × |
| 52 | THORIUM DIOXIDE | 144.8 | × |
| 53 | TITANIUM DIOXIDE | 248-282 | × |
| 54 | URANIUM DIOXIDE | 145 | × |
| 55 | YTTRIUM OXIDE | 114.5 | × |
| 56 | ZIRCONIUM DIOXIDE | 241 | × |
| 57 | ZIRCONIUM DIOXIDE PSZ (stabilized with MgO) | 200 | × |
| 58 | ZIRCONIUM DIOXIDE TZP | 200-210 | × |
| 59 | CORNING 0080 | 71 | × |
| 60 | CORNING 7570 | 56 | × |
| 61 | FLOAT GLASS | 72 | × |
| 62 | PYREX 0211 | 76 | × |
| 63 | PYREX 7070 | 52 | × |
| 64 | PYREX 7740 | 76 | × |
| 65 | PYREX 7789 | 64.3 | × |
| 66 | PYREX 7913 | 89 | × |
| 67 | ROBAX | 92 | × |
| 68 | SAPPHIRE GLASS | 379 | × |
| 69 | SCHOTT BaK1 | 73 | × |
| 70 | SCHOTT Bk1 | 74 | × |
| 71 | SCHOTT BK7 | 82 | × |
| 72 | SCHOTT FK3 | 46 | × |
| 73 | SCHOTT FK5 | 62 | × |

| S.No. | Material | E(GPa) | Selection |
|---|---|---|---|
| 74 | SCHOTT FK51 | 81 | × |
| 75 | SCHOTT FK52 | 78 | × |
| 76 | SCHOTT FK54 | 76 | × |
| 77 | SCHOTT K5 | 71 | × |
| 78 | SCHOTT KF9 | 67 | × |
| 79 | SCHOTT LaK9 | 110 | × |
| 80 | SCHOTT LF5 | 59 | × |
| 81 | SCHOTT PK3 | 84 | × |
| 82 | SCHOTT PK50 | 66 | × |
| 83 | SCHOTT PSK3 | 84 | × |
| 84 | SCHOTT SF63 | 58 | × |
| 85 | SCHOTT SK2 | 78 | × |
| 86 | SCHOTT ZKN7 | 70 | × |
| 87 | ACRYLONITRILE BUTADIENE STYRENE | 1.7-2.6 | ✓ |
| 88 | BUTYL RUBBER | 0.3-3.4 | × |
| 89 | CELLULOSE ACETATE | 1.0-4.0 | ✓ |
| 90 | CELLULOSE ACETATE-BUTYRATE | 0.3-2.0 | ✓ |
| 91 | CELLULOSE ACETATE-PROPIONATE | 0.34-1.38 | ✓ |
| 92 | CHLORINATED POLYVINYL CHLORIDE | 2.48-3.0 | ✓ |
| 93 | EXPOXY RESIN | 1.5-3.6 | × |
| 94 | ETHYLENE TETRAFLUORAETHYLENE | 1.4 | ✓ |
| 95 | ETHYLENE CHLOROTRIFLUOROETHYLENE | 1.7 | ✓ |
| 96 | FLUORINATED ETHYLENE PROPYLENE | 0.62 | ✓ |
| 97 | MELAMINE FORMALDEHYDE | 7.6-10 | × |
| 98 | PERFLUORINATED ALKOXY | 0.66 | ✓ |
| 99 | POLYAMIDE-IMIDE | 4.5-6.8 | ✓ |

| S.No. | Material | E(GPa) | Selection |
|---|---|---|---|
| 100 | POLYAMIDE NYLON 11 | 1.5 | × |
| 101 | POLYAMIDE NYLON 12 | 2 | × |
| 102 | POLYAMIDE NYLON 4,6 | 3.1-3.3 | × |
| 103 | POLYAMIDE NYLON 6 | 2.6-3 | ✓ |
| 104 | POLYAMIDE NYLON 6,12 | 2.1 | × |
| 105 | POLYAMIDE NYLON 6,6 | 3.3 | × |
| 106 | POLYARAMIDE | 59-124 | × |
| 107 | POLYARYLATE RESINS | 16.6 | × |
| 108 | POLYBENZENE-IMIDAZOLE | 5.86 | ✓ |
| 109 | POLYBUTADIENE RUBBER | 2.1-10.3 | × |
| 110 | POLYBUTADIENE TEREPHTALATE | 2.6 | ✓ |
| 111 | POLYBUTYLENE | 0.3 | ✓ |
| 112 | POLYCARBONATE | 2.3-2.4 | ✓ |
| 113 | POLYCHLOROPRENE RUBBER | 0.7-20.1 | × |
| 114 | POLYETHER ETHER KERTONE | 3.7-4 | × |
| 115 | POLYETHER IMIDE | 2.9 | × |
| 116 | POLYETHER SULFONE | 2.4-2.6 | × |
| 117 | POLYETHYLENE (HIGH DENSITY) | 0.414-1.24 | ✓ |
| 118 | POLYETHYLENE (LOW DENSITY) | 0.14-1.86 | |
| 119 | POLYETHYLENE (MEDIUM DENSITY) | 0.17-0.38 | |
| 120 | POLYETHYLENE (ULTRA HIGH MOLECULAR WEIGHT) | 0.135-6.9 | |
| 121 | POLYETHYLENE TEREPHTALATE | 2.0-4.0 | ✓ |
| 122 | POLYHYDROXY BUTYRATE | 3.5 | × |

| S.No. | Material | E(GPa) | Selection |
|---|---|---|---|
| | (BIOPOLYMERS) | | |
| 123 | POLYIMIDE | 2.0-3.0 | ✓ |
| 124 | POLYMETHYL METHACRYLATE | 3.036 | ✓ |
| 125 | POLYMETHYL PENTENE | 1.5 | × |
| 126 | POLYOXYMETHYLENE (HETEROPOLYMER) | 2.9-3.2 | ✓ |
| 127 | POLYOXYMETHYLENE (HOMOPOLYMER) | 3.6 | |
| 128 | POLYPHENYLENE OXIDE | 2.5 | ✓ |
| 129 | POLYPHENYLENE SULFIDE | 1350 | ✓ |
| 130 | POLYPROPYLENE (ATACTIC) | 0.689-1.520 | ✓ |
| 131 | POLYPROPYLENE (ISOTACTIC) | 0.689-1.520 | |
| 132 | POLYSTYRENE (HIGH-IMPACT) | 1.6 | ✓ |
| 133 | POLYSTYRENE (NORMAL) | 2.3-4.1 | |
| 134 | POLYSULFONE | 2.48 | ✓ |
| 135 | POLYTETRAFLUROCHLOROETHYLENE | 0.48-0.76 | ✓ |
| 136 | POLYTRIFLUOROCHLOROETHYLENE | 1.3 | ✓ |
| 137 | POLYVINYL ACETATE | 0.6 | × |
| 138 | POPLYVINYL CHLORIDE | 0.3-0.55 | × |
| 139 | POLYVINYLIDENE FLUORIDE | 1.0-3.0 | ✓ |
| 140 | POLYVINYL CHLORIDE | 21.2.7 | ✓ |
| 141 | PROPYLENE-VINYLIDENE HEXAFLOURIDE | 2.07-15.17 | × |
| 142 | STYRENE BUTADIENE RUBBER | 2.1-10.3 | × |

| S.No. | Material | E(GPa) | Selection |
|---|---|---|---|
| 143 | UNPLASTICIZED POLYVINYL CHLORIDE | 24-40 | × |
| 144 | UNSATURATED POLYESTER | 5.5 | × |
| 145 | GRAY CAST IRON GR.20 | 66-97 | × |
| 146 | GRAY CAST IRON GR.25 | 79-102 | × |
| 147 | GRAY CAST IRON GR.30 | 90-113 | × |
| 148 | GRAY CAST IRON GR.35 | 100-119 | × |
| 149 | GRAY CAST IRON GR.40 | 110-138 | × |
| 150 | GRAY CAST IRON GR.50 | 130-157 | × |
| 151 | GRAY CAST IRON GR.60 | 141-162 | × |
| 152 | DUCTILE CAST IRON (SG) | 169-172 | × |
| 153 | COMPACTED GRAPHITE CAST IRON | 165 | × |
| 154 | MALLEABLE CAST IRON | 168 | × |
| 155 | 15-5PH STAINLESS STEEL | 196 | × |
| 156 | 17-4PH STAINLESS STEEL | 196 | × |
| 157 | 17-7PH STAINLESS STEEL | 204 | × |
| 158 | PH 13-8Mo STAINLESS STEEL | 203 | × |
| 159 | ALLOY 20Mo-4 | 186 | × |
| 160 | CARPENTER 20Mo-6 | 186 | × |
| 161 | DURANICKEL 301 | 207 | × |
| 162 | HASTELLOY C276 | 205 | × |
| 163 | HASTELLOY G3 | 199 | × |
| 164 | HASTELLOY HX | 205 | × |
| 165 | HASTELLOY S | 212 | × |
| 166 | HASTELLOY X | 196 | × |
| 167 | HAYNES 230 | 211 | × |
| 168 | HAYNES 556 | 205 | × |

| S.No. | Material | E(GPa) | Selection |
|---|---|---|---|
| 169 | INCOLOY 909 | 159 | × |
| 170 | INCONEL 800 | 193 | × |
| 171 | INCONEL 800HT | 193 | × |
| 172 | INCONEL 825 | 206 | × |
| 173 | INCONEL 600 | 207 | × |
| 174 | INCONEL 601 | 207 | × |
| 175 | INCONEL 617 | 211 | × |
| 176 | INCONEL 625 | 207 | × |
| 177 | INCONEL 690 | 211 | × |
| 178 | INCONEL 718 | 211 | × |
| 179 | INCONEL X-750 | 207 | × |
| 180 | INVAR 36 | 150 | × |
| 181 | INVAR 42 | 144 | × |
| 182 | MONEL 400 | 180 | × |
| 183 | MONEL 450 | 180 | × |
| 184 | MONEL K500 | 180 | × |
| 185 | NIMONIC 80A | 222 | × |
| 186 | 55NI-45TI SMA AUSTENTIC | 83 | × |
| 187 | 55NI-45TI SMA MARTENSITIC | 28-41 | × |
| 188 | WROUGHT & CAST ALUMINIUM ALLOY | 69-73 | × |
| 189 | ADMIRALTY GUN METAL | 105 | × |
| 190 | ALUMINIUM BRONZE (88Cu-9AL-3Fe) | 105 | × |
| 191 | ALUMINIUM BRONZE (81Cu-11AL-4Fe-4NI) | 110 | × |
| 192 | BERYLLIUM COPPER CAST | 110 | × |
| 193 | BERYLLIUM COPPER 20C | 128 | × |

| S.No. | Material | E(GPa) | Selection |
|---|---|---|---|
| 194 | CAST COPPER | 115 | × |
| 195 | CHROMIUM COPPER | 115 | × |
| 196 | HIGH TENSILE BRASS | 105 | × |
| 197 | HYDRAULIC BRONZE | 92 | × |
| 198 | LEADED GUN METAL | 83 | × |
| 199 | SILICON BRASS | 106-138 | × |
| 200 | TIN BRONZE | 105 | × |
| 201 | PURE ZINC | 104.5 | × |
| 202 | ILZRO 16 | 97 | × |
| 203 | KORLOY 2684 | 68-93 | × |
| 204 | ILZRO 12 | 82.7 | × |
| 205 | ZA-27 | 77.9 | × |
| 206 | ZA-8 | 85.5 | × |
| 207 | ZN-CU-TI ALLOY | 63.5-88 | × |
| 208 | TIN ALLOY | - | × |
| 209 | PURE TIN | 49.9 | × |
| 210 | SOFT SOLDER (62Sn-36Pb-2Ag) | 22.96 | × |
| 211 | SOFT SOLDER (60Sn-40Pb) | 29.99 | × |
| 212 | WHITE METAL | 53 | × |
| 213 | LITHIUM | 4.91 | ✓ |
| 214 | SODIUM | 6.8-10 | ✓ |
| 215 | POTASSIUM | 3.53 | ✓ |
| 216 | RUBIDIUM | 2.35 | ✓ |
| 217 | CESIUM | 1.7 | ✓ |
| 218 | BERYLLIUM | 318 | × |

| S.No. | Material | E(GPa) | Selection |
|---|---|---|---|
| 219 | MAGNESIUM | 44.7 | × |
| 220 | CALCIUM | 19.6 | × |
| 221 | STRONTIUM | 15.7 | × |
| 222 | BARIUM | 12.8 | ✓ |
| 223 | TITANIUM | 120.2 | × |
| 224 | ZIRCONIUM | 97.1 | × |
| 225 | HAFNIUM | 137-141 | × |
| 226 | NIOBIUM | 104.9 | × |
| 227 | TANTALUM | 185.7 | × |
| 228 | MOLYBDENUM | 324.8 | × |
| 229 | TUNGSTEN | 411 | × |
| 230 | RUTHENIUM | 413.8-432 | × |
| 231 | RHODIUM | 344.8-379 | × |
| 232 | PALLADIUM | 117.2-121 | × |
| 233 | OSMIUM | 558.6 | × |
| 234 | IRIDIUM | 524-528 | × |
| 235 | PLATINUM | 172.4 | × |
| 236 | THORIUM | 72.4-78.3 | × |
| 237 | URANIUM | 201-176 | × |

# LIST OF PUBLICATIONS

## International Journals

1. **Rathore JS**, and Sharma NN (2010) Engineering Nanorobot: Chronology of Modeling Flagellar Propulsion. J Nanotechnol Eng Med, Transactions of the ASME 1(3) 031001, pp. 1-6.
2. Deepak K, **Rathore JS**, and Sharma NN (2011) Nanorobot Propulsion using Helical Elastic Filamenst at Low Reynolds Numbers. J Nanotechnol Eng Med, Transactions of the ASME 2(1) 011009, pp. 1-6.
3. **Rathore JS**, Majumdar R, and Sharma NN (2012) Planar Wave Propagation Through a Tapered Flagellated Nanoswimmer. IEEE Transactions on Nanotechnology, 11(6), pp. 1117-1121.
4. Majumdar R, Neha S, **Rathore JS**, and Sharma NN (2013) In Search of Materials for Artificial Flagella of Nanoswimmers. Journal of Materials Science, Springer, 48(1), pp. 240-250.
5. Kotesa RS, **Rathore JS**, and Sharma NN (2013) Tapered Flagellated Nanoswimmer: Comparison of Helical Wave and Planar Wave Propulsion. BioNanoScience, Springer, 3(4), pp. 343-347.

## International Conferences

1. Subramanian S, **Rathore JS**, and Sharma NN (2009) Design and Analysis of Helical Flagella Propelled Nanorobots, Proc 4th IEEE International Conference on Micro/Nano Engineered and Molecular Systems (IEEE-NEMS 2009), 5-8 Jan. 2009 Shenzen, China, pp. 950-953.
2. Majumdar R, **Rathore JS**, and Sharma NN (2009) Simulation of Swimming Nanorobots in Biological Fluids, Proc 4th International Conference on Autonomous Robots and Agents (ICARA 2009), 10-12 Feb. Wellington, New Zealand, pp. 79-82.
3. Londhe N, Majumdar R, **Rathore JS**, and Sharma NN (2011) Simulation of Planar Wave Flagellar Propulsion of Nanorobots using Comsol. COMSOL Conference October 13-15, 2011, Boston, US.

4. Kotesa RS, **Rathore JS**, and Sharma NN (2013) Helical Wave Propulsion for a Tapered Flagellum, International Conference on Emerging Technologies: Micro to Nano 2013 (ETMN-2013), BITS-Pilani Goa Campus, 23-24 Feb, 2013.

## Book Chapter(s)

1. Engineering Nanorobot: Past, Present and Future Perspectives. CRC Press (Under review)

# BRIEF BIOGRAPHY OF THE CANDIDATE

**Jitendra Singh Rathore** received the B.E. degree in Mechanical Engineering from M. B. M. Engineering College, Jodhpur, India in 2000, and the M. Tech. degree in Machine Design Engineering from Indian Institute of Technology, Roorkee, India, in 2005. After working for four years in Indian Ordnance Factories Organisation, he joined the Mechanical Engineering Department, Birla Institute of Technology and Science (BITS), Pilani, India, in December 2006, as a faculty member, where he is presently working as a Lecturer. His research interests include nanorobotics, low Reynolds number hydrodynamics and solid mechanics.

# BRIEF BIOGRAPHY OF THE SUPERVISOR

**Prof. (Dr.) Niti Nipun Sharma** completed his B.E. (Mechanical) from REC, Srinagar (now NIT, Srinagar) and M.E. (Mechanical) and Ph.D. both from BITS, Pilani. He is a faculty in Mechanical Engineering Department for over 17 years now currently serving as full Professor in Mechanical Engineering Department. Prof. Sharma served as visiting professor in EPFL, Switzerland during May-August 2014. He is first recipient of Kris Ramachandran best faculty award in 2010 at BITS, Pilani.

Prof. Sharma specialized in Robotics and was a part of team which developed 'ACYUT', the humanoid from BITS. He later during his Ph.D. worked on dynamics of nanorobots proposed a simple method to include modeling of Brownian motion attributable to thermal agitation to predict the dynamics of Nanorobots. His methodology of analyzing synergism in local and global motion of non-rigid kind of nanoparticles due to thermal agitation from surrounding medium has recently been shown to model radiation of nanoparticle validating with Planck's Radiation Law.

Three patents, over 70 technical papers in high impact factor journals and peer reviewed National and International conferences, around two dozen invited/keynote talks in India and abroad and with ten funded projects from nodal agencies like DBT, UGC, CSIR-CEERI, NPMASS and Industries, currently Prof. Sharma is working in Interdisciplinary areas of MEMS and Nanotechnology.

He is Guest Editor, Journal of Bionanoscience (Springer), Associate Editor of International Journal of Smart Sensors and Intelligent Systems, has reviewed many articles for IEEE Tr. Systems, Man and Cybernetics, IEEE Tr. Education, has been on-board of many Technical Committees of reputed National and International Conference. He was co-chair for Int. Conf. on Emerging Technologies (ETMN 2013), International Conference on Emerging Mechanical Technology Macro to Nano (EMTM2N-2007), co-organized 2$^{nd}$ ISSS-MEMS-2007 conference with CEERI, Pilani and organized Northern Region NPMASS MEMS Software Training Program from 19-24 Feb. 2011.

Prof. Sharma also holds the post of Dean, Academic Registration & Counseling Division at BITS, Pilani since 2010.